

**ACTIVATED CARBON FROM OIL-PALM SOLID
WASTES: PREPARATION AND CFD SIMULATION
OF SPOUTED BED ACTIVATOR**

Pornthep Luangkiattikhun

A Thesis Submitted in Fulfillment of the Requirements for the

Degree of Doctor of Philosophy in Chemical Engineering

Suranaree University of Technology

Academic Year 2007

ถ่านกัมมันต์จากกากผลปาล์มน้ำมัน: การเตรียม และการจำลองแบบ
เตากระตุ้นชนิดสเปาท์เบดโดยวิธีพลศาสตร์ของไหลเชิงคำนวณ

นายพรเทพ เหลืองเกียรติคุณ

วิทยานิพนธ์นี้เป็นส่วนหนึ่งของการศึกษาตามหลักสูตรปริญญาวิศวกรรมศาสตรดุษฎีบัณฑิต
สาขาวิชาวิศวกรรมเคมี
มหาวิทยาลัยเทคโนโลยีสุรนารี
ปีการศึกษา 2550

พรเทพ เหลืองเกียรติคุณ : ถ่านกัมมันต์จากกากผลปาล์มน้ำมัน : การเตรียม และการจำลองแบบเตากระตุ้นชนิดสเปาท์เบดโดยวิธีพลศาสตร์ของไหลเชิงคำนวณ (ACTIVATED CARBON FROM OIL PALM SOLID WASTES: PREPARATION AND CFD SIMULATION OF SPOUTED BED ACTIVATOR) อาจารย์ที่ปรึกษา : รองศาสตราจารย์ ดร.ชัยยศ ตั้งสติย์กุลชัย, 285 หน้า.

งานวิจัยนี้มีวัตถุประสงค์เพื่อศึกษาพฤติกรรมอุทกพลศาสตร์ และ จลนพลศาสตร์ ของปฏิกิริยาการกระตุ้นถ่านกัมมันต์จากกะลาปาล์มน้ำมันด้วยก๊าซคาร์บอนไดออกไซด์ ในเตากระตุ้นแบบสเปาท์เบด โดยใช้วิธีการสร้างแบบจำลองพลศาสตร์ของไหลเชิงคำนวณ ขอบเขตของงานวิจัยนี้ได้ครอบคลุมถึงการวิเคราะห์การสลายตัวทางความร้อนของกากผลปาล์มน้ำมัน ซึ่งประกอบด้วยกะลาปาล์ม กากใย และ กากเมล็ดใน การเตรียมถ่านกัมมันต์จากกากผลปาล์มน้ำมันในเตาเผาแบบท่อ และ แบบสเปาท์เบด และ การเสนอการปรับปรุงแบบจำลองกระบวนการกระตุ้นถ่านกัมมันต์ที่เสนอโดย สุพรรณิ จันท์ภิรมย์และคณะ เพื่อทำนายคุณลักษณะรูพรุนของถ่านกัมมันต์ (พื้นที่ผิว และ ปริมาตรรวมของรูพรุน) ที่เตรียมได้

การสลายตัวทางความร้อนของกากผลปาล์มน้ำมัน ในกระบวนการไพโรไลซิส เกิดขึ้นในช่วงอุณหภูมิระหว่าง 250-400 องศาเซลเซียส สำหรับกะลาปาล์ม 200-400 องศาเซลเซียส สำหรับ กากใยปาล์ม และ 200-350 องศาเซลเซียส สำหรับกากเมล็ดใน การสลายตัวของกะลา และ กากใยปาล์มสามารถอธิบายได้ด้วยแบบจำลองปฏิกิริยาคู่ขนาน ในขณะที่กากเมล็ดในสามารถอธิบายด้วยแบบจำลองปฏิกิริยาเดี่ยว ในส่วนของการเตรียมถ่านกัมมันต์จากกากผลปาล์มน้ำมันในเตาเผาแบบท่อ พบว่า ถ่านกัมมันต์ที่เตรียมจากกะลา และ กากใยปาล์ม ประกอบด้วยรูพรุนขนาดเล็กเป็นส่วนใหญ่ ในขณะที่ถ่านกัมมันต์ที่เตรียมได้จากกากเมล็ดในปาล์ม มีรูพรุนขนาดกลางในสัดส่วนที่มากกว่า สภาวะการเตรียมถ่านกัมมันต์ที่ให้พื้นที่ผิวสูงสุดคือ สภาวะกระตุ้นที่ 950 องศาเซลเซียส เป็นเวลา 2 ชั่วโมง สำหรับกะลาปาล์ม สภาวะกระตุ้นที่ 850 องศาเซลเซียส เป็นเวลา 2 ชั่วโมง สำหรับกากใยปาล์ม และ สภาวะกระตุ้นที่ 850 องศาเซลเซียส เป็นเวลา 2.5 ชั่วโมง สำหรับกากเมล็ดในปาล์ม สภาวะการเตรียมถ่านกัมมันต์ดังกล่าวนี้ให้ค่าร้อยละน้ำหนักที่หายไปในช่วงขั้นตอนการกระตุ้นเท่ากับ 48 52 และ 66 โดยพื้นที่ผิวสูงสุดที่ได้คือ 1067 522 และ 789 ตารางเมตรต่อกรัม สำหรับกะลาปาล์ม กากใยปาล์ม และ กากเมล็ดในปาล์ม ตามลำดับ สำหรับการปรับปรุงแบบจำลองการกระตุ้น เพื่อทำนายคุณลักษณะรูพรุนของถ่านกัมมันต์ที่เตรียมได้ พบว่าแบบจำลองการกระตุ้นถ่านกัมมันต์ที่ผ่านการปรับปรุงในงานนี้ สามารถทำนายคุณลักษณะรูพรุนของถ่านกัมมันต์ได้ถูกต้องสมบูรณ์ดีกว่าแบบจำลองเดิม

ในการจำลองแบบเตากระตุ้นชนิดสเปาท์เบดโดยวิธีพลศาสตร์ของไหลเชิงคำนวณ พบว่าแบบจำลองนี้ทำนายค่าความเร็วต่ำสุดที่เกิดสภาวะสเปาท์เบดต่ำกว่าค่าที่วัดได้จากการทดลอง และสมการอัตราเร็วการเกิดปฏิกิริยาแก๊สซิฟิเคชันที่นำเสนอในแบบจำลองพลศาสตร์ของไหลเชิงคำนวณ เพื่อทำนายกระบวนการกระตุ้นถ่านกัมมันต์ได้ดีที่สุดคือ

$$\text{อัตราเร็วการเกิดปฏิกิริยาแก๊สซิฟิเคชัน} = [7.57 \times 10^{-1} \text{ s}^{-1}][\text{CO}_2]$$

เมื่อ $[\text{CO}_2]$ คือความเข้มข้นของก๊าซคาร์บอนไดออกไซด์ในหน่วย โมลต่อลูกบาศก์เมตร

แบบจำลองการกระตุ้นถ่านกัมมันต์ ที่ได้นำเสนอก่อนหน้านี้ สามารถนำมารวมกับผลการคำนวณที่ได้จากแบบจำลองพลศาสตร์ของไหลเชิงคำนวณของเตากระตุ้นชนิดสเปาท์เบด เพื่อใช้ในการทำนาย พื้นที่ผิว และ ปริมาตรรวมของรูพรุนของถ่านกัมมันต์ ที่เตรียมได้จากเตาเผาแบบสเปาท์เบด ซึ่งพบว่า แบบจำลองการกระตุ้นดังกล่าวสามารถทำนายค่า พื้นที่ผิว และ ปริมาตรรวมของรูพรุนของถ่านกัมมันต์ได้อย่างแม่นยำ

สาขาวิชาวิศวกรรมเคมี

ปีการศึกษา 2550

ลายมือชื่อนักศึกษา พรเทพ นิลอภัยเชิดบุญ

ลายมือชื่ออาจารย์ที่ปรึกษา วิชา วิชาเคมี

ลายมือชื่ออาจารย์ที่ปรึกษาร่วม วิชา วิชาเคมี

PORNTHEP LUANGKIATTIKHUN : ACTIVATED CARBON FROM OIL
PALM SOLID WASTES: PREPARATION AND CFD SIMULATION OF
SPOUTED BED ACTIVATOR. THESIS ADVISOR : ASSOC. PROF.
CHAIYOT TANGSATHITKULCHAI, PhD. 285 PP.

ACTIVATED CARBON / OIL-PALM SOLID WASTES / CFD SIMULATION

The overall objective of this thesis research was to perform a systematic study on the hydrodynamic behavior and kinetic characteristics of CO₂ activation of activated carbon from oil-palm shell in a spouted bed activator using CFD simulation technique. To achieve this aim, the following tasks were also included in this work: thermal analysis of oil-palm solid wastes (oil-palm shell, fiber and kernel cake) using Thermal Gravimetric Analysis (TGA) technique, preparation of activated carbons under different conditions in a laboratory tube furnace and a spouted bed activator, and the improvement of carbon activation model originally proposed by Junpirom et al. (JDTT model) to allow better prediction of porous properties (BET surface area and total pore volume) of the prepared activated carbons.

The TGA technique showed that the main decomposition occurred over the temperature range of 250-400°C for palm shell, 200-400°C for palm fiber, and 200-350°C for palm kernel cake. Thermal decomposition behavior could be best described by the proposed two-parallel reactions model for palm shell and fiber prepared in this work, while the simplest one-step global model worked well for palm kernel. On the preparation of activated carbon in a tube furnace, the palm shell and fiber gave microporosity based activated carbons, while the palm kernel cake carbon possessed

higher proportion of mesoporosity. The optimum activation conditions that gave the maximum in surface area were found to be 950°C and 2.0 hrs for palm shell, 850°C and 2.0 hrs for fiber, and 900°C and 2.5 hrs for palm kernel cake, corresponding to 48%, 52% and 66% of char burn-offs, respectively. The maximum BET surface area obtained were 1067, 522 and 789 m²/g for activated carbons produced from shell, fiber and kernel cake, respectively.

The modified JDTT model for predicting the evolution of pore volume, internal surface area, and pore size distribution of prepared activated carbon with respect to the extent of gasification of char was proposed. This modified model gave significant improvement in predicting the porous properties of prepared activated carbon compared to the original JDTT model.

The CFD modeling was used for simulating the CO₂ activation scheme in the spouted bed activator in terms of burn-off extents. The rate expression that was used to describe the kinetics of activation reaction was found to be:

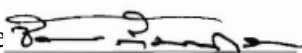
$$\text{Gasification Rate} = [7.57 \times 10^1 \text{ s}^{-1}][\text{CO}_2]$$

By combining the modified JDTT model with the CFD simulated results of char burn-off, it was found possible to estimate accurately the porous properties of activated carbon produced in the spouted bed activator.

School of Chemical Engineering

Academic Year 2007

Student's Signature Pornthep L.

Advisor's Signature 

Co-advisor's Signature 

ACKNOWLEDGEMENTS

With the achievement of this thesis, I would like to express my deep and sincere gratitude to my thesis advisor, Assoc. Prof. Dr. Chaiyot Tangsathitkulchai, for giving me the opportunity to pursue my Ph.D. study. My special thanks are also extended to my co-advisor, Assoc. Prof. Dr. Malee Tangsathitkulchai. Their broad knowledge and their logical way of thinking have been of great value for me. Their understanding, encouraging and personal guidance have provided a good basis for the present thesis. Also, my deep appreciation is extended to Prof. Dr. Doung D. Do who is a great supervisor during my research time at the University of Queensland, Australia.

I am also thankful to Dr. Terasut Sookkumnerd, Assoc. Prof. Dr. Nurak Grisadanurak, and Asst. Prof. Dr. Ratanawan Kiattikomol for their serving as my thesis defense committee and also for their many valuable comments and suggestions.

Also, I would like to sincerely thank to all the academic members in the School of Chemical Engineering, for their educating, support and encouragement. Especially, Assoc. Prof. Dr. Kasem Prabripataloong, Assoc. Prof. Dr. Chaiyot Tangsathitkulchai, Asst. Prof. Dr. Chalongsri Flood, Asst. Prof. Dr. Ratanawan Kiattikomol, Assoc. Prof. Dr. Adrian E. Flood, and Dr. Terasut Sookkumnerd for teaching me the spirit and importance of chemical engineering profession.

The assistances from the technical staffs in the Center for Science and Technology Equipment are acknowledged, especially, Mr. Saran Dokmaikul, Miss

Rungruang Nuanpho. My thank also goes to Mrs. Amporn Ladnongkun for her skillful secretarial work in the School of Chemical Engineering.

Finally, I would like to acknowledge the Thailand Research Fund (TRF) for financial support through the Royal Golden Jubilee Ph.D. Program.

Pornthep Luangkiattikhun

TABLE OF CONTENTS

	Page
ABSTRACT (THAI)	I
ABSTRACT (ENGLISH).....	III
ACKNOWLEDGEMENT	V
TABLE OF CONTENTS.....	VII
LIST OF TABLES	XII
LIST OF FIGURES	XV
SYMBOLS AND ABBREVIATIONS.....	XXXV
CHAPTER	
I INTRODUCTION	1
1.1 Rational of the Study	1
1.2 Research Objectives.....	11
1.3 Scope and Limitations.....	12
1.4 References.....	13
II NON-ISOTHERMAL THERMOGRAVIMETRIC	
ANALYSYS OF OIL-PALM SOLID WASTES	15
2.1 Abstract.....	15
2.2 Introduction.....	16
2.3 Review of the Literatures.....	17

TABLE OF CONTENTS (Continued)

	Page
2.4 Model Description	19
2.5 Research Methods.....	24
2.6 Results and Discussion	25
2.6.1 Analysis of Thermograms	26
2.6.2 One-Step Global Model.....	35
2.6.3 Two-Step Consecutive model	39
2.6.4 Two-Parallel Reactions Model.....	43
2.7 Conclusions.....	51
2.8 References.....	53
III PREPARATION OF ACTIVATED CARBON IN A	
LABORATORY TUBE FURNACE	56
3.1 Abstract.....	56
3.2 Introduction.....	57
3.3 Review of the Literatures.....	59
3.4 Research Methods.....	62
3.5 Results and Discussion	64
3.5.1 Carbonization of Palm Shell.....	64
3.5.2 Carbonization of Palm Fiber and Kernel Cake	73
3.5.2.1 Palm Fiber Char	74
3.5.2.2 Palm Kernel Cake Char	79

TABLE OF CONTENTS (Continued)

	Page
3.5.3 CO ₂ Activation of Palm Solid Wastes.....	82
3.6 Conclusions.....	123
3.7 References.....	124
IV AN IMPROVED CARBON ACTIVATION MODEL FOR PREDICTING THE PORE DEVELOPMENT OF ACTIVATED CARBON	129
4.1 Abstract.....	129
4.2 Introduction.....	130
4.3 Review of the Literatures.....	132
4.4 Model Description	133
4.5 Research Methods.....	139
4.5.1 Preparation of Char	139
4.5.2 Gasification of Char and Characterization of Activated Carbon.....	140
4.6 Results and Discussion	140
4.6.1 Model Testing with Gasification Data of Longan Seed Char	141
4.6.2 Gasification of Palm Shell.....	147
4.6.3 Gasification of Palm Fiber.....	151
4.7 Conclusions.....	155

TABLE OF CONTENTS (Continued)

	Page
4.8 References.....	155
V CFD SIMULATION OF HYDRODYNAMICS AND CHAR ACTIVATION PROCESS IN A CYLINDRICAL SPOUTED BED	157
5.1 Abstract.....	157
5.2 Introduction.....	159
5.3 Review of the Literatures.....	164
5.4 CFD Model Description.....	175
5.4.1 Conservation Equations of Mass and Momentum	176
5.4.2 Kinetic Theory of Granular Flow (KTGF).....	178
5.4.3 Turbulence Model	183
5.4.4 Drag Force Model	185
5.4.5 Kinetics of Activation Reaction	186
5.4.6 Simulation Procedure	189
5.5 Research Methods.....	191
5.5.1 Experimental Study of Spouted Bed Hydrodynamics	191
5.5.2 Preparation of Activated carbons in the Spouted Bed Activator	193

TABLE OF CONTENTS (Continued)

	Page
5.5.3 CFD Simulation of Spouted bed	
Hydrodynamics	196
5.5.4 CFD Simulation of Spouted Bed Activator.....	199
5.6 Results and Discussion	201
5.6.1 Hydrodynamic Study of Spouted Bed.....	201
5.6.2 Preparation of Activated carbons in the	
Spouted Bed Activator	233
5.6.3 Hydrodynamic Study of Spouted Bed by CFD	
Simulation	240
5.6.4 CFD Simulation of Spouted Bed Activator.....	260
5.7 Conclusions.....	266
5.8 References.....	269
VI CONCLUSIONA AND RECOMMENDATIONS	276
6.1 Conclusions.....	276
6.2 Recommendations for Future Work	280
APPENDIX LIST OF PUBLICATIONS	283
BIOGRAPHY	285

LIST OF TABLES

Table	Page
2.1	Proximate and ultimate analyses of palm shell, fiber and kernel cake 25
2.2	First and second maximum rate of decomposition and corresponding temperatures of palm solid wastes 35
2.3	Kinetic parameters of one-step global model for pyrolysis of palm shell, fiber and kernel cake 38
2.4	Kinetic parameters of two-step consecutive model for pyrolysis of palm shell, fiber and kernel cake 43
2.5	Kinetic parameters (a , A_1 , E_1 , A_2 , E_2 and n) of the two-parallel reactions model for pyrolysis of palm shell, fiber and kernel cake 48
2.6	Kinetic parameters of two parallel reactions model for pyrolysis of coconut shell, bagasse, Longan seed, cassava waste pyrolyzed at 10 °C/min 51
3.1	Proximate and ultimate analysis of the palm shell, fiber and kernel cake 63
3.2	Yield, iodine number and proximate analysis of the palm shell chars prepared at various carbonization conditions 66
3.3	Yield, iodine number and proximate analysis of the palm fiber chars prepared at various carbonization conditions 77

LIST OF TABLES (Continued)

Table	Page
3.4	Yield, iodine number and proximate analysis of the palm kernel cake chars prepared at various carbonization conditions 80
3.5	Effect of activation temperature, activation time, CO ₂ flow rate and concentration on percentage burn-off and the porous properties of palm shell based activated carbons 84
3.6	Effect of activation temperature, activation time, CO ₂ flow rate and concentration on percentage burn-off and the porous properties of palm fiber based activated carbons 85
3.7	Effect of activation temperature, activation time, CO ₂ flow rate and concentration on percentage burn-off and the porous properties of palm kernel based activated carbons..... 86
4.1	Comparison between the original JDTT model by Junpirom et al. (2005) and the present modified model 139
5.1	Comparison between the two-fluid and particle transport models 177
5.2	Simulation parameters for CFD simulation of spouted bed..... 199
5.3	Simulation conditions for CFD simulation of spouted bed activator 200
5.4	Minimum spouting velocity (U_{MS}) of spouted bed (experimentally determined) for various geometric factors, particle sizes and static bed heights and U_{MS} calculated from Equation (5.1)..... 217

LIST OF TABLES (Continued)

Table	Page
5.5	Minimum spouting velocity (U_{MS}) of spouted bed (experimentally determined) for various geometric factors, particle sizes and static bed heights and U_{MS} calculated from Equation.(5.45)..... 222
5.6	Minimum spouting velocity (U_{MS}) of spouted bed (experimentally determined) for various geometric factors, particle sizes and bed heights, U_{MS} calculated from Equation (5.51) 227
5.7	Minimum spouting velocity (U_{MS}) of spouted bed (experimentally determined) for various geometric factors, particle sizes and bed heights, and U_{MS} calculated from Equation (5.53)..... 230
5.8	Comparison between Minimum spouting velocity results (U_{MS}) of Zhong et al., 2007 for $\theta = 60^\circ$, $D_I = 0.01$ m, $d_p = 2.3$ mm, and $D_C = 0.10$ m at various pressure and static bed height, and U_{MS} calculated from Equation (5.53) 232

LIST OF FIGURES

Figure	Page
1.1 Pore size distribution in some activated carbons obtained using different precursors (Bansal et al, 1988)	3
1.2 Schematic representation of activated carbon structure	4
1.3 Active edge sites of carbon layer.....	4
1.4 Fresh oil-palm fruit and its longitudinal section.....	7
1.5 Oil-palm production in Thailand and worldwide since 1961 to 2006 (FAO, 2006)	8
2.1 TG and DTG data of palm shell pyrolyzed at heating rate of 20°C/min	28
2.2 TG and DTG data of palm fiber pyrolyzed at heating rate of 20°C/min	28
2.3 TG and DTG data of palm kernel cake pyrolyzed at heating rate of 20°C/min	29
2.4 TG and DTG data of palm shell pyrolyzed at heating rate of 20°C/min for various particle sizes	30
2.5 TG and DTG data of palm shell pyrolyzed at particle size 0.36 mm for various heating rate.....	32
2.6 TG and DTG data of palm fiber pyrolyzed at different heating rate.....	33

LIST OF FIGURES (Continued)

Figure	Page
2.7	TG and DTG data of palm kernel cake cake pyrolyzed at different heating rates..... 34
2.8	TG data and one-step global model fitting of palm shell 36
2.9	TG data and one-step global model fitting of palm fiber 37
2.10	TG data and one-step global model fitting of palm kernel cake 37
2.11	TG data and two-step consecutive model fitting of palm shell 41
2.12	TG data and two-step consecutive model fitting of palm fiber 41
2.13	TG data and two-step consecutive model fitting of palm kernel cake 42
2.14	TG data and two-parallel reaction model fitting for palm shell pyrolyzed at heating rate of 20°C /min for different particle sizes..... 44
2.15	TG data and two-parallel reaction model fitting for palm shell pyrolyzed for particle sizes of 0.36 mm at different heating rates 45
2.16	TG data and two-parallel reaction model fitting for palm fiber pyrolyzed at different heating rates 45
2.17	TG data and two-parallel reaction model fitting for palm kernel cake pyrolyzed at different heating rates 46
2.18	TG data and model fitting for coconut shell pyrolyzed at 10°C/min..... 49
2.19	TG data and model fitting for bagasse pyrolyzed at 10°C/min 50
2.20	TG data and model fitting for longan seed pyrolyzed at 10°C/min..... 50

LIST OF FIGURES (Continued)

Figure	Page
2.21 TG data and model fitting for cassava waste residue pyrolyzed at 10°C/min.....	51
3.1 Effect of carbonization temperature on the final yield of the palm shell chars for particle size of 1.4 mm carbonized at heating rate of 5°C/min and 1.0 hr of holding time	67
3.2 Effect of carbonization temperature on the iodine number of the palm shell chars for particle size of 1.4 mm carbonized at heating rate of 5°C/min and 1.0 hr of holding time.....	67
3.3 Effect of particle size on the final yield and iodine number of the palm shell chars carbonized at 600°C, 5°C/min of heating rate, and 1.0 hr of holding time	68
3.4 Effect of particle size on the final yield and iodine number of the palm shell chars carbonized at 600°C, 5°C/min of heating rate, and 1.0 hr of holding time	68
3.5 Effect of heating rate on the final yield of the palm shell chars for particle size of 1.4 mm carbonized at 1.0 hr of holding time.....	70
3.6 Effect of heating rate on the final yield and iodine number of the palm shell chars for particle size of 1.4 mm carbonized at 1.0 hr of holding time	71

LIST OF FIGURES (Continued)

Figure	Page
3.7	Effect of holding time on the final yield and iodine number of the palm shell chars for particle size of 1.4 mm carbonized at heating rate of 5°C/min 72
3.8	Effect of holding time on the final yield and iodine number of the palm shell chars for particle size of 1.4 mm carbonized at heating rate of 5°C/min 72
3.9	Effect of carbonization temperature on the final yield of the palm fiber chars carbonized at heating rate of 5°C/min and 1.0 hr of holding time..... 75
3.10	Effect of holding time on the final yield of the palm fiber chars carbonized at 1.0 hr of holding time..... 76
3.11	Effect of heating rate on the final yield of the palm fiber chars carbonized at 5°C/min of heating rate 76
3.12	Effect of carbonization temperature on the final yield of the palm kernel cake chars carbonized at heating rate of 5°C/min and 1.0 hr of holding time 79
3.13	Effect of holding time on the final yield of the palm kernel cake chars carbonized at 5°C/min of heating rate..... 81
3.14	Effect of heating rate on the final yield of the palm kernel cake chars carbonized at 1.0 hr of holding time 82

LIST OF FIGURES (Continued)

Figure	Page
3.15	Effect of activation temperature on char burn-off of the palm shell based activated carbon activated with pure CO ₂ for 2.0 hrs 87
3.16	Effect of activation temperature on BET surface area of the palm shell based activated carbon activated with pure CO ₂ for 2.0 hrs 87
3.17	Effect of activation temperature on total pore volume of the palm shell based activated carbon activated with pure CO ₂ for 2.0 hrs 88
3.18	Effect of activation time on char burn-off of the palm shell based activated carbon activated at 900°C 88
3.19	Effect of activation time on BET surface area of the palm shell based activated carbon activated at 900°C 89
3.20	Effect of activation time on total pore volume of the palm shell based activated carbon activated at 900°C 89
3.21	Effect of activation temperature on average pore size of the palm shell based activated carbon activated with pure CO ₂ for 2.0 hrs 90
3.22	Effect of activation time on average pore size of the palm shell based activated carbon activated at 900°C 90
3.23	Effect of activation temperature on percentage microporosity of the palm shell based activated carbon activated with pure CO ₂ for 2.0 hrs 91

LIST OF FIGURES (Continued)

Figure	Page
3.24	Effect of activation time on percentage microporosity of the palm shell based activated carbon activated at 900°C..... 91
3.25	Effect of CO ₂ flow rate on char burn-off of the palm shell based activated carbon activated at 900°C with pure CO ₂ for 2.0 hrs..... 92
3.26	Effect of CO ₂ flow rate on BET surface area of the palm shell based activated carbon activated at 900°C with pure CO ₂ for 2.0 hrs..... 93
3.27	Effect of CO ₂ flow rate on total pore volume of the palm shell based activated carbon activated at 900°C with pure CO ₂ for 2.0 hrs..... 93
3.28	Effect of CO ₂ flow rate on percentage microporosity of the palm shell based activated carbon activated at 900°C with pure CO ₂ for 2.0 hrs 94
3.29	Effect of CO ₂ flow rate on average pore size of the palm shell based activated carbon activated at 900°C with pure CO ₂ for 2.0 hrs..... 94
3.30	Effect of CO ₂ concentration on char burn-off of the palm shell based activated carbon activated at 900°C for 2.0 hrs..... 96
3.31	Effect of CO ₂ concentration on BET surface area of the palm shell based activated carbon activated at 900°C for 2.0 hrs..... 96
3.32	Effect of CO ₂ concentration on total pore volume of the palm shell based activated carbon activated at 900°C for 2.0 hrs..... 97

LIST OF FIGURES (Continued)

Figure	Page
3.33	Effect of CO ₂ concentration on percentage microporosity of the palm shell based activated carbon activated at 900°C for 2.0 hrs 97
3.34	Effect of CO ₂ concentration on average pore size of the palm shell based activated carbon activated at 900°C for 2.0 hrs..... 98
3.35	Effect of activation temperature on char burn-off of the palm fiber based activated carbon activated with pure CO ₂ for 2.0 hrs 99
3.36	Effect of activation temperature on BET surface area of the palm fiber based activated carbon activated with pure CO ₂ for 2.0 hrs 99
3.37	Effect of activation temperature on total pore volume of the palm fiber based activated carbon activated with pure CO ₂ for 2.0 hrs 100
3.38	Effect of activation temperature on percentage microporosity of the palm fiber based activated carbon activated with pure CO ₂ for 2.0 hrs 100
3.39	Effect of activation temperature on average pore size of the palm fiber based activated carbon activated with pure CO ₂ for 2.0 hrs 101
3.40	Effect of activation time on char burn-off of the palm fiber based activated carbon activated at 850°C with pure CO ₂ 101
3.41	Effect of activation time on BET surface area of the palm fiber based activated carbon activated at 850°C with pure CO ₂ 102

LIST OF FIGURES (Continued)

Figure	Page
3.42	Effect of activation time on total pore volume of the palm fiber based activated carbon activated at 850°C with pure CO ₂ 102
3.43	Effect of activation time on average pore size of the palm fiber based activated carbon activated at 850°C with pure CO ₂ 103
3.44	Effect of activation time on percentage microporosity of the palm fiber based activated carbon activated at 850°C with pure CO ₂ 103
3.45	Effect of CO ₂ flow rate on char burn-off of the palm fiber based activated carbon activated at 850°C with pure CO ₂ for 2.0 hrs..... 105
3.46	Effect of CO ₂ flow rate on BET surface area of the palm fiber based activated carbon activated at 850°C with pure CO ₂ for 2.0 hrs..... 105
3.47	Effect of CO ₂ flow rate on total pore volume of the palm fiber based activated carbon activated at 850°C with pure CO ₂ for 2.0 hrs..... 106
3.48	Effect of CO ₂ flow rate on percentage microporosity of the palm fiber based activated carbon activated at 850°C with pure CO ₂ for 2.0 hrs 106
3.49	Effect of CO ₂ flow rate on average pore size of the palm fiber based activated carbon activated at 850°C with pure CO ₂ for 2.0 hrs..... 107
3.50	Effect of CO ₂ concentration on char burn-off of the palm shell based activated carbon activated at 850°C for 2.0 hrs..... 107

LIST OF FIGURES (Continued)

Figure	Page
3.51	Effect of CO ₂ concentration on BET surface area of the palm fiber based activated carbon activated at 850°C for 2.0 hrs..... 108
3.52	Effect of CO ₂ concentration on total pore volume of the palm fiber based activated carbon activated at 850°C for 2.0 hrs..... 108
3.53	Effect of CO ₂ concentration on average pore size of the palm fiber based activated carbon activated at 850°C for 2.0 hrs..... 109
3.54	Effect of CO ₂ concentration on percentage microporosity of the palm fiber based activated carbon activated at 850°C for 2.0 hrs 109
3.55	Effect of activation temperature on char burn-off of the palm kernel cake based activated carbon activated with pure CO ₂ for 2.0 hrs 110
3.56	Effect of activation temperature on BET surface area of the palm kernel cake based activated carbon activated with pure CO ₂ for 2.0 hrs 111
3.57	Effect of activation temperature on total pore volume of the palm kernel cake based activated carbon activated with pure CO ₂ for 2.0 hrs 111
3.58	Effect of activation temperature on average pore size of the palm kernel cake based activated carbon activated with pure CO ₂ for 2.0 hrs 112

LIST OF FIGURES (Continued)

Figure	Page
3.59	Effect of activation temperature on percentage microporosity of the palm kernel cake based activated carbon activated with pure CO ₂ for 2.0 hrs 112
3.60	Effect of activation time on char burn-off of the palm kernel cake based activated carbon activated at 900°C with pure CO ₂ 113
3.61	Effect of activation time on BET surface area of the palm kernel cake based activated carbon activated at 900°C with pure CO ₂ 113
3.62	Effect of activation time on total pore volume of the palm kernel cake based activated carbon activated at 900°C with pure CO ₂ 114
3.63	Effect of activation time on average pore size of the palm kernel cake based activated carbon activated at 900°C with pure CO ₂ 114
3.64	Effect of activation time on percentage microporosity of the palm kernel cake based activated carbon activated at 900°C with pure CO ₂ 115
3.65	Effect of CO ₂ flow rate on char burn-off of the palm kernel cake based activated carbon activated at 850°C with pure CO ₂ for 2.0 hrs..... 115
3.66	Effect of CO ₂ flow rate on BET surface area of the palm kernel cake based activated carbon activated at 900°C with pure CO ₂ for 2.0 hrs..... 116
3.67	Effect of CO ₂ flow rate on total pore volume of the palm kernel cake based activated carbon activated at 900°C with pure CO ₂ for 2.0 hrs..... 116

LIST OF FIGURES (Continued)

Figure	Page
3.68	Effect of CO ₂ flow rate on average pore size of the palm kernel cake based activated carbon activated at 900°C with pure CO ₂ for 2.0 hrs..... 117
3.69	Effect of CO ₂ flow rate on percentage microporosity of the palm kernel cake based activated carbon activated at 900°C with pure CO ₂ for 2.0 hrs..... 117
3.70	Effect of CO ₂ concentration on char burn-off of the palm kernel cake based activated carbon activated at 900°C for 2.0 hrs..... 118
3.71	Effect of CO ₂ concentration on BET surface area of the palm kernel cake based activated carbon activated at 900°C for 2.0 hrs 118
3.72	Effect of CO ₂ concentration on total pore volume of the palm kernel cake based activated carbon activated at 900°C for 2.0 hrs 119
3.73	Effect of CO ₂ concentration on average pore size of the palm kernel cake based activated carbon activated at 900°C for 2.0 hrs 119
3.74	Effect of CO ₂ concentration on percentage microporosity of the palm kernel cake based activated carbon activated at 900°C for 2.0 hrs 120
3.75	Effect of char burn-off on BET surface area..... 121
3.76	Effect of char burn-off on total pore volume 121
3.77	N ₂ adsorption isotherm at -196°C of activated carbons prepared at optimum conditions..... 122

LIST OF FIGURES (Continued)

Figure	Page
3.78	Pore size distribution of activated carbons prepared at optimum conditions, determined by DFT model (El-Merraoui et al., 2000)..... 123
4.1	Schematic diagram of graphite structure 131
4.2	Schematic diagram of char structure 134
4.3	Schematic diagram of a crystallite structure 134
4.4	Schematic representation of pore size, surface area, and total pore volume of graphite crystallite at any char burn-offs 137
4.5	Experimental data and simulated results of surface area of longan seed based activated carbons 142
4.6	Experimental data and simulated results of total pore volume of longan seed based activated carbons 142
4.7	Experimental data and simulated results of total pore volume for various maximum number of burnt out layers of longan seed based activated carbons 143
4.8	Experimental and computed pore size distributions of longan seed based activated carbons at 47.2 % burn-off 145
4.9	Experimental and computed pore size distributions of longan seed based activated carbons at 90.1% burn-off 146
4.10	The simulated pore size distributions of longan seed based activated carbons at various degrees of char burn-off 146

LIST OF FIGURES (Continued)

Figure	Page
4.11	Experimental data and simulated results of surface area of palm shell based activated carbons 148
4.12	Experimental data and simulated results of total pore volume of palm shell based activated carbons 148
4.13	Experimental and computed pore size distributions of palm shell based activated carbons at 48.5 % burn-off 150
4.14	Extrapolation of cumulative pore volume at small pore size for calculation of PSD of palm shell based activated carbons 150
4.15	Experimental, computed and extrapolated pore size distributions and of palm shell based activated carbons at 48.5 % burn-off..... 151
4.16	Experimental data and simulated results of surface area of oil-palm fiber based activated carbons 152
4.17	Experimental data and simulated results of total pore volume of oil-palm fiber based activated carbons 153
4.18	Experimental and computed pore size distributions of oil-palm fiber based activated carbons at 56.5 % burn-off 154
4.19	Experimental, computed and extrapolated pore size distributions and of palm fiber based activated carbons at 56.5 % burn-off..... 154
5.1	Schematic diagram of a conventional spouted bed (Mathur and Epstein, 1974)..... 166

LIST OF FIGURES (Continued)

Figure	Page
5.2	Typical pressure drop-flow rate curves of conventional spouted bed (Mathur and Epstein, 1974)..... 167
5.3	Geometric dimensions of a spouted bed column..... 169
5.4	Flow sheet of the CFD simulation algorithm..... 191
5.5	Schematic diagram of spouted bed activator..... 194
5.6	Numerical grids of spouted bed used in CFD simulation 198
5.7	Typical pressure drop-flow rate diagram and bed height for increasing air flow of spouted bed for $D_I = 7.0$ mm, d_p of 0.5 mm, $\theta = 60^\circ$ and $H_S = 6.30$ cm 202
5.8	Pressure drop-flow rate diagram and bed height of spouted bed for $D_I = 7.0$ mm, d_p of 0.7 mm, $\theta = 60^\circ$ and $H_S = 6.3$ cm..... 204
5.9	Pressure drop-flow rate diagram and bed height of spouted bed for $D_I = 7.0$ mm, d_p of 0.7 mm, $\theta = 60^\circ$ and $H_S = 8.3$ cm..... 204
5.10	Pressure drop-flow rate diagram and bed height of spouted bed for $D_I = 7.0$ mm, d_p of 0.7 mm, $\theta = 60^\circ$ and $H_S = 10.3$ cm..... 205
5.11	Pressure drop-flow rate diagram and bed height of spouted bed for $D_I = 7.0$ mm, $d_p = 1.4$ mm, $\theta = 60^\circ$ and $H_S = 6.3$ cm..... 205
5.12	Pressure drop-flow rate diagram and bed height of spouted bed for $D_I = 7.0$ mm, $d_p = 1.4$ mm, $\theta = 60^\circ$ and $H_S = 8.3$ cm..... 206

LIST OF FIGURES (Continued)

Figure	Page
5.13	Pressure drop–flow rate diagram and bed height of spouted bed for $D_I = 7.0$ mm, $d_p = 0.5$ mm, $\theta = 45^\circ$ and $H_S = 4.9$ cm..... 206
5.14	Pressure drop–flow rate diagram and bed height of spouted bed for $D_I = 7.0$ mm, $d_p = 0.5$ mm, $\theta = 45^\circ$ and $H_S = 6.9$ cm..... 207
5.15	Pressure drop–flow rate diagram and bed height of spouted bed for $D_I = 7.0$ mm, $d_p = 0.5$ mm, $\theta = 45^\circ$ and $H_S = 8.9$ cm..... 207
5.16	Pressure drop–flow rate diagram and bed height of spouted bed for $D_I = 7.0$ mm, $d_p = 0.7$ mm, $\theta = 45^\circ$ and $H_S = 4.9$ cm..... 208
5.17	Pressure drop–flow rate diagram and bed height of spouted bed for $D_I = 7.0$ mm, $d_p = 1.4$ mm, $\theta = 45^\circ$ and $H_S = 4.9$ cm..... 208
5.18	Pressure drop–flow rate diagram and bed height of spouted bed for $D_I = 7.0$ mm, $d_p = 1.4$ mm, $\theta = 45^\circ$ and $H_S = 6.9$ cm..... 209
5.19	Pressure drop–flow rate diagram and bed height of spouted bed for $D_I = 7.0$ mm, $d_p = 1.4$ mm, $\theta = 45^\circ$ and $H_S = 8.9$ cm..... 209
5.20	Pressure drop–flow rate diagram and bed height of spouted bed for $D_I = 5.0$ mm, $d_p = 0.5$ mm, $\theta = 60^\circ$ and $H_S = 6.3$ cm..... 210
5.21	Pressure drop–flow rate diagram and bed height of spouted bed for $D_I = 5.0$ mm, $d_p = 0.5$ mm, $\theta = 60^\circ$ and $H_S = 8.3$ cm..... 210
5.22	Pressure drop–flow rate diagram and bed height of spouted bed for $D_I = 5.0$ mm, $d_p = 0.7$ mm, $\theta = 60^\circ$ and $H_S = 6.3$ cm..... 211

LIST OF FIGURES (Continued)

Figure	Page
5.23	Pressure drop–flow rate diagram and bed height of spouted bed for $D_I = 5.0$ mm, $d_p = 0.5$ mm, $\theta = 45^\circ$ and $H_S = 4.9$ cm..... 211
5.24	Pressure drop–flow rate diagram and bed height of spouted bed for $D_I = 5.0$ mm, $d_p = 0.5$ mm, $\theta = 45^\circ$ and $H_S = 6.9$ cm..... 212
5.25	Pressure drop–flow rate diagram and bed height of spouted bed for $D_I = 5.0$ mm, $d_p = 0.5$ mm, $\theta = 45^\circ$ and $H_S = 8.9$ cm..... 212
5.26	Pressure drop–flow rate diagram and bed height of spouted bed for $D_I = 5.0$ mm, $d_p = 0.7$ mm, $\theta = 45^\circ$ and $H_S = 4.9$ cm..... 213
5.27	Pressure drop–flow rate diagram and bed height of spouted bed for $D_I = 5.0$ mm, $d_p = 0.7$ mm, $\theta = 45^\circ$ and $H_S = 6.9$ cm..... 213
5.28	Pressure drop–flow rate diagram and bed height of spouted bed for $D_I = 5.0$ mm, $d_p = 0.7$ mm, $\theta = 45^\circ$ and $H_S = 8.9$ cm..... 214
5.29	Pressure drop–flow rate diagram and bed height of spouted bed for $D_I = 5.0$ mm, $d_p = 1.4$ mm, $\theta = 45^\circ$ and $H_B = 4.9$ cm..... 2.14
5.30	Pressure drop–flow rate diagram and bed height of spouted bed for $D_I = 5.0$ mm, $d_p = 1.4$ mm, $\theta = 45^\circ$ and $H_B = 6.9$ cm..... 215
5.31	Pressure drop–flow rate diagram and bed height of spouted bed for $D_I = 5.0$ mm, $d_p = 1.4$ mm, $\theta = 45^\circ$ and $H_B = 8.9$ cm..... 215
5.32	Effect of particle size on minimum spouting velocity 218

LIST OF FIGURES (Continued)

Figure	Page
5.33 Effect of initial bed heights on minimum spouting velocity	218
5.34 Effect of gas inlet diameters on minimum spouting velocity for particle size of 0.5 mm and conical base angle 45°	219
5.35 Effect of gas inlet diameters on minimum spouting velocity for particle size of 1.4 mm and conical base angle 45°	219
5.36 Configuration of a turbulent free-jet	224
5.37 Configuration of a turbulent free-jet in spouted bed	224
5.38 Comparison of experimental and calculated minimum spouting velocities by Equation (5.51).....	228
5.39 Comparison of experimental and calculated minimum spouting velocities by Equation (5.53).....	229
5.40 Comparison of experimental and calculated total bed height by Equation (5.54).....	233
5.41 Effect of activation time on the extent of char burn-off during the activation with CO ₂ at 900°C	234
5.42 Effect of activation time on BET and micropore area of activated carbons prepared at 900°C in the batch spouted bed activator	236.
5.43 Effect of activation time on total and micropore volume, and percentage microporosity of activated carbons prepared at 900°C in the batch spouted bed activator	237

LIST OF FIGURES (Continued)

Figure	Page
5.44	Effect of char burn-off on BET surface area 238
5.45	Effect of char burn-off on total pore volume 238
5.46	Effect of char burn-off on percentage microporosity 239
5.47	N ₂ adsorption isotherm at -196°C of activated carbon prepared at 900°C for activation time of 3.0 hrs in the batch spouted bed 239
5.48	The experimental and CFD simulated results of pressure drop-air flow rate diagram..... 240
5.49	Char particle concentration distribution at several air velocities 242
5.50	Simulated fountain height of spouted bed 248
5.51	Velocity profiles of air at air velocity of 1.143U _{MS} 249
5.52	Velocity profiles of palm-shell particles at air velocity of 1.143U _{MS} 250
5.53	Bed voidage profiles of palm-shell char particles at air velocity of 1.143U _{MS} 250
5.54	Bed voidage profiles of palm-shell char particles at air velocity of 1.143U _{MS} for 1.0 cm of height from air inlet..... 251
5.55	Bed voidage profiles of palm-shell char particles at air velocity of 1.143U _{MS} for 2.0 cm of height from air inlet..... 252
5.56	Bed voidage profiles of palm-shell char particles at air velocity of 1.143U _{MS} for 3.0 cm of height from air inlet..... 252

LIST OF FIGURES (Continued)

Figure	Page
5.57	Bed voidage profiles of palm-shell char particles at air velocity of 1.143 U_{MS} for 4.0 cm of height from air inlet..... 253
5.58	Bed voidage profiles of palm-shell char particles at air velocity of 1.143 U_{MS} for 5.0 cm of height from air inlet..... 253
5.59	Bed voidage profiles of palm-shell char particles at air velocity of 1.143 U_{MS} for 1.0 cm of height from air inlet..... 254
5.60	Bed voidage profiles of palm-shell char particles at air velocity of 1.000 U_{MS} to 1.714 U_{MS} for 1.0 cm of heights from air inlet..... 254
5.61	Bed voidage profiles of palm-shell char particles at air velocity of 1.000 U_{MS} to 1.714 U_{MS} for 2.0 cm of heights from air inlet..... 255
5.62	Bed voidage profiles of palm-shell char particles at air velocity of 1.000 U_{MS} to 1.714 U_{MS} for 3.0 cm of heights from air inlet..... 255
5.63	Bed voidage profiles of palm-shell char particles at air velocity of 1.000 U_{MS} to 1.714 U_{MS} for 4.0 cm of heights from air inlet..... 256
5.64	Bed voidage profiles of palm-shell char particles at air velocity of 1.000 U_{MS} to 1.714 U_{MS} for 5.0 cm of heights from air inlet..... 256
5.65	Bed voidage profiles of palm-shell char particles at air velocity of 1.000 U_{MS} to 1.714 U_{MS} for 6.0 cm of heights from air inlet..... 257
5.66	Circulation pattern of char particles at air velocity of 1.143 U_{MS} 258
5.67	Circulation pattern of air at air velocity of 1.143 U_{MS} 259

LIST OF FIGURES (Continued)

Figure		Page
5.68	Steady-state concentration profile of palm-shell char at $t = 0$ in the spouted bed activator	261
5.69	Experimental and CFD simulated char burn-off gasified as a function of activation time in the spouted bed activator	262
5.70	Concentration profiles of palm-shell char at different activation times in the spouted bed activator	263
5.71	Experimental and simulated BET surface area of activated carbons prepared from palm shell in spouted bed activator	265
5.72	Experimental and simulated total pore volume of activated carbons prepared from palm shell in spouted bed activator	265

SYMBOLS AND ABBREVIATIONS

A	=	frequency or pre-exponential factor [s^{-1}]
Ar	=	Archimedes number
C_D	=	drag coefficient
d_p	=	mean solid particle diameter [m]
D_C	=	spouted bed column diameter [m]
D_I	=	nozzle inlet diameter of spouted bed [m]
D_S	=	average diameter of spout core [m]
e_{RC}	=	restitution coefficient of particles
E	=	activation energy [kJ/mol]
g	=	gravitational acceleration [9.81 m/s^2]
g_0	=	radial distribution function
G	=	superficial mass flux of spouting fluid [$\text{kg/m}^2 \cdot \text{s}$]
H_B	=	height of dense solid bed [m]
H_F	=	height of bed fountain [m]
H_M	=	maximum spoutable bed height [m]
H_S	=	static bed height of particle bed [m]
I	=	unit tensor
k	=	pyrolysis rate constant, [s^{-1}]

SYMBOLS AND ABBREVIATIONS (Continued)

k_{θ}	=	diffusion coefficient [J/kg]
K	=	overall effective rate constant for gasification reaction, [s ⁻¹]
M	=	mass fraction
m_f	=	final yield of char
n	=	order of pyrolysis reaction
P	=	pressure [N/m ²]
P_p	=	solid pressure [N/m ²]
R	=	universal gas constant [mol. K/ kJ]
Re_p	=	particle Reynolds number
t	=	time [s]
T	=	absolute temperature [K]
V	=	velocity of dispersed phase [m/s]
V_f	=	random fluctuating velocity of dispersed phase [m/s]
V_M	=	local mean velocity of dispersed phase [m/s]
U	=	velocity of fluid phase [m/s]
U_{MS}	=	minimum spouting velocity [m/s]
W_{AC}	=	final weight of activated carbon produced [g]
W_{Char}	=	initial weight of char fed into activator [g]
X_F	=	volume fraction of fluid phase
X_p	=	volume fraction of dispersed phase

SYMBOLS AND ABBREVIATIONS (Continued)

$X_{P,Max}$	=	maximum particle packing volume fraction
α	=	residual weight fraction
β	=	interphase momentum transfer coefficient [kg/m ³ .s]
	=	heating rate [K/min]
γ	=	dissipation rate due to inelastic mutual particle collisions [kg/m.s ³]
λ_p	=	solid bulk viscosity [kg/m.s]
μ	=	molecular (dynamic) viscosity of fluid [kg/m.s]
μ_t	=	turbulent viscosity of fluid [kg/m.s]
θ	=	granular temperature [m ² /s ²]
ρ_B	=	bulk density of solid particle bed [kg/m ³]
ρ_F	=	densities of fluid [kg/m ³]
$\rho_P,$	=	densities of solid particle [kg/m ³]

CHAPTER I

INTRODUCTION

1.1 Rationale of the Study

In this thesis project, a systematic study on the preparation of activated carbon (also called activated charcoal) was performed. Activated carbon is an amorphous carbon-based material that exhibits a high degree of porosity and internal surface area (typically in the range of 300-3000 m²g⁻¹). Activated carbon can be produced into two forms, granular and powder depending on their applications. The granular form is suitable for the process which requires a large internal surface area and small pore sizes, typically for gas phase applications. The powder form with a larger pore and smaller internal surface area is commonly used for liquid phase applications.

Due to its excellence in adsorptive property, the activated carbon is widely used in purification and separation processes. It can be used as catalyst and catalyst support. The activated carbon has numerous environmental applications in removing pollutants from air or water streams both in the field and in industrial processes such as drinking water filtration, air purification, groundwater remediation, etc. Filters made of activated carbon are usually used in compressed air and gas purification to remove oil vapors, odors, and other hydrocarbons from the air. This carbon is also used in distilled alcoholic beverage purification by filtering organic impurities containing in vodka and whiskey. Additionally, the activated carbon can be employed

in medical applications such as to treat poisonings and overdoses following oral ingestion.

Generally, commercial activated carbons have the internal surface area in the range of 800-1500 m²/g containing predominantly micropore size range (pore diameter < 2 nm) (Bansal et al., 1988). The adsorptive properties of activated carbons depend on the internal porous structure exhibiting by their surface area, surface reactivity (chemistry), and pore size distribution. The pore size distribution of a given activated carbon depends significantly on the raw material and its method of preparation. Figure 1.1 shows the pore size distribution of activated carbon prepared from various raw materials.

The micro-structure of activated carbon consists of disorganized aromatic sheets with the space between the sheets providing the porous structure. The overall structure may be imagined as regions which resemble crumpled sheets of paper interspersed with a variety of differently sized gaps, as shown in Figure 1.2. The porous structure of activated carbon can be practically characterized by the analysis of the adsorption isotherm of some specific gases (such as nitrogen, argon, carbon dioxide, benzene, etc.). The adsorption capacity of activated carbon can be as high as 0.6-0.8 cm³/g which occurs mostly in the pores of molecular dimension called micropores (Bansal et al., 1988). Not only the micropore, the activated carbon also consists of the larger pores, known as mesopores and macropores. Corresponding to the classification of the International Union of Pure and Applied Chemistry (IUPAC), pores with the size smaller than 2 nm are classified as the micropore; pores with the size larger than 50 nm are classified as macropore; and mesopores are pores of the intermediate size (2-50 nm) (Do, 1998).

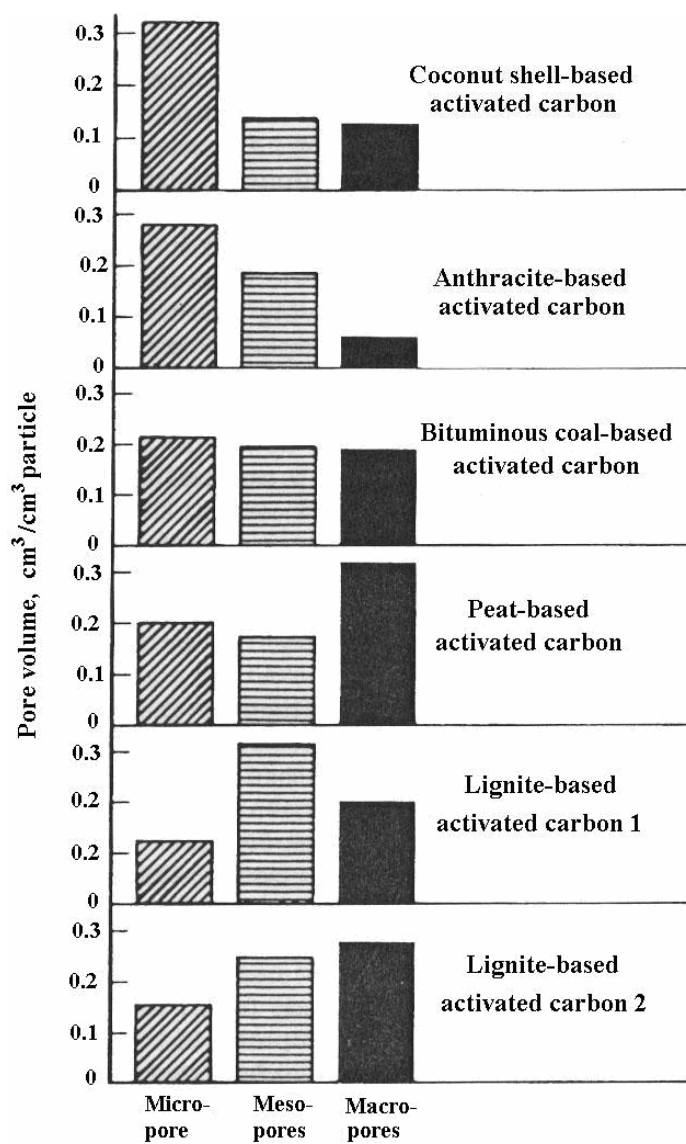


Figure 1.1 Pore size distribution in some activated carbons obtained using different precursors (Bansal et al, 1988).

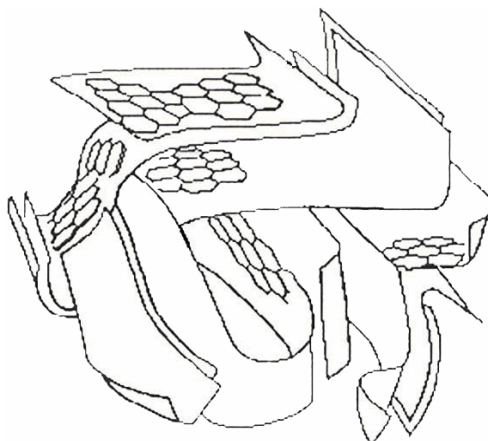


Figure 1.2 Schematic representation of activated carbon structure.

The activated carbon surface contains many active sites which plays an important role on the primary adsorption. These sites include edges of carbon layers and basal plane of defects (e.g. vacancies, dislocations etc), inorganic particle and heteroatoms which are represented diagrammatically in Figure 1.3. The carbon atoms at the active sites are highly reactive because they consist of unpaired electrons, residual valencies and richer potential energy (Bansal et al., 1988).

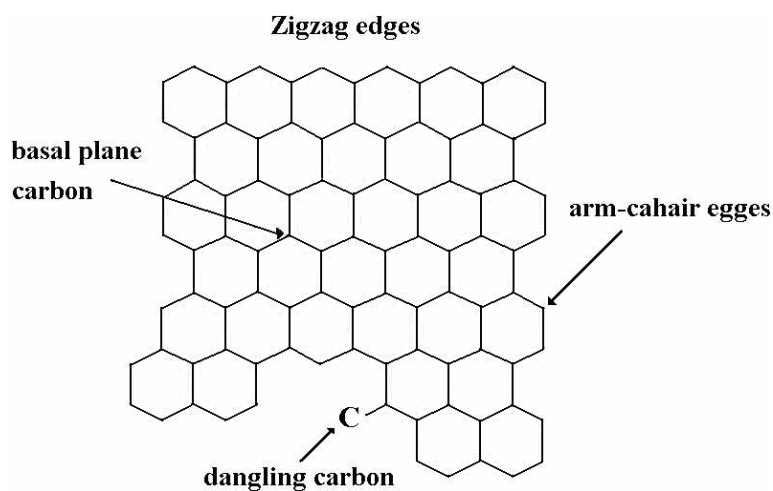


Figure 1.3 Active edge sites of carbon layer.

The adsorption characteristics of porous carbons depend strongly on their porous properties which in turn determined by the types of precursor and the prepared process (carbonization and activation). There are two techniques generally used for preparing the activated carbon, chemical and physical activation. For chemical activation, it is usually carried out when the raw material is of wood based materials. The carbonaceous material is impregnated with the activating agent in the form of concentrated solution. Then, the impregnated material is pyrolyzed in a furnace at the temperature between 400°C and 600°C in the absence of oxygen. This pyrolyzed product (i.e. activated carbon) is then cooled and washed to remove the activating agent. During the pyrolysis process, the activating agent can influence the pyrolysis decomposition and inhibit the formation of tar which enhances the yield of activated carbon. This impregnated chemical dehydrates the raw material that consequently results in charring and aromatization of carbon skeleton leading to the creation of a porous structure (Bansal et al., 1988). The widely used activating agents are phosphoric acid, zinc chloride and sulfuric acid. For physical activation, it involves two main steps: the carbonization of the carbonaceous material at temperatures below 800°C in the absence of oxygen followed by the activation of the carbonized product with gaseous activating agents at temperatures between 800 and 1100°C. The most commonly used activating agents are steam and carbon dioxide. Activation with carbon dioxide providing the activated carbon with smaller pore size compared to those activated with steam (Bansal, 1988). In actual industrial processes, CO₂ is part of the exhausted gas that can be used for activation process on an industrial scale. Therefore, it was decided to employ carbon dioxide as an activating agent in this

thesis work for the preparation of activated carbon using physical activation technique.

In Thailand, the most attractive material that can be used as a precursor for preparing activated carbons are oil-palm solid wastes, including palm shell, palm fiber, and palm kernel cake. These solid wastes have many distinctive advantages for activated carbon production. Firstly, they have long storage life. Secondly, large amount of oil-palm solid wastes are produced each year in Thailand. Thirdly, they contain low inorganic content (Guo and Lua, 2001). And finally, their price is cheap because they are abandoned solid wastes produced during palm-oil milling process.

The oil-palm (*Elaeis guineensis Jacq.*) is a tropical palm tree, which was originally planted in West Africa, where local people have used it to make foodstuffs, fiber material, medicines and wine (Carrere, 2006). At the present time, the oil-palm exists in a wild, semi-wild and cultivated state in the three land areas of the equatorial tropics: Africa, South-East Asia and America (Hartley, 1988). A rapid expanding of the oil-palm cultivation in the world is mainly a result of its domestication by man and the most productive parts of the palm-oil industry entering international trade at present are in Malaysia and Indonesia (Corley and Tinker, 2003).

At the present time, the oil-palm is the oil-crop which gives the highest oil yield per unit cultivation area (Corley and Tinker, 2003). The fresh oil-palm fruit is reddish about the size of large plum and grows in large bunches. A bunch of fruit can weigh between 10 to 40 kilograms each (Wikipedia, 2006). Each fruit consists of the central hard-shelled nut surrounded by an outer pulp (mesocarp) which contributes the most palm oil yield. The central nut is composed of the palm kernel inside the hard-

shell which contains another type of oil, palm kernel oil. The fresh oil-palm fruit and its longitudinal section are shown in Figure 1.4.

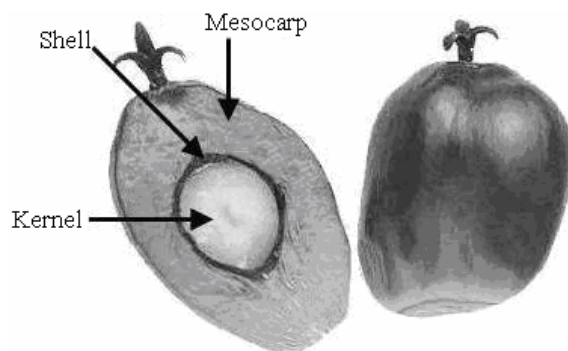


Figure 1.4 Fresh oil-palm fruit and its longitudinal section.

Today there are more than twelve million hectares of oil-palm cultivation worldwide (FAO, 2006). The total oil-palm production in Thailand and worldwide since the year 1961 to 2006 are shown in Figure 1.5. The figure shows that the amount of the oil-palm production (fresh fruits including bunch) increase at an accelerating rate each year since 1961. In the year 2006, the total oil-palm production of Thailand and worldwide are approximately 170 and 6.2 megatons, respectively (FAO, 2006).

The oil-palm solid wastes (including shell, fiber and palm kernel cake) are cheap and abandoned materials produced during palm oil milling process. For every ton of fresh fruit bunch being fed to the palm-oil milling process, about 0.07 tons of palm shell, 0.103 tons of palm fiber and 0.012 tons of palm kernel cake are produced as the solid wastes (Pansamut et al., 2003). Based on the total amount of the oil-palm production in Thailand reported by FAO, more than 0.43 megatons of palm shell, 0.64 megatons of fiber, and 0.07 megatons of palm kernel cake are produced each year.

About 80% of these solid wastes are used as boiler fuel in many industries and 20% are abandoned (Pansamut et al., 2003). With large production each year of these solid wastes, therefore, they will be alternatively used as precursors for preparing activated carbon in this thesis project.

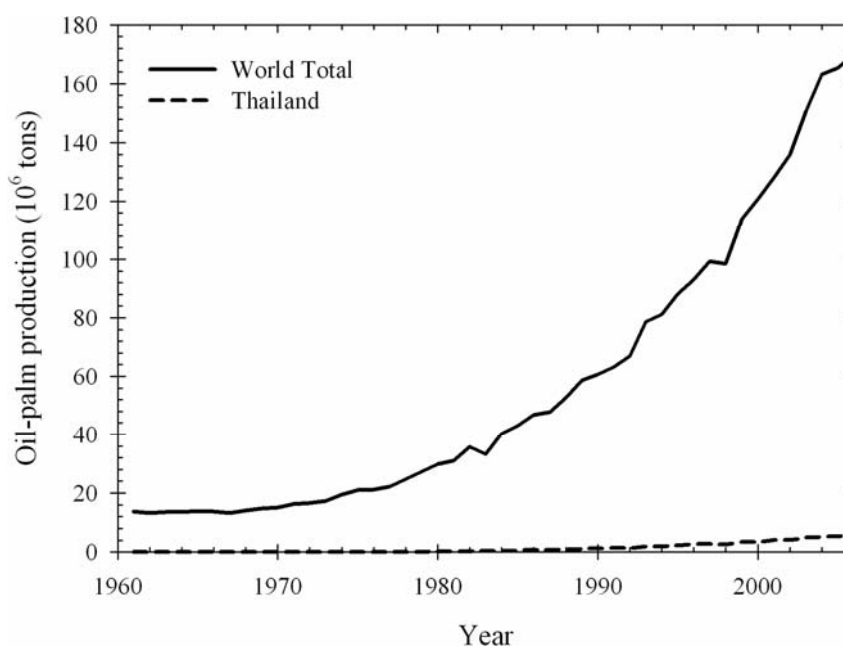


Figure 1.5 Oil-palm production in Thailand and worldwide since 1961 to 2006 (FAO, 2006).

On a commercial scale of activated carbon production, there are three types of furnaces that are widely used as activators for the production of activated carbon, they are rotary kiln, multiple-hearth furnace, and fluidized bed furnace. Rotary kiln is most popularly used by several producers because the product quality is easier to control by regulating the material residence time and temperature profile within the kiln. In general, the rotary kiln is usually used in the production of micropore based activated carbons. For multiple hearth-furnace, the produced activated carbon is slightly lower

in quality with more development of mesoporosity compared to that produced from the rotary kiln. For fluidized bed furnace, it provides high heat and mass transfer and the activating agent is in excellent contact with carbon particles. The activation reaction occurring in the fluidized bed activator is extensive due to its nature of high heat and mass transfer characteristics and there is much external burning of char particles leading to the relatively poor quality.

Apart from the above three commercial activating furnaces, the spouted-bed gas-solid contactor might be another interesting choice for using it as an activator for activated carbon production, especially for coarse particles with irregular shape like palm-shell particles studied in this work. Not only being capable of handling coarse particles, the spouted bed also has other advantages as follows. The product movement in the spouted bed is easy to control by controlling the flow rate of gas fed into the vessel. Increasing in the gas feed rate leads to the increase in particle velocity for all regions (spout core, fountain zone, and annulus region). Bottom screen is not required for the spouted bed as opposed to the fluidized bed. Agglomeration of material often possibly found in other types of reactor (such as fluidized bed and rotary kiln) is minimized by the high circulation of material at the inlet nozzle. Unlike the fluidized bed furnace, the excessive burning of external surface of char particles is less in the spouted bed activator because of its characteristic of short contacting time between activating gas and char particles. The spouted bed apparatus has no moving part, therefore, the construction and maintenance cost of the spouted bed activator might be low. With these mentioned advantages of the spouted bed activator, the capability of using the spouted bed as an activator in the preparation of activated carbon from oil-palm shell was investigated in this thesis.

In several chemical processes, the understanding of hydrodynamic behavior and kinetic characteristics of reactor are necessary for the design and scaling up from laboratory to commercial scale. In recent years, computational fluid dynamic (CFD) simulation is one of the most popular techniques used to explore the hydrodynamic pattern and also the kinetic characteristics in several chemical reactors. Therefore, the CFD is now an established chemical process design tool which can provide complete information that are necessary for such design and scale-up processes throughout the engineering profession with the cheapest cost and short design time. The variation on the process equipment design (for both continuous and batch operation) is easy to achieve without increasing in the design cost.

The CFD simulation is one of the branches of fluid mechanics that uses numerical methods and additional algorithms to solve and analyze problems that involve fluid flows, heat transfer, and other related physical processes. It works by solving the set of equations of fluid flow (in a special form) over a region of interest with particular conditions on the boundary of that region. The computer aided calculation technology is used to perform millions of calculation steps required to simulate the interaction of fluid-fluid and even fluid-solid for several complex systems used in engineering applications.

With the above-mentioned merits, the CFD technique will be used to simulate the hydrodynamic behavior and kinetic characteristics of the spouted bed activator studied in this work. The CFD simulation will be performed to generate the hydrodynamic data including system pressure gradient, spouting gas and solid particles concentration profiles and also their velocity vector components. The kinetic characteristic of activation scheme of palm shell based activated carbon is also

investigated using this CFD technique. These obtained simulated results are expected to yield important data and methodology for the designing and scaling up a spouted bed activator system to the commercial process.

1.2 Research Objectives

The overall objective of this thesis is to study the hydrodynamic characteristics and kinetic scheme of CO₂ activation process of activated carbon prepared from oil-palm solid wastes in the spouted bed activator using CFD simulation technique. The research scheme includes the thermal analysis of oil-palm solid wastes, the preparation of activated carbons in a laboratory tube furnace and spouted bed activator, and the CFD simulation of the spouted bed activator. The specific objectives of this research work are:

- To examine the kinetic characteristics of thermal decomposition of oil-palm shell, fiber and kernel cake in pyrolysis mode using the Thermogravimetric Analysis technique (TGA).
- To prepare the activated carbons from oil-palm shell, fiber, and kernel cake by physical activation method using the laboratory tube furnace and spouted bed activator, and also to characterize the porous characteristics of derived activated carbons.
- To modify the structural model recently proposed by Junpirom et al. (JDTT model) used for describing the evolution of porous structure during the activation process of activated carbons.
- To study the CO₂ activation scheme of activated carbon prepared from palm shell char in the spouted bed activator by using the CFD simulation.

1.3 Scope and Limitations

In this thesis, the study was separated into four parts. In the first part, the pyrolysis process of oil-palm solid wastes, including palm shell, fiber and kernel cake, was studied by using the non-isothermal Thermogravimetric Analysis (TGA) technique. The study was carried out by monitoring the change of sample mass (TGA data) and its first derivative (DTG data) with respect to temperature change or heating time at a constant heating rate. The effects of particle size and heating rate on the kinetic characteristics of pyrolysis reaction were investigated. Three kinetic models (one-step global model, two-step consecutive model, and two-parallel reaction model) were applied for describing the kinetic scheme of the pyrolysis process of oil-palm solid wastes. The kinetic parameters, including activation energy and pre-exponential factor, for each model were determined by fitting the kinetic model with the experimental TGA data. The capabilities of the proposed kinetic models in describing the kinetic scheme of pyrolysis reaction were examined.

The second part involved the preparations of activated carbons from oil-palm solid wastes (i.e. palm shell, fiber and kernel cake) in a laboratory tube furnace by physical activation technique using carbon dioxide as an activating agent. The prepared activated carbons were further characterized to determine their physical and porous properties (such as BET surface area, total pore volume, pore size distribution, etc.). The effects of activation temperature, time and heating rate on the physical and porous properties of the derived activated carbons were investigated. For the third part, the structural JDTT (Junpirom-Do-Tangsathitkulchai-Tangsathitkulchai) model recently proposed by Junpirom et al (2005) was modified to improve its capability and flexibility in describing the evolution of porosity of activated carbon during the

activation process. The simulation results generated from the modified JDTT model was validated with the experimental data of longan seed char gasification obtained by Junpirom et al. and also with the experimental data of oil-palm shell and fiber collected from the present study. Finally, the CO₂ activation scheme of activated carbon prepared from palm-shell char in the spouted bed activator was studied by using the CFD simulation technique. The simulation was performed for both hydrodynamic behavior and kinetic scheme of activation process occurring in the spouted bed activator. Simulated results from CFD study were further combined with the modified JDTT model in order to predict the porous characteristics of activated carbons, including surface area and pore volume.

1.4 References

- Bansal, R.C., Donnet, J.B. and Stoeckli, F. (1988). **Active Carbon**. New York: Marcel Dekker.
- Carrere, R. (2005). **Oil palm: The expansion of another destructive monoculture** [On-line]. Available: <http://www.wrm.org.uy/plantations/material/oilpalm2.html>.
- Corley, R.H.V. and Tinker, P.B. (2003). **The Oil Palm** (4th ed.). Oxford: Blackwell Science.
- Do, D.D. (1998). **Adsorption Analysis: Equilibrium and Kinetics**. London: Imperial College Press.
- Food and Agriculture Organization of the United Nations. **FAO Statistical Database** [On-line]. Available: <http://faostat.fao.org>.

- Guo, J., and Lua, A.C. (2001). Kinetic study on pyrolysis process of oil-palm solid waste using two-step consecutive reaction model. **Biomass & Bioenergy** 20: 223-233.
- Hartley, C.W.S. (1988). **The Oil Palm** (3th ed.). New York: Longman Scientific & Technical.
- Junpirom, S., Do, D.D., Tangsathitkulchai, C. and Tangsathitkulchai, M. (2005). A carbon activation model with application to longan seed char gasification. **Carbon** 43: 1936-1943.
- Pansamut, V., Pongrit, V. and Intarangsi, C. (2003). **The oil palm**. Thailand: Department of Alternative Energy Development and Efficiency: Ministry of Energy.
- Wikipedia Encyclopedia. (2006). **Palm oil** [on-line]. Available: http://en.wikipedia.org/wiki/Palm_oil.

CHAPTER II

NON-ISOTHERMAL THERMOGRAVIMETRIC ANALYSIS OF OIL-PALM SOLID WASTES

2.1 Abstract

Thermal decomposition of oil-palm solid wastes, including palm shell, fiber and kernel cake, was studied by thermogravimetric analysis (TGA). Effects of heating rate and sample particle size on the behavior of thermogram and kinetic parameters were investigated. The one-step global model, two step consecutive model and two-parallel reactions model were used to simulate the pyrolysis processes of the three materials studied. The one-step global model was able to describe the fractional weight loss upon pyrolysis of palm kernel cake reasonably well but gave a large deviation for palm shell and fiber. The two-step consecutive model could improve the fitting for palm shell and fiber, but it cannot account for the inflection characteristic of the thermogram. Prediction by the two-parallel reactions model gave the best fitting with the experimental data of all palm wastes under all pyrolysis conditions investigated. This proposed model was also tested with other biomass materials and proved to be satisfactory.

2.2 Introduction

Presently, solid wastes disposal has become an increasing problem and the available landfill capacity becomes increasingly scarce. Solid waste disposal by combustion is a viable management option which can reduce the solid waste mass and volume up to 80 and 90%, respectively (Ontiveros et al., 1989). However, the waste disposal by process causes many serious environmental problems due to the emissions of dust, odor, many toxic gases and also solid residue. Pyrolysis may alternatively become one of the powerful techniques for solid waste disposal that can help in improving environmental quality by means of energy recovery technology. The term pyrolysis involves chemical degradation process of carbonaceous materials by heating, usually at temperature between 400 to 800°C, in the absence of oxygen. The pyrolysis results in the production of carbon based solid residue (char), liquid (tar and an aqueous solution of organic material) and gaseous products which can be used in many applications. The compositions of these products vary depending upon the type of carbonaceous material used, holding time, temperature and rate of heating (Bansal et al., 1988).

Among the pyrolysis products, the derived char is used as a precursor for producing activated carbon which is the aim of this research. The knowledge and understanding on pyrolysis kinetics of biomass are important for proper design of a pyrolysis reactor which plays an important role in large-scale pyrolysis process. The pyrolysis kinetics can be studied by several methods but the most popular and simplest technique is the thermogravimetric analysis (TGA) (Haines, 1995). In this method, the change of a sample mass is monitored against time or temperature in the absence of oxygen at a specific heating rate. Important parameters that determine the

quality and yield of pyrolysis products are heating rate, final temperature, holding time at the final temperature and the nature and physical properties of raw materials (Bansal et al., 1988).

In this research project, we aim to produce the activated carbons from valuable and abandoned oil palm solid wastes, including palm shell, fiber and kernel cake, using the two-step CO₂ activation process. Therefore, the knowledge of thermal analysis of pyrolysis of this biomass is necessary to better understand and optimize the process of carbonization. The kinetics of pyrolysis reaction of palm shell, fiber and kernel cake were studied by using the thermogravimetric analysis (TGA) technique (Haines, 1995). Effects of raw material particle size and heating rate on the shape of thermograms were investigated. The two-parallel reactions model which leads to only one analytical solution was applied to simulate the pyrolysis process of palm shell, fiber and kernel cake. The validity of this proposed model was also tested with other different carbonaceous materials, including coconut shell, bagasse, longan seed and cassava pulp residue.

2.3 Review of the Literatures

The decomposition of carbonaceous matter during pyrolysis is very complicated and depends also on heat transfer by convection, conduction and radiation. Some simplified numerical models were proposed in literatures to predict the decomposition rate and final yield of char and volatile matter. Wichman and Atreya (1987) applied a one-step global model for predicting the devolatilization rate of pyrolysis process. They assumed that the carbonaceous sample is decomposed in one step to produce the volatile substance and solid char. Shuangning et al. (2006)

studied the devolatilization characteristics of various biomass (wheat straw, coconut shell, rice husk, and cotton stalk) during flash pyrolysis on a plasma heated laminar entrained flow reactor (PHLEFR) with average heating rates of 10^4C/s . Their experiments were conducted at temperatures between 477 and 627°C , and the particle residence time varied from about 0.115 to 0.240 s. They also employed the one-step global model to simulate the flash pyrolytic process and predict the yield of volatile products during pyrolysis. Although, the single-step global model is the simplest kinetic model for describing the pyrolysis process of biomass, but, for some system, the kinetic characteristics of pyrolysis process is too complex which the one-step is not capable to employed. Therefore, more flexible and accurate model is needed for some pyrolysis systems.

Bellais et al. (2003) developed a shrinkage model for the pyrolysis of large wood particles. The shrinkage was considered in three different ways: uniform shrinkage, shrinking shell and shrinking cylinders. All shrinkage models showed good agreements with the experimental results for mass loss versus time at high temperature range (higher than 600°C) but failed to simulate correctly at low temperatures. Thurner and Mann (1981) investigated the degradation kinetics of wood pyrolysis in the temperature range of 300 to 400°C at atmospheric pressure. They used the three-parallel reactions model to describe thermal decomposition of such wood pyrolysis. This kinetic model assumed that the wood was pyrolyzed into gas, tar, and char according to three parallel reactions. They found that the three-parallel reactions model provided the pyrolysis product distributions of gas, tar, and char that agreed considerably well with the experimental data. Chan et al. (1985) developed a pyrolysis model with three primary reactions (parallel reactions) and one secondary

reaction (tar decomposing into gas and char). The products of the secondary tar reaction are assumed to consist of light gases (carbon monoxide, ethene, ethyne) and aromatic tars.

For oil palm solid wastes which were used as raw materials for preparing the activated carbons in this research, Guo and Lua (2001) have applied the one-step global model and the two-step consecutive model for simulating the pyrolysis process of palm shell. The one-step global model showed faster pyrolysis conversion than the actual experimental values, especially, at the high temperature region. The two-step consecutive model agreed reasonably well with the experimental data. However, this model consists of a set of three ODEs which has no analytical solution. Therefore, the weakness of this model is that its accuracy depends on the size of time step and numerical techniques used in the calculation.

2.4 Model Description

The two parallel reactions model used in this work was originally proposed by Font et al. (1991). They used this model for describing the pyrolysis scheme of almond shell by assuming that the almond shell consists of two independent fractions which decompose at different rates and temperatures. Therefore, there are two main competing reactions which occur simultaneously. In addition, the first-order kinetics for both competing reactions was assumed. In the present work, however, the first-order kinetic scheme was also assumed for the first fraction, but the order of reaction was set as a free parameter for the second fraction, with a purpose to increase model flexibility.

Basic assumptions of the two-parallel reactions model are that the reaction is kinetically controlled and there are no secondary reactions among the released gaseous products. It is further assumed that the raw material consists of two homogeneous matters, M_1 and M_2 and each component decomposes simultaneously at different rate and temperature, producing volatile matters and solid char. The overall reaction and the two individual parallel reactions are expressed by Equations (2.1) to (2.3), respectively.



where k_1 and k_2 represent the rate constants of each reaction. The residual weight fraction of char components are defined as follows

$$\alpha = \frac{M - m_f}{1 - m_f}; \quad \alpha_1 = \frac{M_1 - m_{f1}}{1 - m_f}; \quad \alpha_2 = \frac{M_2 - m_{f2}}{1 - m_f} \quad (2.4)$$

where m_f represents the final yield of char which is estimated from the final constant weight of TG curve. m_{f1} and m_{f2} are the final yields of the first and second components present in the raw material, respectively. M , M_1 and M_2 are mass

fractions of total char, solid char of components 1 and 2 present at time t , respectively, with

$$M = M_1 + M_2 \quad (2.5)$$

$$m_f = m_{f1} + m_{f2} \quad (2.6)$$

The rate of decomposition reaction of component 1 in Equation (2.2) is assumed to follow the first-order kinetic reaction, whereas the component 2 in Equation (2.3) is assumed to follow the n -order kinetic reaction. Therefore, the rate expressions for both components can be written as the following.

$$\frac{d\alpha_1}{dt} = -A_1 \exp\left(\frac{-E_1}{RT}\right)\alpha_1 \quad (2.7)$$

$$\frac{d\alpha_2}{dt} = -A_2 \exp\left(\frac{-E_2}{RT}\right)\alpha_2^n \quad (2.8)$$

where A is the frequency or pre-exponential factor, E is the activation energy, R is the universal gas constant, T is the absolute temperature, n is the order of decomposition reaction for component 2 and t is the time. For a constant heating rate, β , we can write

$$\frac{dT}{dt} = \beta \quad (2.9)$$

Dividing Equation (2.7) and (2.8) by Equation (2.9), the rate of decomposition reactions can be expressed as a function of temperature, as follows

$$\frac{d\alpha_1}{dT} = -\frac{A_1}{\beta} \exp\left(\frac{-E_1}{RT}\right) \alpha_1 \quad (2.10)$$

$$\frac{d\alpha_2}{dT} = -\frac{A_2}{\beta} \exp\left(\frac{-E_2}{RT}\right) \alpha_2^n \quad (2.11)$$

Rearranging Equation (2.10) and (2.11), then integrating to obtain

$$\int_a^{\alpha_1} \frac{d\alpha_1}{\alpha_1} = -\frac{A_1}{\beta} \int_0^T \exp\left(\frac{-E_1}{RT}\right) dT \quad (2.12)$$

$$\int_b^{\alpha_2} \frac{d\alpha_2}{\alpha_2^n} = -\frac{A_2}{\beta} \int_0^T \exp\left(\frac{-E_2}{RT}\right) dT \quad (2.13)$$

where a and b are initial values of α_1 and α_2 , respectively, and they indicate the initial weight fractions of component 1 and 2 in the starting raw material. They are assumed constant and depend only on the characteristics of the raw material. The relationship between a and b is expressed as

$$a + b = 1 \quad (2.14)$$

The exponential term on the right-hand side of Equation (2.12) and (2.13) can be expressed in an asymptotic series and by neglecting the higher order terms, the integration yields (Guo and Lua, 2001)

$$\frac{A_i}{\beta} \int_0^T \exp\left(\frac{-E_i}{RT}\right) dT = \frac{A_i RT^2}{\beta E_i} \left[1 - \frac{2RT}{E_i} \right] \exp\left(\frac{-E_i}{RT}\right) \quad (2.15)$$

Substitution of Equation (2.15) into Equation (2.12) and (2.13), the expressions of α_1 and α_2 can be derived as follows

$$\alpha_1 = \exp\left[\frac{-A_1 RT^2}{\beta E_1} \left(1 - \frac{2RT}{E_1} \right) \exp\left(\frac{-E_1}{RT}\right) + \ln(a) \right] \quad (2.16)$$

$$\alpha_2 = \left[\frac{(n-1) A_2 RT^2}{\beta E_2} \left(1 - \frac{2RT}{E_2} \right) \exp\left(\frac{-E_2}{RT}\right) + b^{(1-n)} \right]^{\frac{1}{1-n}} \quad (2.17)$$

The total of remaining mass at any temperature is the sum of each residual fraction. That is,

$$\alpha = \alpha_1 + \alpha_2 = \exp\left[\frac{-A_1 RT^2}{\beta E_1} \left(1 - \frac{2RT}{E_1} \right) \exp\left(\frac{-E_1}{RT}\right) + \ln(a) \right] + \left[\frac{(n-1) A_2 RT^2}{\beta E_2} \left(1 - \frac{2RT}{E_2} \right) \exp\left(\frac{-E_2}{RT}\right) + b^{(1-n)} \right]^{\frac{1}{1-n}} \quad (2.18)$$

Equation (2.18) is used to fit the experimental TG data and the six kinetic parameters (a, A_1, E_1, A_2, E_2 and n) are determined through model fitting by minimizing the Sum of Square of Relative Error (*SSRE*), defined as,

$$SSRE = \left(\frac{\alpha_{\text{exp}} - \alpha_{\text{model}}}{\alpha_{\text{exp}}} \right)^2 \quad (2.19)$$

where α_{exp} and α_{model} are the experimental and simulated residual fractions, respectively.

2.5 Research Methods

The kinetic study of pyrolysis reaction was carried out by following the mass of a sample as a function of temperature using a thermogravimetric analyzer (TGA 7, Perkin Elmer). Palm solid wastes, including shell, fiber and kernel cake were supplied by Golden Palm Industry in Chonburi Province, Thailand. The received materials were washed and dried at 110°C for 24 hr. Then, they were crushed and sieved to obtain average particle sizes of 0.36, 0.51, 0.73, 1.1 and 1.4 mm for palm shell, less than 1.0 mm and 0.25 mm for fiber and kernel cake, respectively. The proximate and ultimate analyses were performed to identify the chemical compositions of the three biomass samples. The solid densities of raw materials were measured by using a helium pycnometer (Micromeritics AccuPyc 1330).

For TGA analysis, a sample of about 10 milligrams was placed into the TGA equipment and heated from room temperature to 700°C at various heating rates from 5 to 40 °C /min. Ultra high purity grade of nitrogen (99.9995% purity supplied by TIG, Thailand) at a constant flow rate of 100 cm³/min was used as a purge gas to provide an inert atmosphere around the sample during devolatilization and to carry away the pyrolyzed products from the reaction zones. Variation of sample mass with respect to temperature change (TG data) and its first derivative (DTG data) were continuously

monitored. The derived TG data was fitted with the one-step global model, two-step consecutive model and two-parallel reactions model to test the predictive capability of the models by using optimization function in MATLAB program. The kinetic parameters were then followed from the model fitting results.

2.6 Results and Discussion

Table 2.1 shows the proximate and ultimate analyses of the three biomass samples studied in this work.

Table 2.1 Proximate and ultimate analyses of palm shell, fiber and kernel cake.

Sample	Ultimate analysis (% w/w)					Proximate Analysis			Solid Density g/cm ³
	C	H	N	S	O	Volatile	Fix-C	Ash	
Shell	47.6	5.38	0.66	0.04	41.38	72.7	23.6	3.6	1.42
Fiber	46.64	5.66	1.73	0.10	39.46	73.7	12.6	6.6	0.75
Kernel	41.47	5.77	3.00	0.03	43.49	80.3	10.3	3.2	1.39

Thermal decompositions of palm shell, fiber and kernel cake were studied at four different heating rates of 5, 10, 20 and 40°C/min and five average particle sizes (only for palm shell) of 0.36, 0.51, 0.72, 1.10 and 1.40 mm to investigate their effect on the behavior of thermogram and kinetic parameters of the pyrolysis process. The experimental data of all three materials were fitted with the simplest kinetic scheme, the one-step global model, and also with the more complex kinetic models, the two-step consecutive model of Guo and Lua (2001) and the two-parallel reactions model of Font et al. (1991) which was modified and used in this work. Also presented in this

section are the pyrolysis data and results of model fitting for other potential biomasses, including coconut shell, bagasse, longan seed and cassava pulp residue.

2.6.1 Analysis of the Thermograms

The thermogravimetric (TG) data and its first derivative (DTG data) of oil palm shell, fiber and kernel cake pyrolyzed at the heating rate of 20°C/min are plotted against the temperature in the same graph in order to show their kinetic scheme (see Figure 2.1 to 2.3 for palm shell, fiber, and kernel cake, respectively). Results show that the pyrolysis of oil-palm solid wastes commences at the temperature above 250°C for palm shell (see Figure 2.1) and above 200°C for palm fiber (see Figure 2.2) and kernel cake (see Figure 2.3). For the pyrolysis of palm shell and fiber, there are two distinct peaks of DTG curves which indicate that there should be at least two main groups of reaction occurring during the decomposition process. It is noted that the two maximum of decomposition rates occur at about 300°C and 375°C for both palm shell and fiber, respectively.

It is known that the major components of lignocellulosic biomass are hemicellulose, cellulose and lignin (Antal, 1983). The main thermal decomposition of lignocellulosic materials generally occurs over the temperature range of 200-400°C. Lignin is the first component to decompose at a low temperature and low rate and continues on until approximately 900°C. Hemicellulose is a light fraction component which also decomposes at the low temperature region between 160 and 360°C. Cellulose is the last component to decompose at the high temperature range of 240-390°C (Vamvuka et al., 2003). The existing of two major peaks observed in DTG curves may be qualitatively explained as follows. The first peak could be generated by

the decomposition of hemicellulose and some of the lignin. The second peak should correspond to the decomposition of cellulose and the remaining lignin (Font et al., 1991; Tsamba et al., 2006). At the temperatures above 400°C, the final decomposition involves the aromatization process of lignin fraction leading to very low weight loss (Fisher et al., 2002). Based on this reasoning, it might be logical to test the experimental kinetic data of palm shell and fiber using the two parallel reactions and two-step consecutive model.

For palm kernel cake (see Figure 2.3), there is only one maximum rate of decomposition observed at about 250°C with a small shoulder located at the higher temperature side on the DTG curve. This indicates that there is at least one major reaction scheme occurring during the pyrolysis process for this type of material. The maximum peak of DTG curve is probably contributed by the decomposition of the lighter fraction (i.e. hemicellulose) and the small shoulder corresponds to the decomposition of the heavier component (i.e. cellulose). It is observed that the rate of decomposition of the light component for the case of palm kernel cake is greater than the rate of decomposition of the heavy component, while for palm shell and fiber, the rate of decomposition of the heavy component is dominated. The one peak of DTG data with small shoulder was also found for the pyrolysis of olive-kernel as reported by Vamvuka et al. (2003). With the existence of only one peak of DTG data, it is expected that the experimental data of palm kernel cake could be described by the one-step global model.

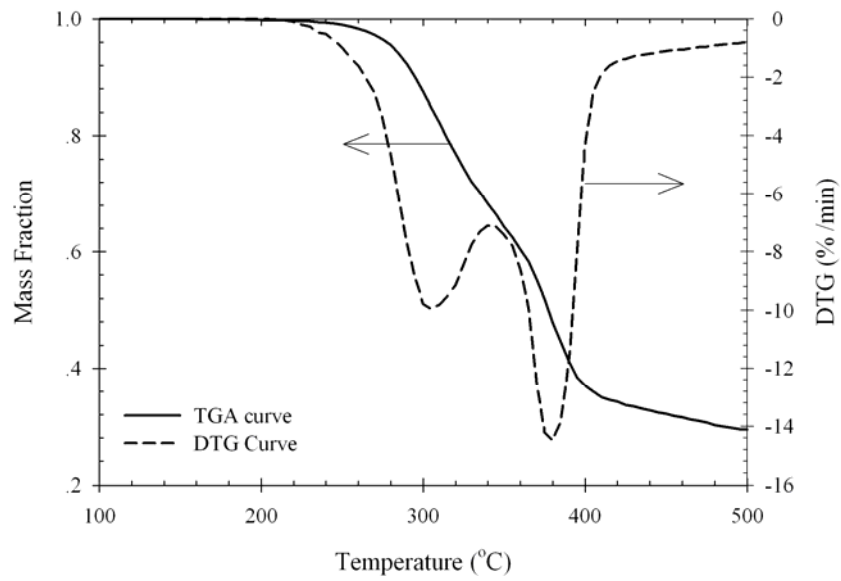


Figure 2.1 TG and DTG data of palm shell pyrolyzed at heating rate of 20°C/min.

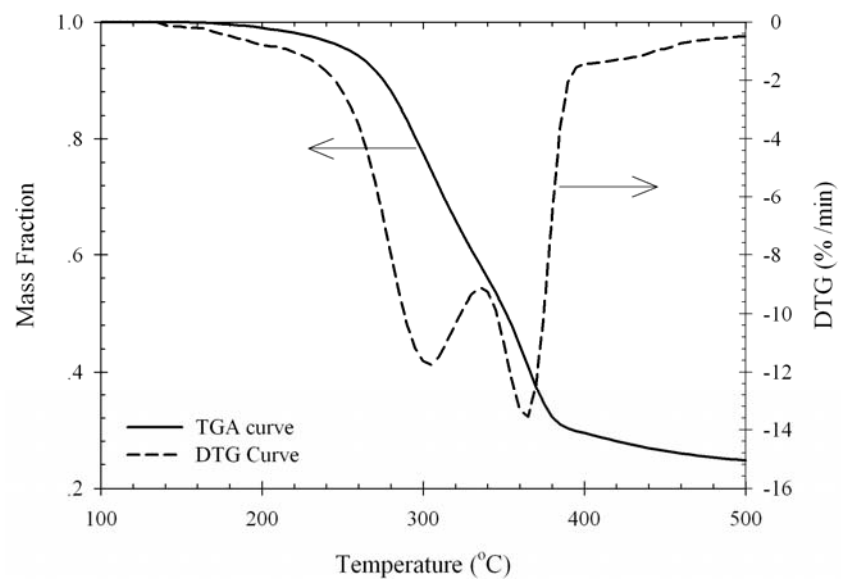


Figure 2.2 TG and DTG data of palm fiber pyrolyzed at heating rate of 20°C/min.

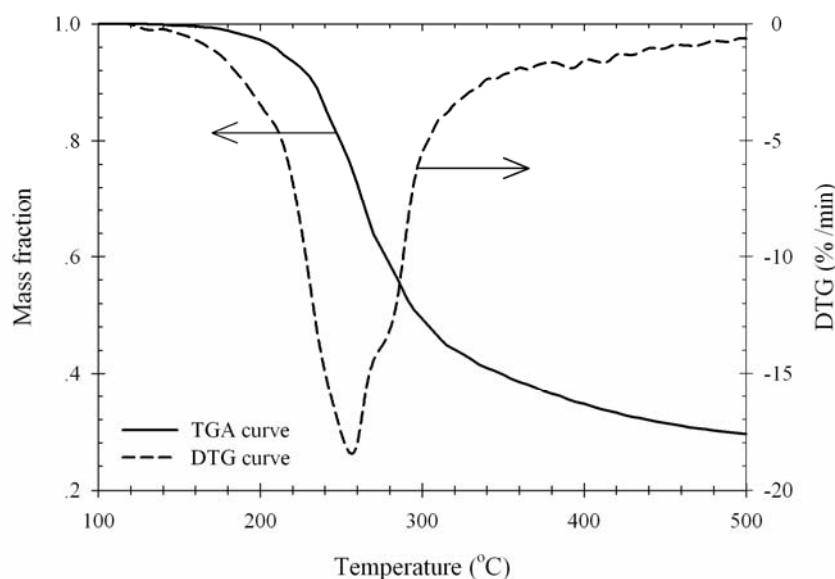


Figure 2.3 TG and DTG data of palm kernel cake pyrolyzed at heating rate of 20°C/min.

It is known that particle size is an important parameter that can affect the pyrolysis behavior (Haykiri-Acma, 2006; Jayaweera et al., 1989; Kok et al., 1998; Larsen et al., 2006). An increasing in particle size can establish the temperature gradient, causing increased heat transfer resistance inside the pyrolyzed particles, which in turn can cause an increase in the final solid yield and a decrease of volatile matter released during the pyrolysis process. The residual weight fractions of palm shell determined during pyrolysis process (TG data) are shown in Figure 2.4, for various particle sizes at the heating rate of 20°C/min. As observed, the particle size has no significant effect on the thermogram of palm shell at the initial stage of pyrolysis (temperature lower than 320°C), after that the residual mass of sample and the final yield of char increase with increasing of particle size at the same pyrolysis temperature. However, the decomposition of solid appears to start and end at

approximately the same temperature range for all particle size studied here. Also shown in Figure 2.4 is the first derivative of mass change with respect to temperature (DTG data) for various particle sizes at the heating rate of 20°C/min. The plots show that the first and second peaks of DTG curve occur at approximately the same temperature independent of particle sizes (see also in Table 2.4).

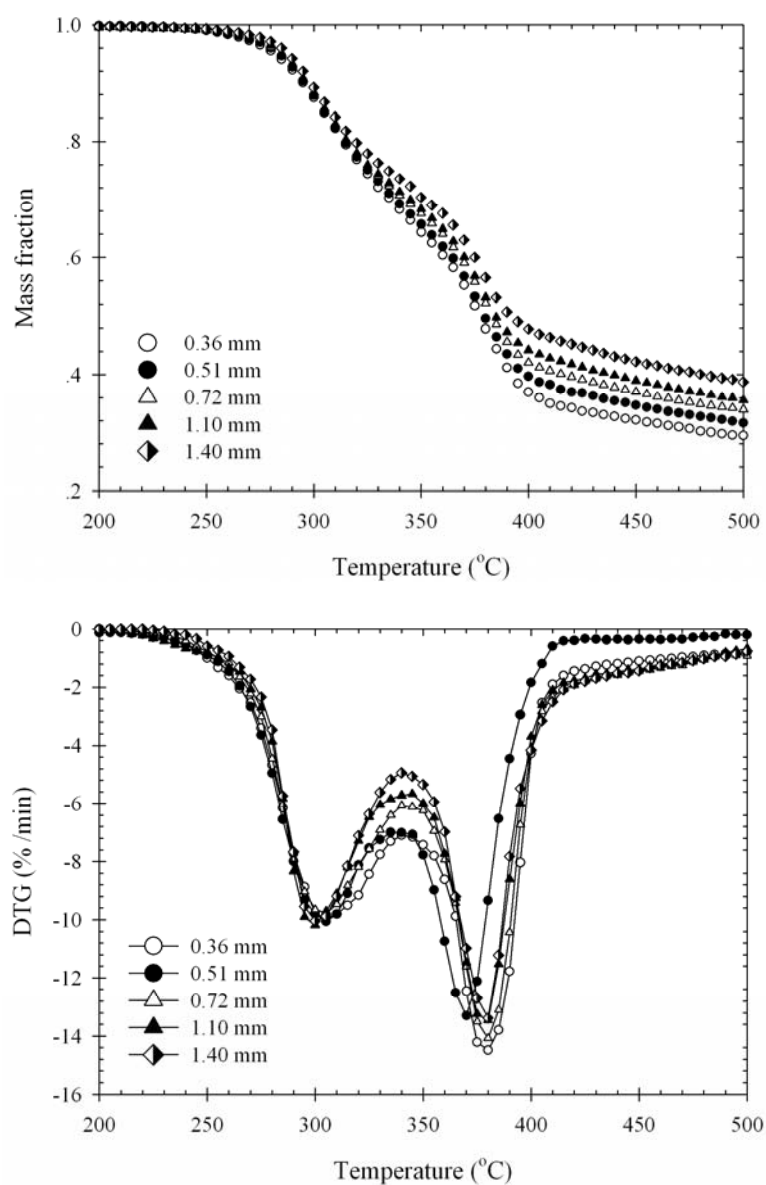


Figure 2.4 TG and DTG data of palm shell pyrolyzed at heating rate of 20°C/min.

Figure 2.5 to 2.7 show, respectively, the thermograms of palm shell, fiber and kernel cake pyrolyzed at various heating rates. It is observed that, as the heating rate is increased, the thermograms of palm shell and fiber shifted systematically to higher temperature region but slightly shifted for the case of palm kernel cake. These results indicate that palm shell and fiber decomposed at a higher temperature when a higher heating rate was applied. The shift of thermograms to higher temperature region is probably due to the effect of heat transfer which causes the temperature lag between the surrounding and inside of the particle. However, there is no measurable effect of heating rate on the final yield of char for all three materials. In other words, the final yield depends only on the final pyrolysis temperature applied. The same results can be observed in the pyrolysis of almond shell and olive stone as reported by Caballero et al. (1997).

Also shown in Figure 2.5 to 2.7 are the DTG data of palm shell, fiber and kernel cake pyrolyzed at various heating rates. The heating rate affects significantly on the maximum decomposition rate, with maximum decomposition rate tending to increase and occur at higher temperatures when pyrolyzed at higher heating rates. The first and second maximum rates of decomposition and the corresponding temperatures are summarized in Table 2.2.

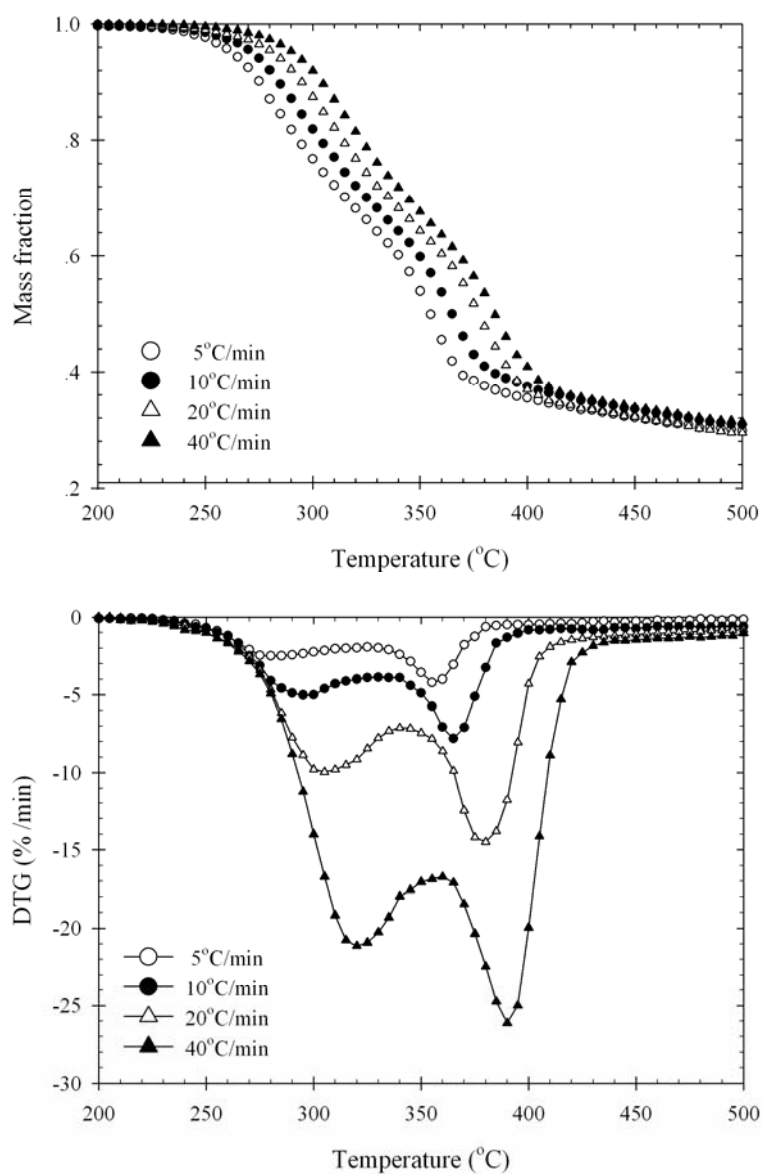


Figure 2.5 TG and DTG data of palm shell pyrolyzed at particle size 0.36 mm for various heating rate.

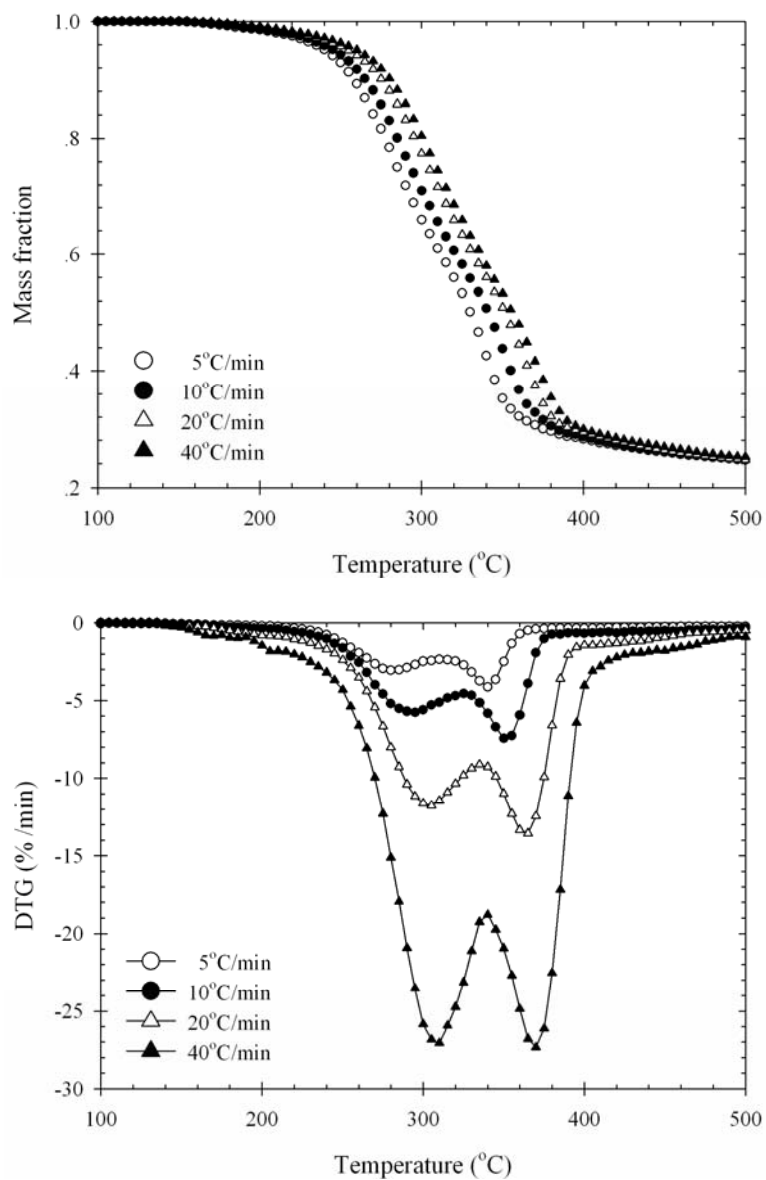


Figure 2.6 TG and DTG data of palm fiber pyrolyzed at different heating rate.

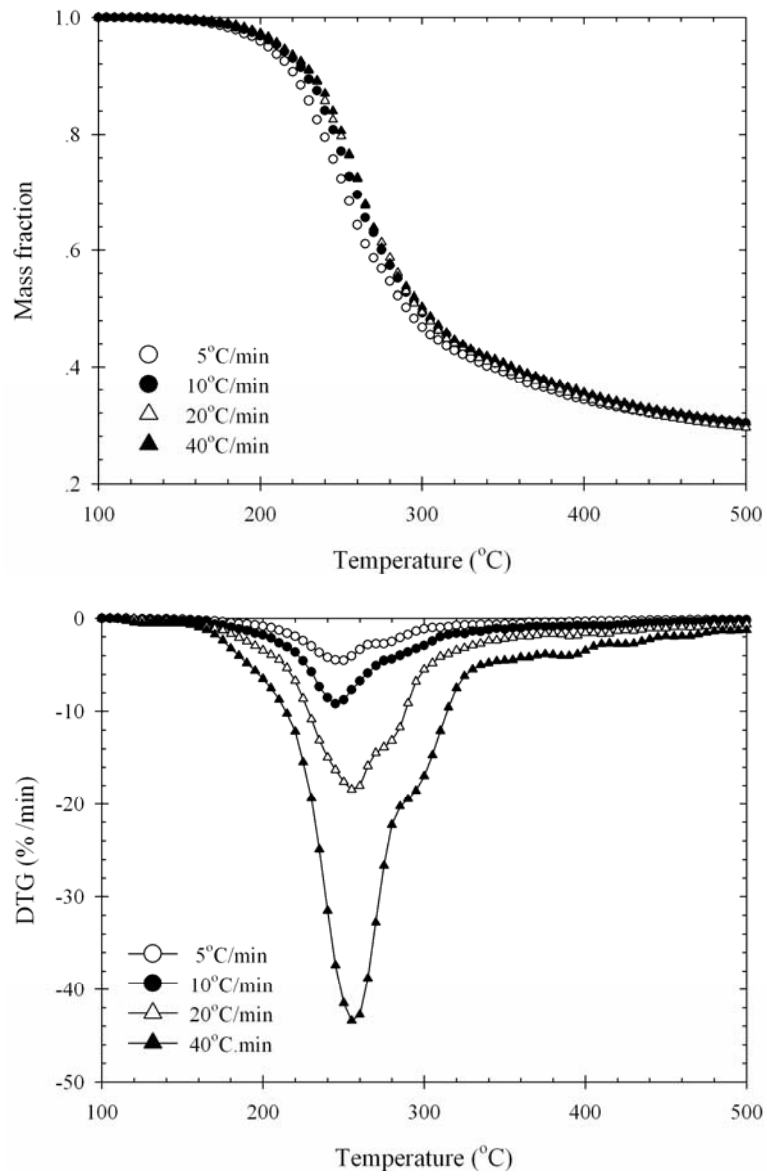


Figure 2.7 TG and DTG data of palm kernel cake cake pyrolyzed at different heating rates.

Table 2.2 First and second maximum rate of decomposition and corresponding temperatures of palm solid wastes.

Sample	Heating Rate (°C/min)	Size (mm)	$T_{1,max}$	1 st maximum rate (%/min)	$T_{2,max}$	2 nd maximum rate (%/min)
Shell	20	0.36	305	-9.95	380	-14.49
		0.51	305	-10.06	375	-13.30
		0.73	305	-9.77	380	-14.08
		1.10	300	-10.19	380	-13.46
		1.40	300	-10.04	380	-13.38
Shell	5	0.36	280	-2.50	355	-4.20
	10		295	-5.02	365	-7.80
	20		305	-9.95	380	-14.49
	40		320	-21.14	390	-26.13
Fiber	5	< 1.00	280	-3.06	340	-4.14
	10		295	-5.76	350	-7.44
	20		305	-11.76	365	-13.55
	40		310	-27.06	370	-27.34
Kernel	5	< 0.15	250	-4.53	-	-
	10		245	-9.20	-	-
	20		255	-18.41	-	-
	40		255	-43.42	-	-

2.6.2 One-Step Global Model

The one-step global model is the simplest kinetic model for describing the decomposition process of carbonaceous materials. This model assumes that the rate of decomposition can be expressed by one kinetic scheme. Mathematically,

$$\frac{d\alpha}{dT} = \frac{A}{\beta} e^{-E/RT} (1-\alpha)^n \quad (2.20)$$

Here, the residual weight fraction, α , is defined in terms of the change in the mass of sample as

$$\alpha = \frac{w_0 - w}{w_0 - w_f} \quad (2.21)$$

where w_0 , w and w_f are the initial, actual and final mass of the sample, respectively.

Figure 2.8 to 2.10 shows the comparison between experimental data and model fitting with the one-step global model for palm shell, fiber and kernel cake at different heating rates. The agreement between experimental data and the one-step global model prediction is considered acceptable, however, the model cannot account for the inflection of thermograms for all heating rates. The maximum deviations for the pyrolysis of palm shell and fiber lie in the range of 10-15%. For palm kernel cake, the model agrees fairly well with the experimental data with less than 4% of the maximum deviation for all heating rates.

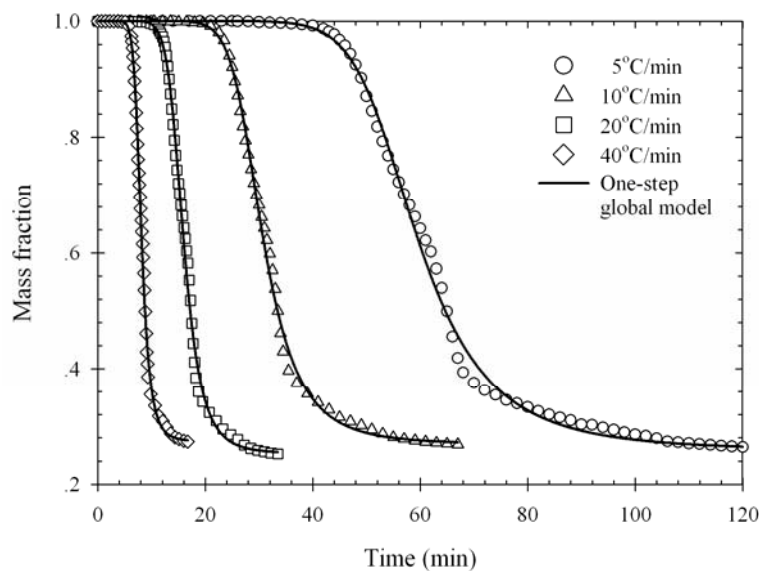


Figure 2.8 TG data and one-step global model fitting of palm shell.

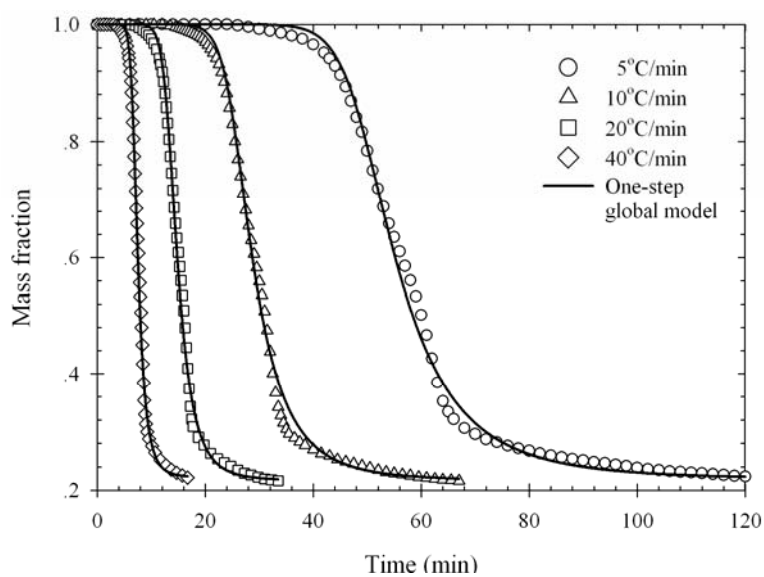


Figure 2.9 TG data and one-step global model fitting of palm fiber.

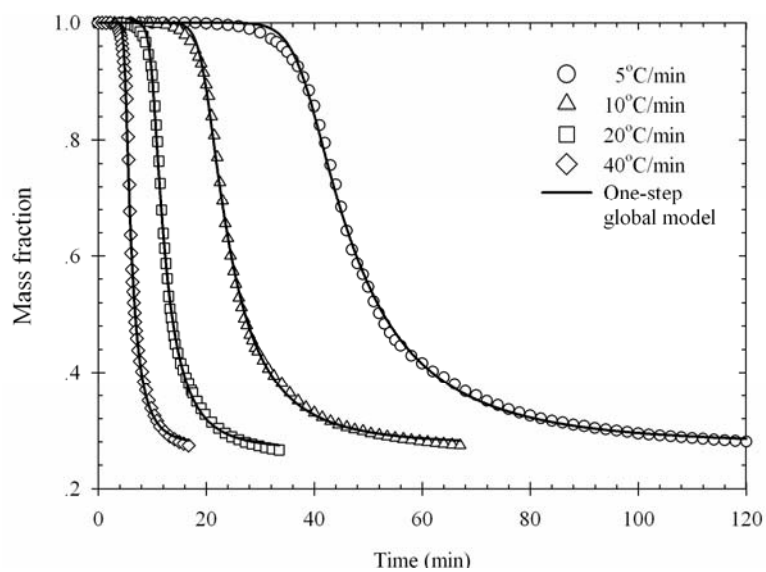


Figure 2.10 TG data and one-step global model fitting of palm kernel cake.

The kinetic parameters, the order of reaction (n), activation energy (E) and frequency factor (A) determined from the model fitting are summarized in Table 2.3. The frequency factor and activation energy of palm shell and kernel cake appear

to increase with increasing of heating rate, while a decrease is observed for the case of palm fiber. The frequency factor and activation energy indicate how fast and easy for the pyrolysis reaction to proceed. The higher frequency factor and lower activation energy, the faster and easier would be for the pyrolysis reaction to occur. The order of reaction decreases with increasing of heating rate for palm shell and fiber, but it increases for the case of palm kernel cake. The order of reaction for all three materials is in the range of 2.5-4.0.

Table 2.3 Kinetic parameters of one-step global model for pyrolysis of palm shell, fiber and kernel cake.

Samples	Heating rate (°C/min)	A (s ⁻¹)	E (kJ/mol)	n	Max. Error
Palm shell	5	7.93×10^6	106.1	2.84	11.90%
	10	2.05×10^7	109.1	2.65	9.22%
	20	4.84×10^7	110.4	2.52	10.71%
	40	5.27×10^7	111.0	2.54	9.51%
Palm fiber	5	1.52×10^{10}	136.0	3.35	10.83%
	10	1.96×10^9	125.9	3.32	14.69%
	20	1.50×10^9	124.1	2.95	11.84%
	40	1.00×10^9	123.3	2.87	10.93%
Palm kernel	5	4.57×10^{13}	156.1	3.37	2.99%
	10	1.24×10^{14}	159.5	3.41	2.98%
	20	1.31×10^{15}	167.5	3.52	3.56%
	40	2.34×10^{16}	176.4	3.85	3.87%

Due to the two-peak characteristic of DTG data, the pyrolysis process of palm shell and fiber should be best described by a model consisting of two-stage kinetic scheme. In this work, two simple kinetic models, which are the two-step consecutive model and the two-parallel reactions model were explored.

2.6.3 Two-Step Consecutive Model

The two-step consecutive model was used by Guo and Lua (2001) in studying the kinetics of pyrolysis reaction of palm shell by using the thermogravimetric method. Basic assumptions of this model are that the reaction is a pure kinetic controlled process and there are no secondary reactions among the gaseous products.

The model was assumed to consist of two reaction steps (as shown in Equations (2.22) and (2.23)). The starting material first decomposes to produce the first group of volatile matters and the intermediate substance which further decomposes to produce the final solid char and the second group of volatile matters. That is,



where W , I and C are the weight fraction of raw material, intermediate and solid char, respectively, and x and y are the stoichiometric coefficients of the reactions.

The kinetic equation for decomposition of raw material and generation of the intermediate and final solid char can be described by the following expressions.

$$\frac{dW}{dT} = -\frac{A_1}{\beta} e^{-E_1/RT} W \quad (2.24)$$

$$\frac{dI}{dT} = -\frac{x A_1}{\beta} e^{-E_1/RT} W - \frac{A_2}{\beta} e^{-E_2/RT} I^n \quad (2.25)$$

$$\frac{dC}{dT} = \frac{yA_2}{\beta} e^{-E_2/RT} I^n \quad (2.26)$$

where n is the order of the second step of pyrolysis reaction. The relationship between x and y can be obtained from the mass balance which is written as the following:

$$x = \frac{m_f}{y} \quad (2.27)$$

where m_f is the final yield of char. The initial conditions for the above three ordinary differential equations are

$$W = 1, I = C = 0 \quad \text{at } T = 0 \text{ K} \quad (2.28)$$

The residual weight fraction of sample at any temperature and time is equal to the summation of weight fraction of raw material, intermediate and char. We solve the above set of ordinary differential equations by using ODE solver in MATLAB program.

The two-step consecutive model was tested against the experimental data of palm shell, fiber and kernel cake from the present study and the results are shown in Figure 2.11 to 2.13, respectively. The two-step consecutive model shows the improvement of model fitting for palm shell and fiber over the one-step global model. The maximum deviation for palm shell and fiber are in the range of 4-7 % (see Table 2.4). However, the two-step consecutive model cannot fully account for the inflection of the thermograms, particularly at low heating rates. For oil-palm kernel cake, the

two step consecutive model also gives good agreement with the experimental data with the range of percentage error being the same order as that of the one-step global model. These results confirm that the one-step global model is sufficient to describe the pyrolysis process of palm kernel cake which shows only one peak of DTG curve.

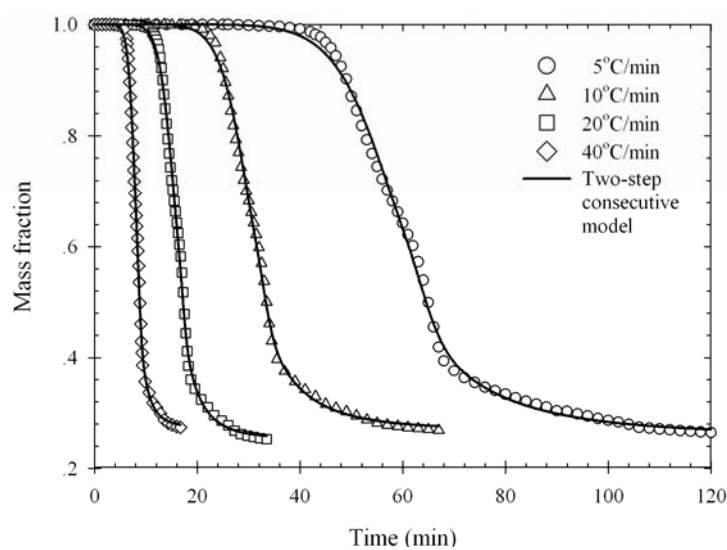


Figure 2.11 TG data and two-step consecutive model fitting of palm shell.

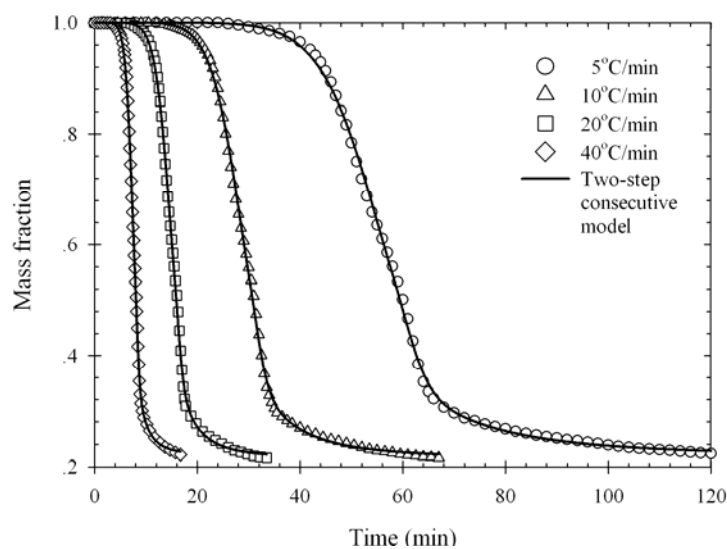


Figure 2.12 TG data and two-step consecutive model fitting of palm fiber.

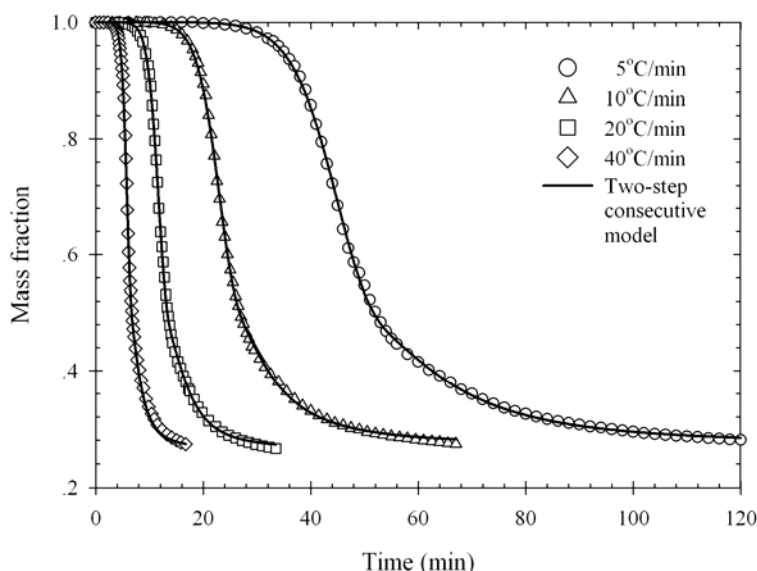


Figure 2.13 TG data and two-step consecutive model fitting of palm kernel cake.

The kinetic parameters determined from the model fitting for the two-step consecutive model are listed in Table 2.4. The frequency factor of raw material (A_1) increases with increasing of heating rate for all three materials studied here. Although the activation energy of raw material (E_1) decrease with increasing of heating rate for all materials, but the overall rate constant still increase. This observation indicates that the raw material decomposes at a faster rate when the heating rate is increased. This trend of simulated results agrees with the experimental data of DTG curves (see Figure 2.5 to 2.7) which show the increasing in decomposition rate for the first peak when heating rate is increased for all three materials. For the decomposition of intermediate to form solid char, the frequency factor (A_2) decreases when the heating rate is increased for the case of palm shell and fiber, whereas it increases for the case of palm kernel cake. For activation energy E_2 , it decreases with increasing of heating rate for the case of palm shell, but to increase

for the case of palm fiber and kernel cake. As to the order of reaction, when a higher heating rate is applied, the order of reaction tends to decrease for all materials.

Table 2.4 Kinetic parameters of two-step consecutive model for pyrolysis of palm shell, fiber and kernel cake.

Sample	Heating Rate (°C/min)	A_1 (s ⁻¹)	E_1 (kJ/mol)	A_2 (s ⁻¹)	E_2 (kJ/mol)	n	Max. error
Shell	5	2.43×10^4	79.0	1.24×10^{25}	301.0	5.89	6.58%
	10	6.99×10^4	82.1	3.89×10^{24}	299.3	5.24	4.37%
	20	9.48×10^4	83.9	6.54×10^{23}	295.4	4.34	5.86%
	40	3.65×10^5	86.3	2.80×10^{17}	221.8	2.94	5.04%
Fiber	5	9.83×10^3	70.4	1.64×10^{29}	325.2	5.98	4.42%
	10	9.73×10^3	71.4	7.93×10^{28}	326.3	5.69	3.80%
	20	2.34×10^4	73.7	5.10×10^{28}	332.4	5.15	5.76%
	40	4.92×10^4	74.5	4.55×10^{28}	339.8	4.90	5.19%
Kernel	5	3.50×10^5	81.5	1.59×10^8	112.9	4.02	2.46%
	10	6.78×10^5	82.5	2.43×10^9	174.2	3.62	2.82%
	20	3.68×10^6	87.2	1.31×10^{10}	198.2	3.47	2.46%
	40	8.19×10^6	87.6	1.89×10^{11}	136.7	2.56	4.33%

2.6.4 Two-Parallel Reactions Model

Figure 2.14 to 2.17 compares the experimental data and model fitting using the two-parallel reaction model for the pyrolysis of oil palm shell, fiber and kernel cake for various particle sizes and heating rates. Excellent agreement between the predicted results of the two parallel reactions model and the experimental data is observed under all pyrolysis conditions. Deviation of model prediction was found to be less than 4% for all samples and conditions (heating rate and particle size) being studied here. In addition, the two-parallel reaction model also shows an excellent description for the inflection of thermograms of palm shell and fiber. Although, the

two-step consecutive model of Guo and Lua (2001) can describe the experimental data of palm shell and fiber quite well, its drawback is that the model consists of three ordinary differential equations which must be solved simultaneously. The accuracy of the model can be seriously affected by the size of time step and the numerical technique used. If smaller time step is applied, more accuracy can be obtained but more time is required for the computation. More importantly, as shown in the previous section the two-step consecutive model cannot account for the inflection of thermograms of palm shell and fiber. On the other hand, the two-parallel reactions model proposed in the present work is more accurate and advantageous because it contains only one analytical solution, thus requiring much less computation time. However, it should be noted that the accuracy of the model calculation can be affected by the initial guess of the kinetic parameters used for the optimization step. Poor initial trials of the kinetic parameters may cause a large deviation in the model fitting.

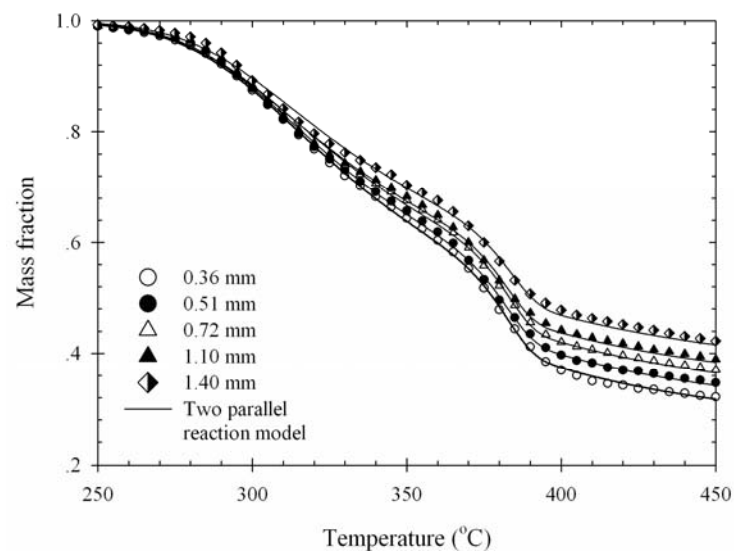


Figure 2.14 TG data and two-parallel reaction model fitting for palm shell pyrolyzed at heating rate of 20°C/min for different particle sizes.

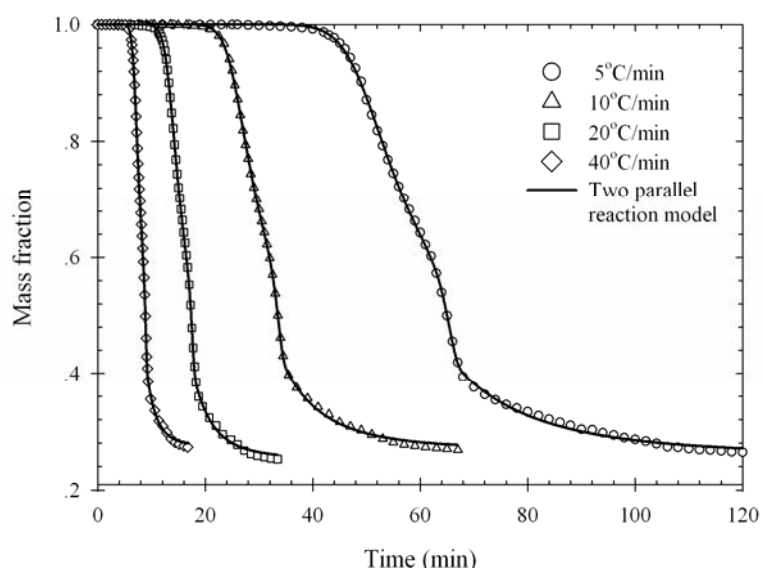


Figure 2.15 TG data and two-parallel reaction model fitting for palm shell pyrolyzed for particle sizes of 0.36 mm at different heating rates.

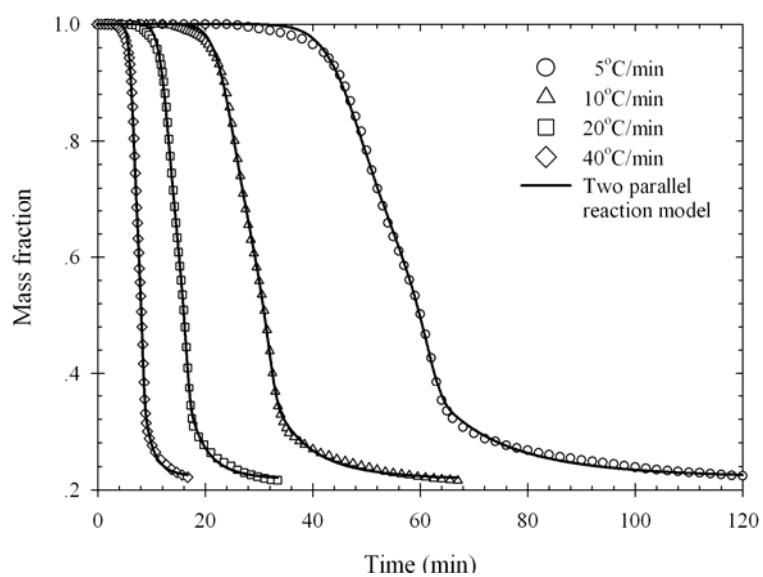


Figure 2.16 TG data and two-parallel reaction model fitting for palm fiber pyrolyzed at different heating rates.

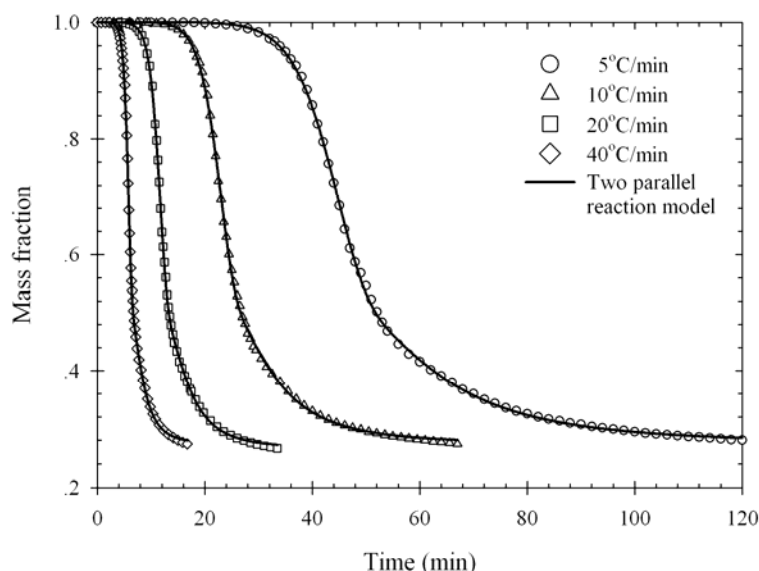


Figure 2.17 TG data and two-parallel reaction model fitting for palm kernel cake pyrolyzed at different heating rates.

Table 2.5 lists the kinetic parameters determined from the model simulation for palm shell, fiber and kernel cake. The first fraction having higher activation energy could represent the decomposition of the heavier component (i.e. cellulose) which follows the first order kinetic scheme. Larger value of b in comparison with the a value indicates that the pyrolysis of palm shell and fiber are mainly contributed by the decomposition of the lighter components (i.e. hemicellulose) ($b = 79\%$ and 74% for palm shell and fiber, respectively). Tsamba et al. (2006) reported the values of the activation energies for pyrolysis of hemicellulose and cellulose. They found that the activation energy of hemicellulose is in the range of 147.24-172.75 kJ/mol and cellulose to be in the range of 176.92-248.64 kJ/mol. For palm shell and fiber, the fitted activation energies of the first fraction (E_1) fall in the same range as those of cellulose, while the fitted activation energies of the second

fraction (E_2) show those of hemicellulose. This agreement further supports that the first and second fractions could represent the decomposition of cellulose and hemicellulose, respectively. The variation of the kinetic parameters, including frequency factor, activation energy and reaction order for different heating rates and particle sizes can be further examined. It is noted that there is no definite trend for the frequency factor and activation energy when the heating rate and particle size are changed. However, the reaction order of the second fraction (n) decreases with the increasing of heating rate but increases as the particle size is increased. Due to model simplification, the two-parallel reaction model assumes that the pyrolysis reaction is purely kinetic control where the effect of heat and mass transfer resistance are neglected. In principle, if the pyrolysis reaction is a true purely kinetic control, the kinetic parameters should be constant independent of heating rate and particle size. The observed variation of kinetic parameters as reported here may result from the complex scheme of pyrolysis reaction and also the effect of heat and mass transfer resistance existing in the real system.

In order to further confirm the validity of the two-parallel reactions model proposed in this study, we also applied this model to the data of other carbonaceous biomass materials, including coconut shell, bagasse, longan fruit seed and cassava pulp residue. All samples were pyrolyzed at 10 °C/min. The particle sizes of the samples are 0.36 mm for coconut shell, 0.1 mm for bagasse, 1.0 mm for longan seed and 0.23 mm for cassava pulp residue. Figure 2.18 to 2.21 shows the experimental TG data and the simulated results which demonstrate that the two-parallel reactions model not only can describe well the pyrolysis of palm solid wastes but it is also capable of predicting the pyrolysis behavior of many other biomass

materials. The maximum deviations for all materials are in the range of 1-4%. The kinetic parameters determined from the model fitting are listed in Table 2.6. The larger value of b in comparison with that of a indicates that the decomposition of coconut shell and bagasse are mainly contributed by the lighter fraction (second fraction).

Table 2.5 Kinetic parameters (a , A_1 , E_1 , A_2 , E_2 and n) of the two-parallel reactions model for pyrolysis of palm shell, fiber and kernel cake.

Sample	Heating Rate (°C/min)	Size (mm)	1 st fraction			2 nd fraction				Max. error
			a	A_1 (s ⁻¹)	E_1 (kJ/mol)	b	A_2 (s ⁻¹)	E_2 (kJ/mol)	n	
Shell	5	0.36	0.21	9.82×10^{17}	243.1	0.79	1.15×10^{14}	173.2	4.02	2.81%
	10			4.05×10^{16}	226.4		1.20×10^{14}	173.5	3.88	2.74%
	20			2.43×10^{17}	238.9		4.58×10^{13}	169.8	3.50	2.61%
	40			1.53×10^{17}	234.6		1.27×10^{14}	173.6	3.39	2.13%
Shell	20	0.36	0.21	2.43×10^{17}	238.9	0.79	4.60×10^{13}	169.8	3.50	2.61%
		0.51		7.48×10^{16}	232.8		8.61×10^{13}	172.2	3.67	2.60%
		0.73		8.20×10^{16}	233.9		7.63×10^{13}	171.5	3.75	2.59%
		1.10		1.08×10^{17}	234.4		6.56×10^{13}	170.1	3.95	2.98%
		1.40		1.10×10^{17}	234.4		8.66×10^{13}	171.8	4.14	3.11%
Fiber	5	< 1.00	0.26	3.89×10^{16}	219.7	0.74	4.65×10^{14}	170.9	4.05	2.40%
	10			9.04×10^{14}	201.8		1.86×10^{13}	156.8	3.69	2.71%
	20			3.85×10^{15}	209.4		2.92×10^{12}	149.3	3.28	2.76%
	40			2.57×10^{14}	193.7		3.21×10^{13}	158.2	3.38	2.64%
Kernel	5	< 0.15	0.60	2.44×10^5	80.0	0.40	4.29×10^2	54.8	2.37	2.28%
	10			7.66×10^5	83.0		6.20×10^2	54.7	2.29	2.30%
	20			3.58×10^6	87.4		2.07×10^2	47.9	2.04	2.66%
	40			1.76×10^7	91.0		4.83×10^2	48.7	2.07	2.81%

The thermograms of coconut shell and bagasse show the existence of inflection which is the same as in the case of the palm shell and fiber. Based purely on these results, it is expected that the chemical compositions of coconut shell and bagasse are probably similar to those of the palm shell and fiber. For longan seed and cassava pulp residue, the thermograms show no inflection of curve as exhibited also by the palm kernel cake. The derived kinetic parameters show that the pyrolysis reactions of longan seed and cassava pulp residue are contributed equally by the first and second fractions (the values of a and b are comparatively the same). Similar conclusion can be inferred that the chemical compositions of these two materials are probably similar to that of the palm kernel cake.

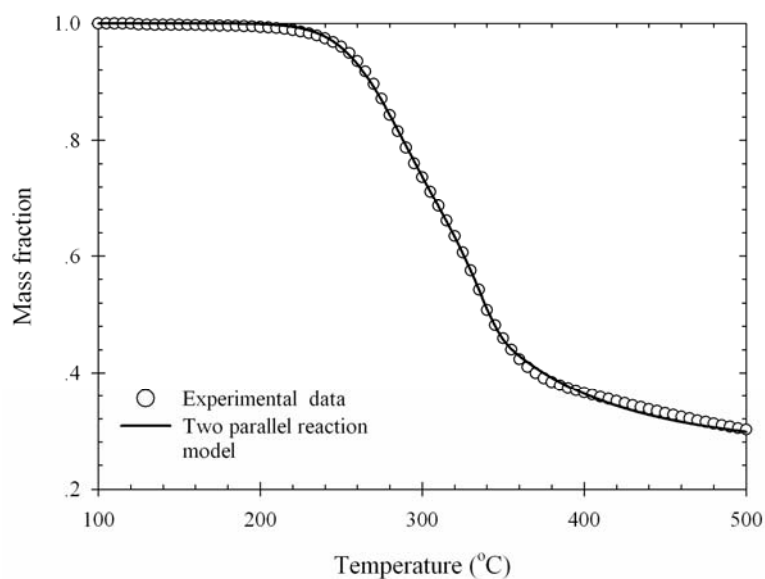


Figure 2.18 TG data and model fitting for coconut shell pyrolyzed at 10°C/min.

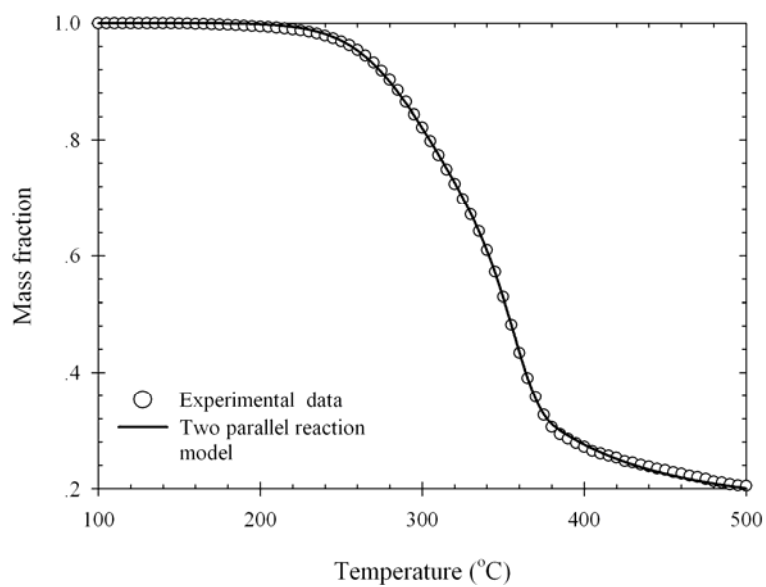


Figure 2.19 TG data and model fitting for bagasse pyrolyzed at 10°C/min.

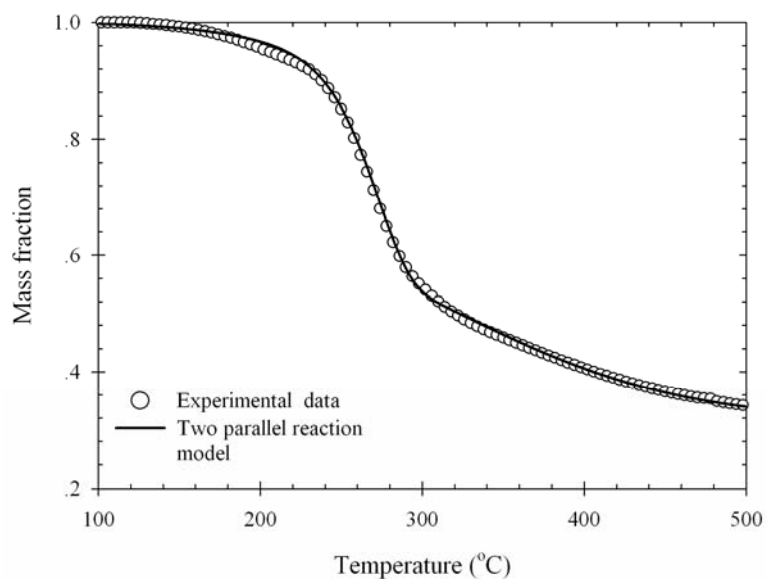


Figure 2.20 TG data and model fitting for longan seed pyrolyzed at 10°C/min.

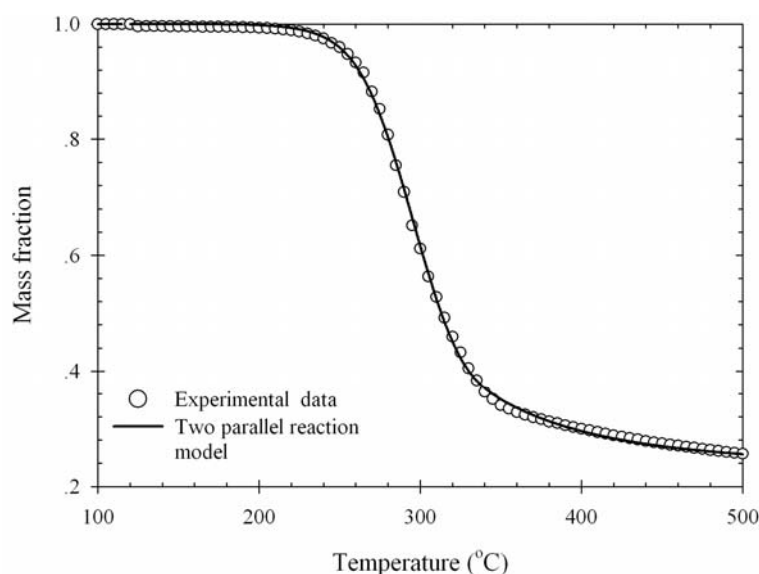


Figure 2.21 TG data and model fitting for cassava waste residue pyrolyzed at 10°C/min.

Table 2.6 Kinetic parameters of two parallel reactions model for pyrolysis of coconut shell, bagasse, Longan seed, cassava waste pyrolyzed at 10 °C/min.

Sample	a	A_1 (s^{-1})	E_1 (kJ/mol)	b	A_2 (s^{-1})	E_2 (kJ/mol)	n	Max. error
Coconut shell	0.14	4.26×10^{21}	254.20	0.86	9.74×10^{10}	138.77	3.43	3.53%
Bagasse	0.30	2.68×10^{17}	233.76	0.70	4.54×10^7	106.26	3.35	3.16%
Longan seed	0.47	1.23×10^{10}	126.96	0.53	1.20×10^1	30.55	1.41	1.41%
Cassava waste	0.49	7.66×10^7	110.0	0.51	7.22×10^{15}	218.2	3.13	3.15%

2.7 Conclusions

The non-isothermal thermogravimetric analysis of palm solid wastes, including palm shell, fiber and kernel cake shows significant influence of raw material size and heating rate on their pyrolysis behavior. The following conclusion can be drawn from this study.

- The pyrolysis process of palm shell and fiber consisted of two distinct kinetic schemes, while only one step of kinetic scheme was observed for palm kernel cake.
- The particle size had no significant effect on the thermogram of palm shell at the initial stage of pyrolysis (temperature lower than 320°C), after that the residual mass of sample and the final yield of char increased with increasing of particle size at the same pyrolysis temperature.
- As the heating rate was increased, the thermograms of palm shell, fiber, and kernel cake shifted systematically to higher temperature region. However, there was no measurable effect of heating rate on the final yield of char for all three materials.
- The one-step global model was able to describe the thermal decomposition of palm kernel cake, while the pyrolysis processes of palm shell and fiber were best described by the two independent kinetic processes namely two-parallel reactions model proposed in this work. This model was capable of describing the experimental data with the maximum deviation being in the range of 2-4%.
- Since the two-parallel reaction model consists of 6 kinetic parameters, it is rather difficult to assign correct initial guesses of the kinetic parameters for the model optimization. As a result of this difficulty, some parameter should be determined experimentally, such as the initial fraction (a and b) of the first and second components.

2.8 References

- Antal, M.J. (1983). Biomass pyrolysis: a review of the literature: Part 1 Carbohydrate pyrolysis. In K.W. Boer and J.A. Duffie (Eds.). **Advances in Solar Energy** (pp 61-111). Colorado: American Solar Energy Society.
- Bansal, R.C., Donnet, J.B. and Stoeckli, F. (1988). **Active Carbon**. New York: Marcel Dekker.
- Bellais, M., Davidsson, K.O., Liliedahl, T., Sjostrom, K and Pettersson, J.B.C. (2003). Pyrolysis of large wood particles: a study of shrinkage importance in simulations. **Fuel** 82: 1541-1548.
- Caballero J.A., Conesa J.A., Font R. and Marcilla A. (1997). Pyrolysis kinetics of almond shells and olive stones considering their organic fractions. **Journal of Analytical and Applied Pyrolysis** 42: 159-175.
- Chan, W.R., Kelbon, M. and Krigger, B.B. (1985). Product formation in the pyrolysis of large wood particles. In: R.P. Overend, T. Milne and L. Mudge (Eds.). **Fundamentals of Thermochemical Biomass Conversion** (pp. 219-236). New York: Elsevier Applied Science.
- Fisher, T., Hajaligol, M., Waymack, B. and Diane, K. (2002). Pyrolysis behaviour and kinetics of biomass derived materials. **Journal of Analytical and Applied Pyrolysis** 62: 331-349.
- Font, R., Marcilla, A., Verdu, E. and Devesa, J. (1991). Thermogravimetric kinetic study of the pyrolysis of almond shells impregnated with CoCl_2 . **Journal of Analytical and Applied Pyrolysis** 21: 249-264.

- Guo J. and Lua A.C. (2001). Kinetic study on pyrolysis process of palm solid waste using two-step consecutive reaction model. **Biomass and Bioenergy** 20: 223-233.
- Haines, P.J. (1995). **Thermal Methods of Analysis: Principles, Applications and Problems**. UK: Blackie Academic & Professional.
- Haykiri-Acma, H. (2006). The role of particle size in the non-isothermal pyrolysis of Hazelnut shell. **Journal of Analytical and Applied Pyrolysis** 75: 211-216.
- Jayaweera, S.A.A., Moss, J.H. and Thwaites, M.W. (1989). The effect of particle size on the combustion of weardale coal. **Thermochimica Acta** 152: 215-225.
- Kok, M.V., Ozbas, E., Karacan, O. and Hicyilmaz, C. (1998). Effect of particle size on coal pyrolysis. **Journal of Analytical and Applied Pyrolysis** 45: 103-110.
- Larsen, M.B., Schultz, L., Glarborg, P., Skaarup-Jensen, L. Dam-Johansen, K., Frandsen, F. and Henriksen, U. (2006). Devolatilization characteristics of large particles of tyre rubber under combustion conditions. **Fuel** 85: 1335-1345.
- Ontiveros, J.L., Clapp, T.L. and Kosson, D.S. (1989). Physical properties and chemical species distributions within municipal waste combustor ashes. **Environmental Progress** 8: 200-206.
- Shuanhning, X., Zhihe, L., Baoming, L., Weiming, Y. and Xueyuan, B. (2006). Devolatilization characteristics of biomass at flash heating rate. **Fuel** 85: 664-670.
- Turner, F. and Mann, U. (1981). Kinetic investigation of wood pyrolysis. **Industrial & Engineering Chemistry Process Design and Development** 20: 482-488.

- Tsamba, A.J., Yang, W. and Blasiak, W. (2006). Pyrolysis characteristics and global kinetic of coconut and cashew nut shells. **Fuel Processing Technology** 87: 523-530.
- Vamvuka, D., Kakaras, E., Kastanaki, E. and Grammelis, P. (2003). Pyrolysis characteristics of biomass residuals mixture with lignite. **Fuel** 82: 1949-1960.
- Wichman, I.S. and Atreya, A. (1987). A simplified model for pyrolysis of charring materials. **Combustion and Flame** 68: 231-247.

CHAPTER III

PREPARATION OF ACTIVATED CARBON IN A LABORATORY TUBE FURNACE

3.1 Abstract

The two-step physical activation process was employed for the preparation of activated carbons from oil-palm solid wastes, including palm shell, fiber and kernel cake – an abandoned agricultural solid wastes produced during palm-oil mill process. These solid wastes were first carbonized in a laboratory tube furnace under constant flow of nitrogen. The effect of carbonization conditions (i.e. temperature, holding time, heating rate and particle size) on the final yield, iodine number and proximate analysis of the produced chars were investigated. The optimum carbonization conditions for preparing chars from those three types of oil-palm solid wastes were determined by considering their iodine number, final yield and proximate analysis.

The derived chars were further activated with carbon dioxide for varying times (1-4 hrs) and temperatures (700-900°C). The porous properties of the resulting activated carbons were characterized using adsorption isotherm data of nitrogen gas at -196°C. The palm shell and fiber based activated carbon exhibited Type I isotherm, while the palm kernel cake based activated carbon showed Type IV isotherm. Over the range of activation temperature used, the BET surface area and pore volume increased with increasing activation temperature. The same tendency for both surface area and pore volume was also observed for the effect of activation time, but with less

significant effect after 2 hrs for the case of palm fiber and kernel cake. The optimum activation conditions that gave the maximum in surface area occurred under the following conditions: 950°C and 2 hrs for palm shell, 850°C and 2 hrs for fiber, and 900°C and 2.5 hrs for palm kernel cake, corresponding to 48%, 52% and 66% of char burn-off, respectively. The maximum BET surface area obtained were 1067, 522 and 789 m²/g for activated carbons produced from shell, fiber and kernel cake, respectively. The level of char burn-off was found to correlate extremely well with the porous properties for each type of activated carbon, irrespective of the activation conditions.

3.2 Introduction

The preparation of activated carbon by physical activation method consists of two main steps: carbonization and activation. For carbonization, the carbonaceous material is decomposed at the temperature below 800°C to eliminate non-carbon species (i.e. oxygen, nitrogen, and hydrogen), hence producing a carbon rich mass. Some of the pores are created during this step but not well developed and interconnected. The quality and the final yield of the carbonized product (i.e. char) depend on the heating rate, carbonization temperature, holding time at final temperature, and the nature and physical state of raw materials (Bansal et al., 1988). Mackay and Roberts (1982a) found that the basic microporous structure of char was formed at the carbonization temperature about 500°C, although some of these pores were blocked by the pyrolysis products (i.e. tar) and these blocked pores could be available when the char is further carbonized at higher temperatures. The carbonization process can be separated into two main stages: softening period and

shrinkage of the char (Bansal et al., 1988). The properties of char during the softening period depend on the carbonization temperature used. The shrinkage of the char plays an important role in the development of porous structure in the char.

For activation step, the aim is to enhance the pore volume and enlarge the pores which are created during the carbonization step and also create some new porosity. The activation of char is commonly carried out at temperatures between 800 to 1100°C in the presence of oxidizing gases (i.e. activating agent) such as carbon dioxide, steam, air and any mixture of these gases. The porous properties (i.e. internal surface area, pore volume, pore size distribution) depend primarily on the nature of raw material and their conditions of carbonization and activation (Mackay and Roberts, 1982b). In the early stage of activation, less than 10% burn-off, the disordered carbon is removed and the aromatic sheet is exposed and creates a reaction with the activation agent, leading to the development of microporous structure. The blocked pores occurring during the carbonization step are opened in this stage. For the next stage, the reaction widens the existing pores or formation of the large size pores by the complete burnout of the walls between the adjacent pores, leading to the transition of the microporosity to mesoporosity or macroporosity and hence the lowering in the micropore volume and surface area.

Although the precise mechanism of the activation process is not fully understood, the major mechanism involved may be viewed as the gasification reaction between carbon atoms contained in the carbonized product and the activating agent. Each carbon atom in the char has different reactivity depending on their arrangement and position. The carbon atom located at the edge and boundary of aromatic sheet or at defect positions and dislocations or discontinuities will have higher reactivity. The

gasification reaction of carbon dioxide (used as the activating agent in this work) with carbon atoms follows the endothermic reaction (Bansal et al., 1988):



In this chapter, the preparation and characterization of activated carbons from oil-palm solid wastes, including palm shell, fiber and kernel cake were studied and presented. The experiments were carried out in a laboratory tube furnace by using physical activation with carbon dioxide. The effects of preparation conditions for both carbonization and activation steps on the physical and porous properties (e.g. internal surface area, pore volume, pore size distribution, etc.) of activated carbon products were investigated.

3.3 Review of the Literatures

To date, considerable work on the preparation and characterization of activated carbons from many different carbonaceous materials by physical activation has been reported in the literatures. Duran-Valle et al. (2006) prepared the chars from cherry stone and examined the effect of carbonization conditions on the chemical composition and porous texture. Their study indicated that the surface functional groups and porous structure of chars depended mainly on the carbonization temperature and holding time at the final temperature. Katyal et al. (2003) studied the effect of process variables (i.e. carbonization temperature, heating rate, and inert sweep gas flow rate and particle size) on the yield and composition of solid char produced from bagasse in a fixed bed reactor. They found that the yield of char

decreased significantly with the increasing of temperature when the char was carbonized at temperatures lower than 500°C and the product yield appeared to be independent of the heating rate and particle size. The flow rate of inert sweep gas affected significantly on the yield of char: the yield decreased with increasing in the inert gas flow rate. Lu et al. (2000) studied the effect of carbonization temperature on the aromatic structure, physical structure and chemistry of derived chars prepared from five Australian black coals. The experimental results indicated that the char became more ordered and condensed when the temperature was increased. They also found that the types of raw materials used affected strongly on the aromatic structure of char. The atomic ratio of H/C and O/C decreased considerably with the increasing of carbonization temperature.

Some researchers have studied the effect of carbonization conditions on the properties of the activated carbon. Daud et al. (2000) investigated the effect of carbonization temperature on the pore development of palm shell based activated carbon prepared in a fluidized bed reactor. They found that the activated carbon prepared from char carbonized at high temperatures consisted mainly of microporous structure. Marcilla et al. (1996) studied the influence of carbonization heating rate on the physical properties of activated carbon derived from a sub-bituminous coal. The results showed that the chars obtained at higher heating rate seemed to have higher gasification reactivity than those carbonized at a lower heating rate. Robert et al. (2003) examined the effect of carbonization pressure on coal based char reactivity. The experiments were carried out in a pressurized thermogravimetric analyzer. They concluded that the carbonization pressure did not affect directly on the gasification reactivity of char. However, the chars prepared at higher pressure appeared to react

with activating agent faster than those prepared at a lower pressure. The increasing in reaction rate is mostly due to the increasing in internal surface area of the char when pyrolyzed at the higher pressure.

Several carbonaceous materials are used as precursors for the preparation of activated carbons. Ganan et al. (2006a, 2006b) used air and carbon dioxide as activating agents for the preparation of high quality activated carbons from almond tree pruning. Their activated carbon gave specific surface area of 959 m²/g with 19.2% burn-off and 840 m²/g with 69.5% burn-off for air and carbon-dioxide activation, respectively. Gonzalez et al. (2006) prepared the activated carbon from used tire by steam and carbon dioxide activation. They found that the activated carbon produced with steam activation exhibited narrower micropores and lower BET surface areas and total pore volumes than those activated with carbon dioxide. For other types of carbonaceous materials, the preparation of activated carbons by physical activation were reported elsewhere, for example, macadamia nut shell (Tam and Antal, 1999), coconut shell (Tam and Antal, 1999; Iwasaki et al., 2002; Su et al., 2006), oil-palm wood (Ahmad, 2006), sewage sludge (Yu and Zhong, 2006), bagasse (Juang et al., 2002; Valix et al., 2004), coal (Pis et al., 1998; Arenas and Chejne, 2004; Scott et al., 2005), etc.

On the preparation of activated carbons from oil-palm solid wastes, both chemical and physical activation have been employed. Guo et al. (2005) and Adinata et al. (2007) prepared activated carbons from oil-palm shell by using chemical activation with sulfuric acid (H₂SO₄) and potassium carbonate (K₂CO₃). The activated carbon derived from H₂SO₄ activation provided the highest BET surface area of about 1250 m²g⁻¹, while the carbon activated with K₂CO₃ gave the highest BET surface area

of $1170 \text{ m}^2\text{g}^{-1}$. Daud and Ali (2004) prepared the activated carbon from palm shell and coconut shell in a fluidized bed reactor by using carbon dioxide as the activating agent. They found that, at any burn-off, the micropore and mesopore volumes created in palm shell- based activated carbon were always higher than those of coconut-shell-based activated carbon. The activation rate of coconut-shell based char is significantly higher than that of palm-shell based char which mean that longer activation time is required for palm shell based activated carbon to achieve a certain level of burn-off during activation process.

3.4 Research Methods

The oil-palm shell, fiber and kernel cake were supplied by the Golden Palm Industry in Chonburi Province, Thailand. The received solid wastes were washed and dried in an oven at 110°C for 24 hrs. The dried materials were crushed and sieved to obtain the average particle size of 0.5, 1.0, 1.4 and 2.0 mm for oil-palm shell, and size smaller than 1.0 mm and 0.25 mm for the palm fiber and kernel cake, respectively. The proximate and ultimate analyses of these solid wastes are shown in Table 3.1 which also appears in Table 2.1 of Chapter 2. About 10 g of each sample was loaded into a ceramic boat and carbonized in a laboratory tube furnace (Carbolite CTF 12/75/700, 6 cm in diameter and 100 cm in length) under constant supply of ultra high purity grade nitrogen (UHP, 99.995% purity) at $100 \text{ cm}^3/\text{min}$. The effects of carbonization temperatures ($400\text{-}800^\circ\text{C}$), times (0.5-3.0 hrs), and heating rates ($5\text{-}40^\circ\text{C}/\text{min}$) on the properties of the resulting chars were investigated. Subsequently, the derived chars were activated in the same tube furnace under a constant flow ($100 \text{ cm}^3/\text{min}$) of high purity grade CO_2 (HP, 99.95% purity). Porous properties of the

derived activated carbons, including BET surface area, pore volume and pore size distribution, were determined as follows. The BET surface area was estimated from adsorption isotherm data of nitrogen at -196°C (collected by using Micromeritics ASAP 2010 adsorption apparatus) by applying the Brunauer-Emmett-Teller (BET) equation (Do, 1998). The total pore volume was computed from the volume of nitrogen gas adsorbed at the relative pressure of 0.99 and converted it to the volume of N_2 in liquid state. Micropore volume was calculated by using the Dubinin-Astakhov (DA) equation (Do, 1998). The pore size distribution (PSD) was determined by applying the Density Functional Theory (DFT) model (El-Merraoui et al., 2000). Percentage of moisture, volatile and ash contents of raw materials, chars and activated carbons were determined according to the ASTM standard (ASTM D2867-95, D5832-95 and D2866-94 for the determination of moisture, volatile and ash contents, respectively). The fixed carbon content was calculated by mass balance.

Table 3.1 Proximate and ultimate analysis of the palm shell, fiber and kernel cake.

Sample	Ultimate analysis (% w/w)					Proximate Analysis			Solid Density g/cm^3
	C	H	N	S	O	Volatile	Fix-C	Ash	
Shell	47.6	5.38	0.66	0.04	41.38	72.7	23.6	3.6	1.42
Fiber	46.64	5.66	1.73	0.10	39.46	73.7	12.6	6.6	0.75
Kernel	41.47	5.77	3.00	0.03	43.49	80.3	10.3	3.2	1.39

3.5 Results and Discussion

3.5.1 Carbonization of Palm Shell

In this section, the effect of carbonization conditions (i.e. carbonization temperature, holding time, heating rate and particle size) on the porous characteristics and proximate analysis of the derived chars are reported for palm shell.

It should be noted that the adsorption isotherm of N₂ at -196°C on the derived chars prepared at some carbonization conditions could not be directly measured, especially at low carbonization temperatures (400-600°C). This is due to the fact that the porous structure of char was not yet fully developed, containing pores of very fine sizes with most pores being blocked by tar products generated during the carbonization step. Therefore, N₂ molecules could not easily get access into the internal pores of the char particles and hence its porous properties cannot be directly determined from the isotherm data. As a result of this difficulty, the porous characteristics of the derived char were characterized by using the iodine number in place of the BET surface area, pore volume and PSD. Iodine number is the most fundamental parameter used to characterize activated carbon performance. It is a measure of activity level (higher number indicates higher degree of activation). It is a measure of the micropore content of the activated carbon (0 to 20 Å, or up to 2 nm) by adsorption of iodine from solution. The iodine number of the palm-shell based chars was determined by following the ASTM D4607-94 (1998) standard.

The numerical data of yield and iodine number and also the proximate analysis of all the chars prepared at various carbonization temperatures, particle sizes, heating rates, and holding times are listed in Table 3.2. For the effect of carbonization temperature on the final yield and iodine number of the resulting chars (see Figure 3.1

and 3.2), the plots show that the yield drops linearly with the increasing of carbonization temperature when the palm shell is carbonized at the temperature lower than 600°C. At higher temperatures, the decrease continues but the relative variation of yield with temperature becomes less. The reverse trend of iodine number with respect to carbonization temperature can be observed. That is iodine number, which is a measure of micropore volume (particle size 1.4 mm) increases rapidly with temperature when the sample is carbonized at the temperature lower than 600°C, and then it increases at a slower rate when the temperature is further increased. These observations indicate that the pyrolysis scheme of palm shell is almost completed at 600°C. This conclusion agrees with the collected TGA and DTG data of palm shell in the previous chapter (Chapter 2, see Figure 2.4) and it is also confirmed by considering the value of proximate analysis. The proximate analysis results show that the fixed carbon and volatile contents of char change significantly when the carbonization temperature is increased up to 600°C, but moderate changes of fixed carbon and volatile contents are observed at the higher carbonization temperatures.

Figure 3.3 and 3.4 shows the effect of particle size on the yield and iodine number of the resulting chars, respectively. The palm shell was carbonized at 600°C for 1.0 hr at heating rate of 5°C/min. The results show that there is almost no measurable effect of particle size (from 0.5 to 2.0 mm) on the value of yield, iodine number and proximate analysis (i.e. fixed carbon, volatile and ash contents) of the prepared char. This observation indicates that the effect of heat and mass transfer resistance inside the char particle can be neglected for the range of particle size studied here.

Table 3.2 Yield, iodine number and proximate analysis of the palm shell chars prepared at various carbonization conditions.

Carbonization conditions				% Yield	Iodine no.	Proximate Analysis (%)		
Temp. (°C)	Time (hr)	Heating rate (°C/min)	Particle size (mm)			Fix-C	Volatile	Ash
400	1	5	1.4	39.25	29.01	69.19	28.59	2.22
500				35.42	54.58	79.36	17.03	3.61
600				32.20	117.35	85.58	11.33	3.10
700				30.73	135.03	88.50	7.72	3.77
800				29.89	152.24	90.18	5.61	4.22
600	1	5	0.5	31.45	114.67	85.75	10.89	3.36
			1.0	31.87	109.50	85.58	11.33	3.10
			1.4	32.20	117.35	84.45	12.56	2.99
			2.0	32.26	113.22	84.26	12.99	2.75
400	1	5	1.4	39.25	29.01	69.19	28.59	2.22
		10		38.91	25.13	68.89	27.69	3.42
		20		37.43	35.45	68.21	28.22	3.56
		30		37.01	32.56	67.09	29.03	3.88
600	1	5	1.4	31.20	117.35	85.58	11.33	3.10
		10		30.69	111.85	85.71	10.31	3.99
		20		30.06	109.58	86.19	9.78	4.03
		30		29.50	107.52	85.87	9.25	4.88
800	1	5	1.4	29.89	152.24	90.18	5.61	4.22
		10		29.62	141.25	87.89	7.65	4.46
		20		29.35	145.26	82.99	12.70	4.31
		30		28.68	138.58	75.13	20.05	4.83
400	0.5	5	1.4	39.89	31.18	68.75	29.24	2.01
	1.0			39.25	29.01	69.19	28.59	2.22
	2.0			39.49	58.82	70.26	26.21	3.53
	3.0			38.96	45.61	71.40	24.28	4.32
600	0.5	5	1.4	31.98	112.29	84.11	13.06	2.83
	1.0			32.20	117.35	85.58	11.33	3.10
	2.0			31.85	135.80	86.34	9.50	4.16
	3.0			31.52	120.16	88.33	6.65	5.03
800	0.5	5	1.4	29.95	131.07	88.78	7.19	4.03
	1.0			29.89	152.24	90.18	5.61	4.22
	2.0			30.09	136.07	91.73	3.72	4.55
	3.0			30.08	127.03	92.95	2.29	4.77

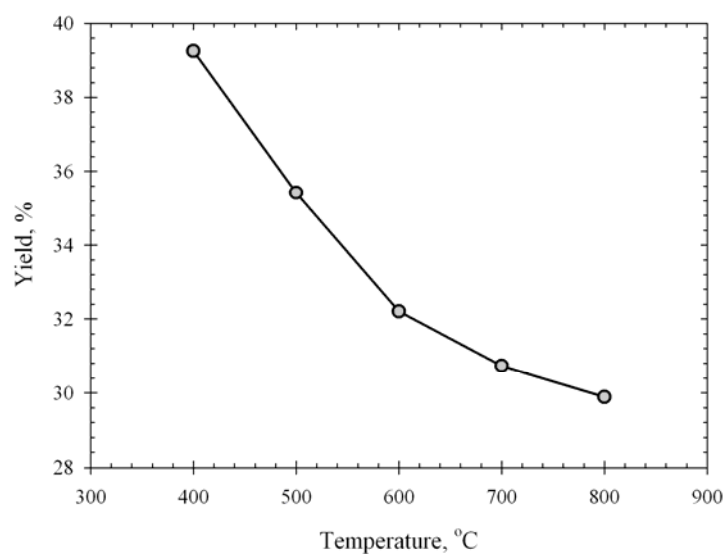


Figure 3.1 Effect of carbonization temperature on the final yield of the palm shell chars for particle size of 1.4 mm carbonized at heating rate of 5°C/min and 1.0 hr of holding time.

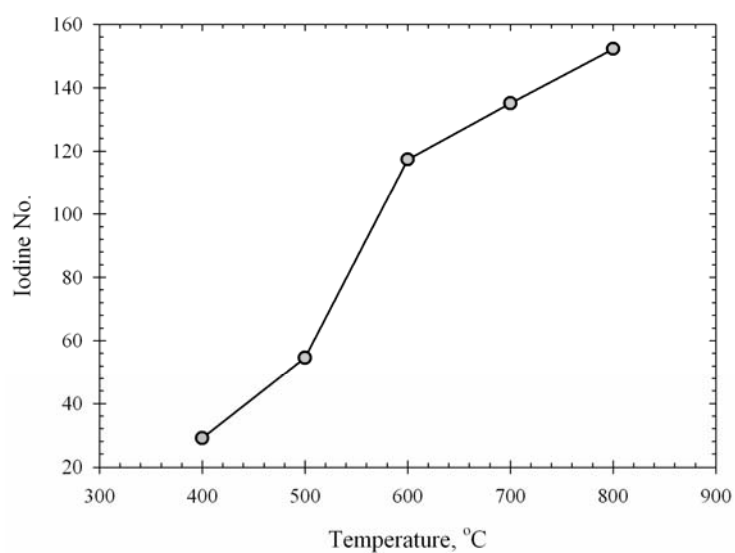


Figure 3.2 Effect of carbonization temperature on the iodine number of the palm shell chars for particle size of 1.4 mm carbonized at heating rate of 5°C/min and 1.0 hr of holding time.

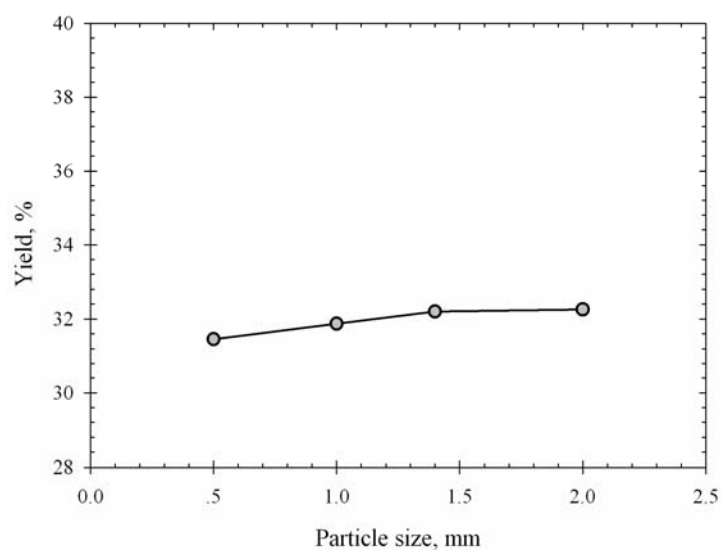


Figure 3.3 Effect of particle size on the final yield and iodine number of the palm shell chars carbonized at 600°C, 5°C/min of heating rate, and 1.0 hr of holding time.

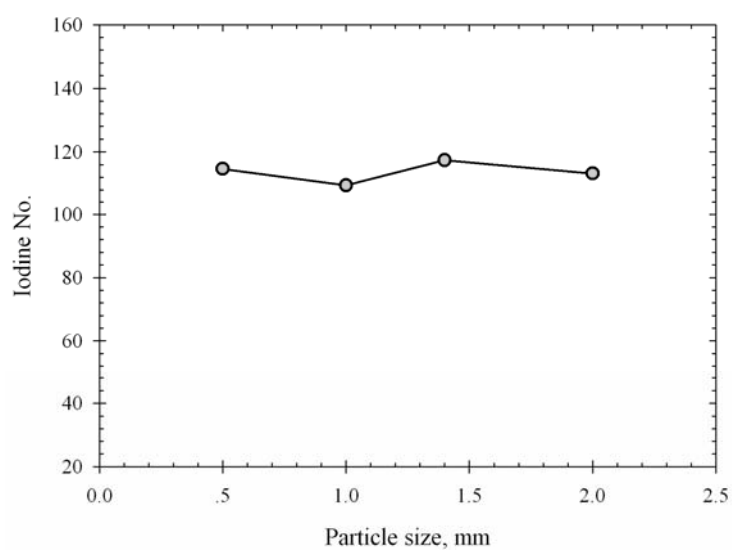


Figure 3.4 Effect of particle size on the final yield and iodine number of the palm shell chars carbonized at 600°C, 5°C/min of heating rate, and 1.0 hr of holding time.

The effect of heating rate on the characteristic of the resulting chars at three carbonization temperatures (i.e. 400, 600 and 800°C) with the same holding time of 1.0 hr are shown in Figure 3.5 and 3.6 for the yield and iodine number, respectively. The heating rate plays a significant effect on the final yield of chars when the palm shell was carbonized at 400°C. At this carbonization temperature, the yield decreases almost linearly with increasing of heating rate. At higher carbonization temperature (i.e. 600°C and 800°C), the same behavior can be observed but the heating rate appears to have lesser effect on the final yield of char as the temperature is increased. These observations could be attributed to the effect of secondary reactions of volatile products generated during the pyrolysis process to form more solid char. That is, at a low heating rate, the volatile matters can be purged by flowing nitrogen from the reaction zone at a lower rate and the volatile matters have longer residence time to undergo the secondary reactions to form solid char (Williams and Besler, 1996). Therefore, additional solid chars are produced when the sample was carbonized at lower heating rates. A decrease in the yield of char with increasing of heating rate were also reported by Katyal et al. (2003), Haykiri-Acma et al. (2006) and Demirbas et al. (2006). Katyal et al. (2003) conducted the carbonization experiments on the samples of sugar cane bagasse in a static fixed bed reactor. Haykiri-Acma et al. (2006) employed the TGA technique to investigate the pyrolysis yield of rapeseed carried out at temperature up to 1000°C for various heating rate up to 50°C/min. Demirbas et al. (2006) studied the pyrolysis of agricultural residues in Turkey.

In addition, the proximate analyses of the resulting char (see Table 3.2) show that variation in the heating rate has no bearing on the fixed carbon content for

the carbonization temperature of 400 and 600°C, but appreciable increase of fixed carbon can be observed for carbonization temperature of 800°C as the heating rate is decreased. These results indicate that the secondary reaction of volatile products play an important role on char production when the carbonization is carried out at a very high temperature (i.e. 800°C), in agreement also with the work of Morf et al. (2002). It was found in their work that the secondary reactions of volatile matters become important at temperatures higher than 650°C. Although heating rate affects significantly on the final yield of char, it shows no effect on the iodine number of char. The iodine number seems to be constant when the heating rate is changed. This tends to indicate that the range of heating rate studied here has no appreciable effect on the pore evolution of char.

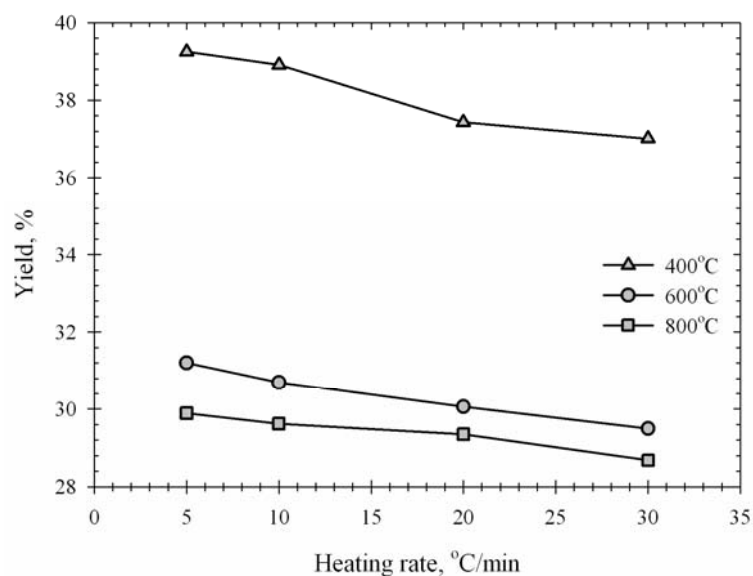


Figure 3.5 Effect of heating rate on the final yield of the palm shell chars for particle size of 1.4 mm carbonized at 1.0 hr of holding time.

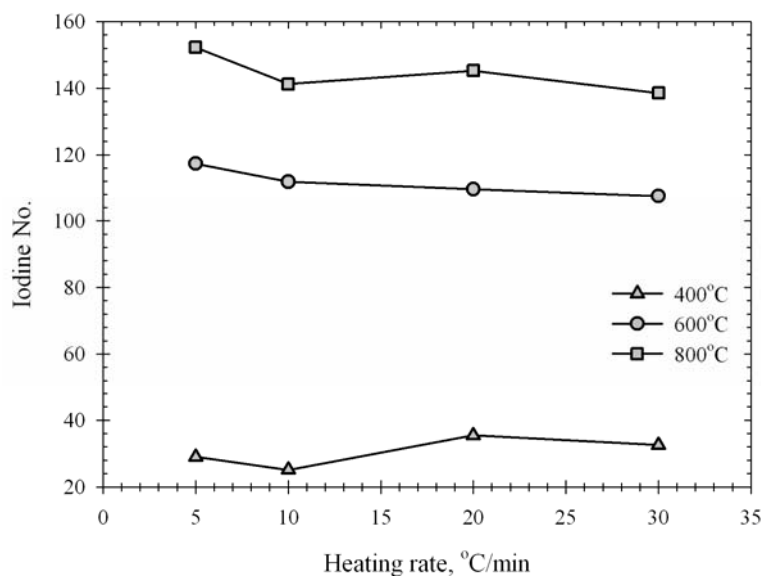


Figure 3.6 Effect of heating rate on the final yield and iodine number of the palm shell chars for particle size of 1.4 mm carbonized at 1.0 hr of holding time.

For the effect of holding time (see Figure 3.7 and 3.8), the yield of char appears to be independent of the holding time for all carbonization temperatures from 400 to 800°C. This means that the pyrolysis process of palm shell is already completed during the heating up stage. The iodine number varies considerably when the holding time is changed. It increases with increasing of holding time and passes through a maximum with the optimum temperature depending on the carbonization temperature. The maximum value of iodine number can be observed at 2.0 hrs for the carbonization temperature of 400°C and 600°C and 1.0 hr for 800°C. The plausible cause for this decreasing of iodine number could result from the shrinkage of char particle, which could cause the collapse of char porous structure, when unnecessary longer activation time was used.

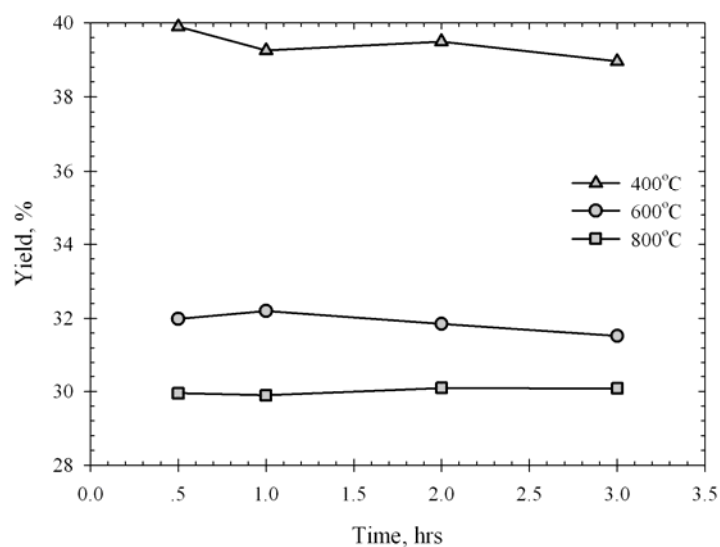


Figure 3.7 Effect of holding time on the final yield and iodine number of the palm shell chars for particle size of 1.4 mm carbonized at heating rate of 5°C/min.

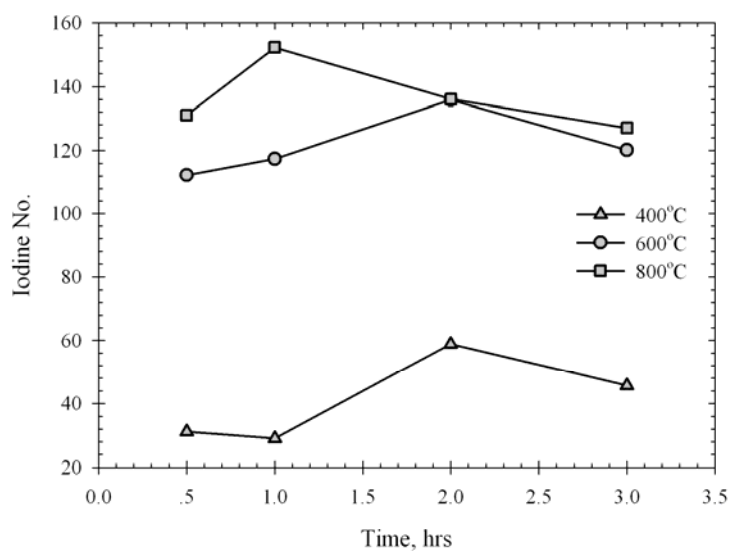


Figure 3.8 Effect of holding time on the final yield and iodine number of the palm shell chars for particle size of 1.4 mm carbonized at heating rate of 5°C/min.

By considering the effect of carbonization conditions on the yield and iodine number of the resulting char, the palm shell was carbonized at the temperature of 600°C to produce char for the next study of CO₂ activation step. The carbonization temperature chosen is well above the main devolatilization temperature (as reported in Chapter 2) to ensure a relatively carbon-rich char, yet not too high to cause char particle shrinkage. Other carbonization conditions, including particle size, heating rate, and holding time, are arbitrarily selected because they seem to have less effect on final yield and iodine number of char when the palm shell is carbonized at the temperatures above 600°C (see Figure 3.3 to 3.8). In this work, the particle size of 1.4 mm, heating rate of 5°C/min and holding time of 2.0 hrs were then chosen for preparing palm shell chars for further activation study.

3.5.2 Carbonization of Palm Fiber and Kernel Cake

The oil palm fiber and kernel cake are solid wastes abandoned from the palm-oil milling process. Their potential use as precursors for preparing activated carbons was also studied in this chapter. The derived chars were also used in the subsequent activation step.

Similar to the case of palm shell, the N₂ isotherm data of palm fiber and kernel cake based chars could not be measured, and therefore the BET surface area, total pore volume and pore size distribution by gas adsorption technique cannot be directly determined. The determination of iodine number, which is a measure of surface area in the micropore size range was not performed in this work for palm fiber and kernel cake chars due to the reason that too large amount of the samples was required for the analysis, indicating that their surface areas are much lower than that of palm shell char. As a result of this problem, only the effect of carbonization

conditions on the final yield and proximate analysis of derived chars will be presented.

3.5.2.1 Palm Fiber Char

Figure 3.9 to 3.11 show the change of char yield with respect to the variation of carbonization conditions (i.e. temperature, holding time and heating rate) for palm fiber. Table 3.3 lists the values of char yield and the corresponding proximate analysis of the char samples.

For the effects of carbonization temperature (see Figure 3.9), the results show that the yield of char decreases rapidly when the carbonization temperature is increased from 400 to 500°C. At higher temperatures up to 800°C, the yield decreases continually but with a slower change. The proximate analysis shows (see Table 3.3) that fixed carbon and volatile contents change drastically when the carbonization temperature is increased from 400 to 500°C. Over the temperature from 500 to 800°C, their changes become less with respect to the change in temperature. This observation indicates that most of volatile matters are released at the temperature lower than 500°C. Therefore, the temperature of 500°C was chosen for the carbonization step of palm fiber to prepare char for the next CO₂ activation step.

The effect of holding time on the yield of char is shown in Figure 3.10 for carbonization temperature of 400, 600 and 800°C. The yield of char decrease significantly for the case of 400°C and the holding time up to 2.0 hrs, but the yield seems to be constant when the holding time is longer than 2.0 hrs. For the cases of 600 and 800°C, it appears that holding time has no appreciable effect on the char yield. The proximate analysis also shows the same trend for fixed carbon and volatile contents. The amount of fixed carbon and volatile matters change significantly for

carbonization temperature of 400°C and holding time up to 2.0 hrs and then become almost constant for further increasing of holding time up to 3.0 hrs. There is almost no change in fixed carbon and volatile contents for carbonization at 600 and 800°C. It can be concluded that the pyrolysis of palm fiber is mostly completed when the carbonization temperature is higher than 400°C or for the holding time longer than 2.0 hrs. By considering the effect of holding time on the yield and proximate analysis of the resulting chars, the palm fiber will be carbonized at the holding time of 2.0 hrs to prepare char for the next CO₂ activation step.

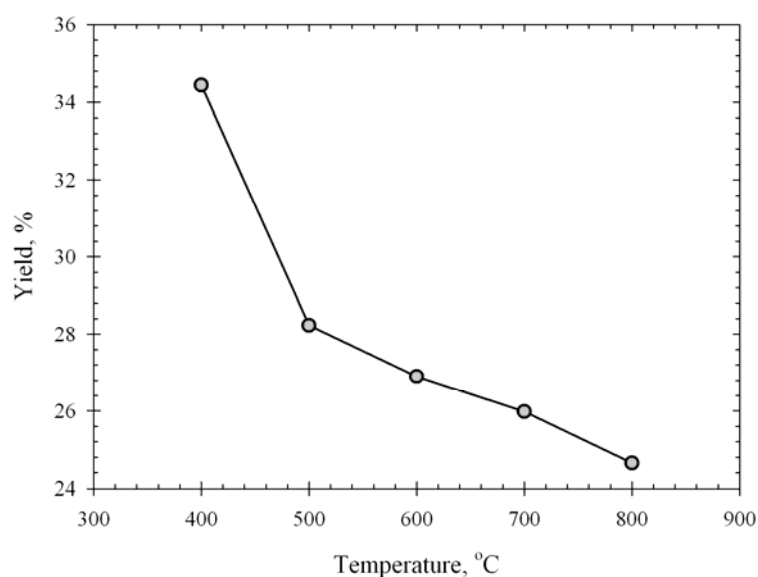


Figure 3.9 Effect of carbonization temperature on the final yield of the palm fiber chars carbonized at heating rate of 5°C/min and 1.0 hr of holding time.

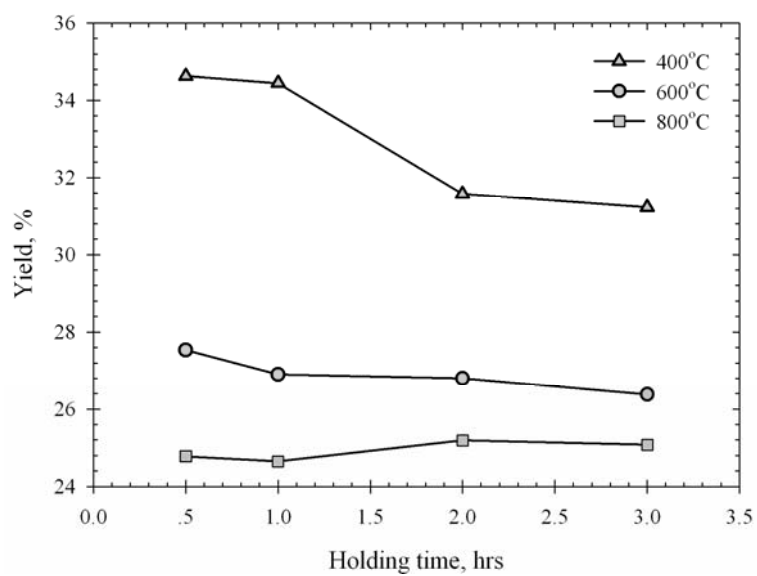


Figure 3.10 Effect of holding time on the final yield of the palm fiber chars carbonized at 1.0 hr of holding time.

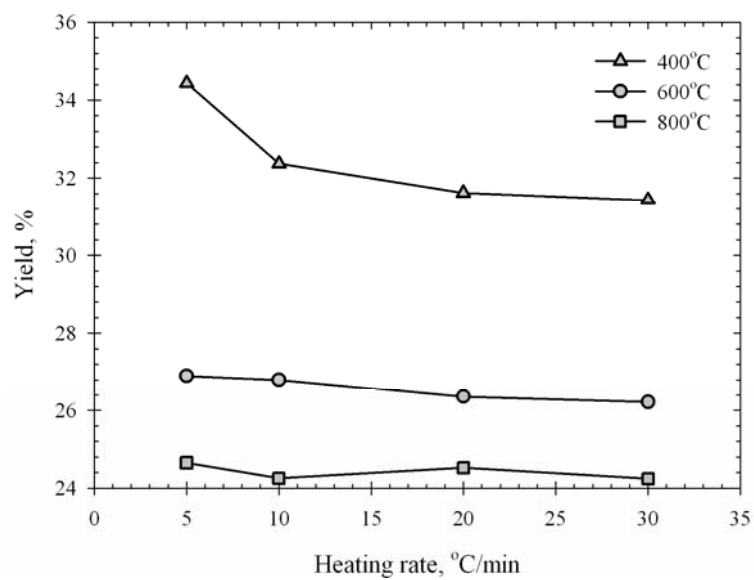


Figure 3.11 Effect of heating rate on the final yield of the palm fiber chars carbonized at 5°C/min of heating rate.

Table 3.3 Yield, iodine number and proximate analysis of the palm fiber chars prepared at various carbonization conditions.

Carbonization conditions			% Yield	Proximate Analysis (%)		
Temp. (°C)	Time (hr)	Heating rate (°C/min)		Fix-C	Volatile	Ash
400	1.0	5	34.44	54.85	31.66	13.49
500			28.23	67.44	16.75	15.81
600			26.90	69.64	14.23	16.13
700			25.98	71.38	12.16	16.46
800			24.65	76.33	6.38	17.29
400	0.5	5	34.63	49.49	38.28	12.23
	1.0		34.44	54.85	31.66	13.49
	2.0		31.58	56.95	30.98	12.07
	3.0		31.23	57.47	29.76	12.76
600	0.5	5	27.53	68.73	14.79	16.48
	1.0		26.90	69.64	14.23	16.13
	2.0		26.80	70.93	13.08	15.99
	3.0		26.38	72.16	12.33	15.51
800	0.5	5	24.78	75.69	8.49	15.82
	1.0		24.65	76.33	6.38	17.29
	2.0		25.19	75.19	8.31	16.50
	3.0		25.08	74.55	8.37	17.07
400	1.0	5	34.44	54.85	31.66	13.49
		10	32.37	52.14	35.26	12.60
		20	31.62	51.88	35.05	13.07
		30	31.43	50.78	35.87	13.35
600	1.0	5	26.90	69.64	14.23	16.13
		10	26.80	67.96	15.15	16.89
		20	26.36	67.26	16.39	16.35
		30	26.22	64.72	18.69	16.59
800	1.0	5	24.65	76.33	6.38	17.29
		10	24.25	75.57	7.28	17.15
		20	24.52	74.69	7.38	17.92
		30	24.24	74.73	7.03	18.25

For the effect of heating rate (see Figure 3.11), the yield decreases continually when the heating rate is increased from 5 to 30°C/min for carbonization temperature of 400°C, while the yield seems to be independent of the heating rate when the palm fiber was carbonized at 600 and 800°C. Similar to the case of palm shell, the decrease of yield with respect to heating rate should be due to the effect of secondary reactions between the volatile products emitted during the pyrolysis process to form more solid char. However, the effect of the secondary reactions between the volatile products seems to be less significant when the palm fiber was carbonized at 600 and 800°C, for which almost negligible change of char yields can be observed when the heating rate is increased. Therefore, it is better to carbonize the palm fiber at the low heating rate to provide the maximum yield of char. As a result of this finding, the palm fiber will be pyrolyzed at the heating rate of 5°C/min for further CO₂ activation to produce activated carbon as reported in the later section.

In addition, from the proximate analysis, it should be noted that the amounts of fixed carbon contained in the palm fiber chars are on the average lower than those for the case of palm shell chars when carbonized at the same condition, and the ash content of palm fiber char is about 5 times higher than that of palm shell char. The ash content indicates the amount of inorganic matters contained in carbon materials. Thus, higher content in the ash means that the palm fiber char contains higher amount of inorganic constituents as compared to the palm shell char.

3.5.2.2 Palm Kernel Cake Char

For palm kernel cake, the effect of carbonization temperature on the yield of derived char is shown in Figure 3.12. The yield of char decreases steadily as the carbonization temperature is increased for the whole range of temperature studied here. The proximate analyses of resulting chars for all preparation conditions are shown in Table 3.4. The fixed carbon content increases and the volatile decreases with increasing of carbonization temperature. The fixed carbon and volatile content change markedly when the carbonization temperature is increased from 400 to 600°C, but lesser changes are observed at higher temperatures. This observation supports that the pyrolysis of palm kernel cake is almost completed at 600°C. It is further noted that the palm kernel cake char also contains high ash content comparable to the case of oil palm fiber char.

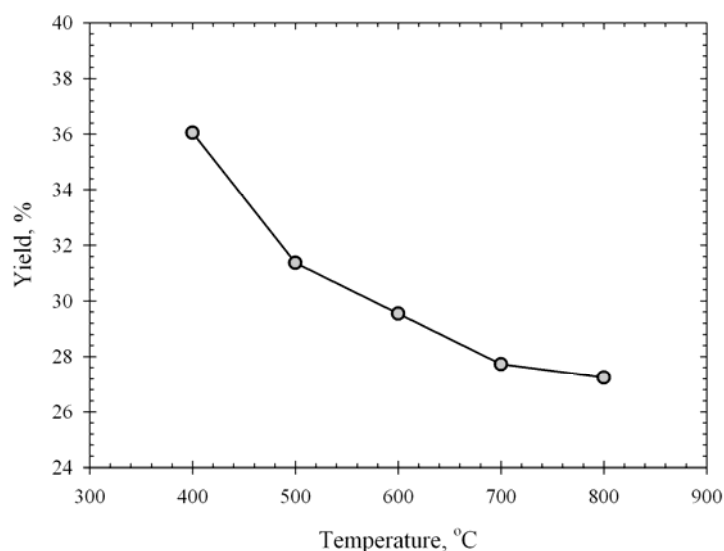


Figure 3.12 Effect of carbonization temperature on the final yield of the palm kernel cake chars carbonized at heating rate of 5°C/min and 1.0 hr of holding time.

Table 3.4 Yield, iodine number and proximate analysis of the palm kernel cake chars prepared at various carbonization conditions.

Carbonization conditions			% Yield	Proximate Analysis (%)		
Temp. (°C)	Time (hr)	Heating rate (°C/min)		Fix-C	Volatile	Ash
400	1.0	5	36.05	59.22	26.85	13.93
500			31.37	65.30	18.35	16.35
600			29.55	71.12	11.61	17.27
700			27.73	72.50	9.94	17.56
800			27.24	74.17	7.88	17.95
400	0.5	5	37.66	58.56	28.11	13.33
	1.0		36.05	59.22	26.85	13.93
	2.0		35.98	58.97	27.04	13.99
	3.0		34.96	59.54	27.07	13.39
600	0.5	5	29.70	69.45	13.64	16.91
	1.0		29.55	71.12	11.61	17.27
	2.0		29.70	71.88	11.16	16.96
	3.0		29.83	69.97	13.22	16.81
800	0.5	5	26.81	74.70	6.95	18.35
	1.0		27.24	74.17	7.88	17.95
	2.0		27.37	74.53	6.90	18.57
	3.0		27.73	74.47	7.17	18.36
400	1.0	5	36.05	59.22	26.85	13.93
		10	36.09	58.89	27.18	13.93
		20	36.13	58.55	27.51	13.94
		30	35.52	58.80	27.02	14.18
600	1.0	5	29.55	71.12	11.61	17.27
		10	28.87	70.91	11.61	17.48
		20	28.06	71.86	10.22	17.92
		30	28.56	71.74	10.66	17.60
800	1.0	5	27.24	74.17	7.88	17.95
		10	26.98	73.27	8.14	18.59
		20	26.11	72.17	8.61	19.22
		30	26.06	72.50	8.06	19.44

The influences of holding time on the final yield of char are shown in Figure 3.13 plotted for three carbonization temperatures (i.e. 400, 600 and 800°C). The plots show that holding time plays an important effect on the yield only at the temperature of 400°C. There is a tendency that when carbonization at this low temperature of 400°C, the decomposition of palm kernel cake still continues even up to the holding time of 3.0 hrs. However, at the carbonization temperatures higher than 600°C, the pyrolysis process is almost completed at the early stage of carbonization. There is no clear effect of holding time on the proximate analysis of the resulting chars. The fixed carbon, volatile and ash content are observed to be constant independent of the change in holding time.

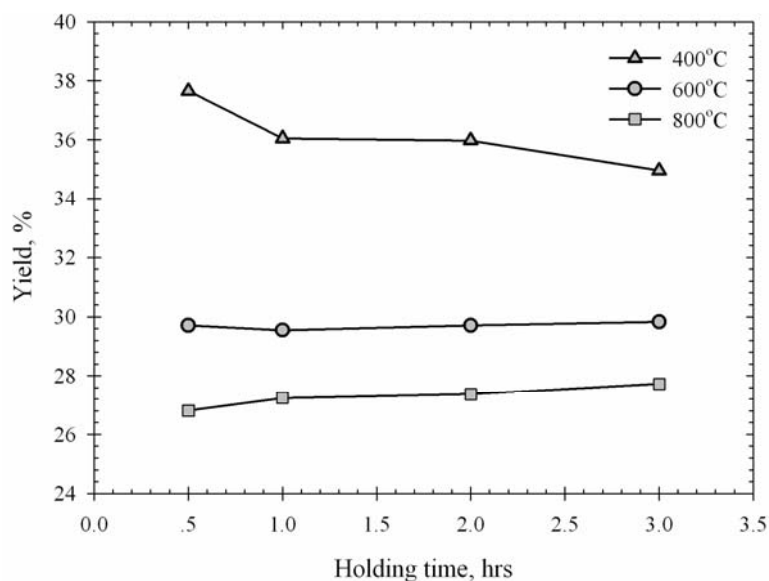


Figure 3.13 Effect of holding time on the final yield of the palm kernel cake chars carbonized at 5°C/min of heating rate.

The effect of heating rate on the yield of char is shown in Figure 3.14. It can be said that heating rate has no significant effect on the final yield of char, although slight variation in the yield can be observed at 600 and 800°C. The heating rate also exerts no important effect on the fixed carbon, volatile and ash content of the resulting chars. To prepare char for the next activation step, the palm kernel cake was carbonized at the temperature of 600°C to ensure that complete carbonization could be achieved. The holding time and heating rate were arbitrary selected as 1.0 hr and 5°C/min, respectively.

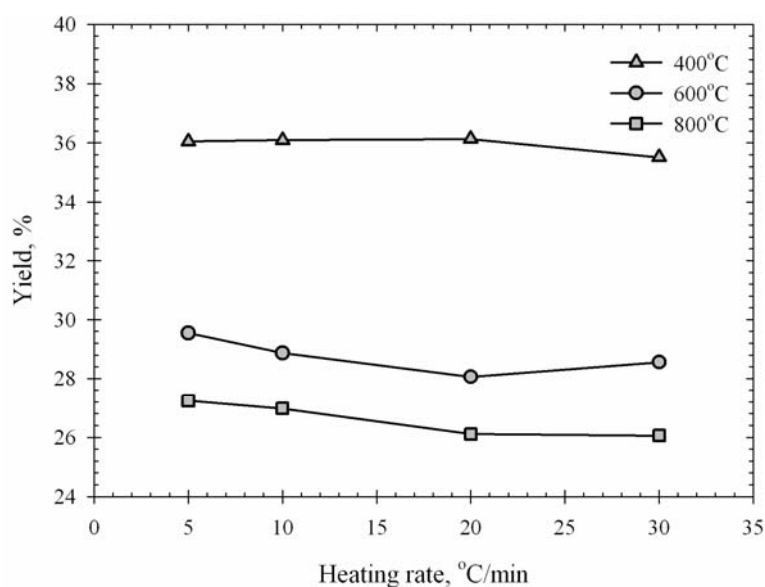


Figure 3.14 Effect of heating rate on the final yield of the palm kernel cake chars carbonized at 1.0 hr of holding time.

3.5.3 CO₂ Activation of Oil-Palm Solid Wastes

The chars prepared from the palm solid wastes, including palm shell, fiber and its kernel cake from the previous sections, were activated with high purity

grade carbon dioxide. The influence of activation conditions (i.e. activation temperature, holding time, CO₂ concentration and flow rate) on the degree of char gasification (% burn-off) and porous characteristics of produced activated carbon including BET surface area, micropore volume, total pore volume and average pore size was investigated. The percentage burn-off and porous characteristics of the activated carbons prepared at various activation temperatures, activation times, CO₂ flow rates and concentrations are listed in Table 3.5, 3.6 and 3.7 for palm shell, fiber and kernel cake, respectively. For the sake of clarity, the effects of activation conditions on percentage burn-off and porous properties of palm shell based activated carbons are displayed graphically in Figure 3.15 to 3.24.

Figure 3.15 to 3.20 show that the char burn-off, BET surface area, and total pore volume of the palm shell based activated carbon increase progressively with increasing of activation temperature and activation time. A slight increasing of the average pore size is observed when the activation temperature is increased (see Figure 3.21). Figure 3.22 shows that the average pore size seems to be independent of the change in activation time. The increase in activation temperature and activation time also leads to the decrease in the percentage of microporosity (also see Figure 3.23 and 3.24). These results indicate that the increase in the BET surface and total pore volume is mostly due to the combined effects of the creation of new small pores, enlargement of existing pores, and the integration of adjacent pores giving larger pore volume.

Table 3.5 Effect of activation temperature, activation time, CO₂ flow rate and concentration on percentage burn-off and the porous properties of palm shell based activated carbons.

Activating Conditions				Burn-off (%)	BET (m ² /g)	Micropore area (m ² /g)	Total pore volume (cc /g)	Micropore volume		Avg. pore size (nm)
Temp (°C)	Time (hr)	CO ₂ flow (cc /min)	CO ₂ conc. (%)					(cc /g)	%	
850	2.0	100	100	16.76	524	465	0.27	0.23	86.7	2.04
900				32.36	776	665	0.41	0.33	80.7	2.12
950				48.35	1067	861	0.60	0.43	72.0	2.26
900	1.0	100	100	21.64	567	507	0.29	0.25	87.6	2.04
	1.5			28.44	651	584	0.33	0.29	88.3	2.03
	2.0			32.36	776	665	0.41	0.33	80.7	2.12
	2.5			35.53	802	686	0.43	0.34	80.9	2.12
	3.0			42.64	921	764	0.50	0.38	76.6	2.18
	3.5			48.67	1026	847	0.55	0.43	77.3	2.15
	4.0			49.48	1046	889	0.59	0.45	76.2	2.16
900	2.0	50	100	28.50	642	555	0.39	0.31	80.5	2.11
		100		32.36	776	665	0.41	0.33	80.7	2.12
		150		36.44	754	646	0.40	0.32	81.0	2.12
		200		36.45	763	653	0.40	0.33	81.6	2.10
		250		36.18	786	673	0.41	0.34	81.2	2.11
		300		38.63	791	691	0.41	0.34	81.2	2.09
900	2.0	200	25	24.22	583	508	0.30	0.25	83.7	2.08
			50	26.70	601	520	0.31	0.26	82.6	2.09
			75	32.02	670	577	0.35	0.29	82.2	2.10
			100	36.45	763	653	0.40	0.33	81.6	2.10

Table 3.6 Effect of activation temperature, activation time, CO₂ flow rate and concentration on percentage burn-off and the porous properties of palm fiber based activated carbons.

Activating Conditions				Burn-off (%)	BET (m ² /g)	Micropore area (m ² /g)	Total pore volume (cc /g)	Micropore volume		Avg. pore size (nm)
Temp (°C)	Time (hr)	CO ₂ flow (cc /min)	CO ₂ conc. (%)					(cc /g)	%	
700	2.0	100	100	13.57	370	306	0.20	0.15	75.9	2.18
750				21.60	405	324	0.22	0.16	72.7	2.20
800				34.09	435	348	0.24	0.17	71.4	2.24
850				51.74	522	411	0.30	0.21	69.1	2.29
850	1.0	100	100	42.46	473	357	0.27	0.18	66.0	2.31
	1.5			45.61	511	379	0.30	0.19	63.1	2.36
	2.0			51.74	522	411	0.30	0.21	69.1	2.29
	2.5			55.73	512	404	0.29	0.20	69.4	2.28
850	2.0	50	100	49.64	513	410	0.30	0.21	67.9	2.28
		100		51.74	522	411	0.30	0.21	69.1	2.29
		150		53.02	519	407	0.30	0.20	69.2	2.27
		200		56.46	506	401	0.28	0.20	69.6	2.24
		250		56.79	515	403	0.29	0.20	68.3	2.25
		300		57.16	510	404	0.30	0.21	68.7	2.22
850	2.0	200	25	45.43	423	372	0.24	0.19	69.1	2.28
			50	47.58	451	359	0.26	0.18	70.3	2.26
			75	50.44	472	373	0.27	0.19	69.8	2.28
			100	56.46	506	401	0.28	0.20	71.0	2.27

Table 3.7 Effect of activation temperature, activation time, CO₂ flow rate and concentration on percentage burn-off and the porous properties of palm kernel based activated carbons.

Activating Conditions				Burn-off (%)	BET (m ² /g)	Micropore area (m ² /g)	Total pore volume (cc /g)	Micropore volume		Avg. pore size (nm)
Temp (°C)	Time (hr)	CO ₂ flow (cc /min)	CO ₂ conc. (%)					(cc /g)	%	
700	2.0	100	100	9.25	266	216	0.15	0.12	78.5	2.03
750				14.27	341	302	0.18	0.14	77.2	2.10
800				20.30	401	335	0.23	0.17	73.9	2.26
850				31.16	512	400	0.32	0.20	63.0	2.49
900				57.04	782	475	0.64	0.24	38.2	3.25
900	1.0	100	100	38.05	577	440	0.37	0.22	59.7	2.57
	1.5			46.47	689	471	0.52	0.24	45.9	3.00
	2.0			57.04	782	475	0.64	0.24	38.2	3.25
	2.5			65.91	789	409	0.76	0.21	27.3	3.87
	3.0			70.51	760	345	0.78	0.18	22.7	4.13
900	2.0	50	100	53.47	736	471	0.60	0.23	38.3	3.23
		100		57.04	782	475	0.64	0.24	38.2	3.25
		150		58.49	787	488	0.64	0.25	38.8	3.22
		200		59.41	784	466	0.64	0.24	37.2	3.26
		250		59.75	788	469	0.66	0.25	38.2	3.24
		300		61.56	786	462	0.66	0.24	37.0	3.32
900	2.0	200	25	47.48	689	408	0.60	0.22	36.7	3.24
			50	50.93	726	428	0.61	0.22	36.1	3.24
			75	58.87	768	455	0.62	0.23	37.1	3.25
			100	59.41	784	466	0.64	0.24	37.2	3.26

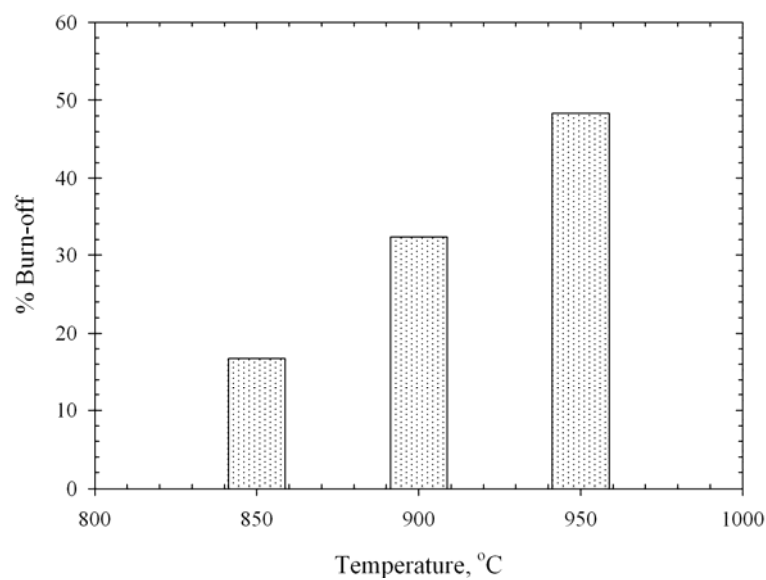


Figure 3.15 Effect of activation temperature on char burn-off of the palm shell based activated carbon activated with pure CO₂ for 2.0 hrs.

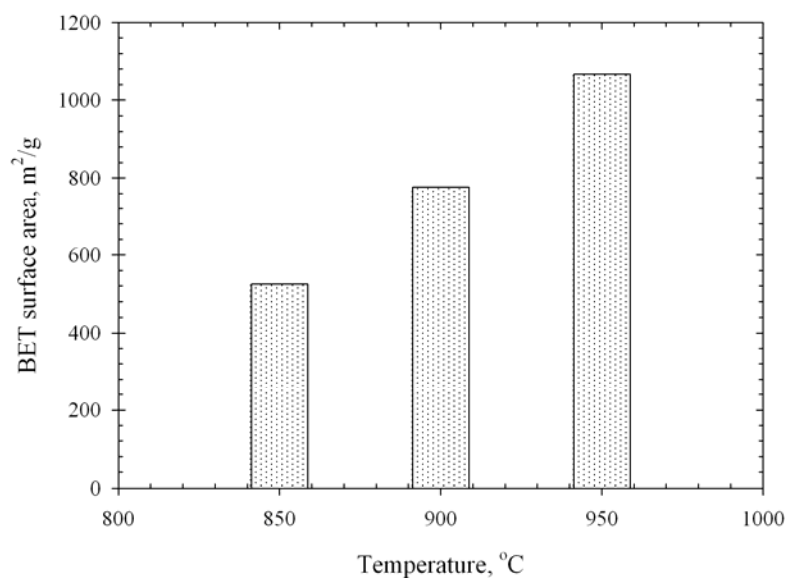


Figure 3.16 Effect of activation temperature on BET surface area of the palm shell based activated carbon activated with pure CO₂ for 2.0 hrs.

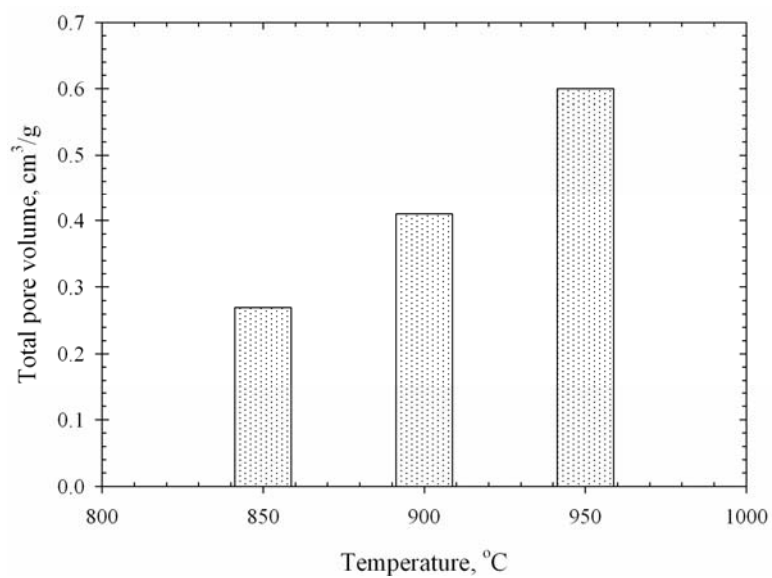


Figure 3.17 Effect of activation temperature on total pore volume of the palm shell based activated carbon activated with pure CO₂ for 2.0 hrs.

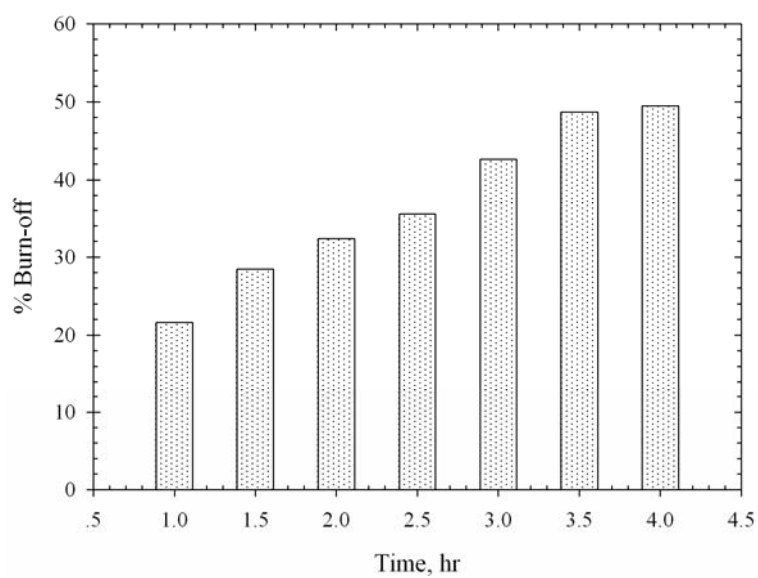


Figure 3.18 Effect of activation time on char burn-off of the palm shell based activated carbon activated at 900°C.

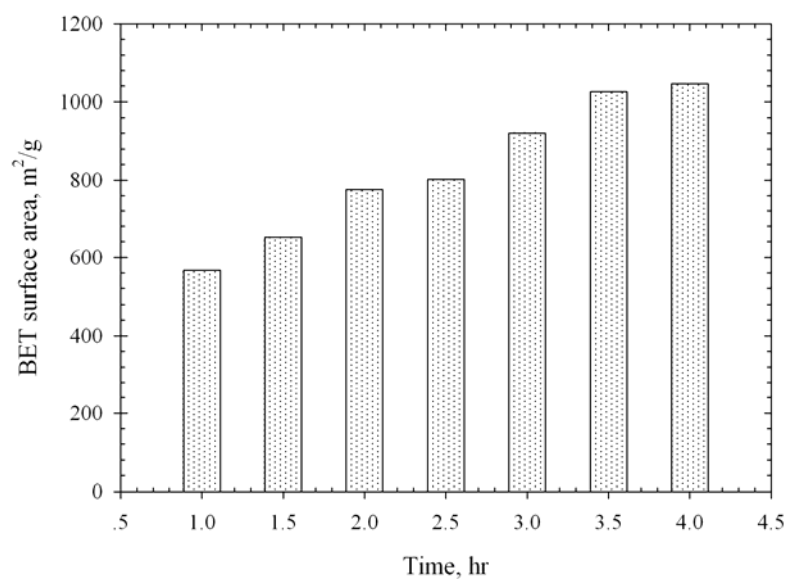


Figure 3.19 Effect of activation time on BET surface area of the palm shell based activated carbon activated at 900°C.

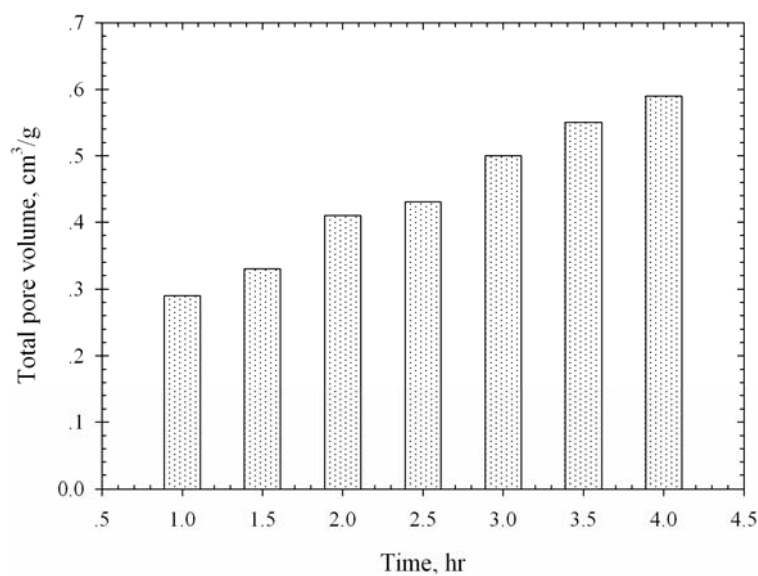


Figure 3.20 Effect of activation time on total pore volume of the palm shell based activated carbon activated at 900°C.

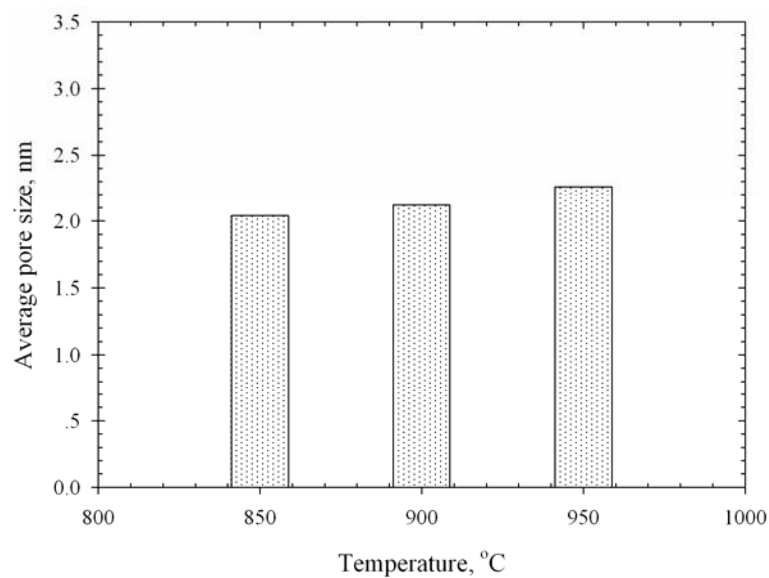


Figure 3.21 Effect of activation temperature on average pore size of the palm shell based activated carbon activated with pure CO₂ for 2.0 hrs.

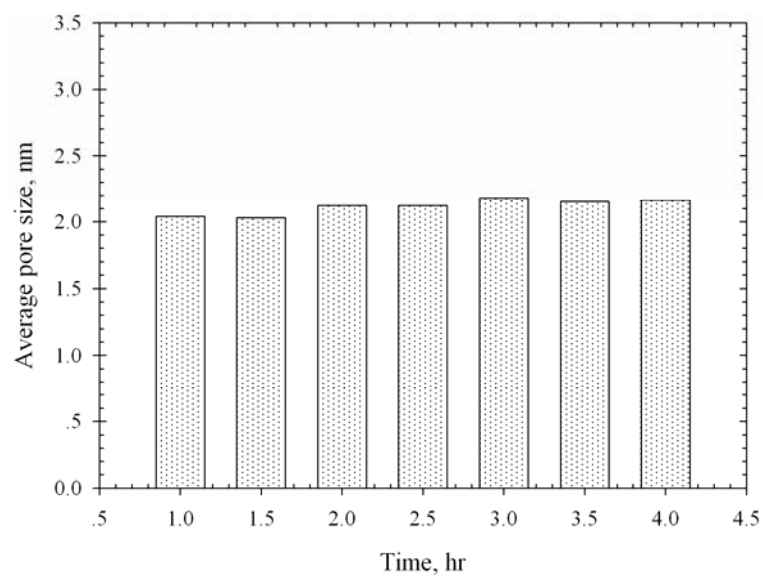


Figure 3.22 Effect of activation time on average pore size of the palm shell based activated carbon activated at 900°C.

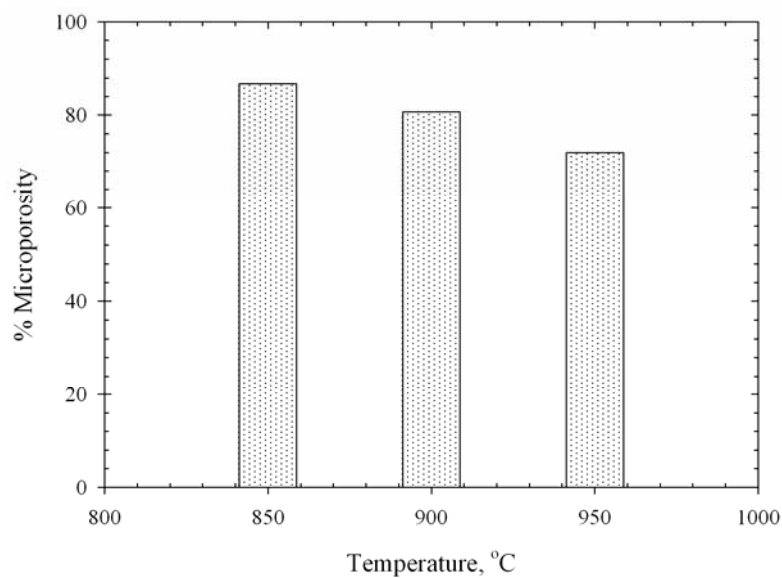


Figure 3.23 Effect of activation temperature on percentage microporosity of the palm shell based activated carbon activated with pure CO₂ for 2.0 hrs.

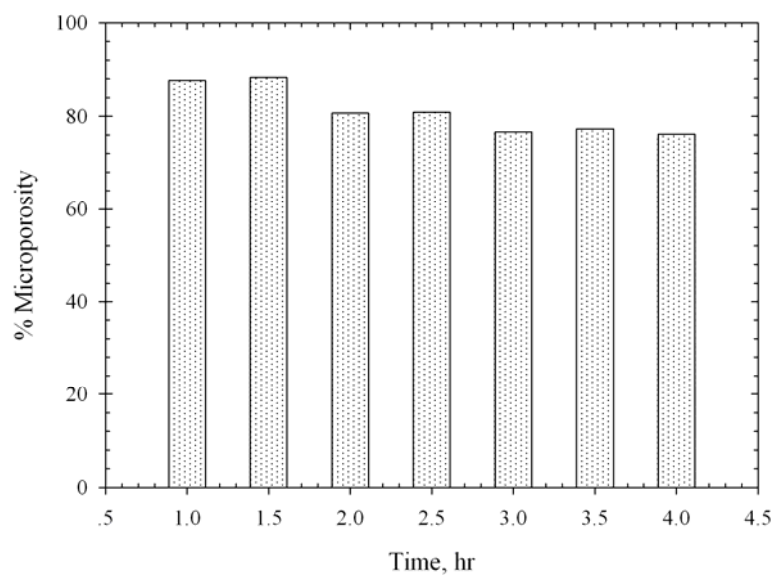


Figure 3.24 Effect of activation time on percentage microporosity of the palm shell based activated carbon activated at 900°C.

Results shown in Figure 3.25 to 3.29 indicate that CO₂ flow rate has a definite influence on the char burn-off for the flow rates lower than 150 cc/min, but it seems to have almost no effect at higher flow rates. This indicates that the amount of CO₂ becomes too excessive for the flow rate higher than 150 cc/min. Figure 3.26 shows that the BET surface area increases when the flow rate is increased up to 100 cc/min and becomes unaffected at higher CO₂ flow rates. Increasing CO₂ flow rate from 50 to 100 cc/min increases slightly the total pore volume but with a lesser extent as compared to its effect on BET surface area. However, percentage microporosity and average pore size seem to be unaffected by the change in CO₂ flow rate.

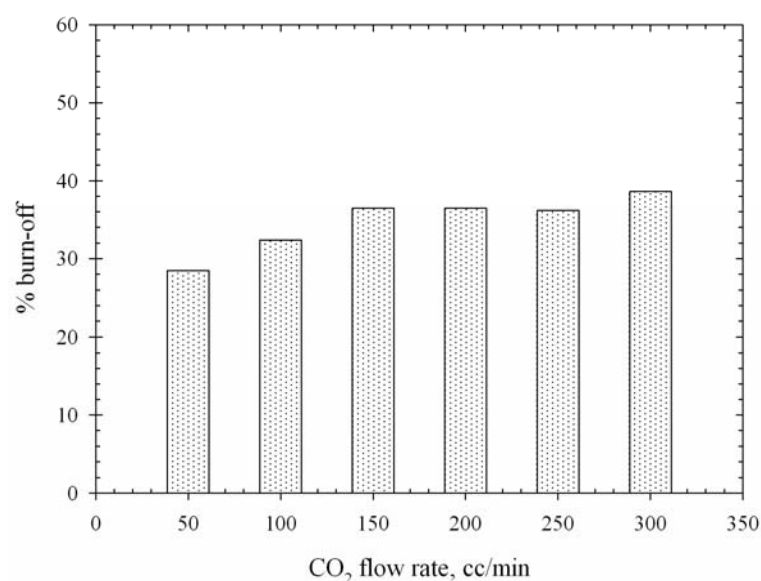


Figure 3.25 Effect of CO₂ flow rate on char burn-off of the palm shell based activated carbon activated at 900°C with pure CO₂ for 2.0 hrs.

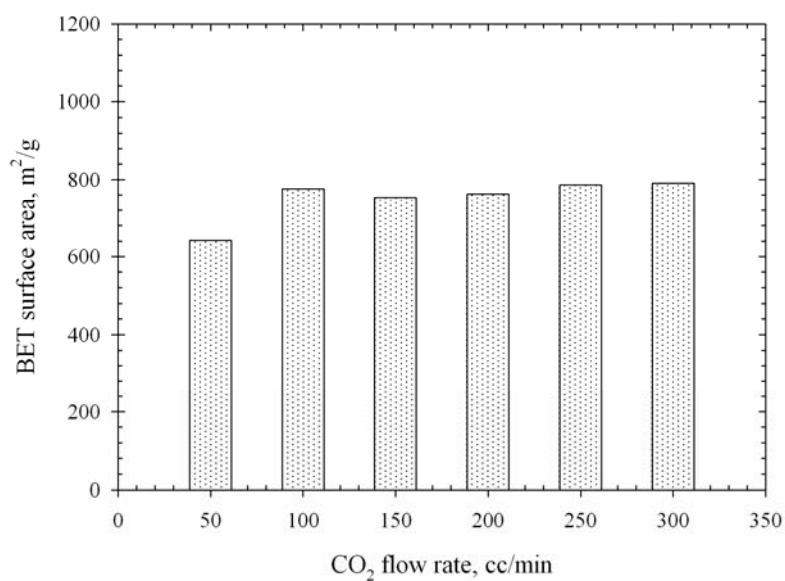


Figure 3.26 Effect of CO₂ flow rate on BET surface area of the palm shell based activated carbon activated at 900°C with pure CO₂ for 2.0 hrs.

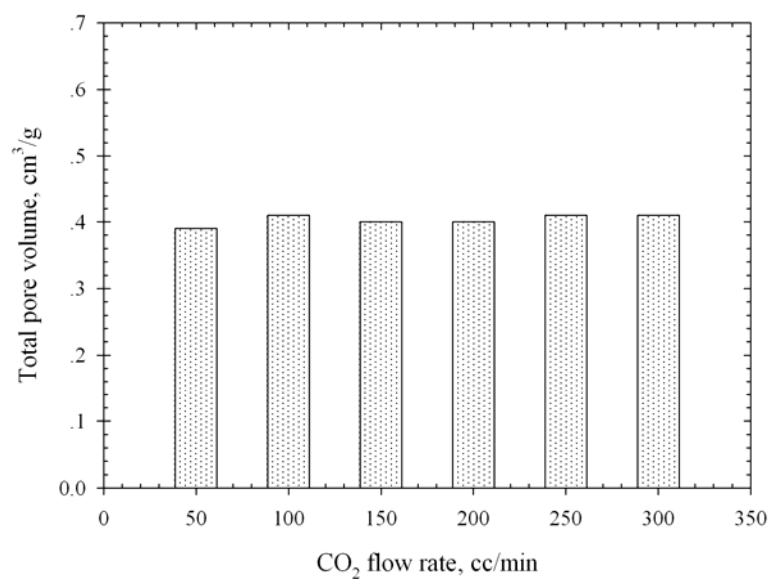


Figure 3.27 Effect of CO₂ flow rate on total pore volume of the palm shell based activated carbon activated at 900°C with pure CO₂ for 2.0 hrs.

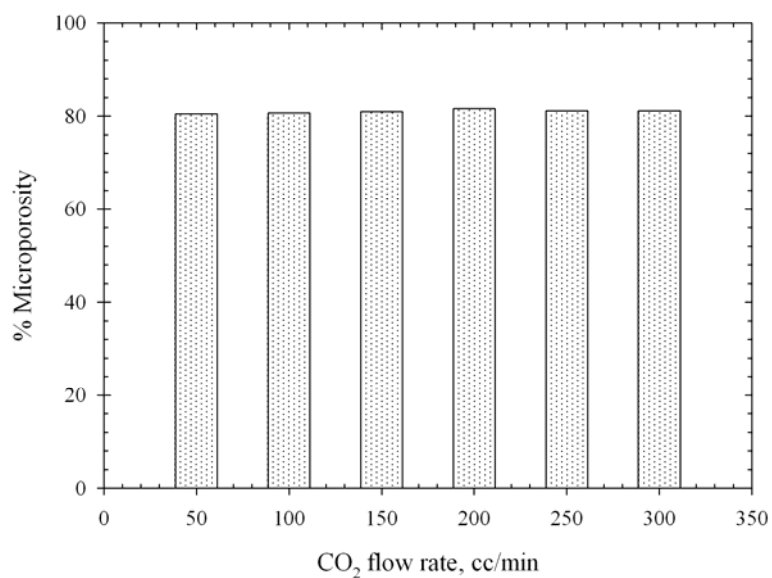


Figure 3.28 Effect of CO₂ flow rate on percentage microporosity of the palm shell based activated carbon activated at 900°C with pure CO₂ for 2.0 hrs.

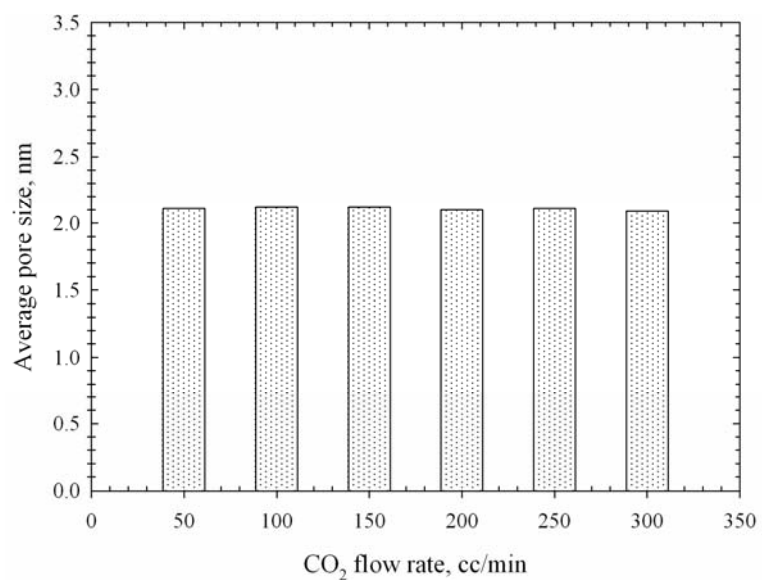


Figure 3.29 Effect of CO₂ flow rate on average pore size of the palm shell based activated carbon activated at 900°C with pure CO₂ for 2.0 hrs.

Figure 3.30 to 3.34 show the effect of CO₂ concentration on the char burn-off, BET surface area, total pore volume, percentage microporosity, and average pore size of palm shell based activated carbon activated with CO₂ for 2.0 hrs, respectively. The char burn-off, BET surface area, and total pore volume increase steadily with the increase in CO₂ concentration up to 100% (see Figure 3.30 to 3.32), while the percentage microporosity and average pore size seem to be independent of the concentration (see Figure 3.33 to 3.34). These results show that the increasing in CO₂ concentration helps to develop the porous structure of the prepared activated carbon by mostly creating new micropores without the development of mesopores from the existing micropores. It should be noted that the maximum percentage burn-off of char that can be achieved is about 50%, because some ash was visually observed on the outer surface of char particles when the burn-off was higher than 50%. Therefore, the char should be activated at the retention time of less than 2.0 hrs and 4.0 hrs for the char being activated at 950°C and 900°C, respectively.

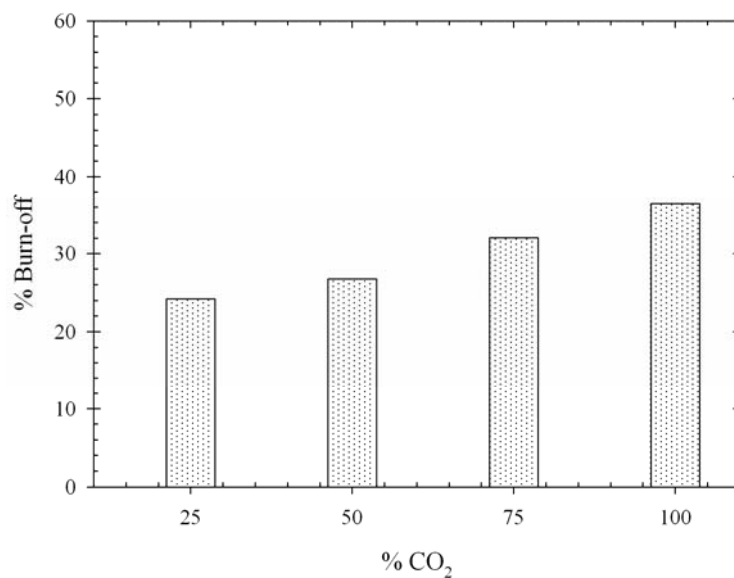


Figure 3.30 Effect of CO₂ concentration on char burn-off of the palm shell based activated carbon activated at 900°C for 2.0 hrs.

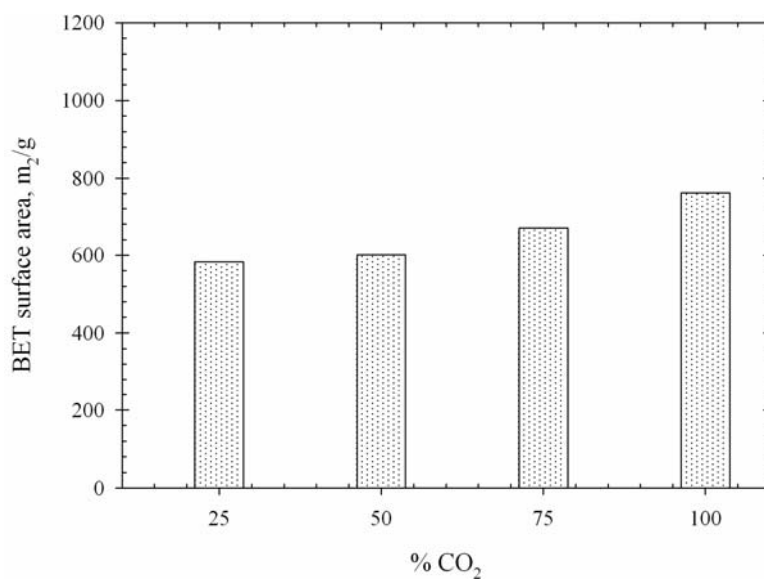


Figure 3.31 Effect of CO₂ concentration on BET surface area of the palm shell based activated carbon activated at 900°C for 2.0 hrs.

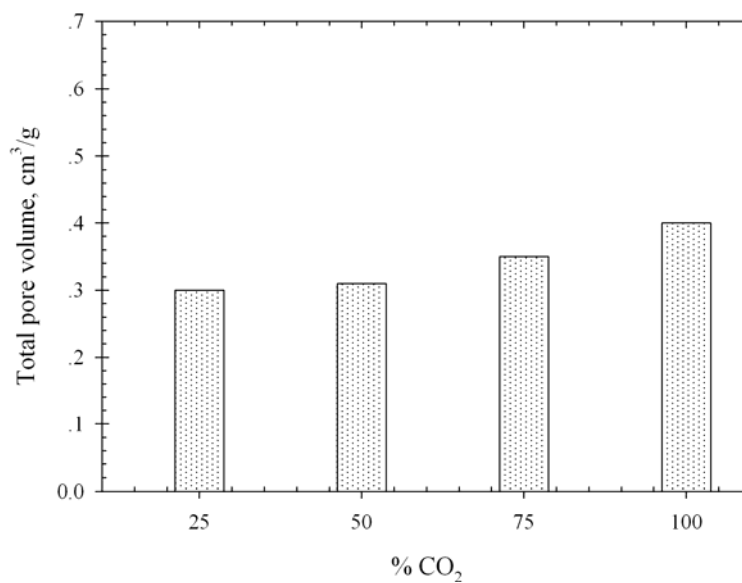


Figure 3.32 Effect of CO₂ concentration on total pore volume of the palm shell based activated carbon activated at 900°C for 2.0 hrs.

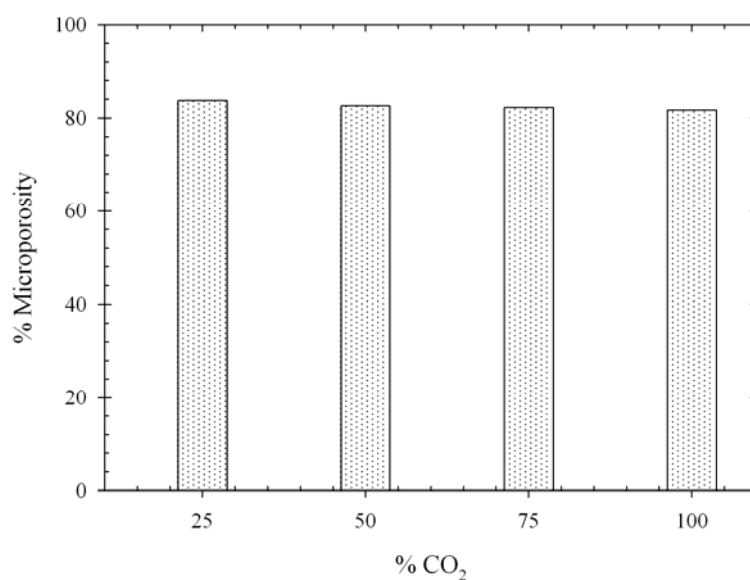


Figure 3.33 Effect of CO₂ concentration on percentage microporosity of the palm shell based activated carbon activated at 900°C for 2.0 hrs.

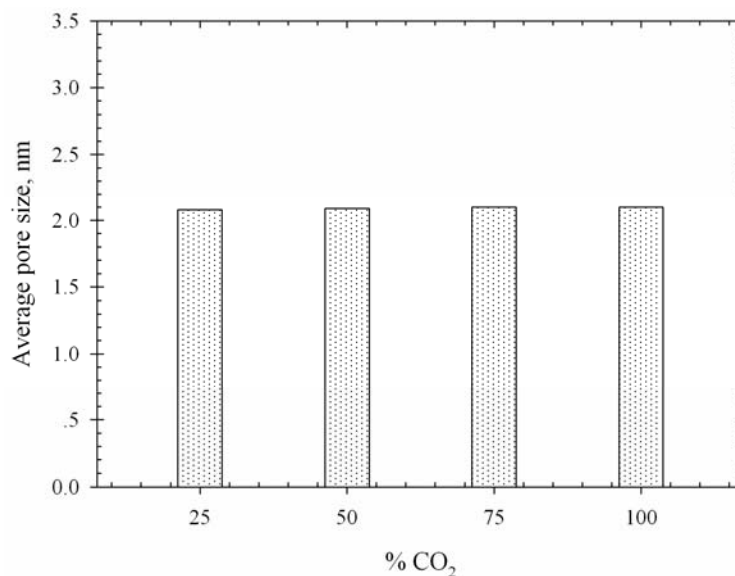


Figure 3.34 Effect of CO₂ concentration on average pore size of the palm shell based activated carbon activated at 900°C for 2.0 hrs.

For palm fiber, as shown in Figure 3.35 to 3.37, the percentage burn-off, BET surface area and total pore volume increase progressively with increasing of activation temperature, while the percentage of microporosity decreases (see Figure 3.38). The average pore size appears to be constant when the activation temperature is increased which yields the same result as for the case of palm shell (see Figure 3.39). The char burn-off increases continuously with increasing of activation time indicating the progression of activation scheme of palm fiber char (see Figure 3.40). When the activation time is increased from 1.0 to 2.0 hrs, the BET area and total pore volume increase and after that they seem to decrease for further increasing of activation time to 2.5 hrs (see Figure 3.41 and 3.42). Although the effect is not so pronounced, the average pore size also increases slight with increasing of time, reaching the maximum at the activation time of 1.5 hrs and then tending to decrease (see Figure 3.43). The

percentage of microporosity decreases, achieving the minimum value at the time of 1.5 hrs, and then increases again for longer activation time (see Figure 3.44).

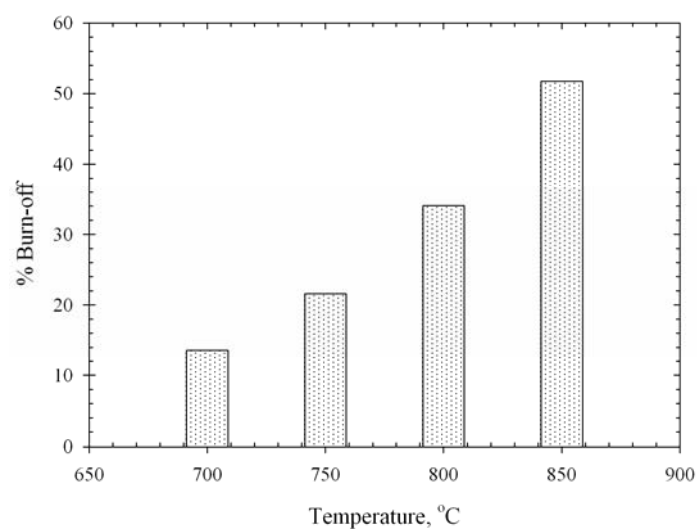


Figure 3.35 Effect of activation temperature on char burn-off of the palm fiber based activated carbon activated with pure CO₂ for 2.0 hrs.

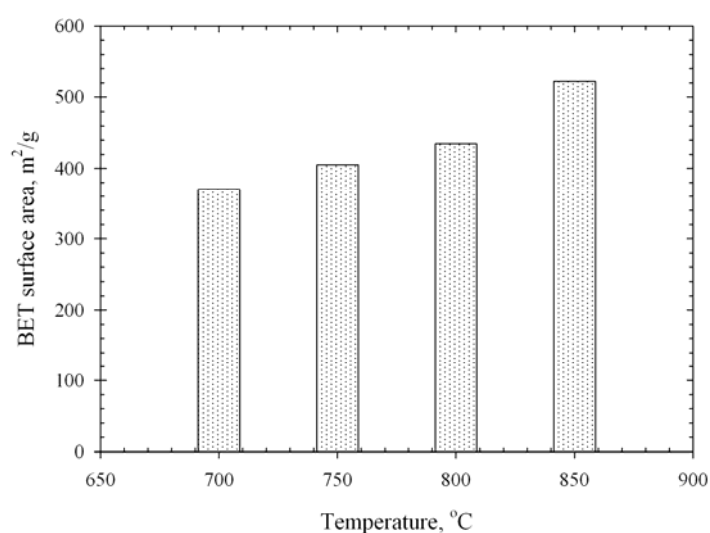


Figure 3.36 Effect of activation temperature on BET surface area of the palm fiber based activated carbon activated with pure CO₂ for 2.0 hrs.

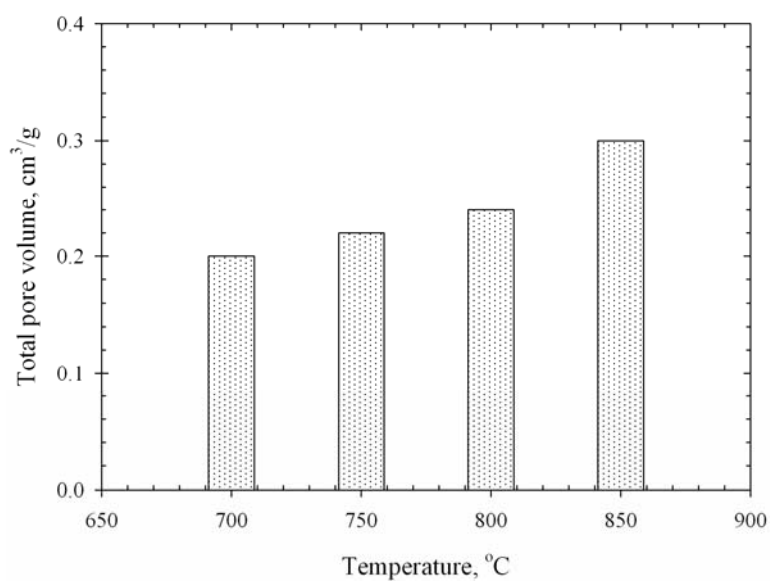


Figure 3.37 Effect of activation temperature on total pore volume of the palm fiber based activated carbon activated with pure CO₂ for 2.0 hrs.

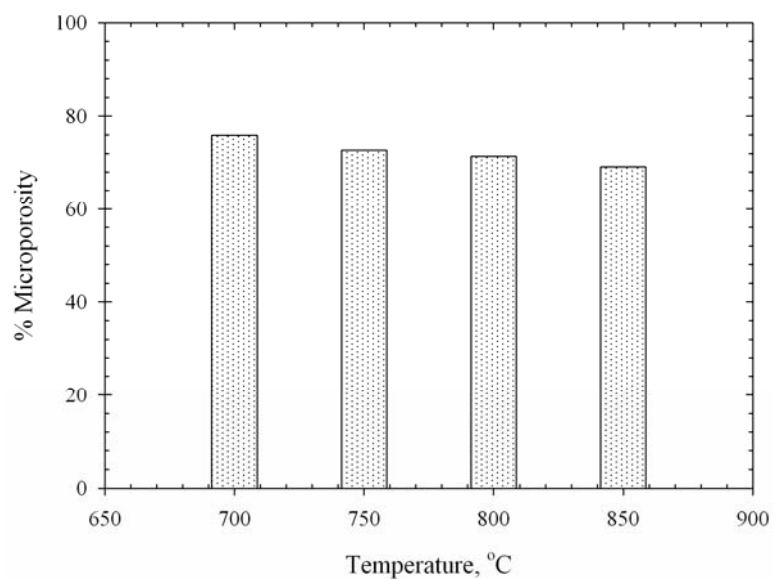


Figure 3.38 Effect of activation temperature on percentage microporosity of the palm fiber based activated carbon activated with pure CO₂ for 2.0 hrs.

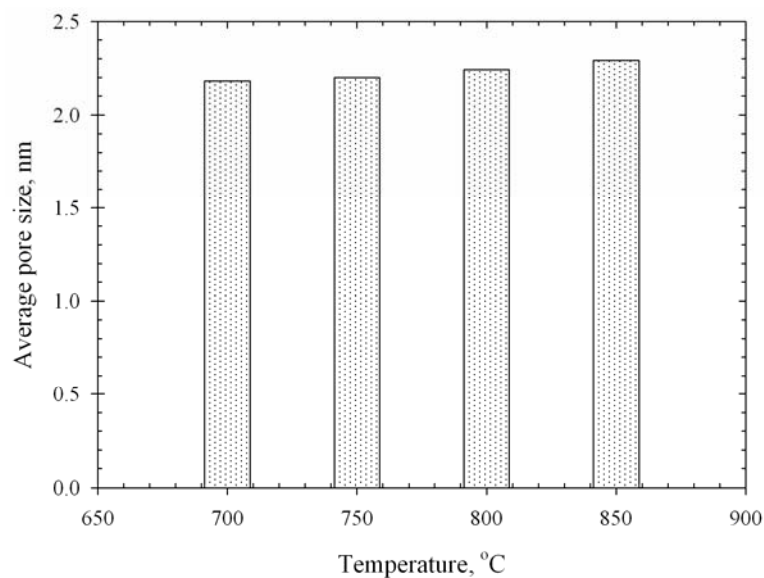


Figure 3.39 Effect of activation temperature on average pore size of the palm fiber based activated carbon activated with pure CO₂ for 2.0 hrs.

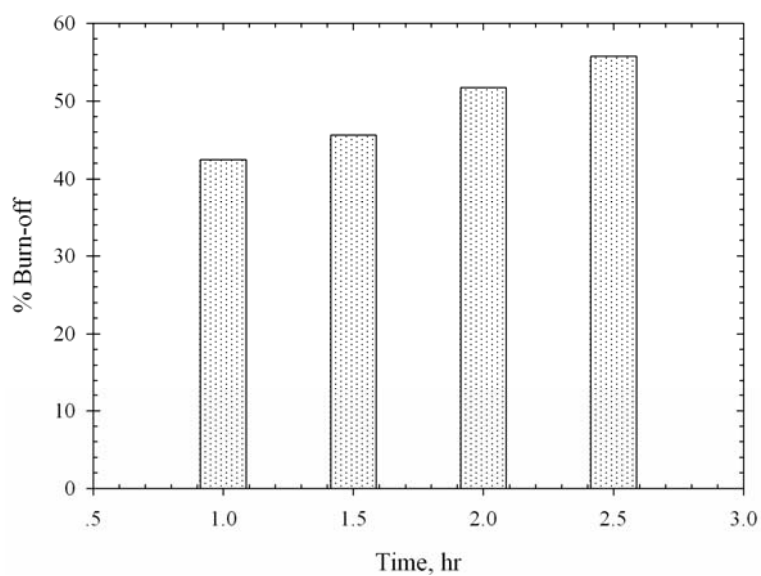


Figure 3.40 Effect of activation time on char burn-off of the palm fiber based activated carbon activated at 850°C with pure CO₂.

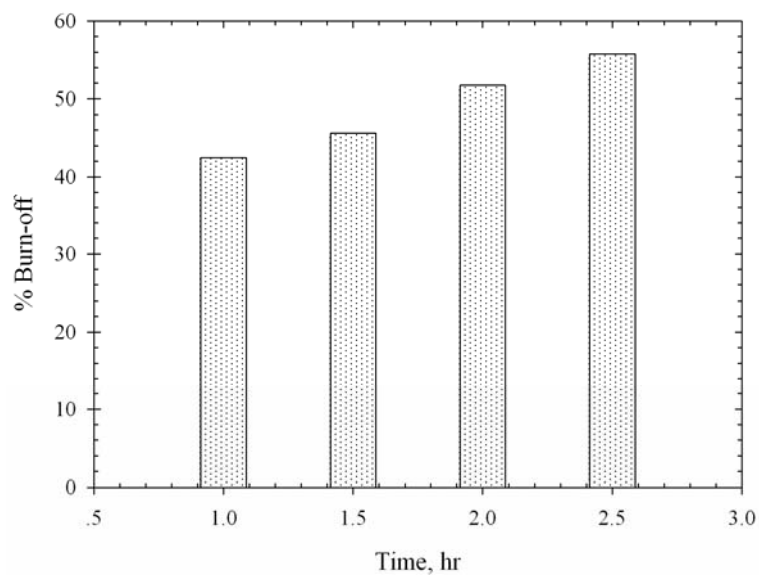


Figure 3.41 Effect of activation time on BET surface area of the palm fiber based activated carbon activated at 850°C with pure CO₂.

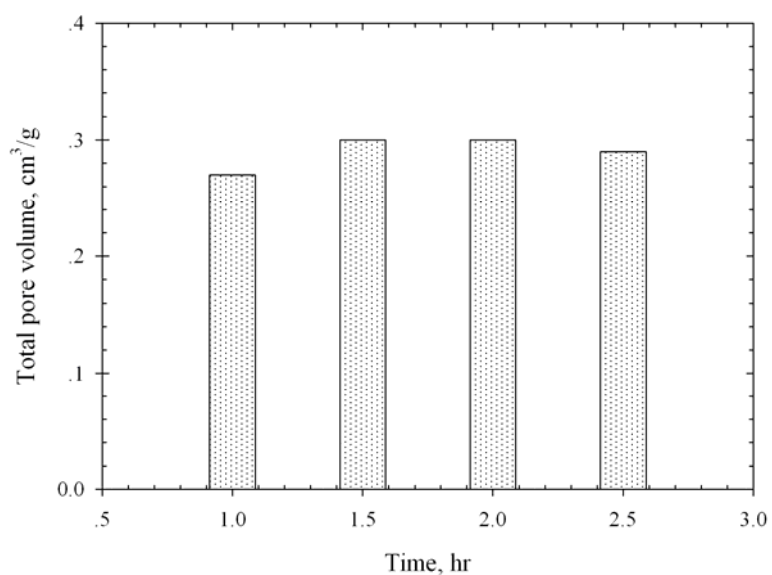


Figure 3.42 Effect of activation time on total pore volume of the palm fiber based activated carbon activated at 850°C with pure CO₂.

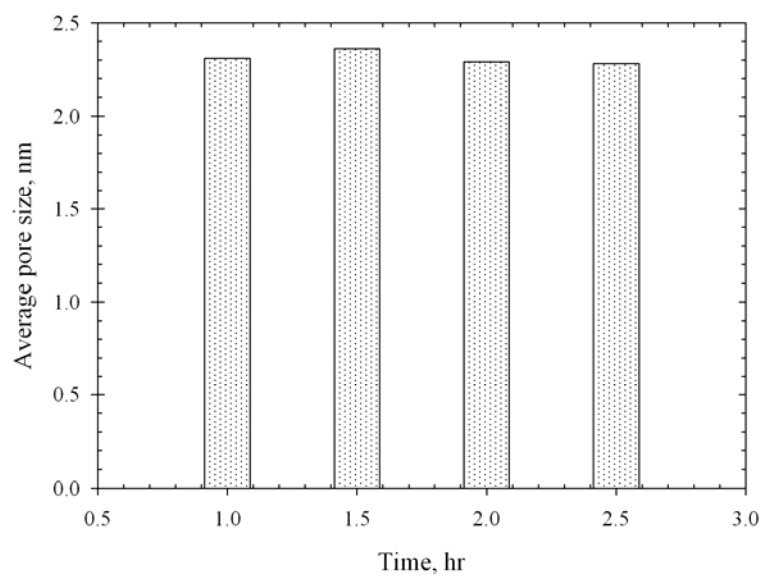


Figure 3.43 Effect of activation time on average pore size of the palm fiber based activated carbon activated at 850°C with pure CO₂.

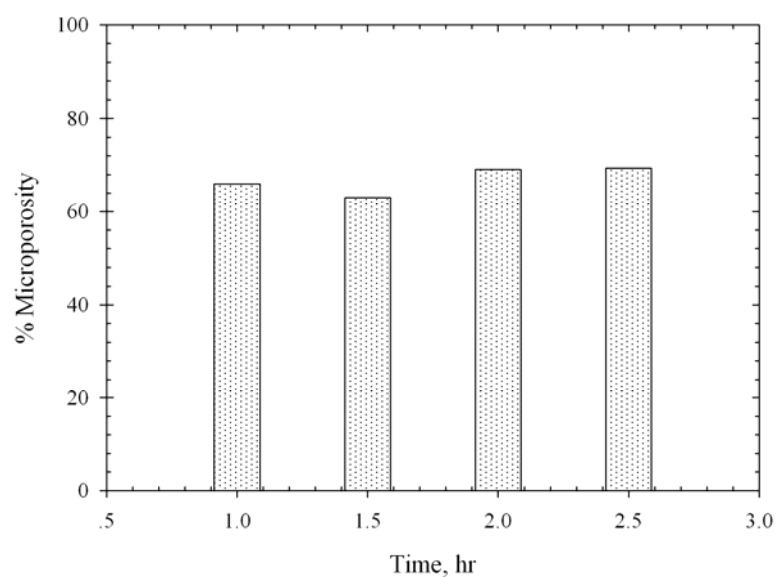


Figure 3.44 Effect of activation time on percentage microporosity of the palm fiber based activated carbon activated at 850°C with pure CO₂.

The decreasing in BET area, total pore volume and average pore size should be due to the shrinkage of porous structure of the resulting activated carbon. It could be concluded that the shrinkage of porous structure could probably occur at the activation time longer than 1.5 hrs when the char is activated at 850°C. The density of the palm fiber is very low when compared to the palm shell and kernel cake (see Table 3.1) which means that the structure of palm fiber is less dense than the other two materials. Thus, the porous structure of the palm fiber based activated carbon is easier to collapse compared to the case of palm shell and kernel cake. It is noted that although the burn-off increases gradually with increasing of CO₂ flow rate (see Figure 3.45), only slight change of BET surface area and total pore volume can be observed (see Figure 3.46 and 3.47). It is also found that the micropore fraction appears to be constant with increasing of CO₂ flow rate (see Figure 3.48), while the slight decreasing of the average pore size can be detected (see Figure 3.49) and these results may give supportive evidence to the collapse of porous structure as previously mentioned. As to the effect of CO₂ concentration, the burn-off, BET surface area and total pore volume increase steadily in the same fashion as CO₂ concentration is increased (Figure 3.50 to 3.52). The average pore size and percentage microporosity seem to be independent of the change in the concentration of CO₂ (Figure 3.53 and 3.54).

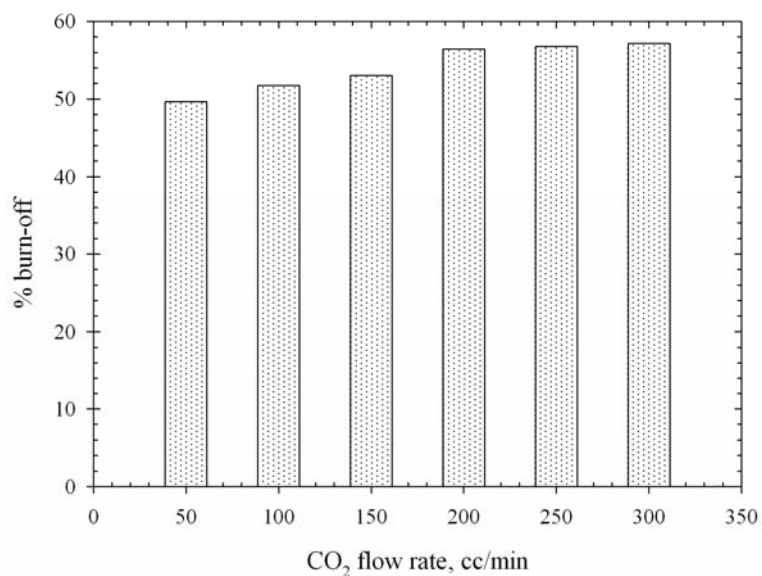


Figure 3.45 Effect of CO₂ flow rate on char burn-off of the palm fiber based activated carbon activated at 850°C with pure CO₂ for 2.0 hrs.

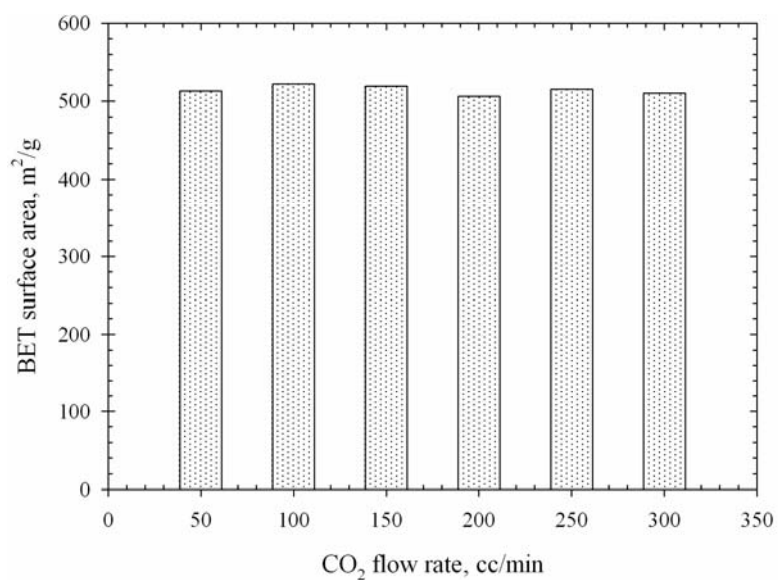


Figure 3.46 Effect of CO₂ flow rate on BET surface area of the palm fiber based activated carbon activated at 850°C with pure CO₂ for 2.0 hrs.

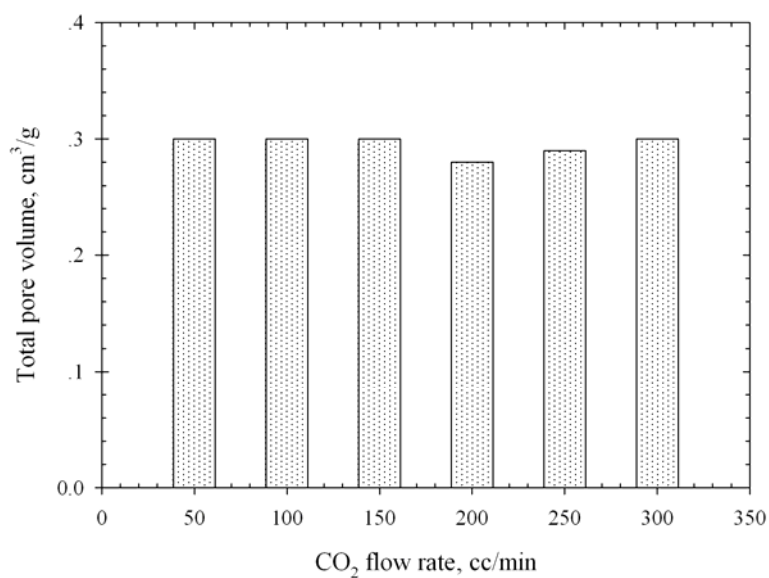


Figure 3.47 Effect of CO₂ flow rate on total pore volume of the palm fiber based activated carbon activated at 850°C with pure CO₂ for 2.0 hrs.

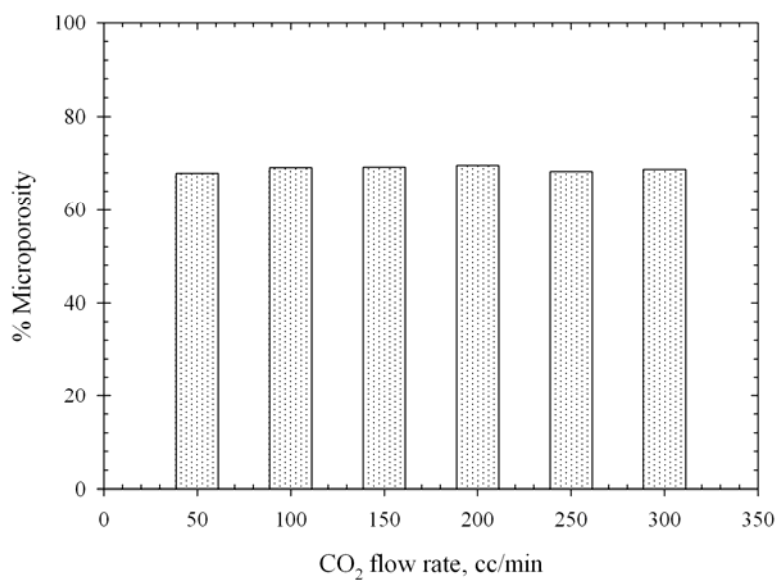


Figure 3.48 Effect of CO₂ flow rate on percentage microporosity of the palm fiber based activated carbon activated at 850°C with pure CO₂ for 2.0 hrs.

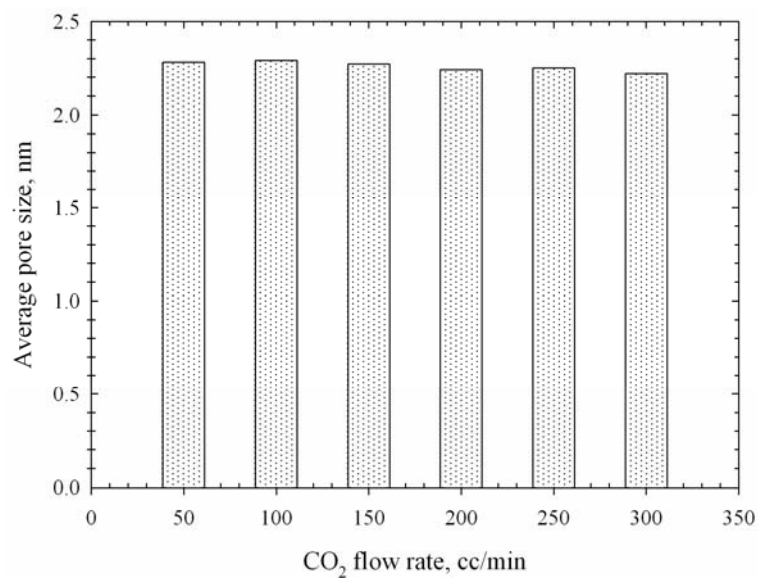


Figure 3.49 Effect of CO₂ flow rate on average pore size of the palm fiber based activated carbon activated at 850°C with pure CO₂ for 2.0 hrs.

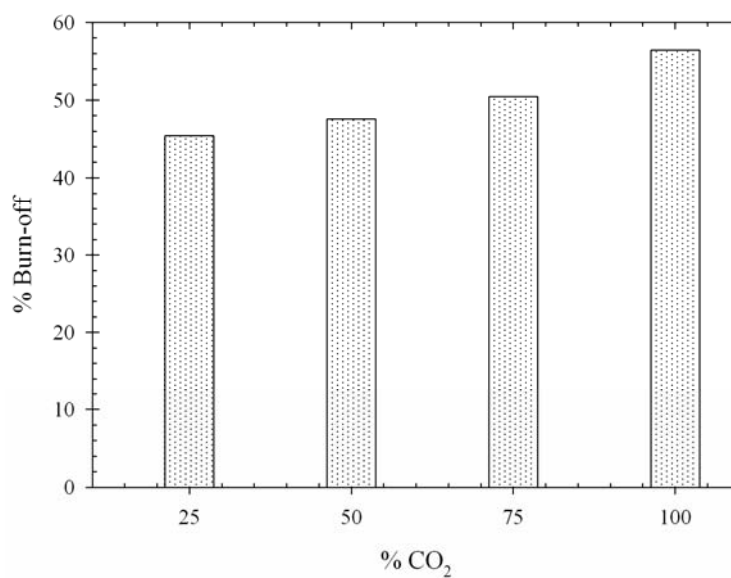


Figure 3.50 Effect of CO₂ concentration on char burn-off of the palm shell based activated carbon activated at 850°C for 2.0 hrs.

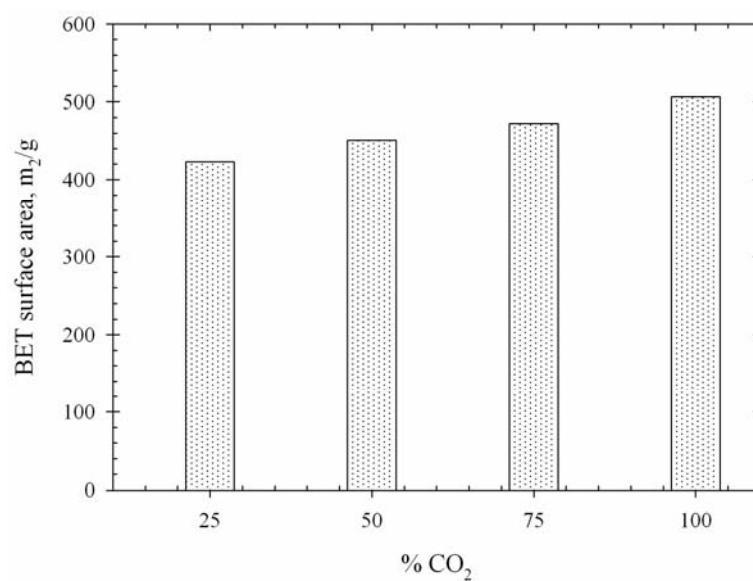


Figure 3.51 Effect of CO₂ concentration on BET surface area of the palm fiber based activated carbon activated at 850°C for 2.0 hrs.

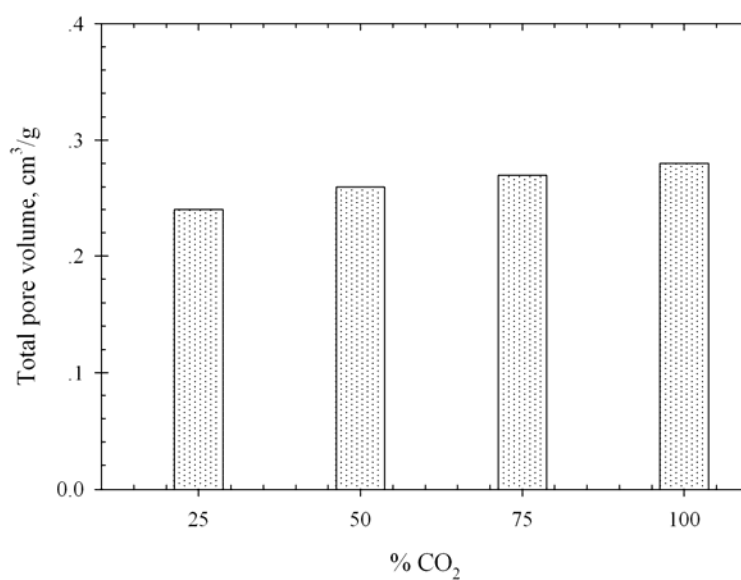


Figure 3.52 Effect of CO₂ concentration on total pore volume of the palm fiber based activated carbon activated at 850°C for 2.0 hrs.

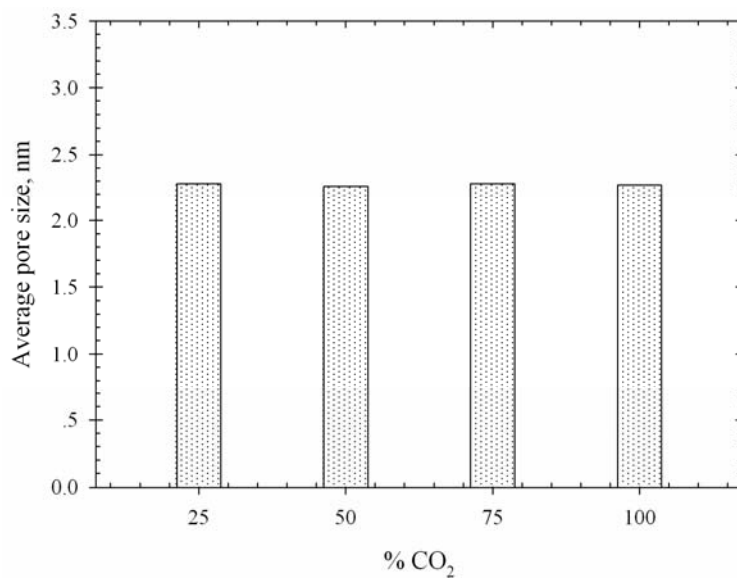


Figure 3.53 Effect of CO₂ concentration on average pore size of the palm fiber based activated carbon activated at 850°C for 2.0 hrs.

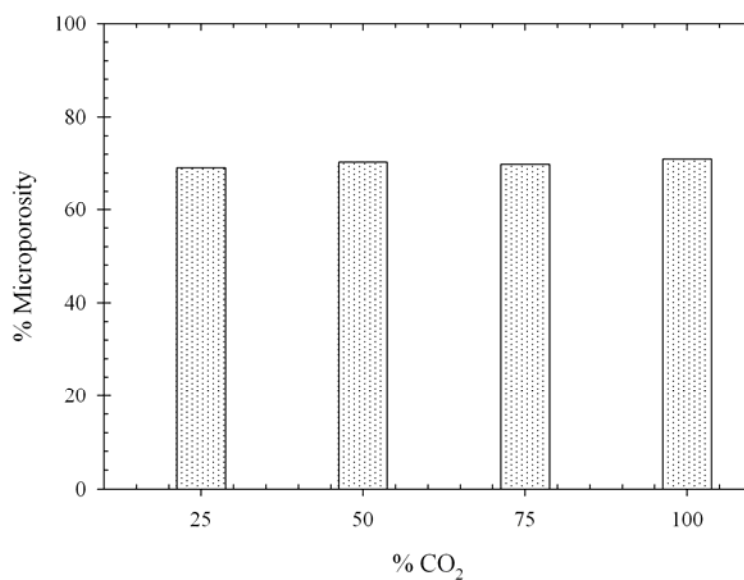


Figure 3.54 Effect of CO₂ concentration on percentage microporosity of the palm fiber based activated carbon activated at 850°C for 2.0 hrs.

For palm kernel cake, the effect of activation conditions on BET surface area, total pore volume, average pore size and percentage of microporosity is similar to the case of palm shell based activated carbon (Figure 3.55 to 3.74). It is evident that a significant change in the total pore volume, average pore size and percentage of microporosity can be observed for the derived activated carbon prepared at the highest temperature of 900°C. This means that the rate of reaction between CO₂ and carbon in the char matrix becomes extremely fast when the char is activated at the activation temperature of 900°C and the activation time longer than 1.0 hr, thus giving considerable impact on the development of porous structure of resulting activated carbon.

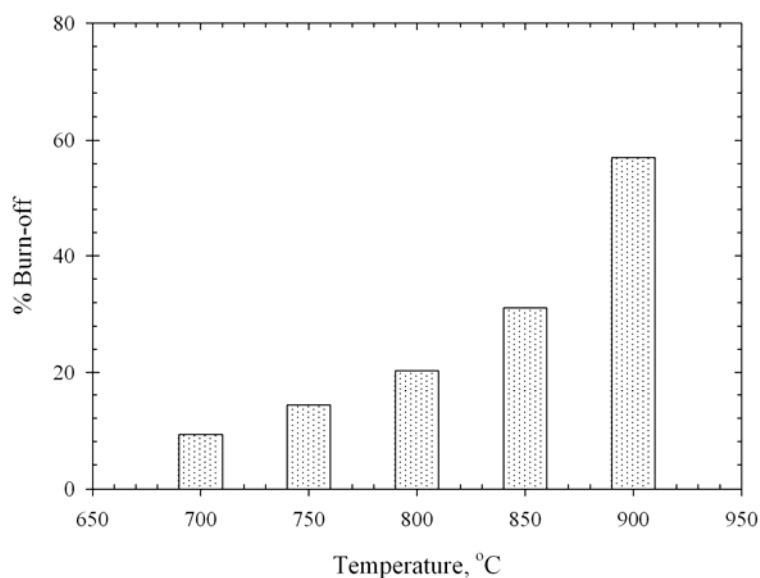


Figure 3.55 Effect of activation temperature on char burn-off of the palm kernel cake based activated carbon activated with pure CO₂ for 2.0 hrs.

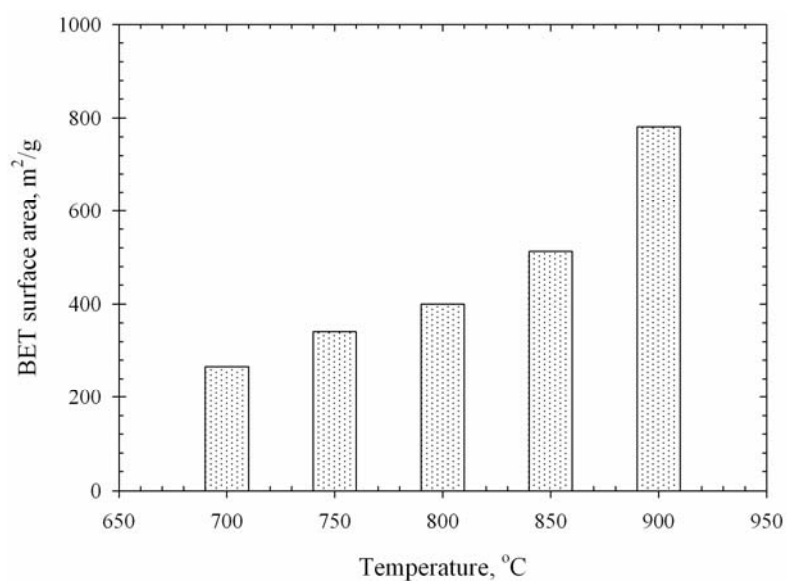


Figure 3.56 Effect of activation temperature on BET surface area of the palm kernel cake based activated carbon activated with pure CO₂ for 2.0 hrs.

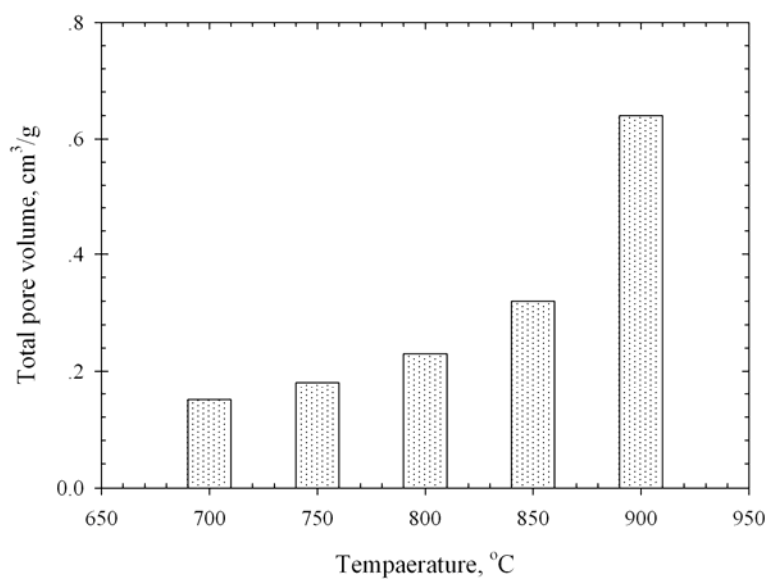


Figure 3.57 Effect of activation temperature on total pore volume of the palm kernel cake based activated carbon activated with pure CO₂ for 2.0 hrs.

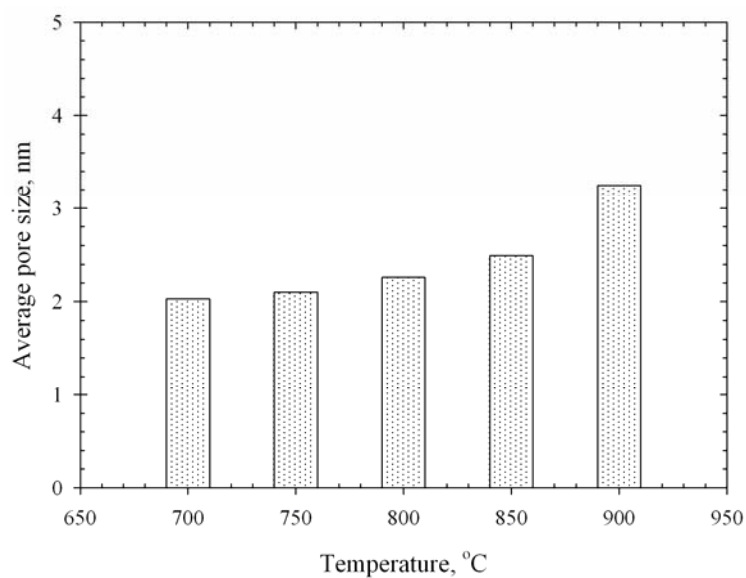


Figure 3.58 Effect of activation temperature on average pore size of the palm kernel cake based activated carbon activated with pure CO₂ for 2.0 hrs.

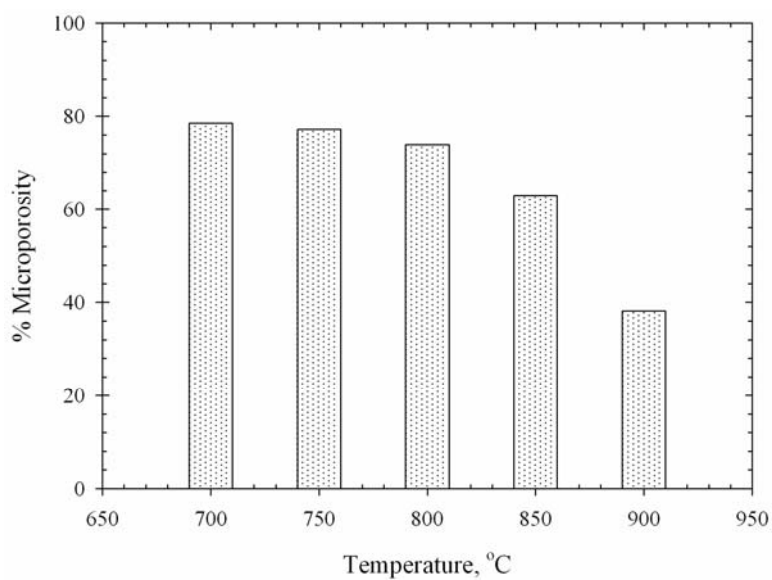


Figure 3.59 Effect of activation temperature on percentage microporosity of the palm kernel cake based activated carbon activated with pure CO₂ for 2.0 hrs.

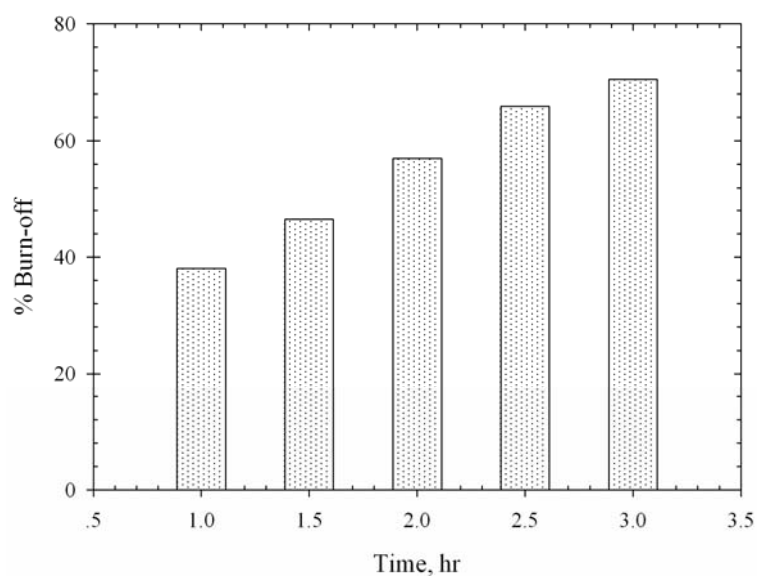


Figure 3.60 Effect of activation time on char burn-off of the palm kernel cake based activated carbon activated at 900°C with pure CO₂.

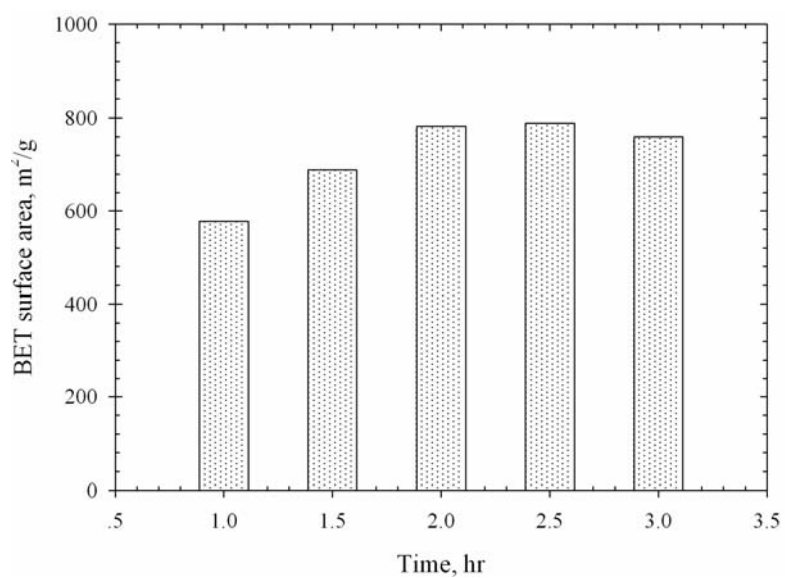


Figure 3.61 Effect of activation time on BET surface area of the palm kernel cake based activated carbon activated at 900°C with pure CO₂.

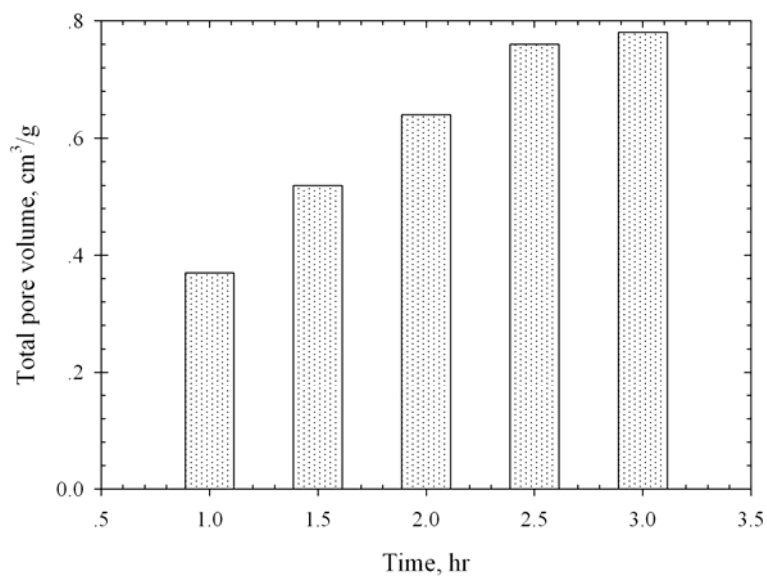


Figure 3.62 Effect of activation time on total pore volume of the palm kernel cake based activated carbon activated at 900°C with pure CO₂.

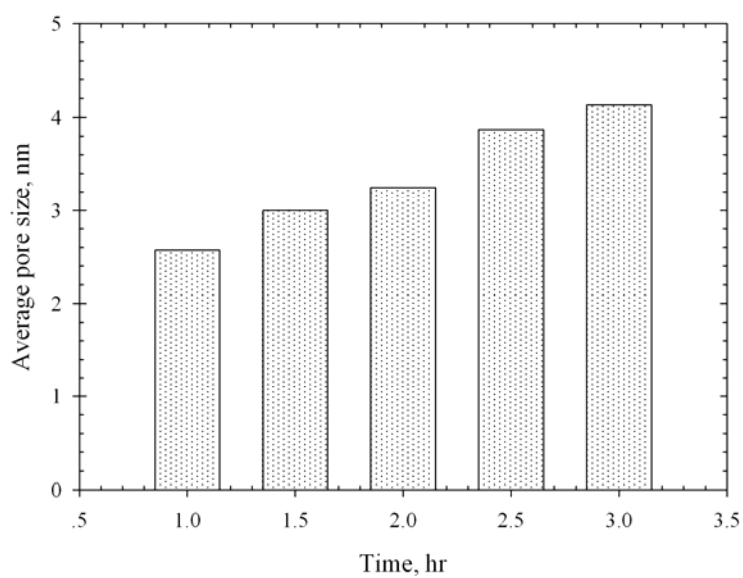


Figure 3.63 Effect of activation time on average pore size of the palm kernel cake based activated carbon activated at 900°C with pure CO₂.

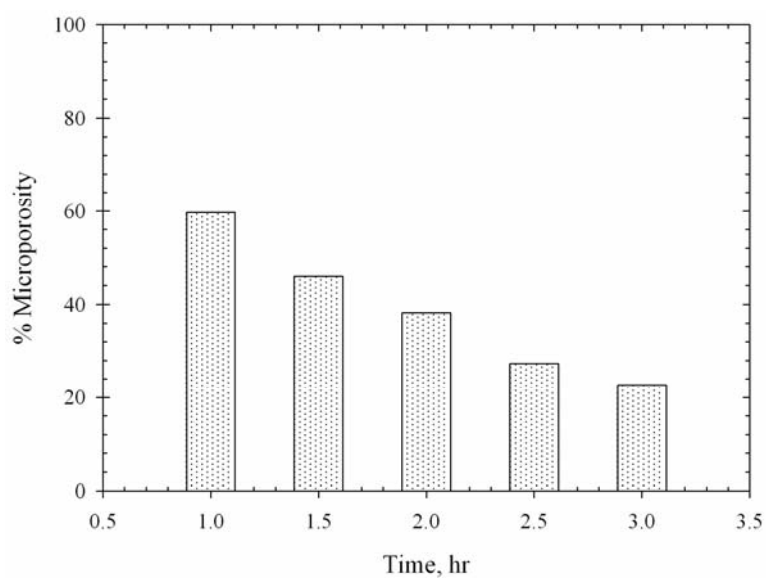


Figure 3.64 Effect of activation time on percentage microporosity of the palm kernel cake based activated carbon activated at 900°C with pure CO₂.

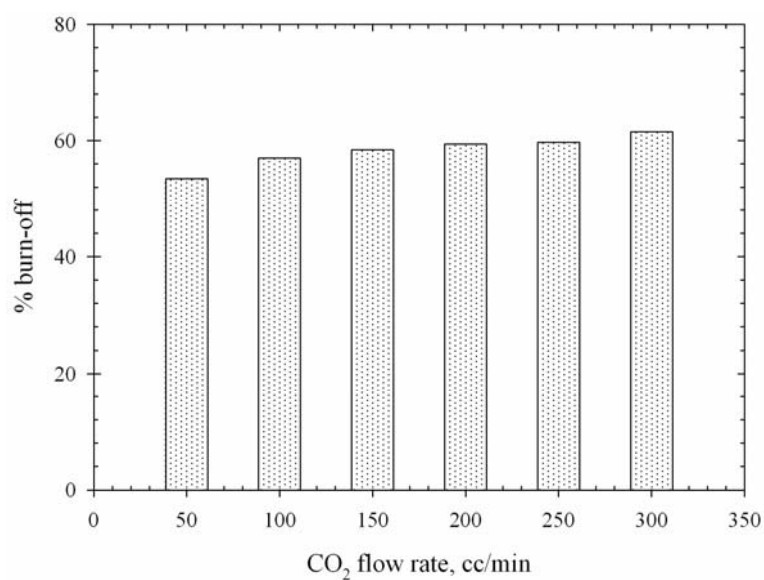


Figure 3.65 Effect of CO₂ flow rate on char burn-off of the palm kernel cake based activated carbon activated at 850°C with pure CO₂ for 2.0 hrs.

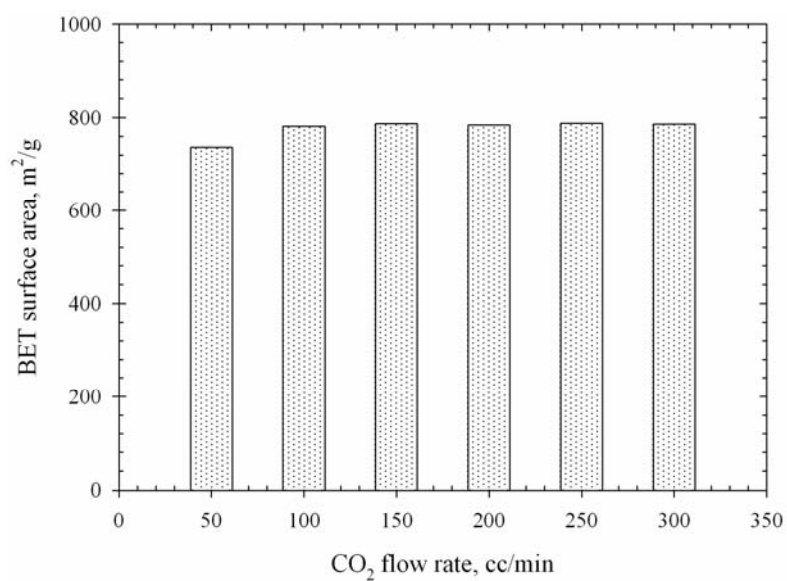


Figure 3.66 Effect of CO₂ flow rate on BET surface area of the palm kernel cake based activated carbon activated at 900°C with pure CO₂ for 2.0 hrs.

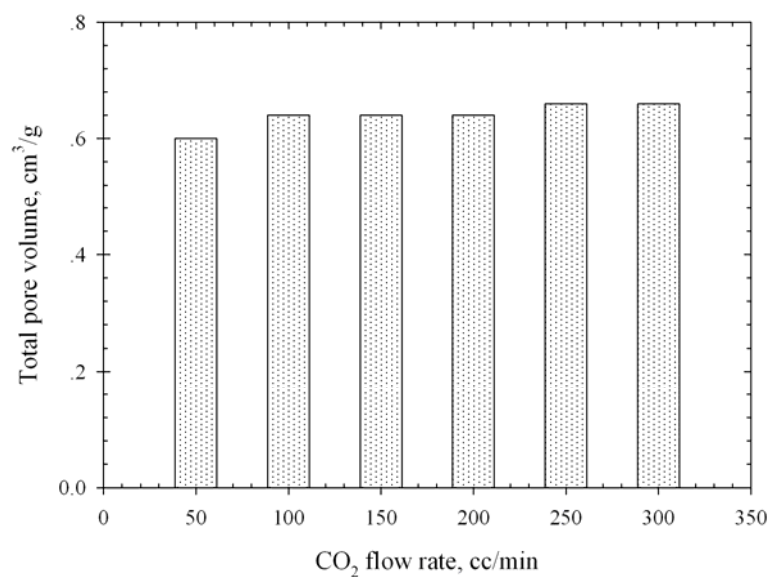


Figure 3.67 Effect of CO₂ flow rate on total pore volume of the palm kernel cake based activated carbon activated at 900°C with pure CO₂ for 2.0 hrs.

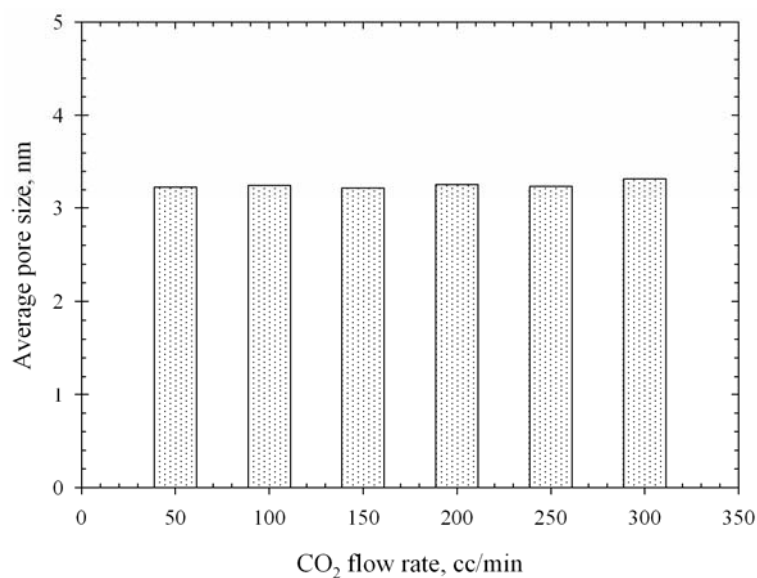


Figure 3.68 Effect of CO₂ flow rate on average pore size of the palm kernel cake based activated carbon activated at 900°C with pure CO₂ for 2.0 hrs.

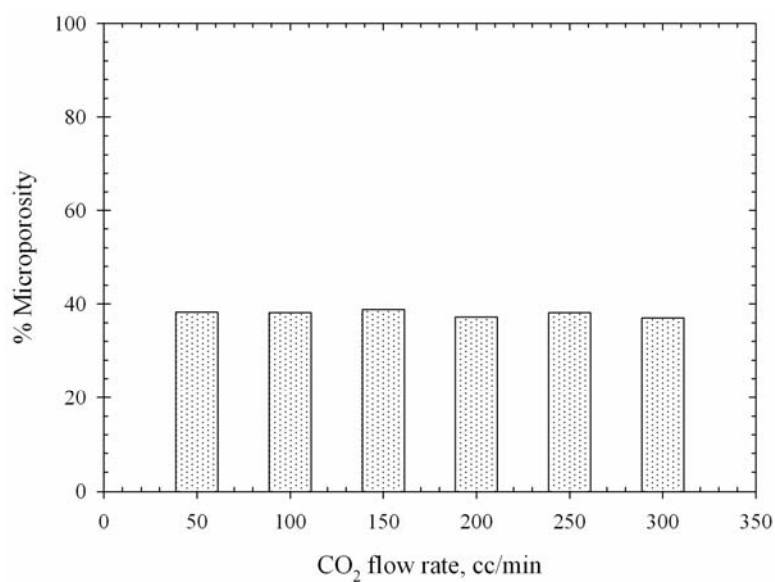


Figure 3.69 Effect of CO₂ flow rate on percentage microporosity of the palm kernel cake based activated carbon activated at 900°C with pure CO₂ for 2.0 hrs.

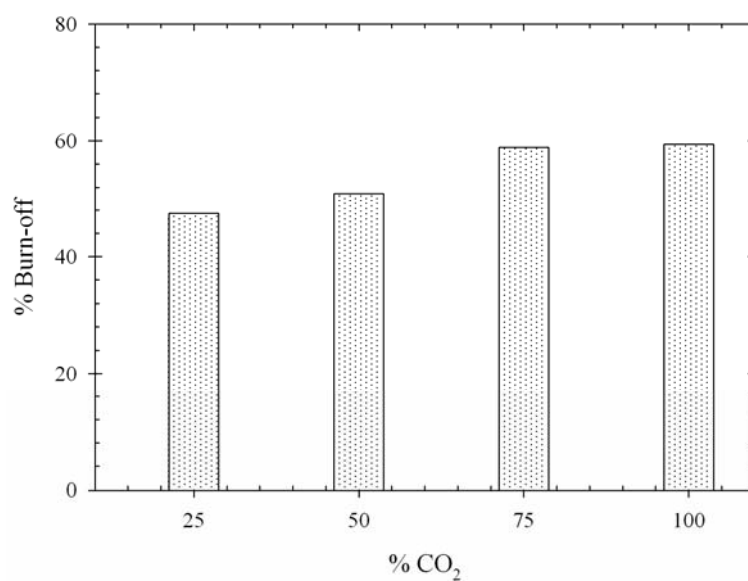


Figure 3.70 Effect of CO₂ concentration on char burn-off of the palm kernel cake based activated carbon activated at 900°C for 2.0 hrs.

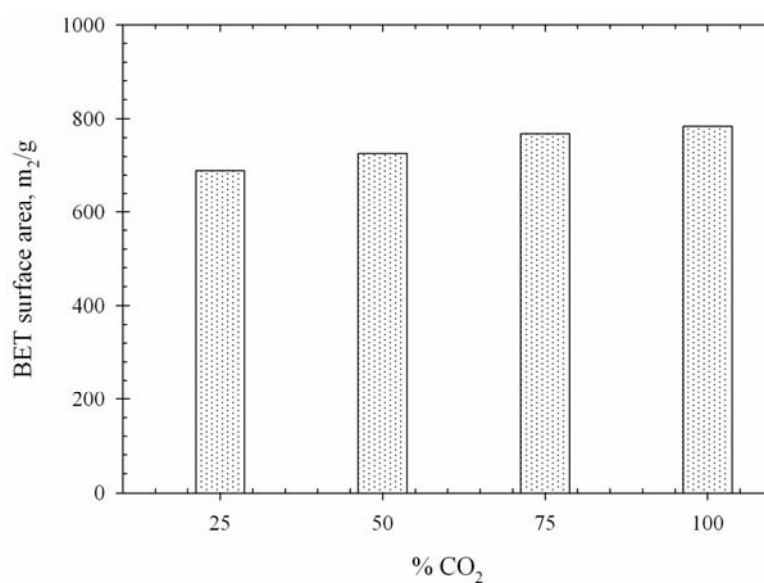


Figure 3.71 Effect of CO₂ concentration on BET surface area of the palm kernel cake based activated carbon activated at 900°C for 2.0 hrs.

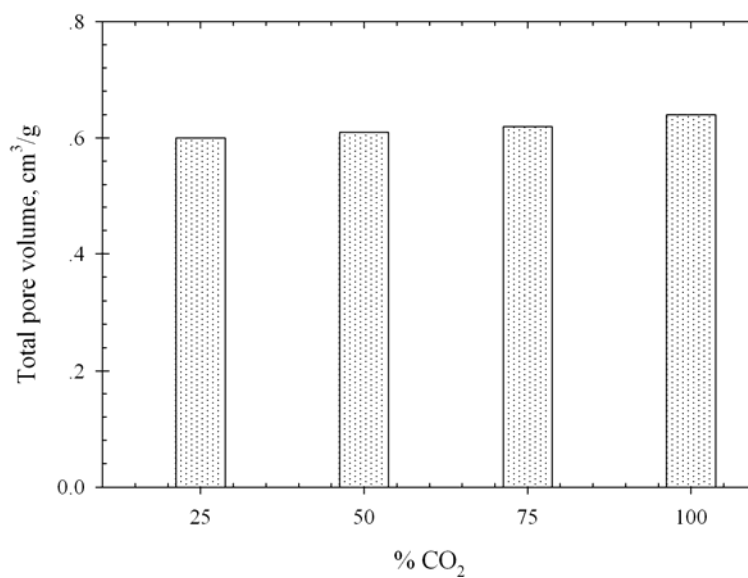


Figure 3.72 Effect of CO₂ concentration on total pore volume of the palm kernel cake based activated carbon activated at 900°C for 2.0 hrs.

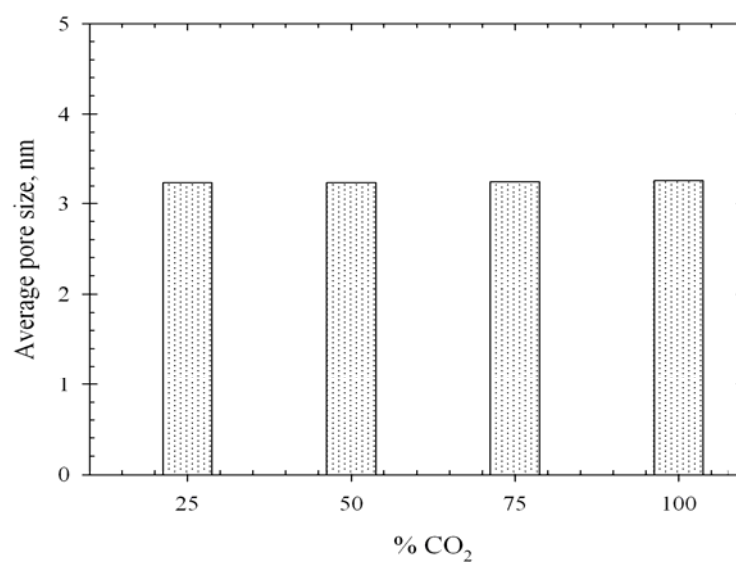


Figure 3.73 Effect of CO₂ concentration on average pore size of the palm kernel cake based activated carbon activated at 900°C for 2.0 hrs.

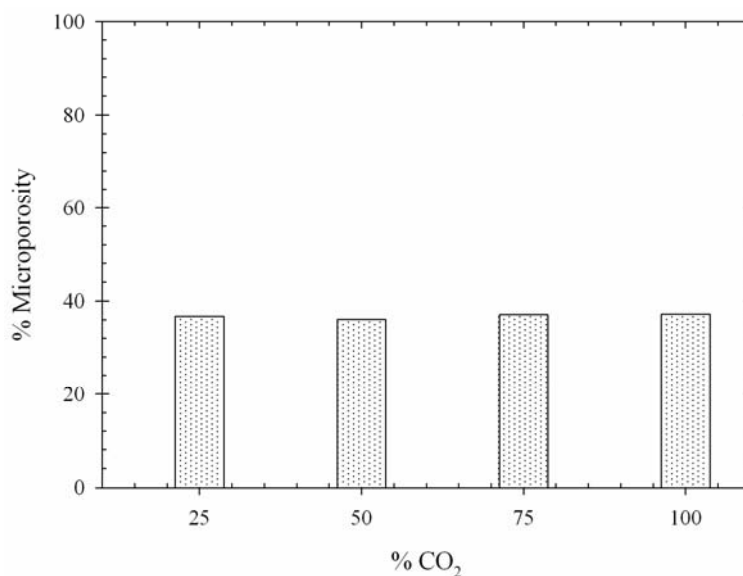


Figure 3.74 Effect of CO₂ concentration on percentage microporosity of the palm kernel cake based activated carbon activated at 900°C for 2.0 hrs.

The effects of activation time and temperature on the porous properties of activated carbon can be combined and represented in terms of burn-off level, as depicted in Figure 3.75 and 3.76. There is a tendency for both the surface area and pore volume to increase with the degree of char burn-off as expected and to decrease once a critical burn-off value has been reached, notably observed with palm shell. This decrease indicates that the volume of large pores continue to increase at the expense of smaller micropores, which could be due to the collapse of pore walls of some adjacent pores at relatively high degree of char burn-off (Junpirom et al., 2005).

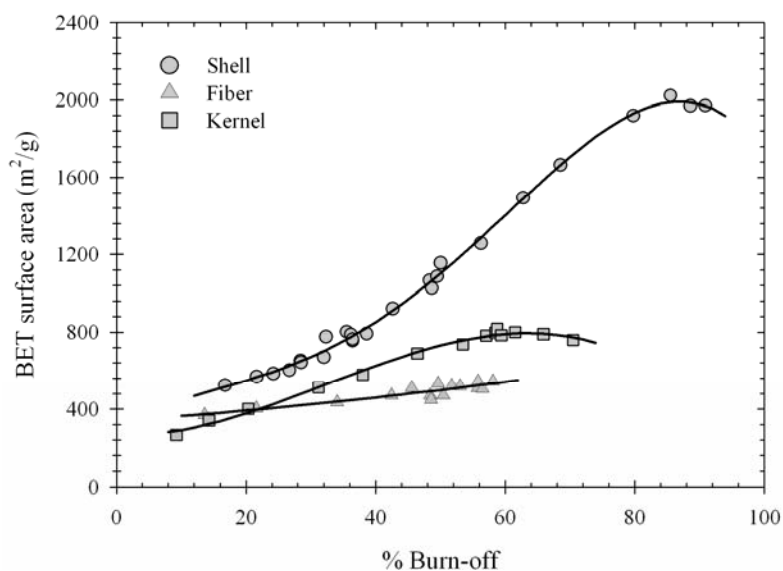


Figure 3.75 Effect of char burn-off on BET surface area.

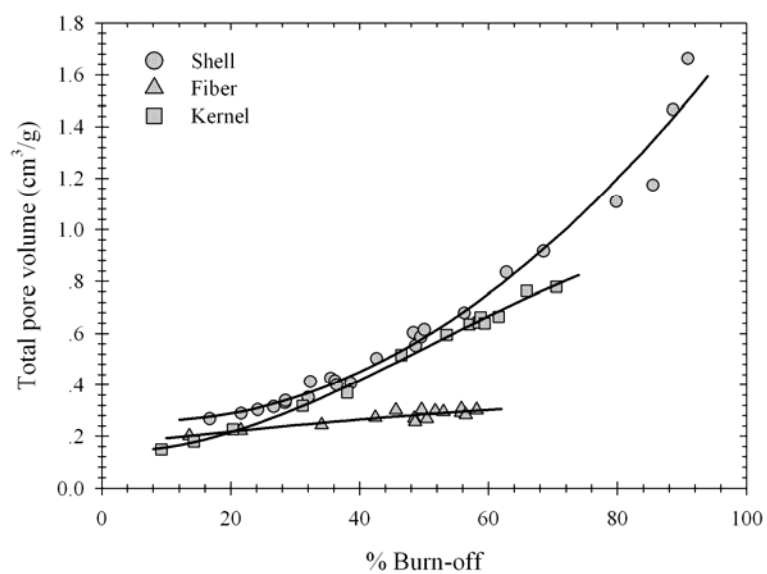


Figure 3.76 Effect of char burn-off on total pore volume.

From Table 3.5, 3.6 and 3.7, the optimum activation conditions that give the maximum in BET surface area occur at the following conditions: 950°C and 2.0 hrs (48.4% burn-off) for palm shell, 850°C and 2.0 hrs (51.7% burn-off) for palm

fiber, and 950°C and 2.5 hrs (65.9% burn-off) for kernel cake, corresponding to 1067, 522 and 789 m²/g of BET surface area, respectively. Figure 3.77 shows the nitrogen adsorption isotherm measured at -196°C and Figure 3.78 shows typical pore size distributions of the activated carbons prepared at these optimum conditions. It is clear that the palm shell and fiber based activated carbons show the Type I isotherm which is indicative of porous solids with microporosity, while the palm kernel cake based activated carbon showed Type IV isotherm, a characteristic of mesoporous structure materials.

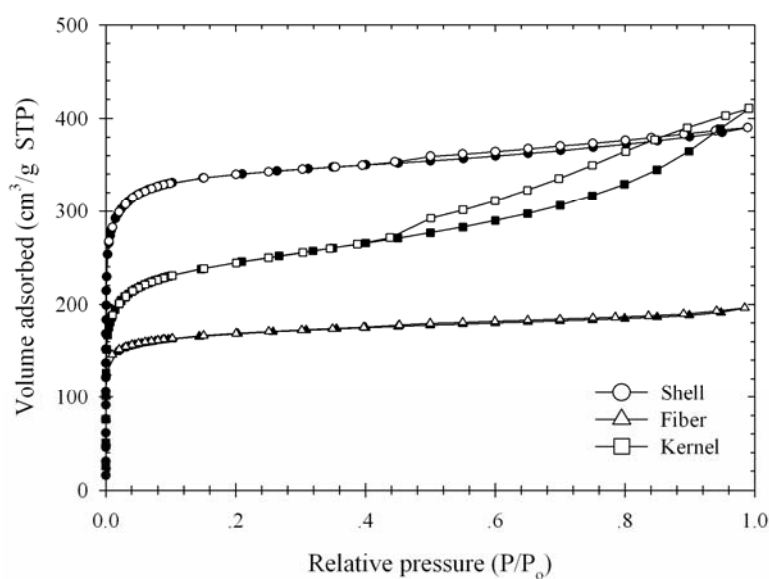


Figure 3.77 N₂ adsorption isotherm at -196°C of activated carbons prepared at optimum conditions.

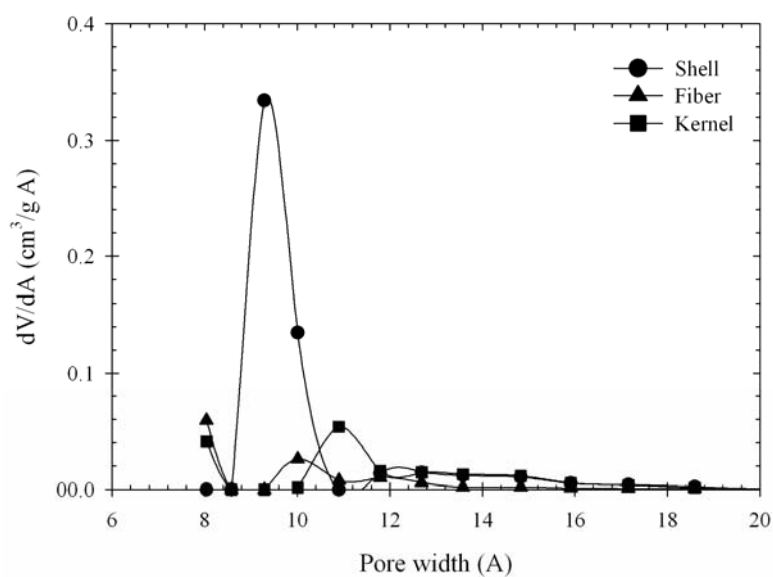


Figure 3.78 Pore size distribution of activated carbons prepared at optimum conditions, determined by DFT model (El-Merraoui et al., 2000).

3.6 Conclusions

Highly porous activated carbon can be produced from the three types of oil-palm solid wastes, including palm shell, fiber, and kernel cake using the process of char gasification with carbon dioxide in laboratory tube furnace. The following conclusion can be drawn from this study.

- The char yield of palm shell, fiber, and kernel cake decreased progressively with the carbonization temperature. The char yields also indicated that the pyrolysis scheme of palm shell and kernel cake are almost completed at about 600°C, while the palm fiber was almost complete at about 500°C. The char yields of all precursors decreased continually with increasing of heating rate.
- Particle sizes of palm shell smaller than 2.0 mm had no significant effect on the yield of char and the evolution of porous structure during carbonization process

- which indicated the insignificant effect of heat and mass transfer on the pyrolysis scheme.

- The conditions that used for preparing the chars were as follow: 600°C and 2.0 hrs for palm shell, 500°C and 1.0 hr for fiber, and 600°C and 1.0 hr for palm kernel cake, corresponding to 31.9%, 28.2% and 29.6% of char yields, respectively. All types of solid wastes were carbonized at heating rate of 5°C/min. These carbonization conditions were chosen to ensure that the devolatilization scheme of each precursor was completed and a carbon-rich char with high yield were obtained.

- The optimum activation conditions that gave the maximum in surface area occurred at the following condition: 950°C and 2 hrs for palm shell, 850°C and 2 hrs for fiber, and 900°C and 2.5 hrs for palm kernel cake, corresponding to 48.4%, 51.7% and 65.9% of char burn-off, respectively. The maximum BET surface area obtainable under the preparation conditions studied were 1067, 522 and 789 m²/g for palm shell, fiber and kernel cake, respectively.

- The palm shell and fiber derived activated carbons consisted mostly of microposity in their structure, while the palm kernel cake based activated carbon was predominated with mesoporosity. The level of char burn-off was found to correlate directly with the porous properties of each derived activated carbon including surface area, micropore volume and total pore volume.

3.7 References

Adinata, D., Daud, W.M.A.W. and Aroua, M.K. (2007). Preparation and characterization of activated carbon from palm shell by chemical activation with K₂CO₃. **Bioresource Technology** 98: 145-149.

- Ahmad, A.L., Loh, M.M. and Aziz, J.A. (2006). Preparation and characterization of activated carbon from oil palm wood and its evaluation on Methylene Blue adsorption. **Dyes and Pigments** 75: 263-272.
- Arenas, E. and Chejne, F. (2004). The effect of the activating agent and temperature on the porosity development of physically activated coal chars. **Carbon** 42: 2451-2455.
- Bansal, R.C., Donnet, J.B. and Stoeckli, F. (1988). **Active Carbon**. New York: Marcel Dekker.
- Daud, W.M.A.W. and Ali, W.S.W. (2004). Comparison on pore development of activated carbon produced from palm shell and coconut shell. **Bioresource Technology** 93: 63-69.
- Daud, W.M.A.W., Ali, W.S.W. and Sulaiman, M.Z. (2000). The effect of carbonization temperature on pore development in palm-shell-based activated carbon. **Carbon** 38: 1925-1932.
- Demirbas, A., Pehlivan, E. and Altun, T. (2006). Potential evolution of Turkish agricultural residues as bio-gas, bio-char and bio-oil sources. **International Journal of Hydrogen Energy** 31: 613-620.
- Do, D.D. (1998). **Adsorption analysis: equilibria and kinetics**. London: Imperial College Press.
- Duran-Valle, C.J., Gomez-Corzo, M., Gomez-Serrano, V., Pastor-Villegas, J. and Rojas-Cervantes, M.L. (2006). Preparation of charcoal from cherry stones. **Applied Surface Science** 252: 5957-5960.

- El-Merraoui, M., Aoshima, M. and Kaneko, K. (2000). Micropore size distribution of activated carbon fiber using the density functional theory and other methods. **Langmuir** 16: 4300-4304.
- Ganan, J., Donzalez, J.F., Gonzalez-Garcia, C.M., Ramiro, A., Sabio, E. and Roman, S. (2006a). Air-activated carbons from almond tree pruning: Preparation and characterization. **Applied Surface Science** 252: 5988-5992.
- Ganan, J., Donzalez, J.F., Gonzalez-Garcia, C.M., Ramiro, A., Sabio, E. and Roman, S. (2006b). Carbon dioxide-activated carbons from almond tree pruning: Preparation and characterization. **Applied Surface Science** 252: 5993-5998.
- Gonzalez, J., Encinar, J.M., Gonzalez-Garcia, C.M., Sabio, E., Ramiro, A., Canito, L.J. and Ganan, J. (2006). Preparation of activated carbons from used tyres by gasification with steam and carbon dioxide. **Applied Surface Science** 252: 5999-6004.
- Guo, J., Xu, W.S., Chen, Y.L. and Lua, A.C. (2005). Adsorption of NH₃ onto activated carbon prepared from palm shells impregnated with H₂SO₄. **Journal of Colloid and Interface Science** 281: 285-290.
- Haykiri-Acma, H., Yaman, S. and Kucukbayrak, S. (2006). Effect of heating rate on the pyrolysis yields of rapeseed. **Renewable Energy** 31: 803-810.
- Iwasaki, S., Fukuhara, T., Abe, I., Yanagi, J., Mouri, M., Iwashima, Y., Tabuchi, T. and Shinohara, O. (2002). Adsorption of alkyphenols onto microporous carbons prepared from coconut shell. **Synthetic Metals** 125: 207-211.
- Juang, R.S., Wu, F.C. and Tseng, R.L. (2002). Characterization and use of activated carbons prepared from bagasses for liquid-phase adsorption. **Colloids and Surfaces A: Physical and Engineering Aspects** 201: 191-199.

- Junpirom, S., Do, D.D., Tangsathitkulchai, C. and Tangsathitkulchai, M. (2005). A carbon activation model with application to longer seed char gasification. **Carbon** 43: 1936-1943.
- Katyal, S., Thambimuthu, K. and Valix, M. (2003). Carbonization of bagasse in a fixed bed reactor: influence of process variables on char yield and characteristics. **Renewable Energy** 28: 713-725.
- Lu, L., Sahajwalla, V. and Harris, D. (2000). Characterization of chars prepared from various pulverized coals at different temperatures using drop-tube furnace. **Energy and Fuels** 14: 869-876.
- Mackay, D.M. and Robert, P.V. (1982a). The influence of pyrolysis conditions on yield and microporosity of lignocellulosic chars. **Carbon** 20: 95-104.
- Mackay, D.M. and Robert, P.V. (1982b). The influence of pyrolysis conditions on the subsequent gasification of lignocellulosic chars. **Carbon**. 20: 105-111.
- Marcilla, A., Asensio, M. and Martin-Gullon, I. (1996). Influence of the carbonization heating rate on the physical properties of activated carbons from a sub-bituminous coal. **Carbon** 34: 449-456.
- Morf, P., Hasler, P. and Nussbaumer, T. (2002). Mechanisms and kinetics of homogeneous secondary reactions of tar from continuous pyrolysis of wood chips. **Fuel** 81: 843-853.
- Pis, J.J., Mahamud, M., Pajares, J.A., Parra, J.B. and Bansal, R.C. (1998). Preparation of active carbons from coal Part III: Activation of char. **Fuel Processing Technology** 57: 149-161.

- Roberts, D.G., Harris, D.J., Wall, T.F., 2003. On the effects of high pressure and heating rate during coal pyrolysis on char gasification reactivity. *Energy and Fuel*. 17, 887-895.
- Scott, S.A., Davidson, J.F., Dennis, J.S., Fennell, P.S. and Hayhurst, A.N. (2005). The rate of gasification by CO₂ of chars from wastes. **Proceeding of the Combustion Institute** 30: 2151-2159.
- Su, W., Zhou, L. and Zhou, Y. (2006). Preparation of microporous activated carbon from raw coconut shell by two-step procedure. **Chinese Journal of Chemical Engineering** 14: 266-269.
- Tam, M.S. and Antal, M.J. (1999). Preparation of activated carbons from macadamia nut shell and coconut shell by air activation. **Industrial and Engineering Chemistry Research** 38: 4268-4276.
- Valix, M., Cheung, W.H. and McKay, G. (2004). Preparation of activated carbon using low temperature carbonisation and physical activation of high ash raw bagasse for acid dye adsorption. **Chemosphere** 56: 493-501.
- Williams, P. and Besler, S. (1996). The influence of temperature and heating rate on the slow pyrolysis of biomass. **Renewable Energy** 7: 233-250.
- Yu, L. and Zhong, Q. (2006). Preparation of adsorbents made from sewage sludges for adsorption of organic materials from wastewater. **Journal of Hazardous Materials** 137: 359-366.

CHAPTER IV

AN IMPROVED CARBON GASIFICATION MODEL FOR PREDICTING THE PORE DEVELOPMENT OF ACTIVATED CARBON

4.1 Abstract

The aim of this work is to modify the structural model recently proposed by Junpirom et al. (JDTT) for describing the evolution of porosity in activated carbon during the course of activation process with an oxidizing gas. The system is assumed to consist of graphitic crystallites. The number of graphene layers in each crystallite is varied randomly within a certain range that depends on the source of chars and its activation conditions. All graphene layers are assigned with different reactivities with respect to the gasifying agent, and therefore pores are randomly created as a result of this difference in the reactivities. The effect of pore collapse at very high extent of gasification is also incorporated in this modified model. With this simple structural model, we are able to obtain the evolution of surface area, total pore volume and pore size distribution from activated carbon as a function of char burn-off. The simulated results from the modified model are tested with the experimental data of longan seed-derived chars activated with carbon dioxide and also compared with the simulated results obtained from the original JDTT model. Furthermore, the simulation capability of the modified model is tested against the experimental data of CO₂-gasification of

oil-palm shell and fiber. The simulated results show that the proposed modified model can describe the evolution of surface area and total pore volume extremely well over the entire range of degree of burn-off being studied.

4.2 Introduction

As mentioned in the previous chapter, there are two main techniques to produce activated carbon, physical and chemical activations, with the former method being most commonly used. The physical activation technique can be separated into two different steps, carbonization (pyrolysis) and activation of carbonization product with an oxidizing gas (gasification). The pyrolysis mechanism of oil-palm solid wastes has been studied and reported in Chapter 2. In this chapter, the porosity evolution mechanism during activation step of activated carbon derived from oil-palm solid wastes was studied by applying the modified carbon activation model originally proposed by Junpirom et al. (2005). A full description of porosity evolution mechanism will lead to the determination of the porous properties and adsorption capacities of the derived activated carbons.

The porous properties of activated carbon, such as surface area, pore volume, and pore size distribution, are progressively developed during the activation process which is a typical gas-solid (gasification) reaction between carbon (chars) and an activating agent (oxidizing gas), such as steam and carbon dioxide. The factors that affect directly the porous properties and also the pore development of the derived activated carbon are the initial structure of char, activating conditions (i.e. temperature, holding time and applied heating rate) and type of oxidizing agent used.

The structure of derived char depends upon the source of carbonaceous precursors used and the condition of carbonization. Franklin (1951) used X-ray diffraction to study the structure of carbon, and found that the char consists of two main groups, the crystalline structure of graphite and the non-graphitic amorphous carbon. For the graphitic carbons, the crystallite composed of a group of parallel graphite-like layers with their number varying from 30 to more than 150 layers and its size varying from 80 to more than 600 Å. The inter-layer spacing between these graphene layers is constant at 3.354 Å. Figure 4.1 shows the schematic diagram of graphite.

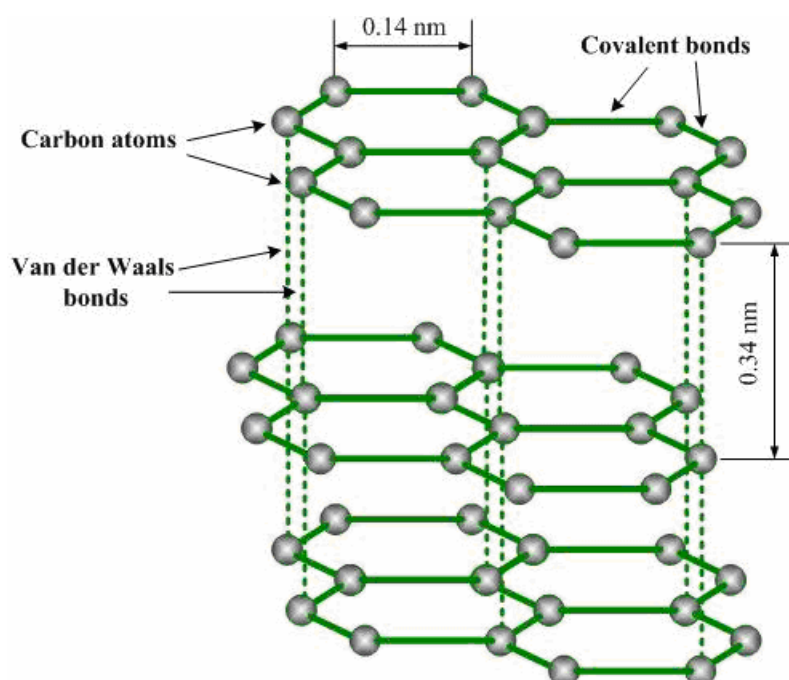


Figure 4.1 Schematic diagram of graphite structure.

The aim of this chapter is to modify the Junpirom et al.'s model (JDTT) to improve the model predictive capability. The simulation results generated from this

modified model is validated with the experimental data of longan seed char gasification obtained by Junpirom et al. (2005) and also with the experimental data of oil-palm solid wastes (palm-shell and fiber) collected in the present study. It should be noted that the JDTT model can be applied only for the activated carbon consisting mainly with the microporous structure. For oil-palm kernel based activated carbon, as shown previously in Chapter 3, it consists mainly of mesoporous structure. Therefore, the JDTT model will not be used for predicting the porosity evolution of oil-palm kernel derived activated carbon.

4.3 Review of the Literatures

Presently, many models have been proposed in the literatures for predicting the porosity evolution of activated carbon as a function of burn-off. Petersen (1957) modeled the activation system by considering the diffusion and reaction of an activating agent in a single cylindrical pore and also in a random assembly of pores with initial uniform diameter. Since the model was dealt with on the assumption of uniform pores, it is not suitable for modeling the activation process of the solid adsorbent with a broad pore size distribution, especially activated carbons. Szekely and Evans (1970, 1971) presented two structural model, shrinking core models of carbon pellets and pore model. Other developed models based on the population balance method to describe the change in porous structure during gasification process were proposed by Hashimoto and Silveston (1973), and Bhatia and Perlmutter (1979). Another approach employing a random pore model to illustrate the fluid-solid reactions was proposed by Bhatia and Perlmutter (1980). Sandmann and Zygourakis (1986) used the discrete numerical model to describe the evolution of pore structure.

All of these models are primarily focused on the macroscopic properties of the porous solid.

In another approach, some researchers have considered the porous structure in microscopic scale. Miura and Hashimoto (1984) proposed a model for calculating the pore evolution during the activation of carbonaceous materials. The model was developed based on the structure of graphitic carbons studied by Franklin (1951). The solid carbon is assumed to consist of two parts, non-organized carbon and graphitic crystallite. The initial stage of the gasification reaction was performed with the more reactive non-organized carbon and then the less reactive graphitic crystallite is gasified steadily. Junpirom et al. (2005) proposed a new structural model by considering only the graphitic crystallites and ignored the gasification of amorphous carbon. They assumed that the char is composed of bundles of graphene layers and the porosity is created via the consumption of these graphene layers by the oxidizing gas. The total pore volume predicted by Junpirom et al.'s model agreed well with the experimental data up to 25% burn-off.

4.4 Model Description

As mentioned in the previous section, char obtained from carbonaceous materials consists of two parts, amorphous carbon and graphitic crystallite (Franklin, 1951; Bansal, 1988; Byrne, 1995). The schematic representation of char structure is shown in Figure 4.2. The amorphous part is more reactive than the crystallite carbon and it will be gasified at the initial stage of the activation process. Because of the highly disorganized structure of amorphous part and its high reactivity, the gasification reaction is very fast and the porous structure developed from this falls in

the mesopore and macropore regions. Since we are mainly interested in the evolution of the micropores, we shall study only the gasification of the graphitic crystalline structure. The schematic diagram of one crystallite is shown in Figure 4.3a.

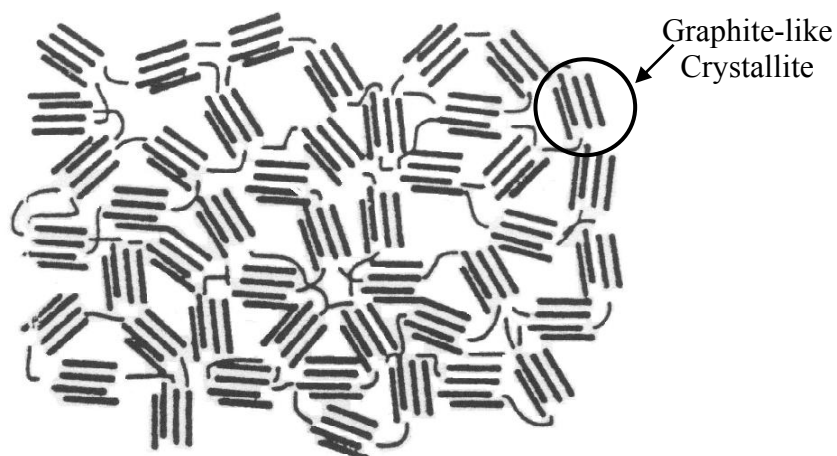


Figure 4.2 Schematic diagram of char structure.

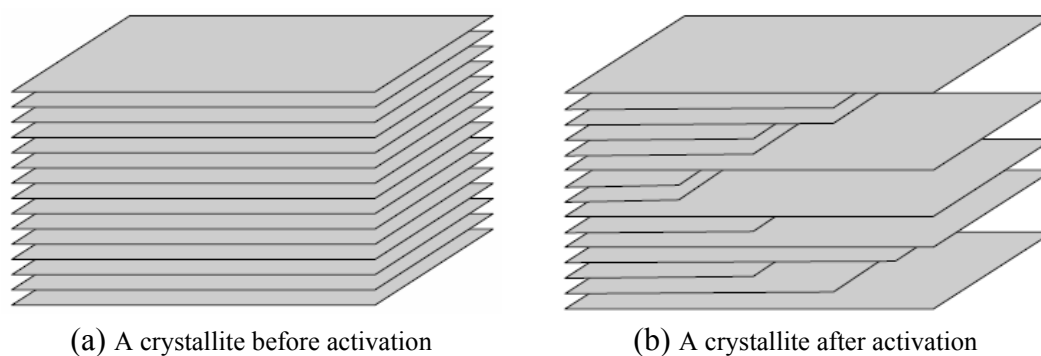


Figure 4.3 Schematic diagram of a crystallite structure.

The model system consists of a large number of crystallites to ensure a good statistical averaging. Each crystallite contains N equal-sized graphene layers, and this number is chosen randomly between N_{\min} and N_{\max} using random generator in

FORTRAN. We found that the number of crystallites in the model system of 10,000 crystallites is large enough to ensure that the effect of the random choosing for the number of graphene layers per crystallite can be ignored. This means that each run of modeling scheme will give the same simulated result when the number of crystallites is larger than 10,000 crystallites for the same model conditions. For the number of crystallites lesser than 10,000 crystallites, the simulated result is considerably depend on the number of crystallites used. The interlayer spacing of graphene layer is 3.354 Å as reported by Franklin (1951). The range (N_{\min}, N_{\max}) for each crystallite is an adjusting parameter, and it is chosen such that a good agreement between the experimental data and the simulation results is achieved. It is found that this parameter depends on the source of char used. Because of the different reactivities of graphene layers in the same crystallite, pores are continually created in that crystallite as the gasification is progressing with time. The difference in reactivities of each graphene layer is the result of the energetic heterogeneity with reference to the chemical reaction as to be expected in the real system. We also assign a group of adjacent layers with the same reactivity. This number of layers, N_L , is selected in random between 1 and 5. This would give the largest pore width of 20 Å at the initial stage of gasification (based on an interlayer spacing of 3.354 Å), which is in the micropore size range. However, at high extent of gasification, the effect of N_L becomes less significant, therefore pores with pore width larger than 20 Å can be possibly observed. To make the model more realistic, it is necessary to assign a non-reactive layer (i.e. zero reactivity) to some of the graphene layers to represent the diffusion resistance inside the char at the initial stage of the activation process (lower than 30% burn-off). The first and last layers of all crystallites are also assigned with

zero reactivity in the early stage of gasification. These non-reactive layers will be reassigned with reactivity at a later stage of reaction, that is, at high burn-off, and this condition represents kinetic-controlled gasification.

The degree of gasification reaction for each graphene layer can be expressed by the following reaction equation.

$$L_t = L_{t,o} - at \quad (4.1)$$

where L_t is the length of graphene layer at a theoretical time t , $L_{t,o}$ is its initial length, and a is the reactivity of carbon layer. The graphene layer is gasified along one side of graphene plane in a lengthwise direction. Figure 4.3b illustrates the typical porous structure of the crystallite containing a number of slit pores at a given burn-off. The theoretical time is defined as an incremental integer starting from zero. The simulation is performed for a given theoretical time and the burn-off calculated along with the porous properties of the carbon. The calculation is repeated for the next value of time.

For example, at any burn-off, the remained linear length (L_t) of all graphene layer can be calculated via Equation (4.1). By using the data of the remained length and interlayer spacing of 3.354 Å for the graphene layer, the mass, surface area, total pore volume, and pore size distribution can be evaluated. The initial total mass of char is calculated from the total number of carbon atoms contained in all graphene layers in the system. At any theoretical time, the burn-off of char can be estimated from the following equation.

$$\text{Burn-off} = \frac{L_{t,o} - L_t}{L_{t,o}} \times 100\% \quad (4.2)$$

Surface area is calculated from the area of two opposite graphene planes. Total pore volume is estimated from the void volume bounded by the two opposite graphene planes. Figure 4.4 shows the schematic representation of pore size, BET surface area, and total pore volume of graphite crystallite at any char burn-offs. Pore size distribution is obtained directly from the data of pore volume of different pore sizes. The initial surface area and total pore volume of char is estimated from the actual experimental data. For longan seed char in this study, the initial surface area is $300 \text{ m}^2/\text{g}$ and total pore volume is $0.14 \text{ cm}^3/\text{g}$ (Junpirom et al., 2005).

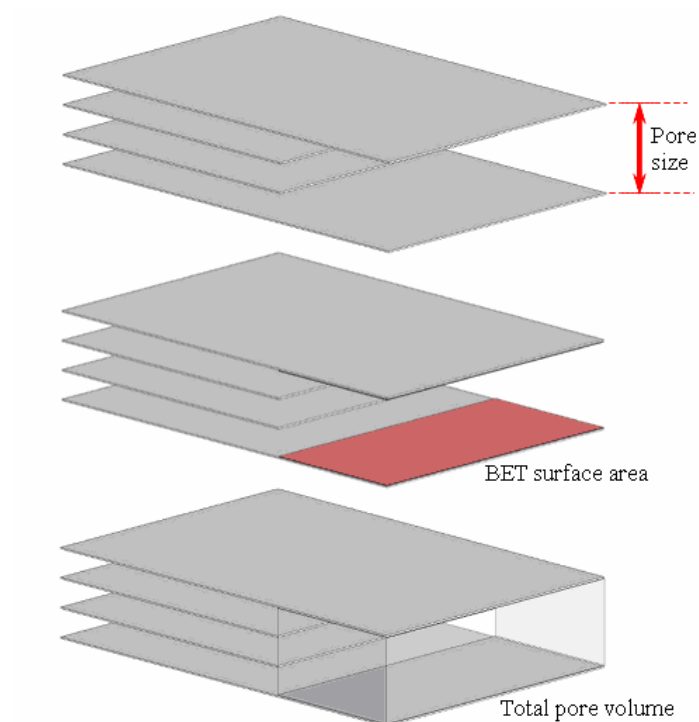


Figure 4.4 Schematic representation of pore size, surface area, and total pore volume of graphite crystallite at any char burn-offs.

During the activation process of activated carbon, the important phenomenon that is usually observed, especially at high burn-off is the collapse of some pore structure. This would cause the reduction in pore size, surface area and pore volume. The effect of pore collapse in activated carbon is also considered in this modified model at high extent of burn-off (greater than 50% burn-off). We assume that the collapse of pore will occur when the number of adjacent layers which has burnt out (zero length) exceeds a certain value, defined here as maximum number of burnt out layers. The burnt out layer which exceeds the maximum burnt out layers will be deleted and replaced by the nearby layer. This will causes the reduction in pore width and the number of graphene layers contained in that crystallite. The maximum burnt out layer depends on the mechanical strength of char used and it is arbitrarily selected and adjusted until good agreement between the experiment data and simulated result is obtained. For the case of longan seed char, we found that the pores will collapse when the number of connected layers being burnt out exceeds 3 layers (maximum burnt out layers). The differences between the original model proposed by Junpirom et al. and the modified model in this work are summarized in Table 4.1.

It should be noted that the most important parameters that can affect the accuracy of model prediction are the selection of layer group pattern, number of non-reactive layers, and maximum number of burnt out layer as described previously. The sum of square of relative error is used as the objective function for the optimization to provide the best fitting of porous properties between the simulation results and the experimental data.

Table 4.1 Comparison between the original JDTT model by Junpirom et al. (2005) and the present modified model.

Model conditions	Original model	Modified model
total no. of crystallite	100	10,000
no. of graphene layer per crystallite	15 (constant)	varied in a certain range
interspacing between layers (Å)	3.354	3.354
non-reactive layer (zero reactivity)	selected randomly	assigned for the first and last layer of all crystallites and the other layers selected randomly
pore collapse	not applied	applied

4.5 Research Methods

4.5.1 Preparation of Char

The oil palm solid wastes (including palm shell and fiber) are an abandoned by-product produced during palm-oil milling process and were supplied by The Golden Palm Industry in Chon Buri Province, Thailand. The received solid wastes were first washed and dried at 120°C for 24 hr to remove excess moisture. The pre-dried solids were further milled to the average size of 1.0 mm for oil palm shell and less than 1 mm for fiber. The carbonization of the precursors was carried out in a horizontal ceramic tube furnace (Carbolite, UK). The sample was first heated from room temperature at the rate of 5°C/min to the desired final temperature of 600°C for

palm shell and 500°C for palm fiber. Subsequently, the sample was held at this activation temperature for 2.0 hr for palm shell and 1.0 hr for palm fiber. After that, the sample was cooled down to room temperature. During the carbonization of char and cooling-down period, 100 cc/min of ultrahigh purity grade nitrogen (99.999%, Thai Industrial Gases) was supplied to provide inert atmosphere around the sample.

4.5.2 Gasification of Char and Characterization of Activated Carbon

The gasification of char was carried out in the horizontal tube furnace (Carbolite, UK). The char was activated by high purity grade carbon dioxide (99.95%) supplied by Thai Industrial Gases. The activation temperature was varied from 700-950°C and the activation time was varied in the range of 1-6 hr. The percentage burn-off of the activated carbon was calculated based on the initial mass of the char used. The porous properties of the derived activated carbons (BET surface, total pore volume, and pore size distribution) were estimated based on the adsorption isotherm of nitrogen at 77 K measured by using an Accelerated Surface Area and Porosimetry Analyzer (ASAP 2010, Micromeritics, USA). The pore size distribution of the derived activated carbon was derived by using the density functional theory (DFT) method (El-Merraoui, 2000).

4.6 Results and Discussion

The new modified gasification model developed in this work was tested against the porous property data of longan seed and oil-palm solid wastes activated carbon. The simulated results using the original model was also compared to demonstrate the improvement of this new model.

4.6.1 Model Testing with Gasification Data of Longan Seed Char

For the structural model, the number of carbon layer per graphitic crystallite is the most significant parameter which plays an important role in the simulation of pore development in activated carbon. For longan seed chars, we found that the number of graphene layers per crystallite which provided the best fit between the experimental data and the simulated result varied in the range of 10 to 30 layers. Junpirom et al. used constant 15 layers in their structural model, and this number falls into the range proposed in this work.

The evolution of surface area and total pore volume versus the extent of the gasification for longan seed chars collected experimentally by Junpirom et al. (2005) are shown in Figure 4.5 and 4.6 as filled symbols. Also shown in this figure are the simulated results from the structural model proposed by Junpirom et al. (dash lines) and the results from the present modified model (solid lines). Substantial improvement of the prediction of the modified model on the total pore volume data is discernible. The modified model can describe the total pore volume data properly for the whole range of gasification extent, while the total pore volume obtained from the original model agree with the experimental data only up to 25% burn-off. The maximum total pore volume of the derived activated carbon estimated from the experimental data is about 0.82 cc/g occurring at about 70% burn-off, which is much better described by the proposed modified model as seen in Figure 4.6.

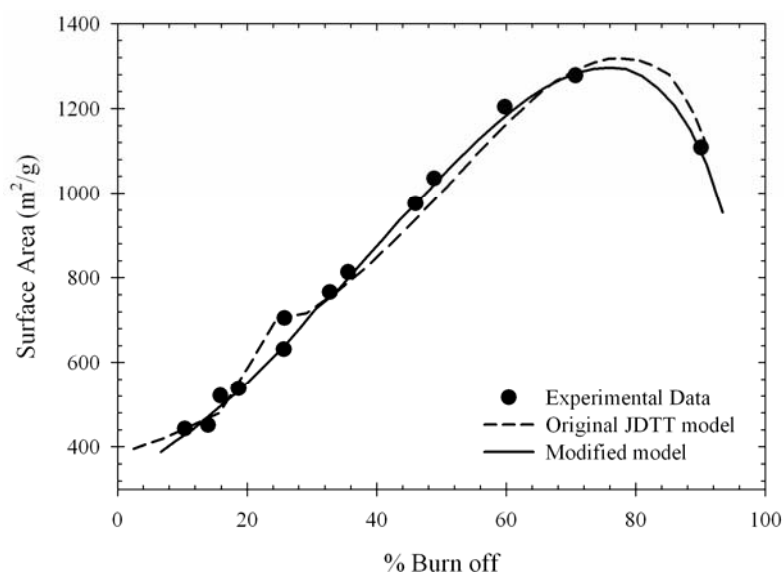


Figure 4.5 Experimental data and simulated results of surface area of longan seed based activated carbons.

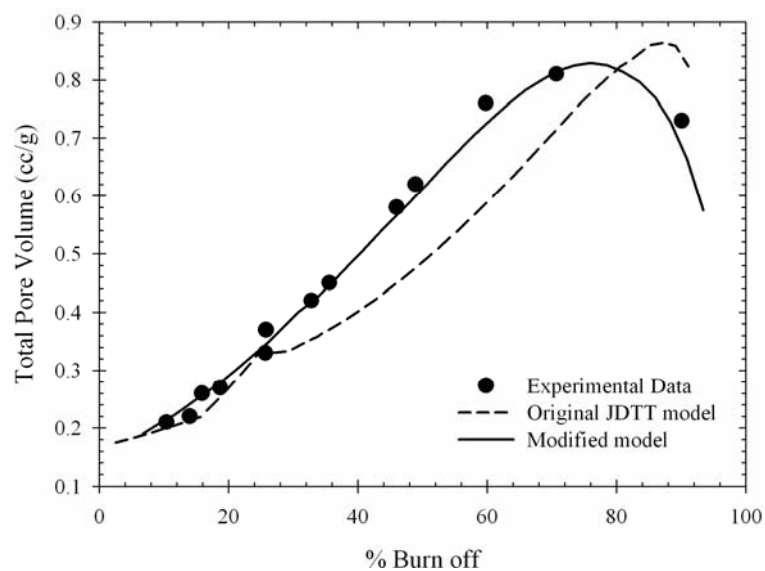


Figure 4.6 Experimental data and simulated results of total pore volume of longan seed based activated carbons.

In order to show the effect of pore collapse on the simulated results of longan seed based activated carbon, the calculated total pore volume is plotted against the extent of gasification by varying the maximum number of burnt out layers (see Figure 4.7). In all cases, there is no effect of pore collapse on the predicted total pore volume of activated carbon at the initial stage of gasification (lower than 40% burn-off). The pore collapse becomes significant when the burn-off is greater than 40% and this extent is more pronounced when the maximum number of burnt out layers is one. For this case of longan seed based activated carbon, it is found that the maximum number of burnt out layers is three.

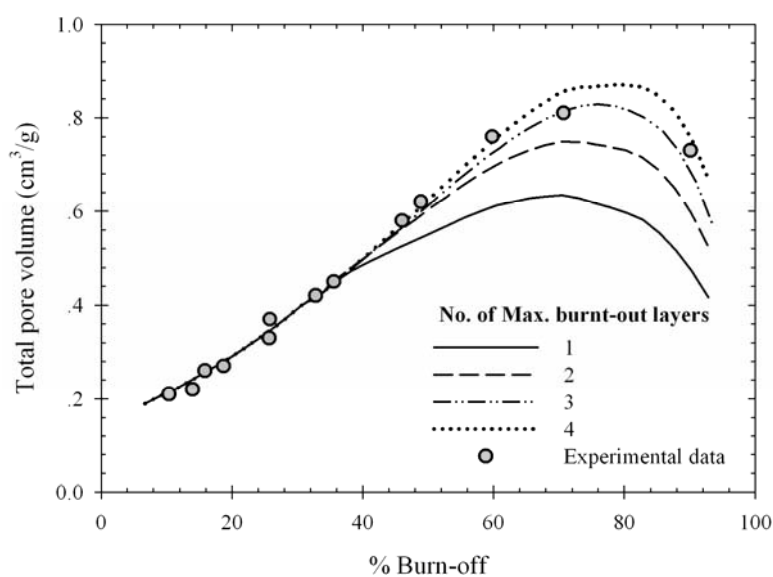


Figure 4.7 Experimental data and simulated results of total pore volume for various maximum number of burnt out layers of longan seed based activated carbons.

We further investigate the potential of the model by comparing the pore size distribution (PSD) obtained from the simulation and that obtained with the DFT

analysis of nitrogen adsorption data at 77 K. The DFT-derived PSDs calculated at 47.2% and 90.1% burn-off of longan seed derived char are shown as solid lines in Figure 4.8 and 4.9, respectively. The simulated PSD obtained from the original and modified models are also shown in the same figure for comparison. The DFT-PSDs for both extents of gasification consist of two distinct peaks at pore width of about 7 and 11 Å, with the major peak at 7 Å. The simulated results obtained from the original and modified models give much broader size PSDs into the smaller size range. The original model predicts that the activated carbon for both burn-offs consist mainly of pores with 5 Å pore width. The modified model also predicts the highest peak at 5 Å for 47.2% burn-off, but for 90.1% burn-off, it gives the highest peak at 8.4 Å. Although the modified model can provide a good agreement between the experimental data and the simulated results for surface area and total pore volume, the disagreement can still be observed for PSD, especially at the low degree of burn-off. This deviation could be that at low degree of burn-off the interconnected pore structure of carbon may not be well developed, so that adsorptive N₂ molecules could not penetrate deep into the very small pores.

In order to show the development of the porous structure during activation process of activated carbon as predicted by the modified model, the predicted PSD are plotted for a number of burn-off in the range of 6.7% to 90% (Figure 4.10). The evolution of the porous structure of activated carbon during activation process is separated into three stages. First, only new pores have been created in the early stage of gasification. The total pore volume of activated carbon is increased by the increasing of the pore length, while the average pore width remains constant. This observation is indicated by the existing of only one peak in the plot of PSD in the low

burn-off region (0-10%). For the next stage, some new pores are still continually created as well as the enlargement of the existing pores. In the last stage, the existing pores are still continually enlarge which cause the increasing in the number of large pore (mesopore). The large pores are created from the enlargement of the individual pore and possibly the combination of small pores. At this stage, some of graphene layers have been burnt out which cause the collapse of porous structure.

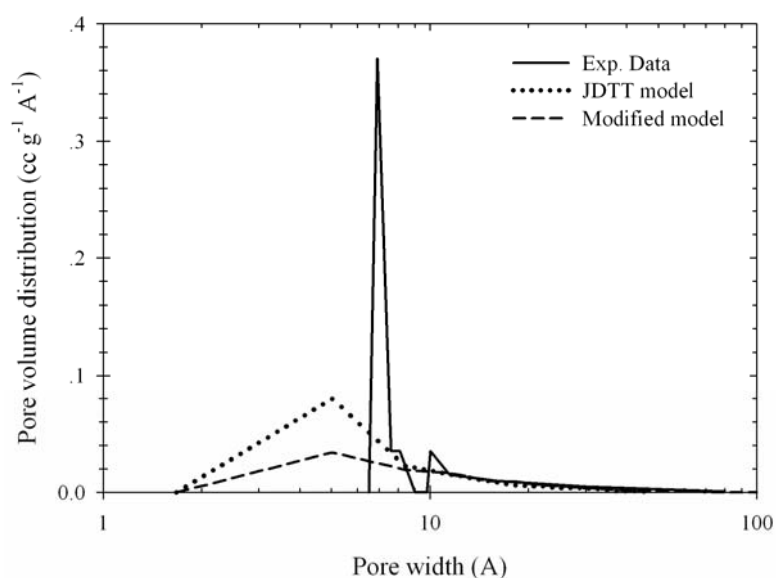


Figure 4.8 Experimental and computed pore size distributions of longan seed based activated carbons at 47.2 % burn-off.

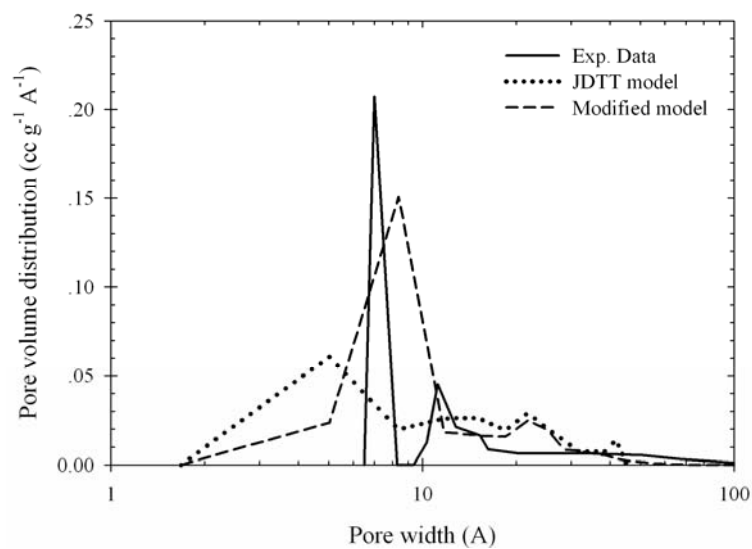


Figure 4.9 Experimental and computed pore size distributions of longan seed based activated carbons at 90.1% burn-off.

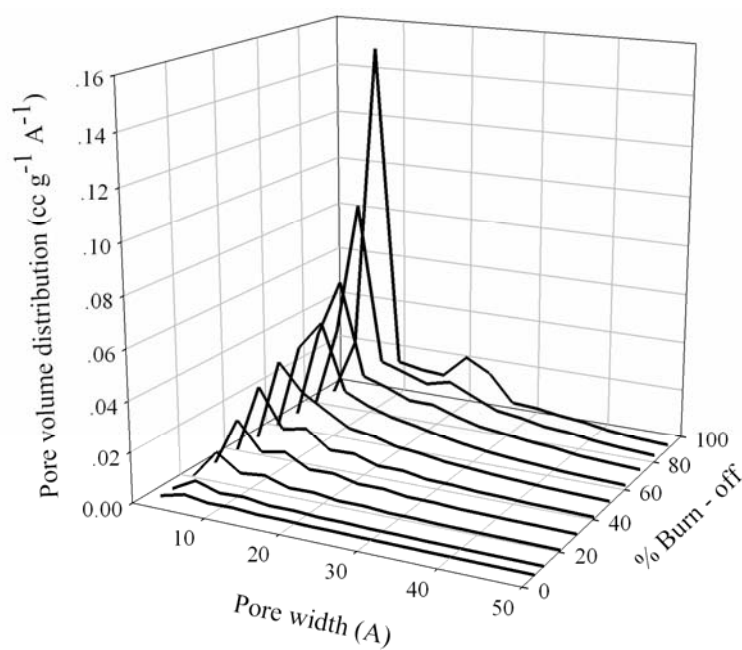


Figure 4.10 The simulated pore size distributions of longan seed based activated carbons at various degrees of char burn-off.

4.6.2 Gasification of Palm Shell

Next, the modified model is further tested against the experimental data of the gasification of oil-palm solid wastes, including palm shell and fiber. For palm shell and fiber, the experimental data were collected from 10% to 90% and 10% to 60% burn-offs for palm shell and fiber, respectively.

The number of carbon layer per graphitic crystallite for the palm shell char is varied in the range of 10 to 30 layers which is the same as for the case of longan seed char, but the number of non-reactive layers applied at the initial stage of gasification is different. This means that the carbon structures of longan seed char and palm shell char can be treated the same, but the diffusion resistance of activating agent in both chars could be different. For palm shell char, the initial values of surface area and total pore volume were measured and found to be 400 m²/g and 0.15 cc/g, respectively. Figure 4.11 and 4.12 show the experimental data and simulated result of surface area and total pore volume as a function of the extent of gasification of palm shell char, respectively. The simulated results agree well with the experimental data for both surface area and total pore volume over the range of burn-off studied. The experimental data show the maximum of BET surface area of 2022 m²/g which occurs at 85.5% burn-off and no maximum value of the total pore volume is observed. The simulated results show that the predicted highest surface area of palm shell based activated carbon is 2040 m²/g occurring at 88.7% burn-off which agrees closely with that observed experimentally. For predicted total pore volume, the maximum value is about 1.31 cm³/g at 88.7% burn-off.

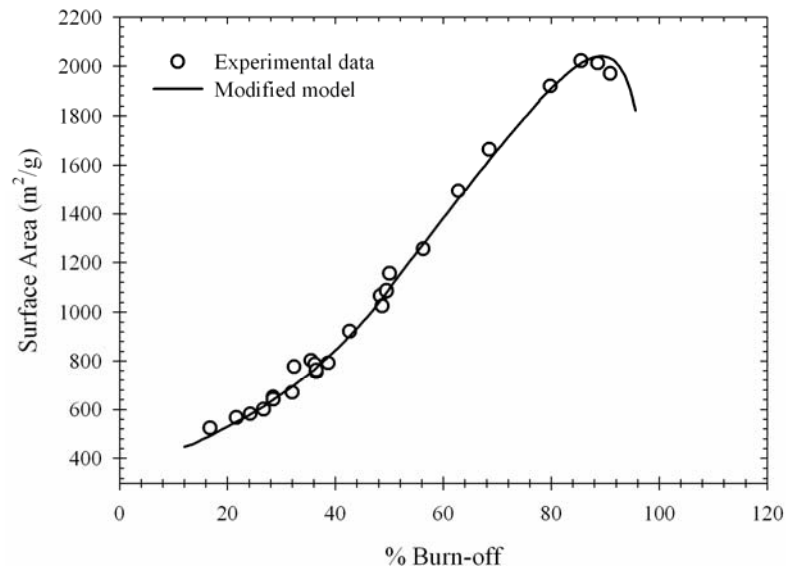


Figure 4.11 Experimental data and simulated results of surface area of palm shell based activated carbons.

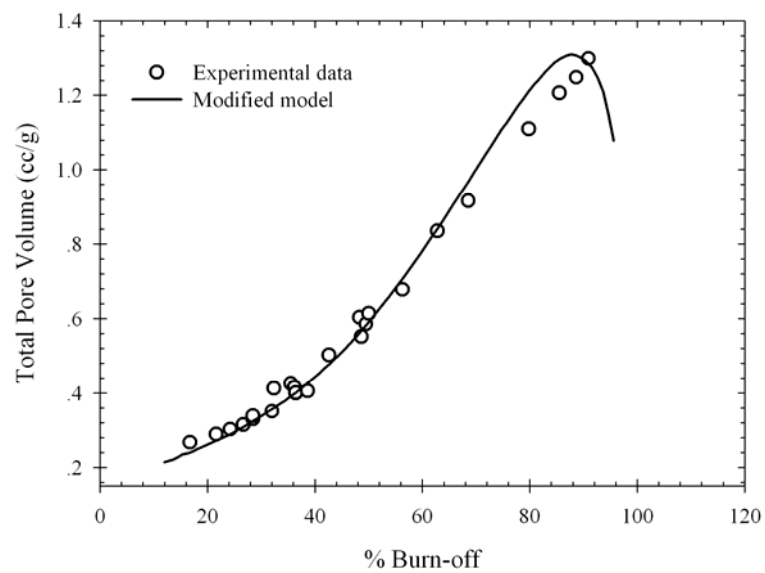


Figure 4.12 Experimental data and simulated results of total pore volume of palm shell based activated carbons.

For the PSD data, the typical experimental and calculated PSD of the oil-palm shell based activated carbon with 48.5% burn-off are shown in Figure 4.13. The experimental PSD shows two distinct peaks and the highest peak is at 9.6 Å. The simulated PSD shows a broader distribution and the highest peak can be observed at 8.4 Å. The difference was ascribed to the possible inaccessibility of N₂ molecules into very small pores during the isotherm measurement. The experimental PSD derived is based on adsorption isotherm of N₂ and presents the pore volume for pore sizes larger than about 10 Å, while the simulated PSD covers the pore volume data into very small pore sizes. To better compare the experimental and simulated PSD, attempt was made to extend the experimental PSD into pore sizes smaller than 10 Å. This was achieved by first plotting the experimental cumulative pore size distributions and extrapolating the curve down to finer sizes using polynomial function fitting as shown by the dotted line in Figure 4.14. This overall cumulative distribution was then used to recalculate the differential pore size distribution and the result was compared with the simulated pore size distribution, as shown in Figure 4.15. As noted, the simulated pore size distribution from the modified model now gives similar shape of pore size distribution to the extrapolated experimental pore size distribution, thus confirming the possible hypothesis of inaccessibility of N₂ molecules during isotherm measurement.

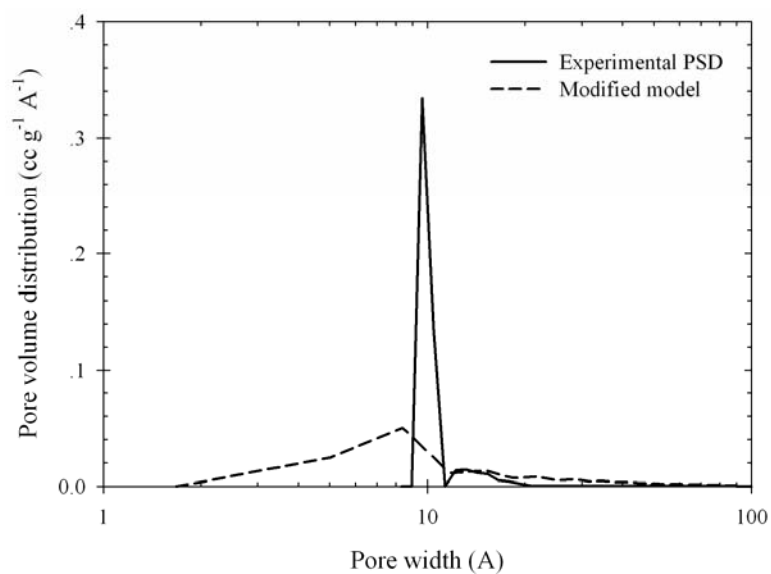


Figure 4.13 Experimental and computed pore size distributions of palm shell based activated carbons at 48.5% burn-off.

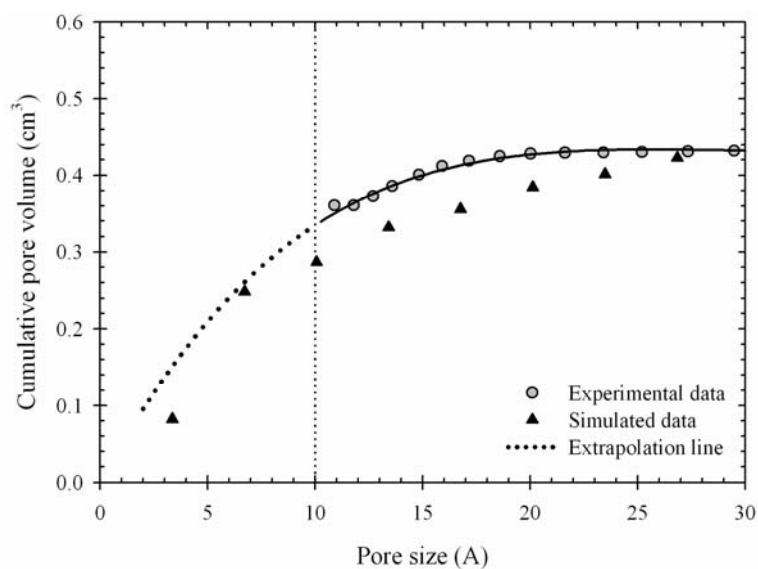


Figure 4.14 Extrapolation of cumulative pore volume at small pore size for calculation of PSD of palm shell based activated carbons.

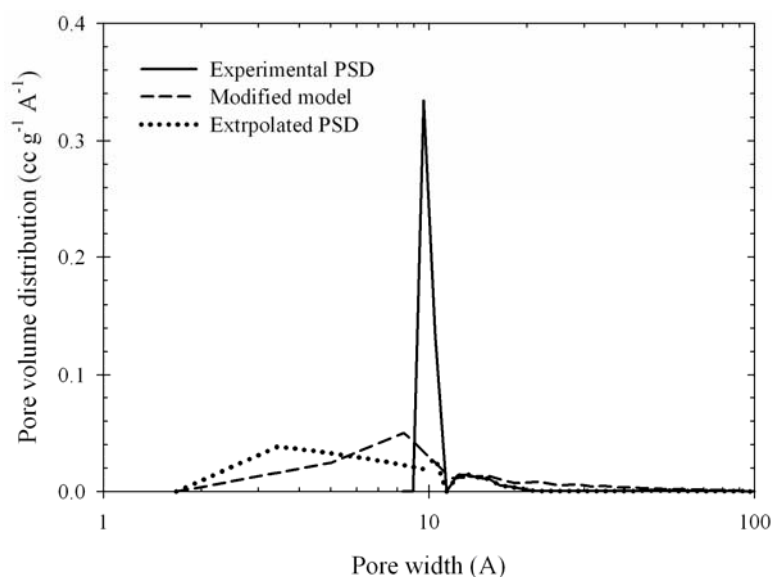


Figure 4.15 Experimental, computed and extrapolated pore size distributions and of palm shell based activated carbons at 48.5% burn-off.

4.6.3 Gasification of Palm Fiber

For the gasification of oil-palm fiber, the experimental data (empty symbols) and simulated results (solid line) for surface area and total pore volume are plotted against the extent of gasification and shown in Figure 4.16 and 4.17, respectively. The number of carbon layers per crystallite is in the range of 10 to 40 layers which is different from the case of longan seed and oil-palm shell chars. The initial condition of measured surface area and total pore volume are $340 \text{ m}^2/\text{g}$ and $0.18 \text{ cm}^3/\text{g}$, respectively. The simulated results agree fairly well with the experimental data for both surface area and total pore volume data. We also found that it is not necessary to apply the non-reactive layers at the early stage of gasification for oil-palm fiber. This observation means that the reaction mechanism between carbon and activating agent is kinetically controlled with no significant effect of the diffusion

resistance inside the char. This finding is reasonable since the structure of palm fiber is not as dense as the structure of longan seed and palm shell, hence faster transport of reactant molecules.

We further calculate the surface area and total pore volume for the extent of gasification higher than those collected experimentally using the same model parameters as the highest burn-off condition to predict the maximum value of surface area and total pore volume of activated carbon. The predicted maximum surface area of palm fiber based activated carbon is about $654 \text{ m}^2/\text{g}$ occurring at 80.2% burn-off and the maximum total pore volume is 0.35 cc/g occurring at 76.2% burn-off.

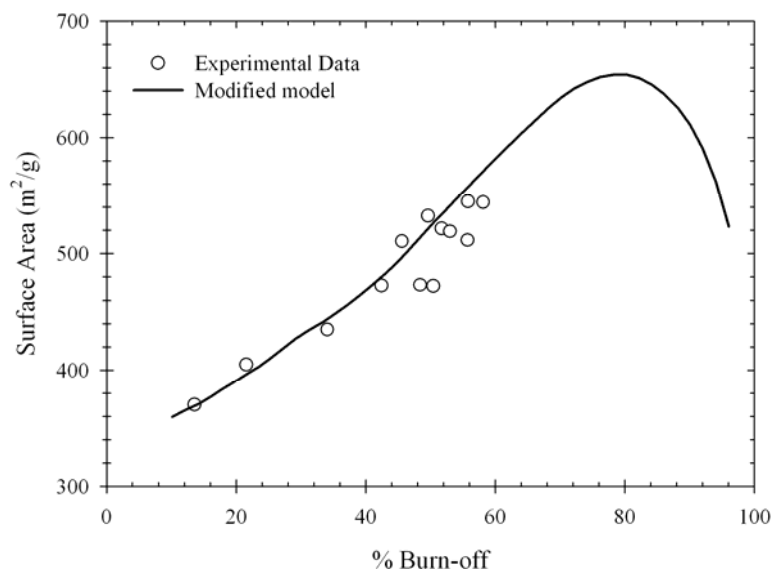


Figure 4.16 Experimental data and simulated results of surface area of oil-palm fiber based activated carbons.

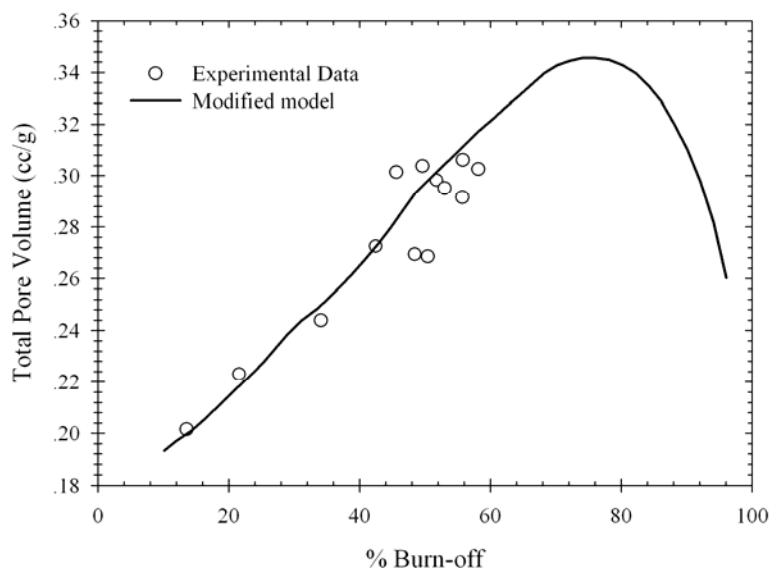


Figure 4.17 Experimental data and simulated results of total pore volume of oil-palm fiber based activated carbons.

Figure 4.18 shows the DFT-derived PSD (solid line) and simulated PSD for palm fiber (dash line) at 56.5% burn-off. The experimental data shows the highest peak at 10.5 Å and most pores are in the micropore size range (less than 20 Å). Again, the simulated PSD shows the highest peak at 8.4 Å with broader distribution into the micropore and mesopore range (greater than 20 Å). The same extrapolation procedure was performed for experimental PSD of palm fiber carbon to obtain the complete PSD down to pore sizes smaller than 10 Å. The results are shown in Figure 4.19, which again indicates better PSD agreement between the two methods.

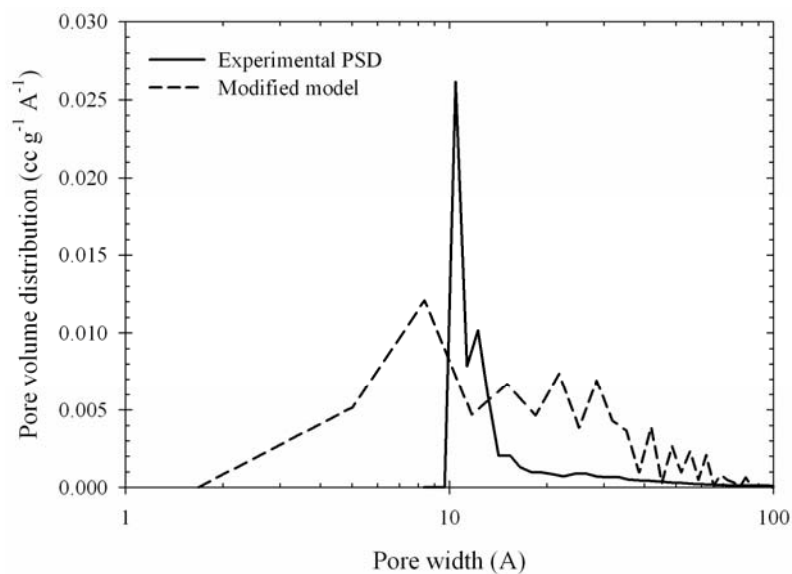


Figure 4.18 Experimental and computed pore size distributions of oil-palm fiber based activated carbons at 56.5% burn-off.

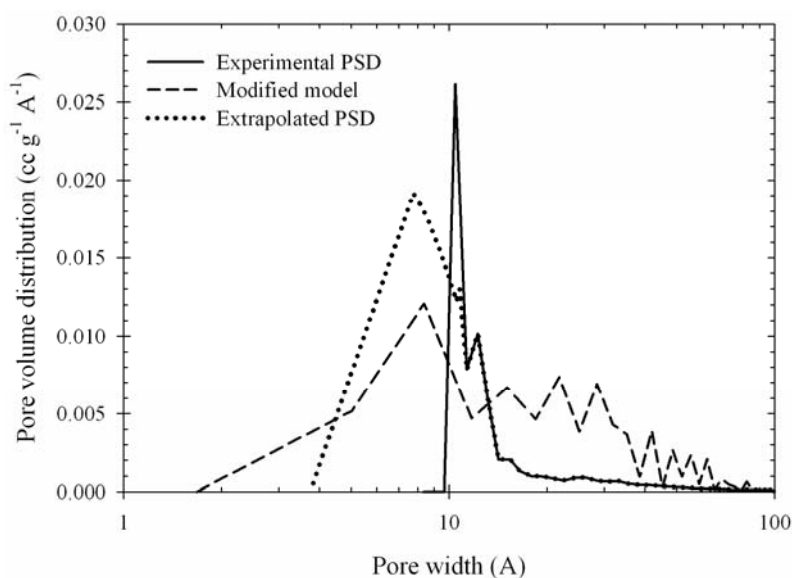


Figure 4.19 Experimental, computed and extrapolated pore size distributions and of palm fiber based activated carbons at 56.5% burn-off.

4.7 Conclusions

The structural model proposed originally by Junpirom et al. (JDTT model) for predicting the pore evolution in activated carbon during CO₂ activation process was modified and presented in this paper. The simulated results obtained from the modified model were tested using the experimental data of longan fruit seed activated carbon and also with the activated carbons derived from palm shell and fiber. The following conclusion can be drawn from this study.

- The modified JDTT model provided an excellent agreement between the experimental data and simulated results for both surface area and total pore volume data for all extent of char gasification.
- PSD from the model prediction gave a broader pore size distribution as compared to the measured PSD, particularly for activated carbon with low degree of char burn-off. The difference was ascribed to the possible inaccessibility of N₂ molecules into very small pores during the isotherm measurement. This hypothesis was supported by recalculating experimental PSD by the extrapolation technique down to very small pore sizes.

4.8 References

- Bansal, R.C., Donnet, J.B. and Stoeckli, F. (1988). **Active Carbon**. New York: Marcel Dekker.
- Bhatia, S.K. and Perlmutter, D.D. (1979). A population balance approach to the modeling of solid phase reactions. **AIChE Journal** 25: 298-306.
- Bhatia, S.K. and Perimutter, D.D. (1980). A random pore model for fluid-solid reactions. I. Isothermal, kinetic control. **AIChE Journal** 26: 379-386.

- Byrne, J.F. and Marsh, H.,1995. Introductory overview. In: J.W. Patrick (ed.) **Porosity in Carbons** (pp 2-48). London: Edward Arnold.
- El-Merraoui M, Aoshima M. and Kaneko K. (2000). Micropore size distribution of activated carbon fiber using the density functional theory and other methods. **Langmuir** 16: 4300-4304.
- Franklin, R.E. (1951). The structure of graphitic carbons. **Acta Crystallographica** 4: 253-261.
- Hashimoto, K. and Silveston, P.L. (1973). Gasification. II. Extension to diffusion control. **AIChE Journal** 19: 268-77.
- Junpirom, S., Do, D.D., Tangsathitkulchai, C. and Tangsathitkulchai, M. (2005). A carbon activation model with application to longan seed char gasification. **Carbon** 43: 1936-1943.
- Miura, K. and Hashimoto, K. (1984). A model representing the change of pore structure during the activation of carbonaceous materials. **Industrial & Engineering Chemistry Process Design and Development** 23: 138-145.
- Petersen, E.E. (1957). Reaction of porous solids. **AIChE Journal** 3: 443-448.
- Sandmann, Jr. C. W. and Zygourakis, K. (1986). Evolution of pore structure during gas-solid reactions: discrete models. **Chemical Engineering Science** 41: 733-739.
- Szekely, J. and Evans, J.W. (1970). Structural model for gas-solid reactions with a moving boundary. **Chemical Engineering Science** 25: 1091-1107.
- Szekely, J. and Evans, J.W. (1971). Structural model for gas-solid reactions with a moving boundary. II. Effect of grain size, porosity, and temperature on the reaction of porous pellets. **Chemical Engineering Science** 26: 1901-1913.

CHAPTER V

CFD SIMULATION OF HYDRODYNAMICS AND CHAR ACTIVATION PROCESS IN A CYLINDRICAL SPOUTED BED

5.1 Abstract

The preparation of activated carbon from palm shell in a batch spouted bed activator was carried out in this study. The received palm shell was first carbonized at 600°C for 2.0 hrs in a laboratory tube furnace to produce chars and then activated in a spouted bed activator with carbon dioxide at 900°C for different periods of time up to 3.0 hrs. The fluid velocity was maintained at 1.2 times the minimum spouting velocity (0.182 m/s of superficial velocity). Porous properties of produced activated carbons were estimated based on adsorption isotherm data of N₂ at -196°C. It was found that under the same activation temperature and time, the spouted bed activator produced activated carbons with 8-17% lower in char burn-off as compared to those prepared in the laboratory-scale tube furnace. This discrepancy could arise from lesser gas-particle contact per unit time in the spouted bed activator since the major portion of gas flows through the central core region where particle concentration is relatively low. However, the activated carbons produced from both types of activator showed similar values of the BET surface area and the total pore volume for the same char burn-off, indicating the same activation mechanism during pore development.

Hydrodynamic behavior of spouted bed system was studied by using air as a spouting fluid and palm-shell char particles as a solid bed. The effects of geometric factors (fluid inlet diameter and conical base angle), initial static bed height and air feed velocity on pressure drop across the bed, expanded bed height, and minimum spouting velocity were investigated experimentally. In addition, simulation of spouted bed behavior for air-palm shell char particles was also performed by using the commercial CFD package software (CFX 10.0). The applicability of CFD simulator was tested by comparing the simulated results with the obtained experimental data. It was found that the minimum spouting velocity predicted from CFD simulation was much lower than those observed from the experiment. This should result from the lower values of drag force between fluid and solid particles and the friction forces between solid particles and its neighbors, due mainly to the assumed spherical particle shape in CFD simulation.

Information on fluid mechanics of spouted bed derived from this CFD computation was further used to simulate the CO₂ activation process of palm-shell char in the spouted bed activator. For comparison purposes, the simulation conditions including gas inlet velocity, initial feed amount of char, activation temperature and particle size were chosen to duplicate those used in the experiment. To facilitate the computation scheme, the simple first-order reaction of carbon and CO₂ was assumed for describing the kinetics of activation process with the rate of reaction being dependent only on the molar concentration of CO₂. In running the simulation, the simulated result of char burn-off for the initial stage of activation time at 30 min was first matched with the experimental data and the overall first-order rate constant of activation reaction was determined and found to be $7.57 \times 10^1 \text{ s}^{-1}$. This rate constant

was further applied to predict the char burn-off for the next longer activation times up to 180 min. The overall prediction of char burn-off agreed extremely well with those obtained from the experiment over the entire range of activation time studied. In order to extend the simulated results for the prediction of porous properties of activated carbons, including surface area and total pore volume, the modified activation model developed in Chapter 4 from the tube furnace results was incorporated into the spouted bed simulation scheme. The agreement between the experimental and simulated results on the porous properties was considered to be excellent, further proving that the pore evolution mechanism of activated carbons prepared in the tube furnace and the spouted bed activator are fundamentally the same.

5.2 Introduction

On a commercial scale, there are three types of furnaces that are commonly used as activators for the production of activated carbon, they are rotary kiln, multiple-hearth furnace, and fluidized bed furnace. Rotary kiln is most commonly used because the product quality is easier to control by regulating the material residence time and temperature profile within the kiln. Fundamentally, the residence time of solid in a rotary kiln is longer than in the other two furnaces and is basically controlled by adjusting the rotational speed, the angle of the kiln, the rate of carbon feeding and withdrawal, and also the length of the kiln. The temperature profile within the rotary kiln is also easy to regulate by managing the position of burner along the kiln and the amount of fuel supply. In general, the rotary kiln is usually used in the production of micropore based activated carbons. For multiple hearth-furnace, the produced activated carbon is slightly lower in quality with more development of

mesoporosity compared to those produced from the rotary kiln. This type of furnace is also used for regeneration of spent activated carbon. For the fluidized bed furnace, it provides a good heat and mass transfer characteristics and the activation agent being in excellent contact with carbon particles. The residence time is shortest of all activating furnaces. The activation reaction occurring in the fluidized bed activator is extensive and there is much external burning of char particles leading to the relatively poor product quality.

Apart from the above three commercial activating furnaces, the spouted-bed gas-solid contactor might be another interesting choice for using it as an activator for activated carbon production, especially, for coarse particles with irregular shape like palm-shell particles studied in the work. Not only being capable of handling coarse particles, the spouted bed also has other certain advantages as follows. The product movement in the spouted bed is easy to control by controlling the flow rate of gas being fed into the vessel. Increasing in gas feed leads to the increase in particle velocity for all regions (spout core, fountain zone, and annulus region). Bottom screen is not required for the spouted bed as apposed to the fluidized bed. Agglomeration of material often possibly found in other types of reactor (such as fluidized bed and rotary kiln) is minimized by the high circulation of material at the inlet nozzle. Unlike the fluidized bed furnace, the excessive burning of external surface of char particles is less likely encountered in the spouted bed activator because of its characteristic of short contacting time between activating gas and moving char particles. The spouted bed apparatus has no moving part, therefore, the construction and maintenance cost of the spouted bed activator might be low.

In several chemical processes, the understanding of hydrodynamic behavior and kinetic characteristics of reactor are necessary for the design and scaling up from laboratory to commercial scale. In recent years, computational fluid dynamic (CFD) simulation is one of the most popular techniques used to explore the hydrodynamic pattern and also the chemical kinetic characteristics in several chemical reactors. Therefore, CFD is now an established chemical process design tool which can provide complete information required for such design and scale up processes throughout the engineering profession with the cheapest cost and short design time. The modification of process equipment design (for both continuous and batch operation) is easy to achieve without increasing in the design cost. With these merits, the CFD technique will be used to simulate the hydrodynamic behavior and kinetic characteristics of the spouted bed activator studied in this work.

The CFD simulation uses numerical methods and additional algorithms to solve and analyze problems that involve fluid flows, heat transfer, and other related physical processes. It works by solving the set of equations of fluid flow (in a special form) over a region of interest along with particular characteristic conditions on the boundary of that region. The computer aided calculation technology is used to perform millions of calculations required to simulate the interaction of fluid-fluid and even fluid-solid for several complex systems commonly used in engineering applications. Presently, although the simplified governing equations used in CFD calculation have been proposed and high-speed supercomputers has been utilized, only approximate solutions can be achieved in many cases. Higher performance and more accurate CFD technique have been extensively developed by many researchers in the field.

The basic fundamental of CFD problem is the Navier-Stokes equations which define the motion of single phase fluid substances, including liquids and gases. These equations describe the change in momentum in infinitesimal volume of fluid by considering the sum of dissipative viscous forces, change in pressure, gravity and other forces acting inside the fluid. The Navier-Stokes equations being nonlinear partial differential equations when applied to almost any real situations are difficult or impossible to solve analytically. However, the Navier-Stokes equations can be simplified by removing terms that describe viscosity and heat conduction to obtain the Euler equations. By further simplification, terms describing vorticity can be removed to yield the full potential equations. Finally, these equations can be linearized to yield the linearized potential equations. Historically, the first CFD calculation was developed to solve these linearized potential equations for two-dimensional problems and then the three-dimensional calculation was put forward.

In this chapter, the aim of work is to study the CO₂ activation scheme of activated carbon prepared from palm shell char in the spouted bed activator by using the CFD simulation. The simulation was carried out for both hydrodynamic behavior and kinetic scheme of activation process occurring in the spouted bed activator. The study was separated into three main parts. The first part is concerned with the experimental study of hydrodynamics of spouted bed for air and palm shell char particles operated at room temperature. Pressure drop across the bed and total bed height of spouting bed were monitored as a function of increasing and decreasing air flow rate. The minimum spouting velocity was defined and determined from the velocity-pressure drop diagram. The effects of static bed height, conical base angle, air inlet diameter and palm-shell char particle size on the hydrodynamic behavior and

minimum spouting velocity of the spouted bed were investigated. The experimental results of pressure drop and minimum spouting velocity were compared with those calculated from CFD simulation under the same operating conditions. The CFD simulation of spouted bed of air-palm shell particles system was achieved by using the commercial CFD software package, ANSYS CFX 10.0.

For the second part, the preparation and characterization of activated carbons from palm shell char were studied in a cylindrical spouted bed reactor by using CO_2 as an activating agent. The effect of activation time on the porous characteristics (i.e. BET surface area, total pore volume, and pore size distribution) and char burn-off of produced activated carbons was investigated. These porous characteristics and char burn-off of produced activated carbons were compared with those of activated carbons obtained from the tube furnace reported previously. Finally, the CFD simulation results from the hydrodynamic study was used to simulate the CO_2 activation process of palm shell char in the spouted bed reactor by imposing the gasification reaction between CO_2 and solid chars into the CFD software. The CFD simulation program was run to generate the useful data of degree of char burn-off at several activation times and the kinetic characteristics of activation process of char in the spouted bed activator was explored. By fitting the experimental burn-off data of palm-shell char at the early stage of activation process (at the activation time of 30 min) with those computed from the CFD simulation, the effective rate constant of gasification reaction for CO_2 activation scheme could be initially estimated. This rate constant was then used for subsequent CFD calculation for char activation scheme at longer activation times up to 3.0 hrs. The predicted results for the degree of char burn-offs were then compared with the experimental data to test the validity of the CFD

technique in describing the activation process in the spouted bed activator. The porous properties of the produced activated carbons, including internal surface area and total pore volume, were then estimated by applying the structural activation model proposed in Chapter 4 using the computed char-burn-off obtaining from CFD simulation for several periods of activation times. These predicted surface area and total pore volume were compared with those obtained experimentally.

5.3 Review of the Literatures

Because of the distinct advantages in handling coarse particles and unique flow characteristics, the spouted bed has been applied in a wide range of physical operations such as drying (Mathur and Gishler, 1955; Devahastin and Mujumdar, 2001; Benali and Amazouz, 2006), coating and granulation (Vieira and Rocha, 2004; Paulo Filho et al., 2006). In recent years, increasing attention has been paid to the application of spouted beds as chemical reactors, including coal gasification reactors (Hoque and Bhattacharya, 2001; Adegoroye et al., 2004; Salam and Bhattacharya, 2006), fuel combustors (Konduri et al., 1999; Rasul, 2001; Vuthaluru and Zhang, 2001), pyrolysis reactors (Elordi et al., 2007a, 2007b; Arabiourrutia et al., 2007), catalytic partial oxidation reactors (Marnasidou, 1999), chemical vapor deposition (CVD) reactors (Juarez et al., 2003; Pan et al., 2006), and catalytic hydrocracking reactors (Al-Mayman and Al-Zahrani, 2003). In spite of its potential applications in many areas, limited amounts of work have been reported in the literature concerning the use of spouted bed as an activator for activated carbon production. Dalai et al. (1996) prepared activated carbons from Canadian coals using steam activation technique in a fixed bed and spouted bed reactors. They found that activated carbons

prepared in the spouted bed reactor had the same degree of surface area but lower density compared to those prepared in the fixed-bed system.

Spouted bed was originally invented by Mathur and Gishler (1955) at the National Research Council of Canada during the development of a technique for drying wheat. The spouted bed is an alternative to fluidized bed for handling coarse particles which is not amenable to fluidization. A schematic representation of the conventional spouted bed is shown Figure 5.1. Basically, the spouted bed column consists of two main parts, a conical base and a cylindrical vessel. The fluid, either gas or liquid, is introduced vertically through a single nozzle at the center of a conical or flat base. If the fluid injection rate is high and the bed height is low enough, the fluid stream will push through the bed as a spout in which the solid particles are rapidly carried upward to the top of bed by the fluid in a central well-defined core and form a fountain above the bed. After that, the solid particles will move uniformly downward in the annular surrounding the central core, providing a dense-phase. There also exists a countercurrent contact in the annular region between the solid particles and the fluid which escapes from the central core through the spout-annulus interface. A systematic cyclic pattern of solids movement is thus established, giving rise to a unique hydrodynamic system which is more suitable for certain applications than more conventional fluid-solid contacting equipment. Like the fluidized bed equipment, solid particles can be appended into and removed from the spouted bed, therefore, it can be performed in mode of continuous operation. The solid particles may be fed into the spouted bed either at the top near the wall, so that they join the downward moving mass of particles in the annulus, or with the incoming gas.

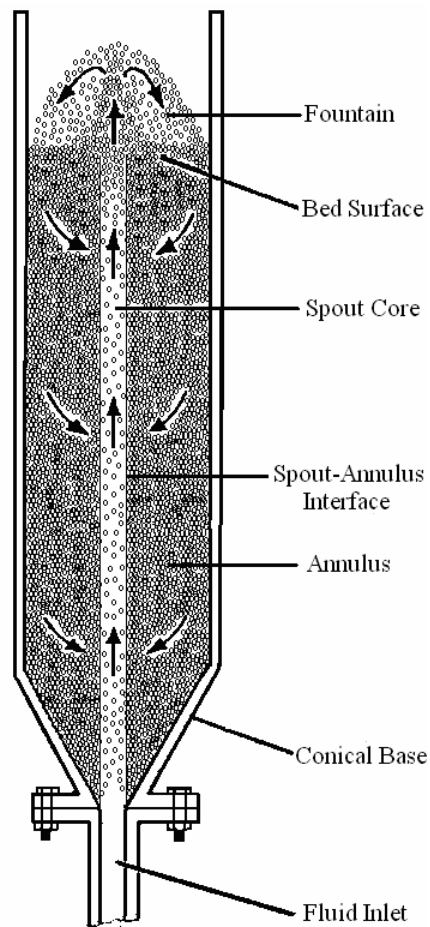


Figure 5.1 Schematic diagram of a conventional spouted bed
(Mathur and Epstein, 1974).

The mechanism of transition from a static to spouted bed can be described by considering the typical pressure drop-flow rate curves collected from air-wheat particles system which are shown in Figure 5.2 (Mathur and Epstein, 1974). The experimental data were determined for wheat particle size of 3.6 mm carried out in a spouted bed column with 15.2 cm of diameter, 1.27 cm of nozzle size and conical base angle of 60° . The solid line in the plot for static bed height of 30 cm (A-B-C-D) represents the pressure drop for increasing step of air flow rate and the dash line (D-

C*-B*-A) illustrates the reverse process of decreasing air flow. The change of hydrodynamic behavior of spouted bed for increasing air flow rate can be observed as the following sequences of events.

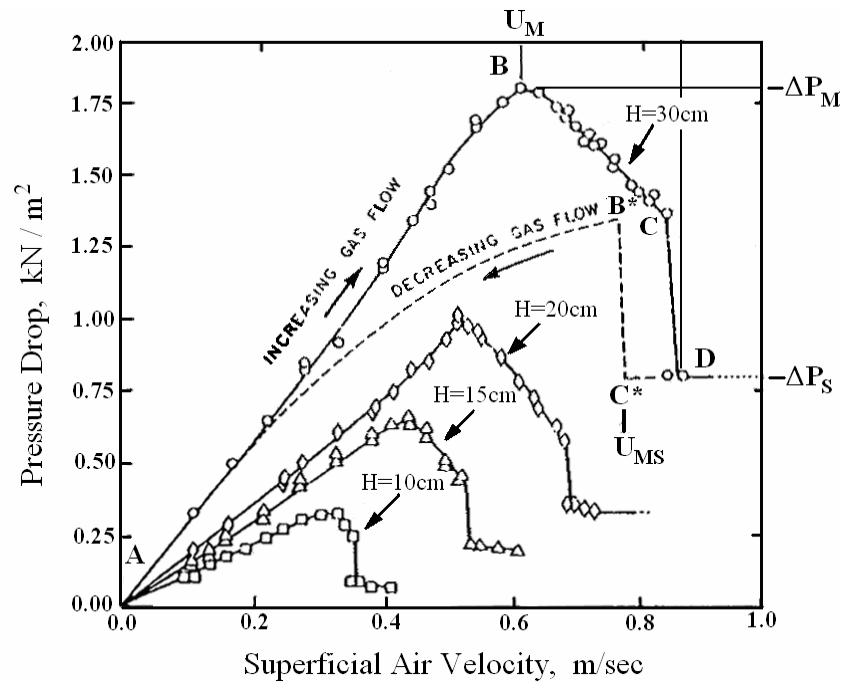


Figure 5.2 Typical pressure drop-flow rate curves of conventional spouted bed (Mathur and Epstein, 1974).

At low flow rate of fluid, the fluid just flows upward through the bed without disturbing the particles causing the linear increasing of pressure drop across the bed (along A-B) with rising of fluid flow rate. When the flow rate is increased to a certain value which is high enough, the solid particle is pushed up and a small empty cavity above the gas inlet is created. The particles surrounding the cavity are packed together against the upper particles and provide a compacted arch causing a greater resistance to fluid flow. With further increase in fluid flow, the cavity is lengthened steadily and

forms an internal spout. The arch of compacted particles still exists above the internal spout, so that the increase in pressure drop continues until it reaches a maximum value of $-\Delta P_M$ corresponding to superficial velocity of U_M (point B). As the flow rate is increased beyond point B at which the height of the central core become large relative to the above packed particles, the decreasing of pressure drop will be observed (along B-C).

Near point C, sufficient amount of solid particles has been displaced from the central core and a slight increase in flow rate of fluid will cause a noticeable expansion of the central core until point C is reached. At a slightly higher fluid flow rate from point C, the internal spout now breaks through the bed surface to form an initial spouting condition. At this stage, the particle concentration above the central core decreases suddenly, resulting in a sharp decline in pressure drop to point D, where the steady spouting condition is established and the entire bed starts moving. It should be noted that the pressure drop history for this increasing step of fluid flow is not exactly reproducible, depending on the packed condition of particle bed at initial static state, especially, for non-spherical particles (Mathur and Epstein, 1974). With continued increase in fluid flow rate, the supplementary fluid flowing through the spout zone will cause only the increase in fountain height without causing any significant change on the total pressure drop. Therefore, the pressure drop across the bed remains relatively constant and it is denoted as $-\Delta P_S$.

On slowly decreasing the fluid flow from point D, the bed remains in the spouted state until point C* which represents the minimum spouting action is reached. The superficial air velocity at this minimum spouting condition is denoted as *minimum spouting velocity*, U_{MS} . A slightly decreasing of fluid flow rate at U_{MS}

condition will cause the collapse of spout and the pressure drop then rises rapidly to point B*. With further reduction in fluid flow rate, the pressure drop across the bed decreases gradually along B*-A. However, the pressure drop curve now stays below that for increasing step of fluid flow rate. This is due to the fact that the energy expended by the fluid jet to penetrate the solid bed and expand the internal core is no longer required.

The hydrodynamic behavior and its stability of spouted bed depend largely on its geometric dimensions which are defined and shown in Figure 5.3, where H_B is the height of dense solid bed, H_F is the height of bed fountain, H_T is the total bed height ($H_B + H_F$), D_C and D_I are column and fluid inlet nozzle diameter, respectively, and θ is an angle of conical base.

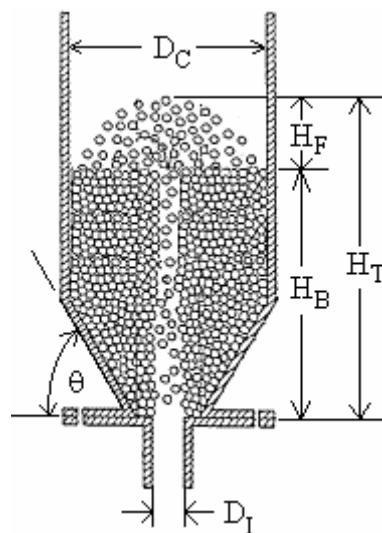


Figure 5.3 Geometric dimensions of a spouted bed column.

The hydrodynamic behavior of spouted bed and its stability have been studied and reported by many researchers. Mathur and Gishler (1955) proposed the simplest

equation to estimate the minimum spouting velocity, U_{MS} , with accuracy of $\pm 15\%$ for size of cylindrical vessel, D_C , up to about 0.5 m..

$$(U_{MS})_{0.5} = \left(\frac{d_p}{D_C} \right) \left(\frac{D_I}{D_C} \right)^{1/3} \sqrt{\frac{2gH_S(\rho_p - \rho_F)}{\rho_F}} \quad (5.1)$$

where H_S is static bed height, d_p is the mean solid particle diameter, ρ_p and ρ_F are densities of solid particle and fluid, respectively. For nonspherical particles, d_p is the equivalent sphere diameter having the same volume as the particle, and g is the gravitational acceleration.

For the cylindrical vessel with the size larger than 0.5 m ($D_C > 0.5$ m),

$$U_{MS} = 2.0D_C (U_{MS})_{0.5} \quad (5.2)$$

where D_C has the unit of meters.

King and Harrison (1980) proposed a modified version of Mathur and Gishler (1955) equation for the spouted bed operated at high operating pressures up to 20 bars, as the following

$$(U_{MS})_{0.5} = \left[\frac{\rho_F}{\rho_{air(p=1)}} \right]^{0.2} \left(\frac{d_p}{D_C} \right) \left(\frac{D_I}{D_C} \right)^{1/3} \sqrt{\frac{2gH_S(\rho_p - \rho_F)}{\rho_F}} \quad (5.3)$$

where $\rho_{air(p=1)}$ is the density of air at one atmosphere and room temperature.

It is well known that the spouting will be unstable when the initial static bed height is higher than a certain limit value denoted as *maximum spoutable bed height*, H_M . This unstable state of spouting could result from three individual mechanisms (Mathur and Epstein, 1974). Firstly, when the bed height is increased, the amount of fluid that leaks into the annulus zone through the spout core-annulus interface will be increased. This will cause the increasing of upward fluid flow rate in the annulus zone. If the flow rate of fluid in the annulus is high enough to fluidize the solid particles, the occurring fluidization will disturb the stability of the spouting. Secondly, the spouted bed will change to either bubbling fluidization or slugging bed when the bed is higher than the maximum spoutable bed height. Finally, higher static bed height will cause the instability growth of spout core. The spout core-annulus interface which is not a rigid surface will exhibit an observable rippling movement during the growth of spout core. The rippling movement of spout core-annulus interface becomes higher when the bed height is increased. It should be noted also that the maximum spoutable bed height becomes larger when the operating pressure is increased. Therefore, higher operating pressure provides the expansion of spoutability region of spouted bed (Yang, 2003).

The following empirical correlation can be used for estimating the maximum spoutable bed height (Epstein and Grace, 1997).

$$H_M = \frac{D_c^2}{d_p} \left(\frac{D_c}{D_t} \right)^{2/3} \frac{568b^2}{Ar} \left(\sqrt{1 + 35.9 \times 10^{-6} Ar} - 1 \right)^2 \quad (5.4)$$

where b is a constant. McNab and Bridgwater (1977) found that Equation (5.4) with $b = 1.11$ gave the best fit with the experimental data. However, for high temperature

applications, taking $b = 0.9$ is more suitable. The dimensionless variable, Ar , is Archimedes number defined as:

$$Ar = \frac{\rho_f (\rho_p - \rho_f) d_p^3 g}{\mu^2} \quad (5.5)$$

where μ is the viscosity of fluid.

The average diameter of spout core, D_s , has been correlated empirically and proposed as the following expression by McNab in 1972 for spouted bed operated at room temperature. In SI units, the equation reads (Yang, 2003)

$$D_s = \frac{2.00 G^{0.49} D_C^{0.68}}{\rho_B^{0.41}} \quad (5.6)$$

where G is the superficial mass flux of spouting fluid based on diameter of cylindrical vessel, and ρ_B is bed density or bulk density of bed. For high temperature operation, the dimensionally consistent semi-empirical equation of average spout diameter proposed by Wu et al. in year 1987 was suggested instead as the following (Yang, 2003)

$$D_s = 5.61 \left(\frac{G^{0.433} D_C^{0.583} \mu^{0.133}}{(\rho_F \rho_B g)^{0.283}} \right) \quad (5.7)$$

Bed voidage distribution in a cylindrical spouted bed was studied extensively by Olazar et al. (2001a). They used an optical fiber probe for measuring the local bed voidage in the spout core, annulus, and both fountain core and periphery (particle

downflow zone) of spouted bed. The effects of base angle, gas inlet diameter, static bed height, particle size, and gas velocity on longitudinal and radial profiles of bed voidage were investigated. They found that the bed voidage at the fluid inlet region was nearly unity and decreased in the radial and longitudinal directions. The factor that had the greatest influence on the bed voidage along the axis of the spouted bed was the total height of the spouting bed. There are significant differences between the bed voidage in the fountain core and fountain periphery. The bed voidage in the fountain core followed a trend similar to that in the spout core, while the bed voidage in the fountain periphery was clearly higher and almost independent of operating conditions. They also observed that the average bed voidage, either in the spout core or in the annulus zone, increased with increasing of static bed height.

Practically, it is difficult to monitor the moving characteristics of solid particles inside gas-solid two-phase flow operations (such as spouted bed, and fluidized bed), due principally to the existence of numerous colliding particles. Although the optical fiber probe can be used for monitoring the particle velocity profiles and its flow pattern (Olazar et al., 2001b) as well as bed voidage distribution (San Jose et al., 1998; Olazar et al., 2001a), the presence of the optical fiber probe may affect the flow field and it is almost impossible to observe the immediate flow field that fluctuates in unsteady state operation. In order to observe the solid motion at the central plane of spouted bed, He et al. (1994) measured the particle velocity in spouted beds with half-cylindrical vessels, using an optical fiber probe and compared the results with the case of full cylindrical vessel. They found that the flat wall of the half-cylindrical vessel interfered significantly on the velocity of particles. The particle velocity near that flat wall was much reduced.

In recent years, the advent of high performance computer aided calculation technology has made numerical simulations the most popular technique in the study of dense gas-solid two-phase flows system (such as spouted bed, fluidized bed, etc.). This technique is a useful tool to obtain detailed information on the hydrodynamic behavior of spouted bed or fluidized bed without performing direct measurement which could disturb the flow field. The most popular tool in performing numerical simulation of gas-solid two-phase flows is the computational fluid dynamic (CFD) technique.

The most popular CFD softwares that are typically used by many researchers in the CFD simulation of solid particle-fluid system are FLUENT and ANSYS CFX. Benyahia et al (2000) simulated a two-dimensional air-fluid catalytic cracking (FCC) particles flow behavior in the riser section of a circulating fluidized bed (CFB) by using FLUENT. Their simulation provided gas and particle flow profile data of velocities, volume fractions, pressure and turbulence parameters which agreed reasonably well with the experimental results. Taghipour et al. (2005) applied FLUENT in studying the hydrodynamic of a two-dimensional fluidized bed for air-glass beads (250-300 μm in diameter) system. They claimed the validation of CFD simulation for fluidized bed system by showing good agreement between their simulated results and experimental data (i.e. gas-solid flow pattern, voidage profile, pressure drop and minimum fluidization velocity) for both phases.

Witt et al. (1998) modeled the isothermal flow in 3-dimensional bubbling fluidized bed system by using ANSYS CFX. Lettieri et al. (2006) also used ANSYS CFX to simulate a liquid fluidized bed in slugging mode. Their CFD modeling gave the pressure drop which was greater than those obtained experimentally for all fluid

velocities. In addition to the fluidized bed and spouted bed system, CFD simulation can be applied for other complex gas-solid flow systems. Chu and Yu (2008) presented the CFD simulations of glass bead-air flow in three complex three-dimensional systems, including pneumatic conveying bend, gas cyclone and circulating fluidized beds (CFB), by using FLUENT. Their CFD simulation also generated hydrodynamic information which agreed well with the measured values.

Due to the reliability of CFD simulation in modeling hydrodynamic behavior of fluid-solid two phase flow system, there has been a growing interest in using CFD method to demonstrate a gas-solid contacting based reactor used in several chemical processes. Watanabe and Otaka (2006) employed the CFD modeling to predict the performance of an entrained flow coal gasifier. The reaction scheme considered in their model consisted of three processes which are pyrolysis, char gasification and gas phase reactions. Marschall and Mleczko (1999) had studied the simulation of an internally circulating fluidized bed reactor. They proved that the CFD model was able to explain the effect of different reactor designs and various hydrodynamic parameters on the flow fields.

5.4 CFD Model Description

In running the CFD simulation for gas-solid two-phase flow, two distinct multiphase flow approaches may be used, Lagrangian particle tracking multiphase model or discrete element method (DEM) and Eulerian-Eulerian multiphase flow model or two fluid model (TFM). The Lagrangian particle tracking multiphase model is capable of modeling dispersed phases which are discretely distributed in a continuous phase. The modeling involves separate calculation of each phase where

the two-way interactions between the dispersed and continuous phase will be considered. As to the Eulerian-Eulerian multiphase flow model, both fluid and solid particle phases are treated mathematically as interpenetrating continua using the concept of phase volume fraction. The phase volume fraction represents the space occupied by each phase and the sum is equal to unity. Both fluid and solid particle phase are assumed to satisfy the conservation laws of mass and momentum. The mean and fluctuating velocity of solid particles are described by the kinetic theory of granular flow (KTGF). Table 5.1 compares the characteristics of these two multiphase approaches.

The simulation of spouted bed system studied in this work consists of a large number of particles and in principle it is not necessary to know the complete information on the behavior and residence time of every particle in the system which can cause excessive calculation time. Further, the global flow pattern information is still sufficient to explore the hydrodynamic behavior of dispersed solid phase in the flow field. As a result, the two-fluid model was adopted in this work for performing the simulation task.

Details of the governing equations, including mass and momentum conservation equations, KTGF model, drag force correlations, and turbulence model, used in CFD calculation are briefly presented in the following section.

5.4.1 Conservation Equations of Mass and Momentum

For volume fraction balance equation, the sum of all phase volume fraction, X , is equal to unity, that is

$$X_F + X_P = 1 \quad (5.8)$$

where the subscripts F and P represent fluid and particle phases, respectively.

Table 5.1 Comparison between the two-fluid and particle transport models

Two-fluid model	Particle transport model
Provide complete global information for the particle phase.	Provide complete information on behavior and residence time of individual particles.
Many set equations are necessary for many particle sizes.	Easy to model a system consisting of a wide range of particle size.
Easy to include turbulent model.	Difficult to include turbulent model.
Cheaper calculation cost for system with large number of particles	Expensive calculation cost for system with large number of particles.

The mass conservation equations and equations of motion for fluid and dispersed solid phase can be expressed as the following in Cartesian coordinates.

$$\frac{\partial}{\partial t}(X_F \rho_F) + \frac{\partial}{\partial x}(X_F \rho_F U_x) + \frac{\partial}{\partial y}(X_F \rho_F U_y) + \frac{\partial}{\partial z}(X_F \rho_F U_z) = 0 \quad (5.9)$$

$$\frac{\partial}{\partial t}(X_P \rho_P) + \frac{\partial}{\partial x}(X_P \rho_P V_x) + \frac{\partial}{\partial y}(X_P \rho_P V_y) + \frac{\partial}{\partial z}(X_P \rho_P V_z) = 0 \quad (5.10)$$

where U and V are velocity components of the fluid and dispersed phase, respectively.

$$\frac{\partial}{\partial t}(X_F \rho_F \bar{U}) + \nabla \cdot (X_F \rho_F \bar{U} \bar{U}) = -X_F \nabla P + \nabla \cdot \overline{\overline{\tau}}_F + \overline{F}_{D,F} \quad (5.11)$$

$$\frac{\partial}{\partial t}(X_P \rho_P \bar{V}) + \nabla \cdot (X_P \rho_P \bar{V} \bar{V}) = X_P \nabla P + \nabla \cdot \overline{\overline{\tau}}_P + \overline{F}_{D,P} + \overline{F}_S + X_P \rho_P g \quad (5.12)$$

where \overline{F}_D is the interaction force between the fluid and dispersed phase (drag force) and \overline{F}_S is solid pressure force due to collision between solid particle and its neighbors. $\overline{\overline{\tau}}_F$ and $\overline{\overline{\tau}}_P$ are viscous stress tensor of continuous (fluid) and dispersed (particle) phase, respectively. The details on the calculation of these parameters will be discussed later.

The last term in Equation (5.12) represents the force exerted by gravity which is generally neglected for fluid phase (i.e. gas in this study) because the fluid phase has very low density, hence small gravity force in comparison with drag force and pressure gradient forces. In this investigation, smooth wall boundary condition is assumed for the wall of spouted bed column, thus the interaction force between the wall and particles or fluid phase (wall lubricant force) will not be considered. The buoyancy force acting on the solid particles is also neglected because of very low density character of the gas phase.

5.4.2 Kinetic Theory of Granular Flow (KTGF)

The kinetic theory of granular flow is an extension of the classical kinetic theory of dense gas. It has been developed based on statistical mechanics to describe the mean and fluctuating velocity of particles found in continuous granular media.

By an analogy with the kinetic theory of dense gas, which explains the pressure in gas to result from collision of gas particles with its neighborhood, the basic principle in the kinetic theory of granular flow has been developed (Lun et al., 1984; Gidaspow, 1994). The basic governing concept in the KTGF is that the particles are in a continuous and chaotic movement within the fluid phase. This chaotic random motion exists at both low concentration (due to drag force between gas and solid particles, gas turbulence and pressure variation in the fluid) and at higher concentration (due to an inelastic collisions of particles). The KTGF describes the dependence of the rheological properties of the moving particles on local particle concentration and the fluctuating motion of the particles.

In the KTGF, the actual particle velocity (V) is calculated from the combination of local mean velocity (V_M) and a random fluctuating velocity (V_f). This is

$$\vec{V} = \vec{V}_M + \vec{V}_f \quad (5.13)$$

In relation to the random motion of the particles and analogy to the definition of the thermodynamic temperature of a gas in the classical kinetic theory, the granular temperature (θ) for a group of particles can be defined as

$$\theta = \frac{1}{3} \langle \vec{V}_f^2 \rangle \quad (5.14)$$

where the bracket denotes ensemble averaging. The granular temperature is described by a separated conservation equation,

$$\frac{3}{2} \left[\frac{\partial}{\partial t} (\rho_p X_p \theta) + \nabla \cdot (\rho_p X_p \overline{V_M} \theta) \right] = - \left(F_s \overline{I} + X_p \overline{\tau_p} \right) : \nabla \overline{V_M} - \nabla \cdot (k_\theta \nabla \theta) - 3\beta\theta - \gamma \quad (5.15)$$

where the term $-\left(F_s \overline{I} + X_p \overline{\tau_p}\right) : \nabla \overline{V_M}$ is the generation of energy by the solid stress tensor, $k_\theta \nabla \theta$ is the diffusion of energy (k_θ is the diffusion coefficient), $-3\beta\theta$ is the energy exchange between fluid and solid phase (β is interphase momentum transfer coefficient calculated based on the Gidaspow drag model and it will be discussed later in details), \overline{I} is a unit tensor, and γ is the dissipation rate due to inelastic mutual particle collisions.

There are variables that must be defined and substituted into Equation (5.15) to solve for the granular temperature, including the dissipation rate (γ), solid pressure force (F_s), and viscous stress tensor solid phase ($\overline{\tau_p}$). First, γ can be expressed as the following expression.

$$\gamma = 3 \left(1 - e_{RC}^2 \right) X_p^2 \rho_p g_0 \theta \left[\frac{4}{d_p} \sqrt{\frac{\theta}{\pi}} - \left(\nabla \cdot \overline{V_M} \right) \right] \quad (5.16)$$

where e_{RC} is the restitution coefficient of particles. This coefficient is a fractional value representing the ratio of velocities before and after the collision of particles. A particle with the restitution coefficient equal to unity collides elastically with another particle, while a particle with restitution coefficient of zero will collide inelastically with its neighbor. The influence of e_{RC} on CFD simulation of the spouted bed had been studied by Du et al. (2006). They found that the simulation results are sensitive

to the value of e_{RC} . Increasing the value of e_{RC} leads to the decreasing in fountain height and slightly improves the stability of the spout shape. The variable g_0 is the radial distribution function expressed by Gidaspow (1994) as

$$g_0(X_P) = 0.6 \left[1 - \left(\frac{X_P}{X_{P,Max}} \right)^{1/3} \right]^{-1} \quad (5.17)$$

It is noted that the radial distribution function goes to infinity when solid volume fraction is approaching the maximum particle packing volume fraction ($X_{P,Max}$). This limitation is resolved in ANSYS CFX 10.0 by setting:

$$g_0(X_P) = C_0 + C_1(X_P - X_C) + C_2(X_P - X_C)^2 + C_3(X_P - X_C)^3 \quad (5.18)$$

where $X_C = X_{P,Max} - 0.001$, $C_0 = 1079$, $C_1 = 1.08 \times 10^6$, $C_2 = 1.08 \times 10^9$ and $C_3 = 1.08 \times 10^{12}$

The solid pressure force (F_s in Equation (5.15)) can be expressed as a function of granular temperature. That is,

$$F_s = \rho_P X_P \theta \left[1 + 2(1 + e_{RC}) g_0 X_P \right] \quad (5.19)$$

The solid phase viscous stress tensor ($\overline{\tau_p}$) in Equation (5.12) and Equation (5.15) can be expressed by the following expression,

$$\overline{\overline{\tau}}_p = - \left[\left(\lambda_p - \frac{2}{3} \mu_p \right) (\nabla \cdot \overline{\mathbf{V}}_M) \overline{\mathbf{I}} + \mu_p \left[(\nabla \overline{\mathbf{V}}_M) + (\nabla \overline{\mathbf{V}}_M)^T \right] \right] \quad (5.20)$$

where the superscript T represents the transpose operation and λ_p is the solid bulk viscosity given by Lun et al. (1984) as

$$\lambda_p = \frac{4}{3} X_p^2 \rho_p d_p g_0 (1 + e_{RC}) \sqrt{\frac{\theta}{\pi}} \quad (5.21)$$

where μ_p is the shear viscosity expressed as a summation of two contributions, kinetic ($\mu_{p,Col}$) and collision ($\mu_{p,Kin}$) contributions. Thus,

$$\mu_p = \mu_{p,Col} + \mu_{p,Kin} \quad (5.22)$$

There is a general agreement on the appropriate form of the collision contribution. As in the kinetic theory of gases, it is taken to be proportional to the square root of the granular temperature (Ding and Gidaspow, 1990).

$$\mu_{p,Col} = \frac{4}{5} X_p^2 \rho_p d_p g_0 (1 + e_{RC}) \sqrt{\frac{\theta}{\pi}} \quad (5.23)$$

The kinetic contribution term is given by Lun and Savage (1986) to be

$$\mu_{p,Kin} = \frac{5\sqrt{\pi}}{96} \rho_p d_p \left(\frac{1}{\eta g_0} + \frac{8}{5} X_p \right) \left(\frac{1 + [(8\eta(3\eta - 2) X_p g_0)/5]}{2 - \eta} \right) \sqrt{\theta} \quad (5.24)$$

where $\eta = (1 + e_{RC})/2$

5.4.3 Turbulence Model

Turbulence plays an important role on the characteristics of the flow when chaotic three-dimensional vorticity exists randomly in the flow field. It occurs when the inertia forces in the fluid become significant compared to viscous forces for fluid flow at high Reynolds number. When turbulence is present, it affects all flow phenomena, including the increase in energy dissipation, mixing, heat and mass transfer, and drag force. For this reason, the effect of turbulence on the flow field needs to be predicted in most CFD simulations.

In this CFD simulation, the turbulence predictions of the continuous phase are carried out using the standard k-epsilon model proposed by Jones and Launder (1972). It is the most prominent turbulent model implemented in most general purpose CFD codes. This turbulent model has proven to be stable and provides a well predictive capability. In k-epsilon model, k is the turbulence kinetic energy and is defined as the variance of the fluctuations in velocity. It has dimensions of (length² time⁻²), e.g. m²/s² in SI unit. Epsilon (ϵ) is the turbulence eddy dissipation (the rate at which the velocity fluctuations dissipate) and has dimensions of k per unit time (length² time⁻³), e.g. m²/s³ in SI unit. .

The values of k and epsilon (ϵ) appear in the differential transport equations for the turbulence kinetic energy and turbulence dissipation rate:

$$\frac{\partial}{\partial t}(X_F \rho_F k) + \nabla \cdot (X_F \rho_F \bar{U} k) = \nabla \cdot \left(X_F \left(\mu + \frac{\mu_t}{\sigma_k} \right) \nabla k \right) + X_F P_k - X_F \rho_F \epsilon \quad (5.25)$$

$$\begin{aligned}
& \frac{\partial}{\partial t}(X_F \rho_F \varepsilon) + \nabla \cdot (X_F \rho_F \vec{U} \varepsilon) \\
& = \nabla \cdot \left(X_F \left(\mu + \frac{\mu_t}{\sigma_\varepsilon} \right) \nabla \varepsilon \right) + X_F \frac{\varepsilon}{k} (C_1 P_k - C_2 \rho_F \varepsilon)
\end{aligned} \tag{5.26}$$

where C_1 , C_2 , σ_ε and σ_k are constants which have the values of 1.44, 1.92, 1.3 and 1.0, respectively. μ is the fluid molecular (dynamic) viscosity and μ_t is the fluid turbulent viscosity defined as:

$$\mu_t = C_\mu \rho_F \frac{k^2}{\varepsilon} \tag{5.27}$$

where C_μ is a constant and its value is 0.09.

The term P_k is the turbulence production due to viscous and buoyancy forces, which is modeled using the relation,

$$P_k = \mu_t \nabla U \cdot (\nabla U + \nabla U^T) - \frac{2}{3} \nabla \cdot V (3\mu_t \nabla \cdot U + \rho_F k) - \frac{\mu_t}{\rho_F Pr} g \cdot \nabla \rho_F \tag{5.28}$$

where Pr is turbulent Prandtl number defined as:

$$Pr = \frac{C_p \mu_t}{\phi} \tag{5.29}$$

where C_p is the fluid specific heat capacity at constant pressure and ϕ is the thermal conductivity.

The viscous stress tensor for the continuous phase ($\overline{\overline{\tau_F}}$) appearing in the conservation equation of momentum for fluid phase (Equation (5.11)) and the conservation equation of granular temperature (Equation (5.15)) can be determined from the following expression.

$$\overline{\overline{\tau_F}} = -\frac{2}{3}(\rho_F k + \rho_F \mu_t \nabla \cdot \overline{\overline{U}}) \overline{\overline{I}} + \rho_F \mu_t (\nabla \cdot \overline{\overline{U}} + \nabla \cdot \overline{\overline{U}}^T) \quad (5.30)$$

5.4.4 Drag Force Model

The drag force exerted on an immersed body by a moving fluid arises from two mechanisms. Firstly, the drag is caused by the viscous shear stress denoted as the skin friction. The second form is due to the pressure distribution around the immersed body, and is called the form drag. The total drag force is most conveniently expressed in terms of the dimensionless drag coefficient, C_D . For a particle of simple shape, such as a sphere, immersed in a Newtonian fluid and is not rotating relative to the surrounding free fluid stream, the drag coefficient depends only on the particle Reynolds number, Re_p . The function $C_D(Re_p)$ may be determined experimentally, and is known as the drag curve.

The drag force acting on a particle, $F_{D,P}$, in fluid-dispersed solid system can be represented by the product of the interphase momentum transfer coefficient, β , and the slip velocity, $(U - V)$, between the two-phase. That is

$$F_{D,P} = \beta(U - V) \quad (5.31)$$

Note that the drag force acting on the continuous phase by dispersed phase, $F_{D,F}$, are equal and has opposite direction to $F_{D,P}$.

Gidaspow et al. (Ding and Gidaspow, 1990) employed the Ergun equation (Ergun, 1952) for calculating the interphase momentum transfer coefficient (β) for dense phase and the Wen-Yu equation (Wen and Yu, 1966) for dilute phase.

$$\beta_{Dense} = 150 \frac{X_P^2 \mu}{X_F d_p^2} + 1.75 \frac{X_P \rho_F}{d_p} |U - V| \quad \text{for } X_F < 0.8 \quad (5.32)$$

$$\beta_{Dilute} = \frac{3}{4} C_D \frac{X_P \rho_F}{d_p} |U - V| X_F^{-2.65} \quad \text{for } X_F \geq 0.8 \quad (5.33)$$

where the drag coefficient, C_D , was expressed by

$$C_D = \begin{cases} \frac{24}{X_F \text{Re}_p} \left[1 + 0.15 (X_F \text{Re}_p)^{0.687} \right] & \text{for } \text{Re}_p < 1000 \\ 0.44 & \text{for } \text{Re}_p \geq 1000 \end{cases} \quad (5.34)$$

and the particle Reynolds number is defined as

$$\text{Re}_p = \frac{\rho_F |U - V| d_p}{\mu} \quad (5.35)$$

5.4.5 Kinetics of Activation Reaction

The kinetic scheme of activation process of palm-shell char with CO₂ taken place in a spouted bed activator is calculated based on the concentration distribution of all substances, including reactants (carbon and CO₂) and gaseous

product (CO). These concentration profiles are calculated using CFD modeling. The following assumptions are applied in this simulation.

- There exists only one reaction between carbon atom and CO₂ and there is no secondary reaction among the gaseous components.



- The system was considered to be isothermal. Therefore, there is no effect of heat transfer on the kinetics of gasification reaction.
- The reaction is kinetically controlled without the effect of mass transfer resistance.

In a spouted bed activator, the mass of char per unit volume of activator is very high compared to the amounts of CO and CO₂. With this reasoning, it is reasonable to assume that the amount of char is excess relative to that of CO₂ during the activation reaction and therefore its amount will not affect the progress of kinetic scheme. Because high flow rate of CO₂ is fed into the spouted bed activator, the amount of CO generated during activation process should be quickly removed from the reaction zone by the flowing gas. Therefore, the rate of gasification reaction shown in Equation (5.36) can be practically expressed based on the first-order kinetics with respect to molar concentration of carbon dioxide for all regions in the spouted bed system, including annulus zone, spout core and fountain. That is,

$$\text{Gasification Rate} = K[CO_2] \quad (5.37)$$

where K is the overall effective rate constant and $[CO_2]$ is the molar concentration of CO_2 in gas phase in unit of mole/m³. This concentration refers to the average value for each numerical grid distributed in the spouted bed activator. The amount of char and CO_2 consumed, including the generation of CO , are calculated individually for each numerical grid and the overall kinetic scheme is calculated from the contribution of all numerical grids.

It should be noted that, for the Eulerian-Eulerian multiphase flow (two fluid approach) employed in this work, the option for multiphase reaction is not available for the current release of the commercial CFD software used, CFX 10.0. The char activation process for the preparation of activated carbon involves the multiphase reaction (i.e. gasification) between oxidizing gas (i.e. carbon dioxide) and carbon rich solid phase (i.e. palm-shell char). Therefore, in the model setting, the solid char will be assumed to convert first to an intermediate matter denoted as IC . This intermediate matter has density and molecular weight being equal to solid char but its transport property (i.e. dynamic viscosity) will be that of the gas phase. This intermediate matter is allowed to react with the oxidizing gas instead of solid char. The generation rate of intermediate matter is set to equal the rate of gasification reaction. Thus, the rate of generation and consumption of the intermediate matter will be the same, giving no accumulation in the spouted bed activator system. The rate of activation reaction scheme used in the CFD simulation can be rewritten as the following expressions.



5.4.6 Simulation Procedure

The simplified flow sheet for the simulation algorithm is displayed in Figure 5.4. The calculation procedure commences by setting the initial and boundary conditions. Some unknown system variables, such as turbulent quantities (i.e. turbulence kinetic energy and turbulence eddy dissipation), require the initial guess for the first step of calculation. The initial guesses of these system variables are given automatically by commercial CFD software used (ANSYS CFX 10.0). The conservation equation of momentum is first solved using SIMPLEC (Semi-Implicit Method for Pressure-Linked Equations-Consistent) algorithm which uses the pressure distribution and velocity components from the previous iteration or initial and boundary conditions to obtain new corrected pressure and velocity data of both phases and then they will be updated and used in the next calculations. Details on the SIMPLEC algorithm can be found in the recent book of Versteeg and Malalasekera (1995). Next, the conservation equation of mass is solved to obtain volume fraction (X_p and X_f) and mass flow rates for both phases. Finally, other governing equations are then solved, including turbulence model, drag force model, and KTGF model to obtain the other remaining system variables. The Gidaspow drag model is solved to calculate the interphase momentum transfer coefficient (β) which will be used in the calculation of KTGF model and drag force ($\overline{F_{D,p}}$ and $\overline{F_{D,f}}$). The KTGF model is then solved to obtain granular temperature (θ) used for the determination of the viscous stress tensor of solid phase ($\overline{\tau_p}$) and solid pressure force ($\overline{F_s}$). Next, the viscous stress tensor of fluid phase ($\overline{\tau_f}$) is calculated from the turbulent model of standard k-

epsilon model. Finally, the calculated solutions are checked for the convergence criteria or final steady-state condition.

The convergence or final steady-state criterion of simulated system is achieved by considering the RMS of residual values of the governing equations used in CFD simulation. The residual value is calculated as the inequality between the two sides of governing equations (see model description section). This residual is caused by the truncated error of the numerical computation and the differences of computed values resulted from the iteration scheme. All the RMS of residual values of all physical parameters (such as velocity components, particle concentration, pressure, ..., etc.) are set as 10^{-5} . This means that if the RMS of residual value is lower than 10^{-5} , the iteration is considered convergent or the steady-state condition is achieved. The RMS of residual is calculated from the following equation:

$$\text{RMS of Residual } \langle r_{rms} \rangle = \sqrt{\frac{1}{n} \sum_{i=1}^n r_i^2} \quad (5.40)$$

where r_i is the residual value collected from n control volume of all numerical grids.

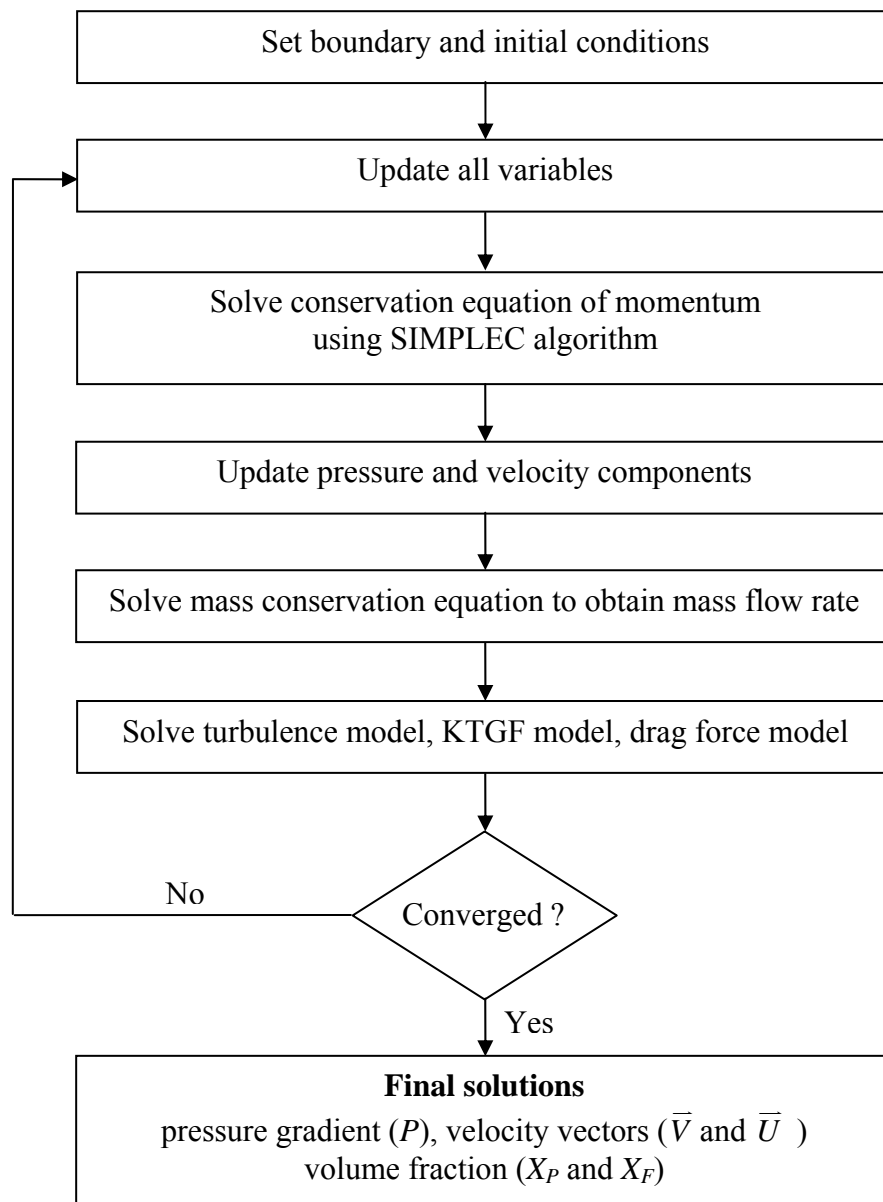


Figure 5.4 Flow sheet of the CFD simulation algorithm.

5.5 Research Methods

5.5.1 Experimental Study of Spouted Bed Hydrodynamics

This part of work involves the study of hydrodynamic behavior of spouted bed using air as the spouting fluid and oil-palm shell char particle as the

dispersed solid phase. The hydrodynamics was characterized by monitoring pressure drop across the bed and developed bed height as a function of increasing and decreasing of air flow rate. The influence of geometric factors (including conical base angle and fluid inlet nozzle size) and initial static bed height on the hydrodynamic behavior and minimum spouting velocity was investigated.

The experimental procedure was started with the preparation of oil-palm shell char particles. The raw palm shell, solid waste produced from a palm oil milling process, was supplied by Golden Palm Industry Co., Ltd in Chon Buri, Thailand. This received palm shell was first washed and dried at 150°C for 24 hrs to remove moisture content adsorbed during the land dumping process. The pre-dried palm shell was crushed and sieved to obtain the average size fractions of 0.5 mm (30×40 mesh), 0.7 mm (20×30 mesh), and 1.4 mm (12×16 mesh) and then kept in a desiccator for subsequent experiments.

The prepared palm shell sample was carbonized in a laboratory ceramic tube furnace (Carbolite CTF 12/75/700, 6 cm in diameter and 100 cm in length) to produce char. For this experiment, about 30 g of palm-shell particles were placed in a ceramic boat and then put into the tube furnace and heated up from room temperature to the desired carbonization temperature of 600°C at the heating rate of 10°C/min and held at this temperature for 2.0 hrs. The final char yield obtained was about 30% by weight. The carbonization temperature chosen was well above the main devolatilization temperature (as reported in Chapter 2) to ensure that a carbon-rich char was obtained. During carbonization process, ultra high purity grade nitrogen (UHP, 99.995% purity) at constant flow rate of 100 cm³/min was used as the sweeping gas to provide an inert atmosphere for pyrolysis and to remove any gaseous

and condensable products emitted. This nitrogen gas was supplied by Thai Industrial Gas Pub Co., Ltd (TIG) in Rayong, Thailand. When the carbonization was completed, the sample was allowed to cooled down to room temperature under the flow of N₂.

The spouted bed column was made from stainless steel (grade 304) for the conical base and acrylic plastic column for the cylindrical section. The geometric dimensions of spouted bed column are: 44 mm of column inside diameter, 5 and 7 mm for air inlet size, and 45° and 60° for conical base angle. A U-tube manometer was fabricated from glass tubing and filled with CCl₄ for measuring pressure drop across the spouted bed. One end of the manometer was connected to the air inlet pipeline just below the nozzle opening and the other was exposed to the atmosphere. The experimental procedure for hydrodynamic study was started by packing the palm shell char particles to the initial static bed height in the range of 5 to 10 cm. For each condition, compressed air was allowed to flow into the spouted bed at gradually increasing of air flow rate. Pressure drop across the bed and developed bed height at each air flow rate were noted until the fully spouting state was observed. After that, the air flow rate was gradually decreased to zero and the change of pressure drop was monitored. The minimum spouting velocity is defined here as the minimum air velocity at which the particle bed still remains in spouting condition for the step of decreasing air flow.

5.5.2 Preparation of Activated Carbons in the Spouted Bed Activator

In this part, the work covered the preparation of activated carbons from oil-palm shell in the spouted bed activator. The influence of activation time on the degree of char burn-off and porous characteristics of produced activated carbons, including internal surface area and total pore volume, was studied.

The palm shell char particles prepared in the previous part of hydrodynamic study with the average size of 0.5 mm were activated with high purity grade CO₂ (HP, 99.95% purity) in a stainless steel spouted bed activator (grade 310S). The geometric dimensions of this spouted bed activator are: 30 cm in length and 4 cm in column diameter, 7 mm of nozzle inlet diameter and 60° of conical base angle. Figure 5.5 shows the schematic diagram of the spouted bed activator. About 30 g of fresh palm-shell char particles were put into the column to the initial static bed height of 4.0 cm which was the only height used for running the spouted bed activation experiment as a function of activation time. The flow of 100 cm³/min of UHP grade N₂ was fed into the spouted bed activator for 30 min at room temperature to ensure that the char sample was truly under the inert atmosphere. Next, the activation process was started by heating up the char sample from room temperature to the desired activation temperature of 900°C at a heating rate of 10°C/min under the constant flow of N₂.

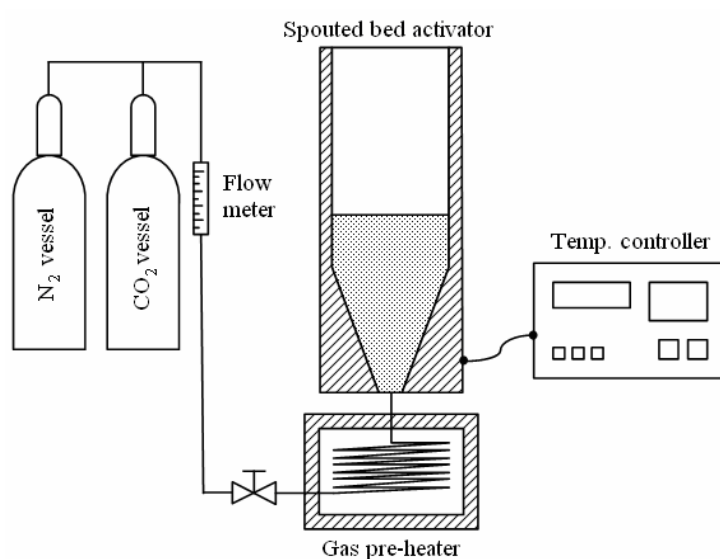


Figure 5.5 Schematic diagram of spouted bed activator.

When the desired activation temperature was reached, the gas was switched from N₂ to CO₂ to start the activation process by gasification reaction. The CO₂ flow rate was selected at the fluid velocity of 1.2 times the minimum spouting velocity (0.182 m/s of superficial velocity). The minimum spouting velocity was measured experimentally at 900°C based on the experimental pressure drop-gas flow data which was found to be 0.152 m/s of superficial velocity based on cylindrical cross-sectional area. When the activation step was completed, the char sample was cooled down to room temperature under the constant flow of N₂. The activated carbon produced at each period of activation time was weighed and kept in a desiccator for further characterization of its porous properties. The percentage of char burn-off was calculated from the following expression.

$$\% \text{ Char burn-off} = \frac{W_{Char} - W_{AC}}{W_{AC}} \times 100\% \quad (5.41)$$

where W_{Char} and W_{AC} are the initial weight of char and the final weight of activated carbon produced, respectively.

Six values of activation times (0.5, 1.0, 1.5, 2.0, 2.5, and 3.0 hrs) were employed to obtain activated carbons with different char burn-offs. It was noted that, for relatively shallow bed height used in this work, the application of too high the gas velocity would induce a violent motion of particles without the establishment of uniform spouting pattern. For this reason, it was decided to operate the spouted bed activator at the gas velocity near the U_{MS} . Therefore, in this work the spouted bed activator was operated at 1.2 times the minimum spouting velocity of CO₂.

Porous properties of the derived activated carbons were determined from the adsorption isotherm data of N₂ at -196°C, acquired with the Accelerated Surface Area and Porosimetry Analyzer (ASAP2010, Micromeritics, USA). The BET surface area was estimated from adsorption isotherm data of nitrogen by applying the Brunauer-Emmett-Teller (BET) equation (Do, 1998), assuming the value of 0.162 nm² for cross-sectional area of N₂ molecule. The total pore volume was computed from the volume of nitrogen adsorbed at a relative pressure of 0.99 and converted this value to the volume of N₂ in liquid state at -196°C. Micropore volume and area were calculated by applying the Dubinin-Astakhov (DA) equation (Do, 1998). The true density of prepared activated carbon, which is an important parameter for using in the CFD simulation, was measured by a pycnometer (Micromeritics AccuPyc 1330). The determined char burn-off and porous properties of produced activated carbons were compared with the activated carbons prepared in the tube furnace reported in the previous chapter (Chapter 3).

5.5.3 CFD Simulation of Spouted Bed Hydrodynamics

The aim of this section is to apply CFD simulation technique to simulate the hydrodynamic behavior of spouted bed under conditions similar to the experimental study. The capability of CFD model prediction was confirmed by comparing the simulated results of pressure drop and minimum spouting velocity with those obtained by direct measurement.

The CFD simulation of spouted bed hydrodynamics was performed by using the Eulerian-Eulerian multiphase flow model (two-fluid model) incorporated in the commercial CFD software package, ANSYS CFX 10.0. The set of governing equations, as shown in the previous section of model description, was solved by a

finite control volume method. Generally, the computation of CFD modeling was started by creating numerical grids in the chosen system geometry. In this study, the numerical grid was generated by using commercial engineering CAD software, ANSYS Workbench 10.0.

Because of the significant difference in the velocities of both gas and solid phases within the three regions of spouted bed (Mathur and Epstein, 1974), it is logical to construct the numerical grids with different size for each zone. The velocities of gas and solid phase are maximum in the spouting core and minimum in the annulus zone. Due to the rapid change of velocity at the spout core and annulus interface, care must also be taken in the generation of numerical grids in this region. Therefore, small numerical grid size was used in the vicinity of spouting core region (near the central core of column) and larger grid size can be employed in the expected annulus zone and empty zone above the solid bed to reduce the calculation time. In this simulation, the minimum and maximum numerical grid sizes were 0.5 and 2.0 mm, respectively. The numerical grid distribution of spouted bed used in this work is shown as in Figure 5.6.

In running the CFD simulation, the following initial and boundary conditions were employed:

- For initial condition, the system was assumed to consist of static bed of spherical palm-shell char particles with volume fraction of 0.6 and the velocity of air is set to be zero. The initial system pressure is set to be constant at 1.0 atm.
- At air entrance, the gas was injected only in the axial direction with zero velocity gradient (plug flow boundary condition).

- At air outlet, the column is exposed to ambient pressure with no velocity gradient of air (static condition).
- On the wall, a non-slip boundary condition was assumed for both gas and solid phase.

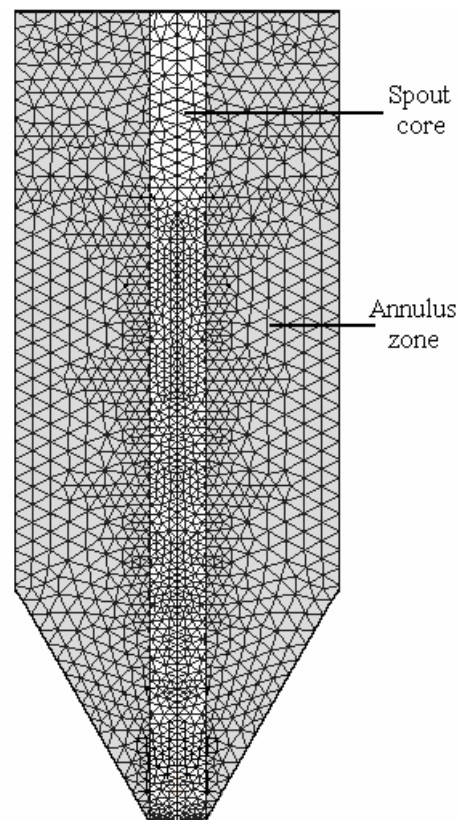


Figure 5.6 Numerical grids of spouted bed used in CFD simulation.

The CFD simulation in this section was computed using a time step of 10^{-5} sec until the steady-state condition was attained. The corresponding experimental conditions, including geometric factors, properties of dispersed and fluid phases and simulation parameters are listed in Table 5.2. The simulations were performed for air inlet velocity varying in the range of 0-1.7 times the minimum spouting velocity. The

expected results generated from CFD simulation were pressure gradient data, pressure drop across the bed, velocity profiles of gas and solid phases, concentration profile of gas and solid phases, and the minimum spouting velocity.

Table 5.2 Simulation parameters for CFD simulation of spouted bed.

Parameters	Description	Value
ρ_p (kg / m ³)	Solid density	980
ρ_f (kg / m ³)	Air density (25°C)	1.185
μ_f (kg / m.s)	Air viscosity (25°C)	1.831×10^{-5}
d_p (mm)	Particle diameter	0.70
e_{RC}	Particle restitution coefficient	0.90
$X_{P,Max}$	Maximum particle packing volume fraction	0.60
H_s (cm)	Static bed height	7.2
D_I (cm)	Inlet nozzle diameter	0.7
D_C (cm)	Column diameter	4.40
θ	Conical base angle	60°

5.5.4 CFD Simulation of Spouted Bed Activator

The CFD software package, ANSYS CFX10.0 was also used to simulate the CO₂ activation process of palm shell chars in the spouted bed activator. This simulation was run by employing the same simulation parameters and boundary conditions as in the case of CFD simulation of hydrodynamic study. However, the fluid phase was changed from air to the gas mixture of CO₂ and CO occurring from the gasification reaction of carbon mass and CO₂. The geometric dimensions of

spouted bed used in the simulation were those of the experimental spouted bed activator. In this respect, the percentage burn-offs of char was calculated as a function of activation time as follows. First by matching the burn-off results from simulation with those from experiments at the short activation time of 0.5 hrs, the effective first-order rate constant for the gasification reaction between CO₂ and palm-shell char could be estimated. This rate constant was then used for further CFD simulation to compute the degree of char burn-off at longer activation time up to 3.0 hrs. These calculated char burn-offs were compared with those measured directly from the experimental runs to test the capability of the CFD modeling in describing the activation process in the spouted bed activator.

The CFD simulation was performed at a time step interval of 10^{-4} s. The numerical grid size created was the same as that used in the previous part of hydrodynamic study. The simulation parameters used are listed in Table 5.3.

Table 5.3 Simulation conditions for CFD simulation of spouted bed activator.

Parameters	Description	Value
ρ_p (kg / m ³)	Solid density	980
ρ_f (kg / m ³)	CO ₂ density (900°C)	0.458
μ_f (kg / m.s)	CO ₂ viscosity (900°C)	1.490×10^{-5}
d_p (mm)	Particle diameter	0.50
e_{RC}	Particle restitution coefficient	0.90
$X_{p,Max}$	Maximum particle packing volume fraction	0.60
H_s (cm)	Static bed height	4.0
D_i (cm)	Inlet nozzle diameter	0.7
D_c (cm)	Column diameter	4.0
θ	Conical base angle	60°

5.6 Results and Discussion

5.6.1 Hydrodynamic Study of Spouted Bed

The pressure drop across the bed and total bed height were measured as a function of increasing and decreasing air flow rate and are shown in Figure 5.7 to 5.31 for mean particle sizes of 0.5, 0.7, 1.4 mm and various initial static bed heights and geometric factors (i.e. conical base angle and gas inlet diameter). These figures show that the behavior of pressure drop-air flow rate curve is different from those reported by Mathur and Epstein (1974) for the case of wheat particles (see Figure 5.2). This difference should be due to the differences in their nature of particle shape and outer surface characteristic of palm-shell char and wheat which affect directly on packing characteristic of particles in the bed and hence the friction between neighboring particles. The palm-shell char consists of highly irregular shaped particles with distribution of sizes, while the wheat particles have rather uniform size and shape.

The transition behavior from a static to spouting condition of air-palm shell char particle system can be observed by considering the typical pressure drop-air flow rate diagram presented in Figure 5.7 for particle size of 0.5 mm, air inlet diameter of 7.0 mm, base angle of 60° and 6.30 cm of initial static bed height. The air superficial velocity shown in the figure was calculated based on cross-section area of cylindrical vessel of spouted bed. The bed heights shown in the figure include height of dense solid bed (H_B) and total height of spout bed ($H_T = H_B + H_F$) for increasing air flow.

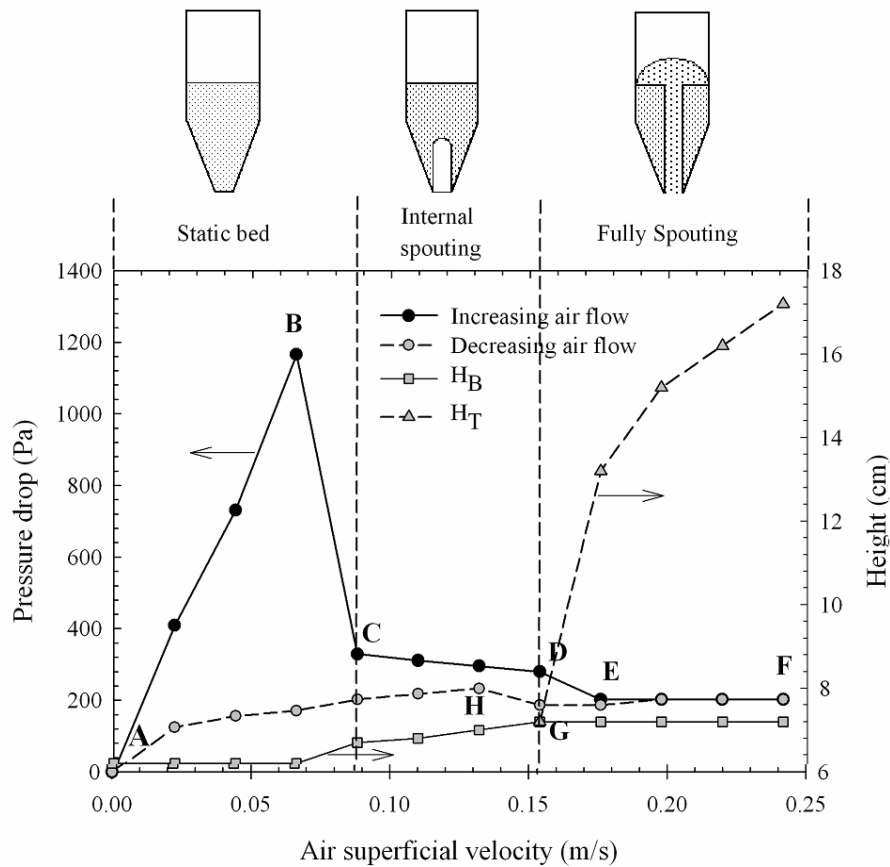


Figure 5.7 Typical pressure drop–flow rate diagram and bed height for increasing air flow of spouted bed for $D_I = 7.0$ mm, d_p of 0.50 mm, $\theta = 60^\circ$ and $H_S = 6.3$ cm.

At low flow rates, air just flows upward through the bed without disturbing the particles causing linear increasing of pressure drop across the bed (along A-B) and reaching the maximum value at point B. With further increasing of air flow rate, the bed is suddenly pushed up causing an expansion of bed (along B-C). The bed now becomes loosely packed so that there is a dramatic reduction of bed pressure drop from point B to point C. By continued increasing of air flow rate, the bed is now steadily expanded and the pressure drop continues to decline along C-D.

Further increasing of air flow rate from point D will initiate the spouting of solid bed and a slight drop of pressure drop to point E can be observed. The increasing of air flow rate from point E on will lengthen only the height of fountain with no consequent effect on the height of dense bed (H_B) and pressure drop across the bed (along line E-F).

On the decreasing of air flow rate, the pressure drop is still constant from point F to G. At this point, the spouting condition is still observed but further decreasing of air flow rate from point G will cause the collapse of spouting state back to the static bed condition and bring the pressure drop to a higher value at point H. The minimum air velocity that still maintains the spouting phenomenon of bed particles on decreasing air flow (point G in Figure 5.7) is defined here as the minimum spouting velocity (U_{MS}). With further decreasing in air flow rate, the pressure drop decreases steadily to point A (no feeding of air) and the bed height still remains constant along line H-A in Figure 5.7.

It should be observed that the measured pressure drop at low flow rate of air before the initial expansion of particle bed was not reproducible (along line A-B in Figure 5.7). The value of pressure drop depends specifically on initial packing condition of char particles. However, at air flow rates higher than the point that the bed has been expanded (point B), the measured pressure drop was repeatedly reproducible. Therefore, at low air flow rates, the pressure drop for each experimental run was measured for at least 3 times (starting with new particle loading for each time) and their values at a given air flow rate were averaged to obtain the representative pressure drop for that condition.

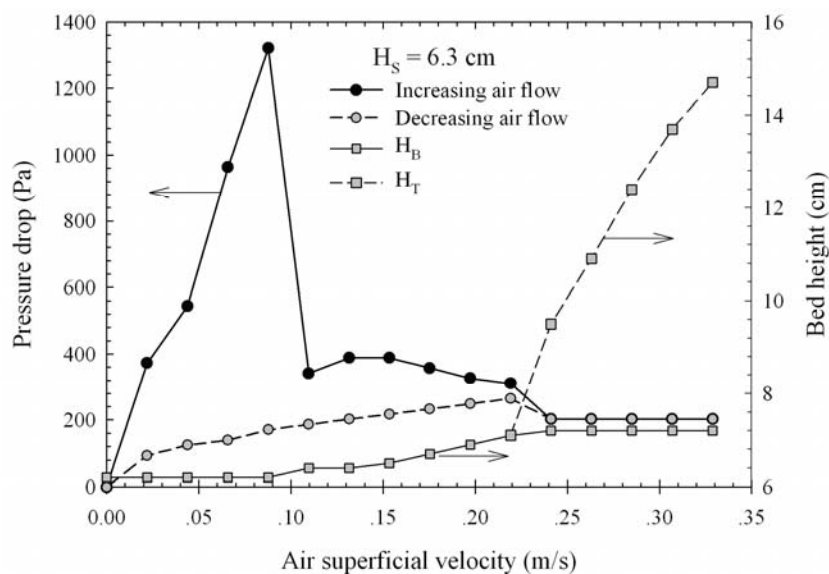


Figure 5.8 Pressure drop–flow rate diagram and bed height of spouted bed for

$D_I = 7.0$ mm, d_P of 0.7 mm, $\theta = 60^\circ$ and $H_S = 6.3$ cm.

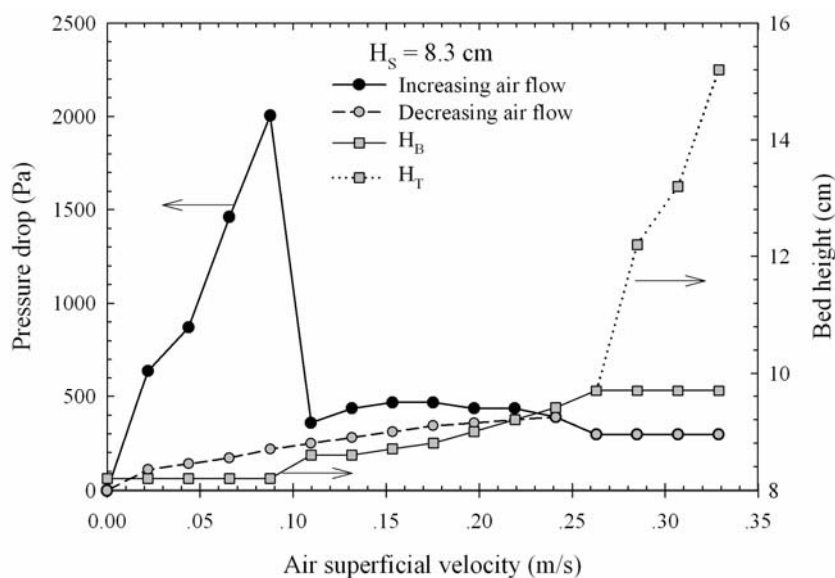


Figure 5.9 Pressure drop–flow rate diagram and bed height of spouted bed for

$D_I = 7.0$ mm, d_P of 0.7 mm, $\theta = 60^\circ$ and $H_S = 8.3$ cm.

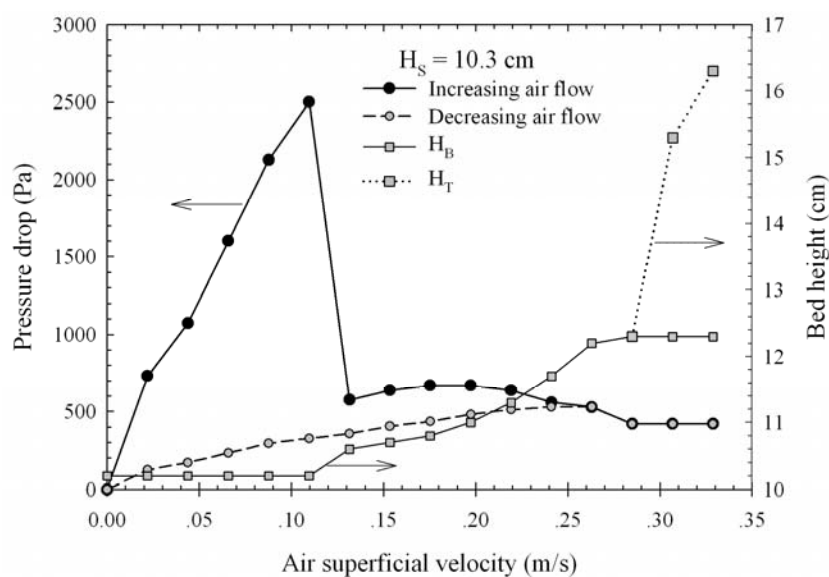


Figure 5.10 Pressure drop–flow rate diagram and bed height of spouted bed for

$D_I = 7.0$ mm, d_p of 0.7 mm, $\theta = 60^\circ$ and $H_S = 10.3$ cm.

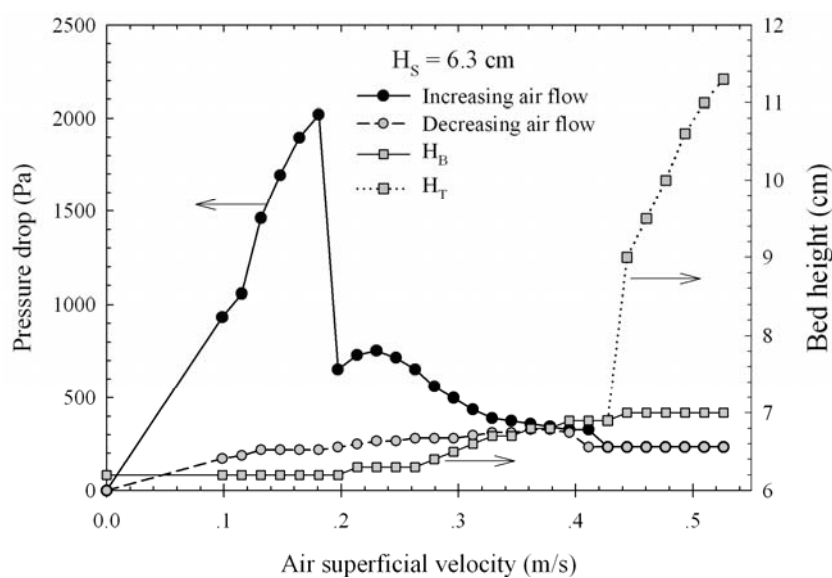


Figure 5.11 Pressure drop–flow rate diagram and bed height of spouted bed for

$D_I = 7.0$ mm, $d_p = 1.4$ mm, $\theta = 60^\circ$ and $H_S = 6.3$ cm.

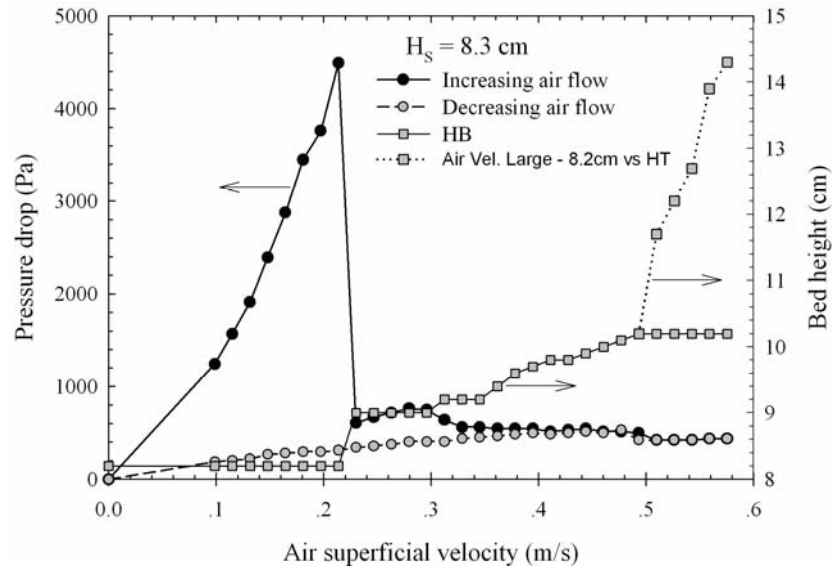


Figure 5.12 Pressure drop–flow rate diagram and bed height of spouted bed for

$$D_I = 7.0 \text{ mm}, d_p = 1.4 \text{ mm}, \theta = 60^\circ \text{ and } H_S = 8.3 \text{ cm.}$$

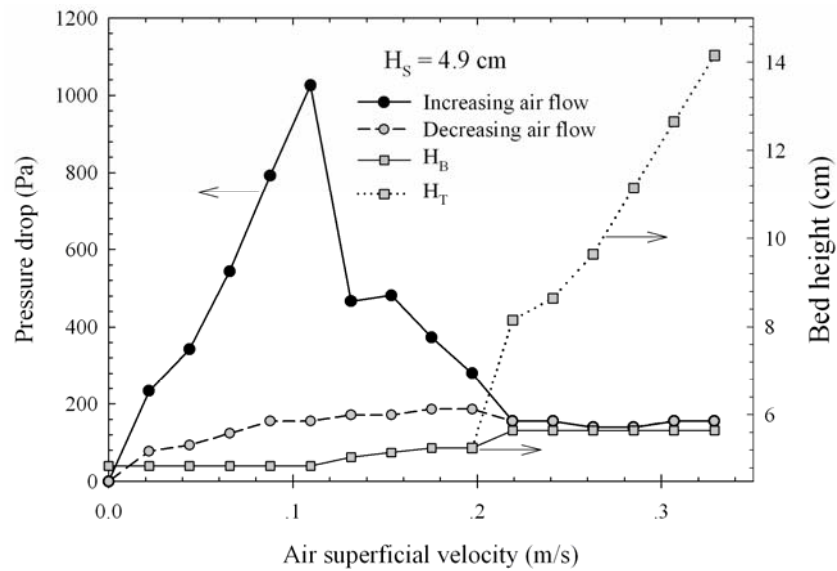


Figure 5.13 Pressure drop–flow rate diagram and bed height of spouted bed for

$$D_I = 7.0 \text{ mm}, d_p = 0.5 \text{ mm}, \theta = 45^\circ \text{ and } H_S = 4.9 \text{ cm.}$$

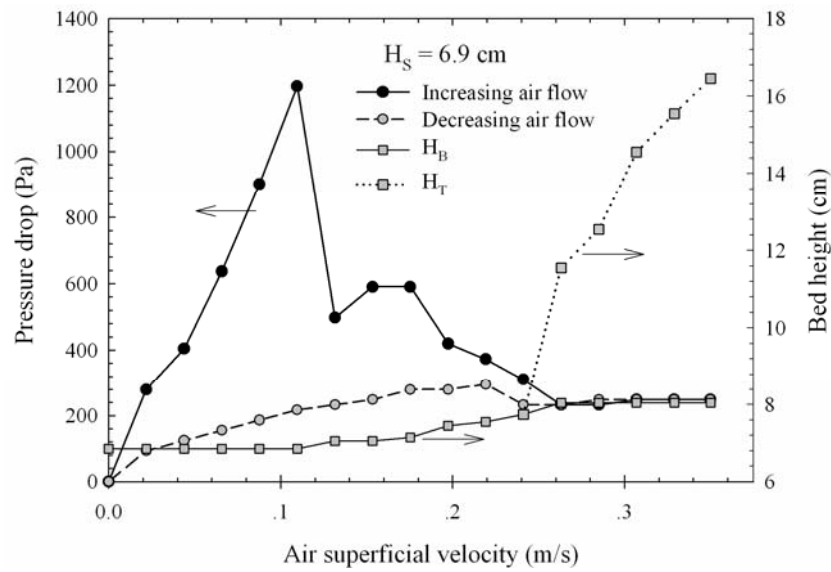


Figure 5.14 Pressure drop–flow rate diagram and bed height of spouted bed for

$D_I = 7.0$ mm, $d_p = 0.5$ mm, $\theta = 45^\circ$ and $H_S = 6.9$ cm.

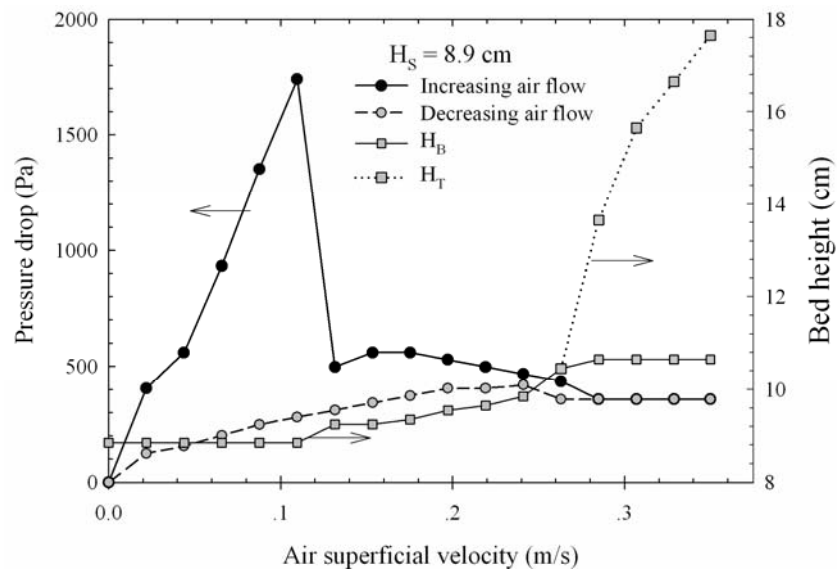


Figure 5.15 Pressure drop–flow rate diagram and bed height of spouted bed for

$D_I = 7.0$ mm, $d_p = 0.5$ mm, $\theta = 45^\circ$ and $H_S = 8.9$ cm.

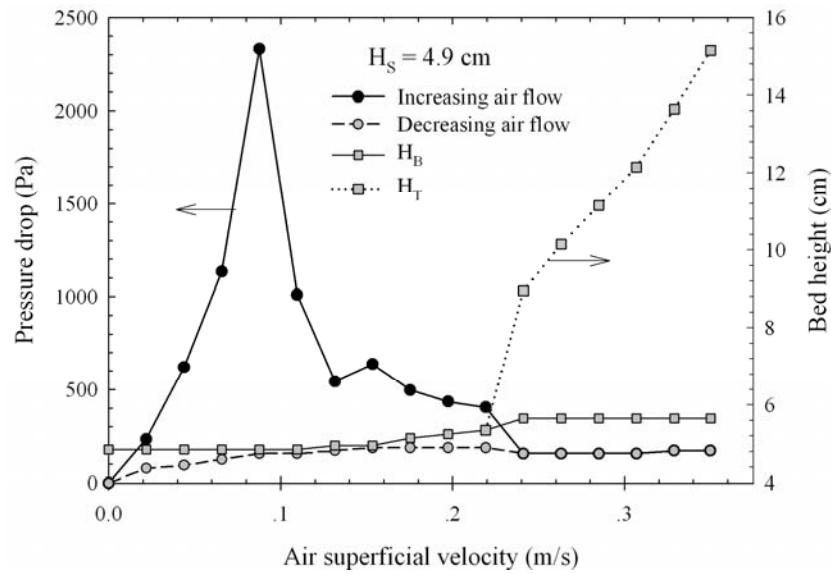


Figure 5.16 Pressure drop–flow rate diagram and bed height of spouted bed for

$$D_I = 7.0 \text{ mm}, d_p = 0.7 \text{ mm}, \theta = 45^\circ \text{ and } H_S = 4.9 \text{ cm.}$$

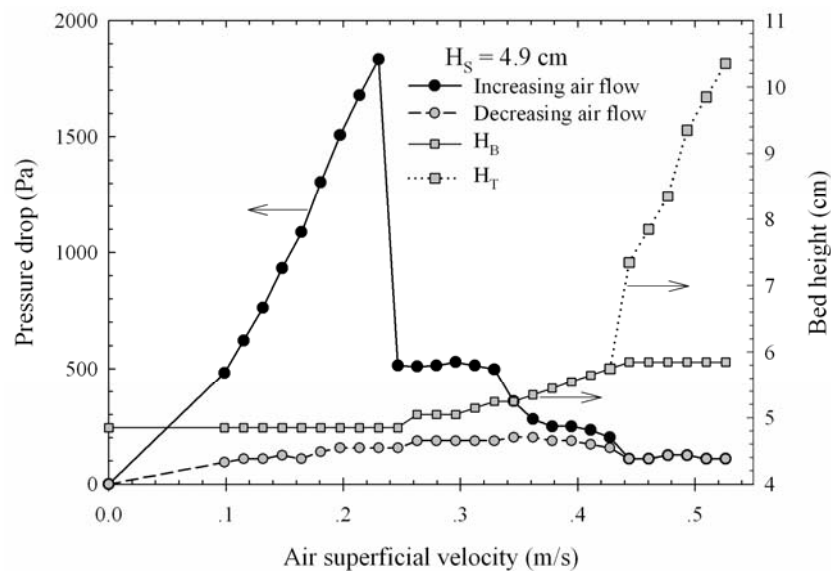


Figure 5.17 Pressure drop–flow rate diagram and bed height of spouted bed for

$$D_I = 7.0 \text{ mm}, d_p = 1.4 \text{ mm}, \theta = 45^\circ \text{ and } H_S = 4.9 \text{ cm.}$$

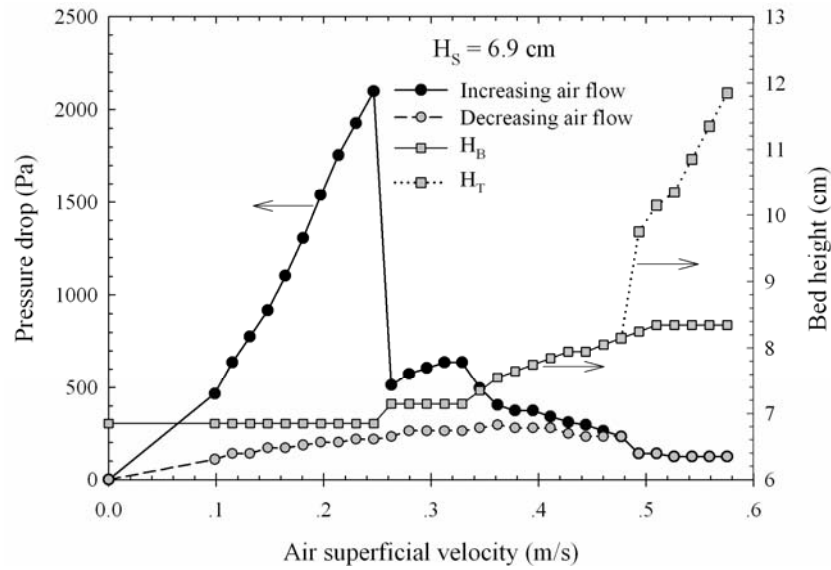


Figure 5.18 Pressure drop–flow rate diagram and bed height of spouted bed for

$$D_I = 7.0 \text{ mm}, d_p = 1.4 \text{ mm}, \theta = 45^\circ \text{ and } H_S = 6.9 \text{ cm.}$$

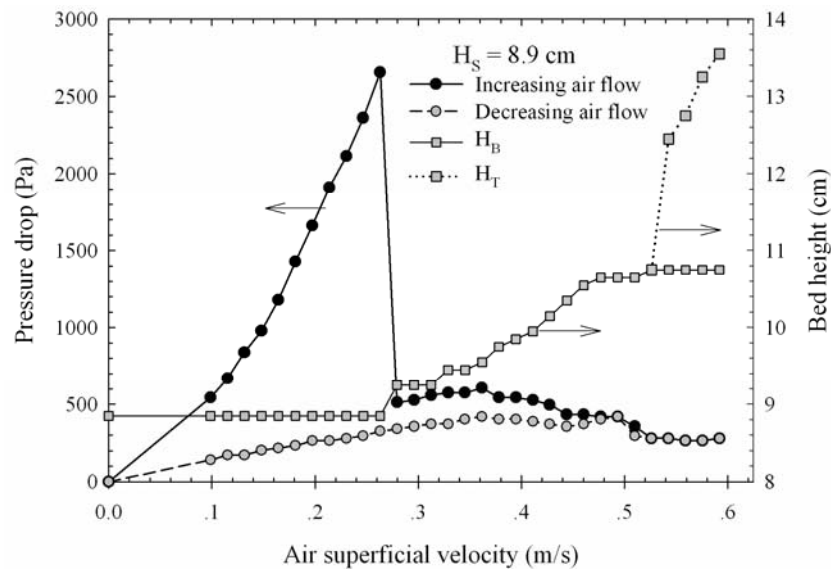


Figure 5.19 Pressure drop–flow rate diagram and bed height of spouted bed for

$$D_I = 7.0 \text{ mm}, d_p = 1.4 \text{ mm}, \theta = 45^\circ \text{ and } H_S = 8.9 \text{ cm.}$$

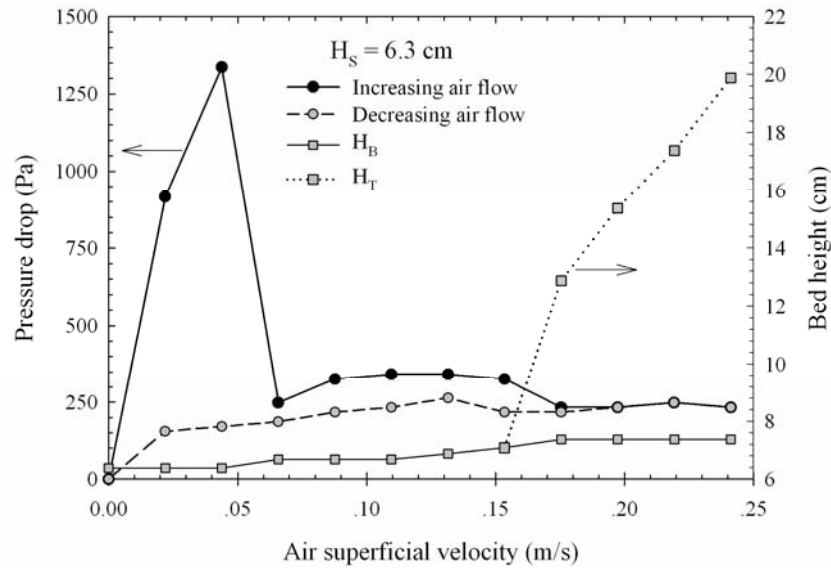


Figure 5.20 Pressure drop–flow rate diagram and bed height of spouted bed for

$D_I = 5.0$ mm, $d_p = 0.5$ mm, $\theta = 60^\circ$ and $H_S = 6.3$ cm.

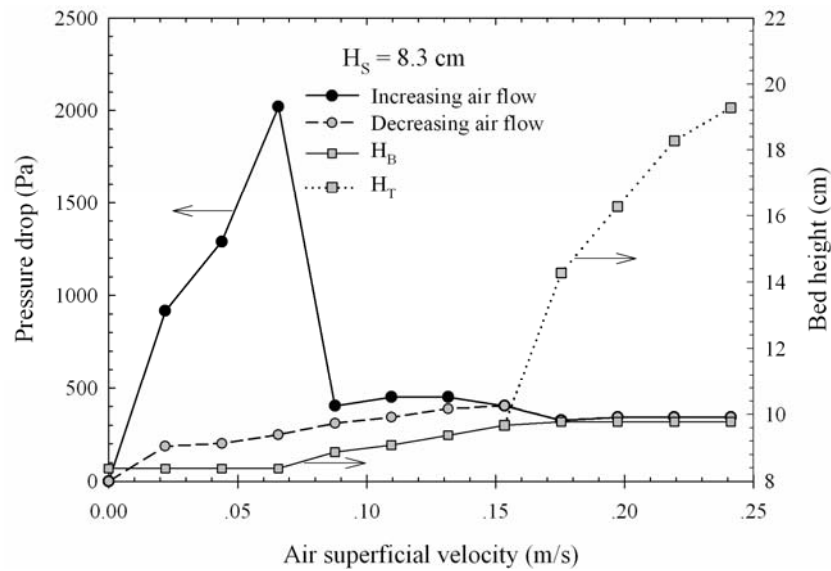


Figure 5.21 Pressure drop–flow rate diagram and bed height of spouted bed for

$D_I = 5.0$ mm, $d_p = 0.5$ mm, $\theta = 60^\circ$ and $H_S = 8.3$ cm.

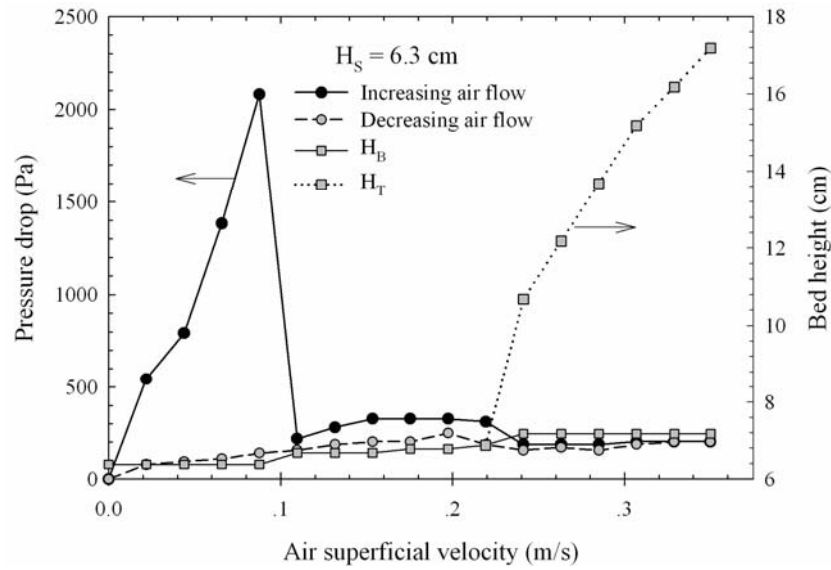


Figure 5.22 Pressure drop–flow rate diagram and bed height of spouted bed for

$D_I = 5.0$ mm, $d_p = 0.7$ mm, $\theta = 60^\circ$ and $H_S = 6.3$ cm.

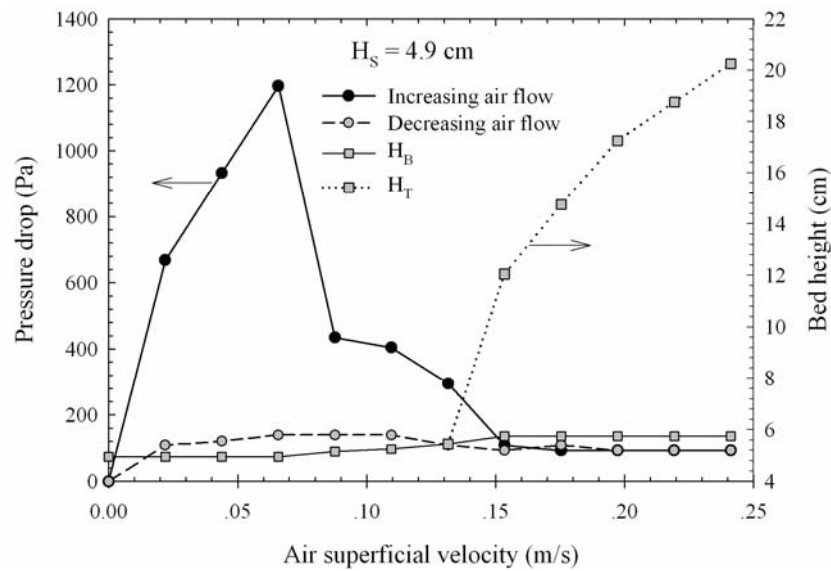


Figure 5.23 Pressure drop–flow rate diagram and bed height of spouted bed for

$D_I = 5.0$ mm, $d_p = 0.5$ mm, $\theta = 45^\circ$ and $H_S = 4.9$ cm.

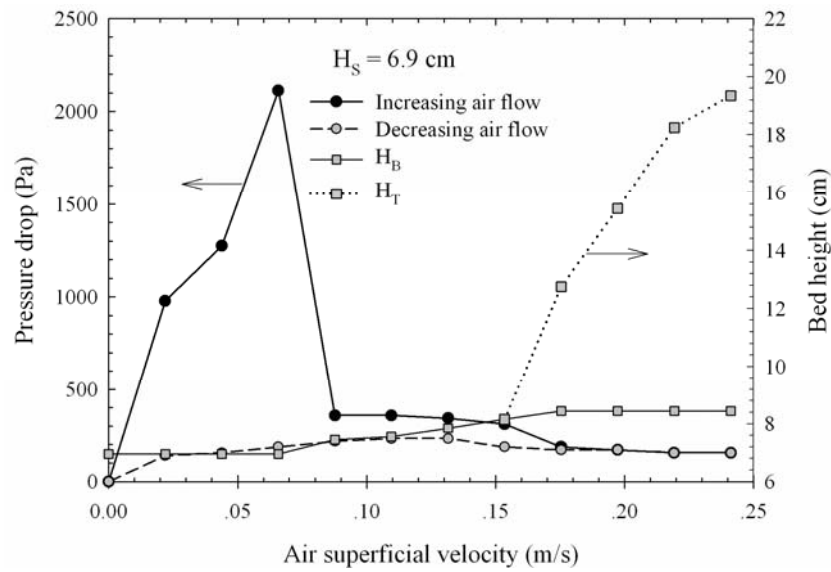


Figure 5.24 Pressure drop–flow rate diagram and bed height of spouted bed for

$D_I = 5.0$ mm, $d_p = 0.5$ mm, $\theta = 45^\circ$ and $H_S = 6.9$ cm.

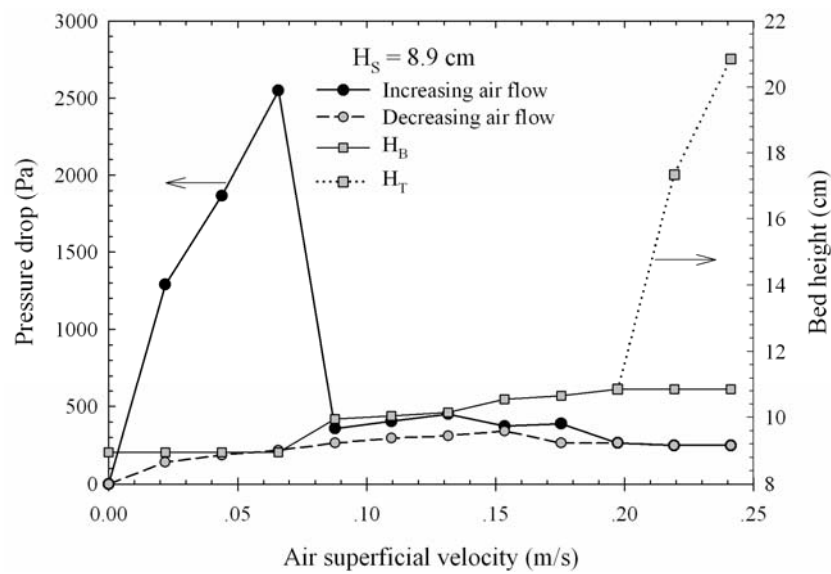


Figure 5.25 Pressure drop–flow rate diagram and bed height of spouted bed for

$D_I = 5.0$ mm, $d_p = 0.5$ mm, $\theta = 45^\circ$ and $H_S = 8.9$ cm.

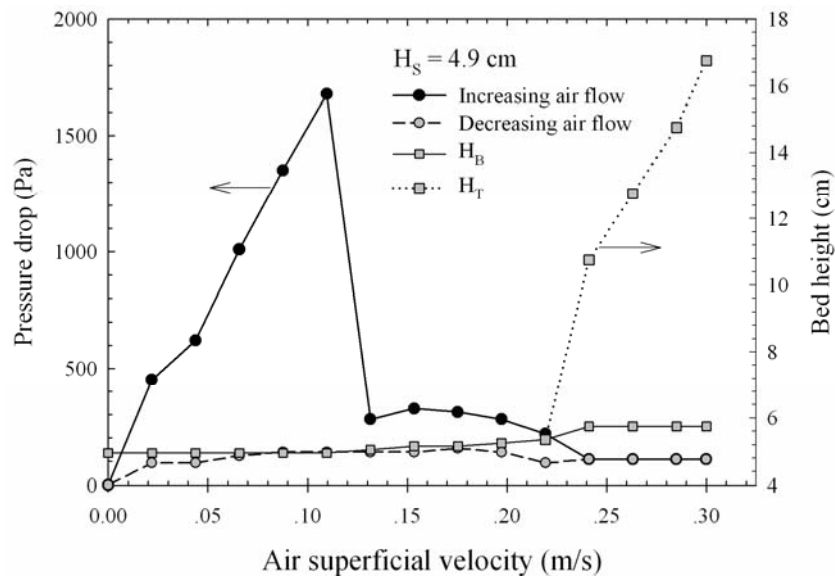


Figure 5.26 Pressure drop–flow rate diagram and bed height of spouted bed for

$D_I = 5.0$ mm, $d_p = 0.7$ mm, $\theta = 45^\circ$ and $H_S = 4.9$ cm.

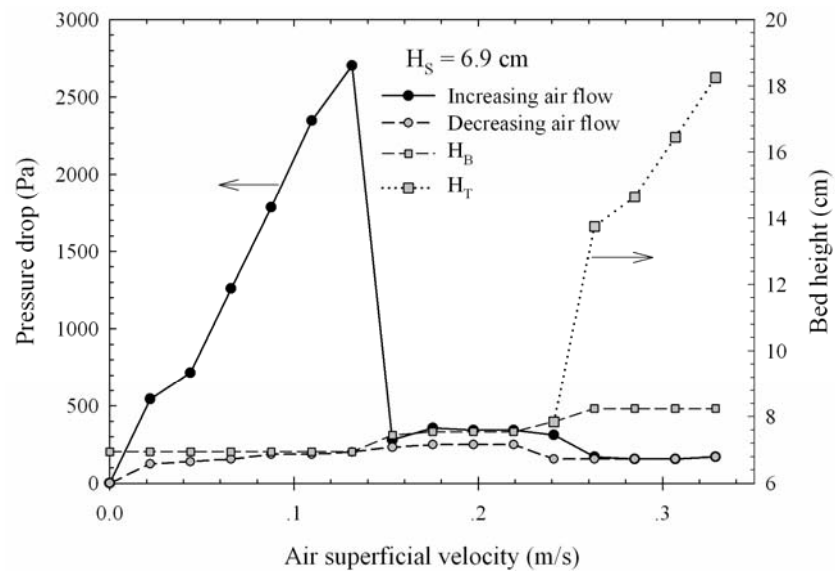


Figure 5.27 Pressure drop–flow rate diagram and bed height of spouted bed for

$D_I = 5.0$ mm, $d_p = 0.7$ mm, $\theta = 45^\circ$ and $H_S = 6.9$ cm.

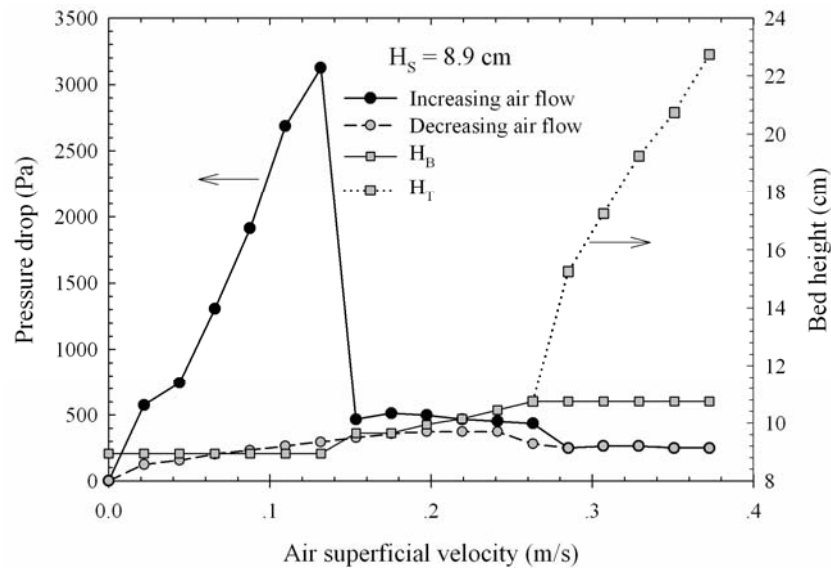


Figure 5.28 Pressure drop–flow rate diagram and bed height of spouted bed for

$D_I = 5.0$ mm, $d_p = 0.7$ mm, $\theta = 45^\circ$ and $H_S = 8.9$ cm.

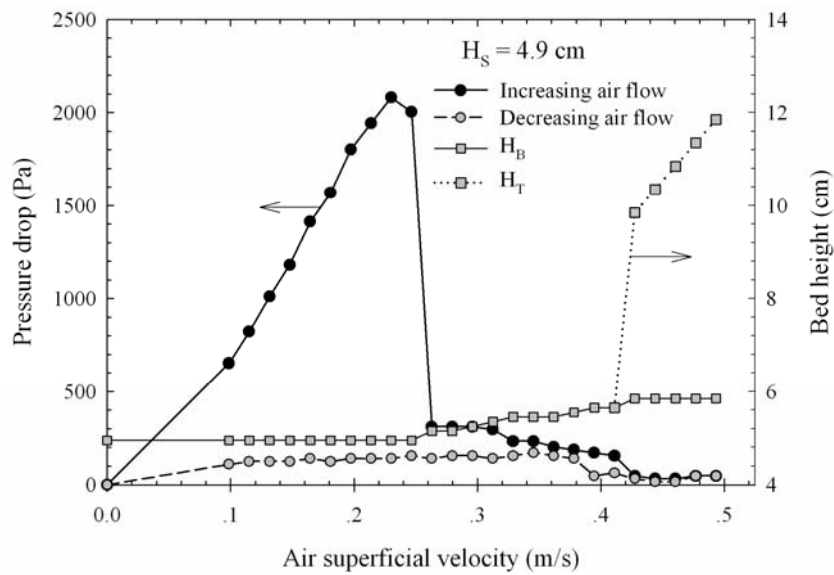


Figure 5.29 Pressure drop–flow rate diagram and bed height of spouted bed for

$D_I = 5.0$ mm, $d_p = 1.4$ mm, $\theta = 45^\circ$ and $H_B = 4.9$ cm.

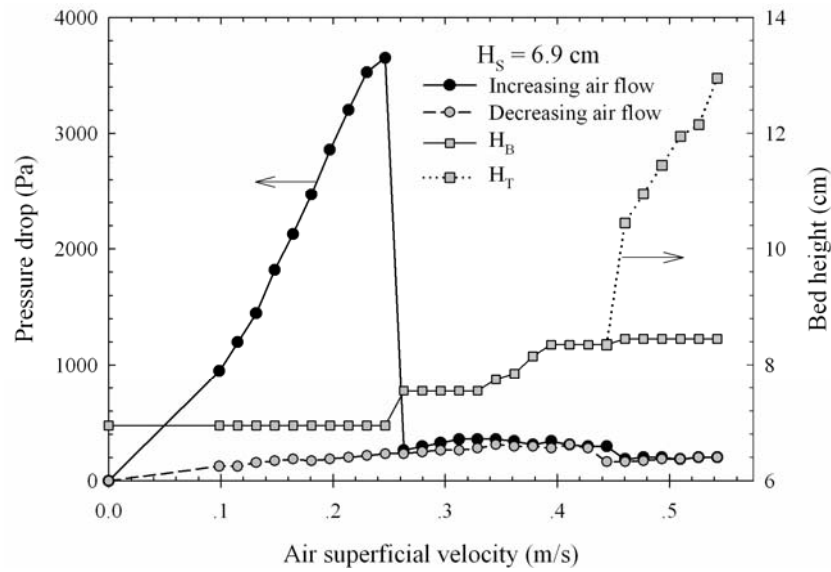


Figure 5.30 Pressure drop–flow rate diagram and bed height of spouted bed for

$$D_I = 5.0 \text{ mm}, d_p = 1.4 \text{ mm}, \theta = 45^\circ \text{ and } H_B = 6.9 \text{ cm.}$$

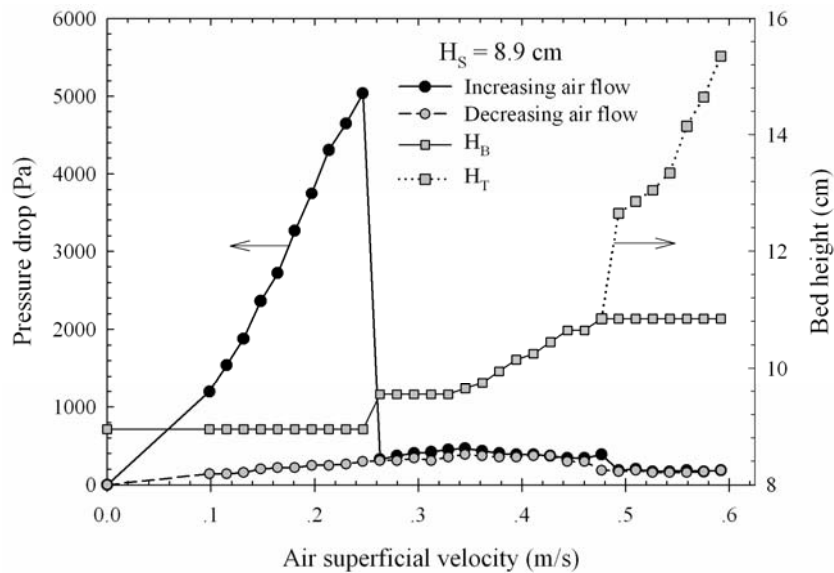


Figure 5.31 Pressure drop–flow rate diagram and bed height of spouted bed for

$$D_I = 5.0 \text{ mm}, d_p = 1.4 \text{ mm}, \theta = 45^\circ \text{ and } H_B = 8.9 \text{ cm.}$$

Generally, the most important parameter that is necessary for designing spouted bed based equipment is the minimum spouting velocity (U_{MS}). This velocity is the minimum fluid velocity at which a bed is transformed from the fixed bed mode in a loosest state to the spouted bed state and depends on solid and fluid properties, and also on the geometric dimensions of the system. The experimental minimum spouting velocity for the air-palm shell char particle system for various air inlet diameters, conical base angles, particle sizes and initial static bed heights are listed in Table 5.4.

In order to show the effect of geometric factors, static bed height, and particle size on the minimum spouting velocity, the experimental data of the minimum spouting velocity listed in Table 5.4 were plotted graphically as shown in Figure 5.32 to 5.35. The results show clearly that the minimum spouting velocity increases with increasing of particle size (d_p , see Figure 5.32), initial static bed height (H_B , see Figure 5.33), and gas inlet size (D_I , see Figure 5.34 and 5.35). When the particle size is increased, the force required to push the particle moving upward in the spouting core is also increased. Therefore, higher gas flow rate (or higher minimum spouting velocity) must be supplied to increase the lift force. The increasing in static bed height leads to the increasing in interface area between spouting core and annulus zone. The expansion of the interface area causes the increasing of gas leaking from spouting core to annulus zone through that interface. Thus, higher gas flow must be supplied into spouted bed to compensate for gas leakage to maintain spouting state of solid bed. For gas inlet diameter, larger size of spout core is expected when the gas inlet diameter is increased. Therefore, higher gas flow is required to maintain the same velocity for spouting the bed.

Table 5.4 Minimum spouting velocity (U_{MS}) of spouted bed (experimentally determined) for various geometric dimensions, particle sizes and static bed heights and U_{MS} calculated from Equation (5.1).

Nozzle diameter (D_I , mm)	Base Angle (θ)	Particle size (d_p , mm)	Bed height (H_s , cm)	Min. Spouting Velocity (U_{MS} , m/s)		% Error
				Exp.	Cal (Eq.(5.1))	
7	60°	0.50	6.3	0.154	0.195	-26.6%
7	60°	0.70	6.3	0.230	0.273	-18.8%
			8.3	0.252	0.314	-24.7%
			10.3	0.274	0.350	-27.9%
7	60°	1.39	6.3	0.436	0.543	-24.4%
			8.3	0.485	0.624	-28.7%
7	45°	0.50	4.9	0.208	0.173	16.8%
			6.9	0.230	0.205	10.9%
			8.9	0.274	0.233	15.0%
7	45°	0.70	4.9	0.230	0.242	-5.1%
7	45°	1.39	4.9	0.436	0.480	-10.1%
			6.9	0.485	0.570	-17.6%
			8.9	0.501	0.648	-29.4%
5	60°	0.50	6.3	0.142	0.177	-24.6%
			8.3	0.164	0.203	-23.8%
5	60°	0.70	6.3	0.230	0.248	-7.7%
5	45°	0.50	4.9	0.142	0.156	-9.9%
			6.9	0.152	0.185	-21.7%
			8.9	0.164	0.210	-28.0%
5	45°	0.70	4.9	0.208	0.218	-4.9%
			6.9	0.230	0.259	-12.4%
			8.9	0.274	0.293	-7.1%
5	45°	1.39	4.9	0.386	0.433	-12.3%
			6.9	0.436	0.514	-17.8%
			8.9	0.469	0.583	-24.3%

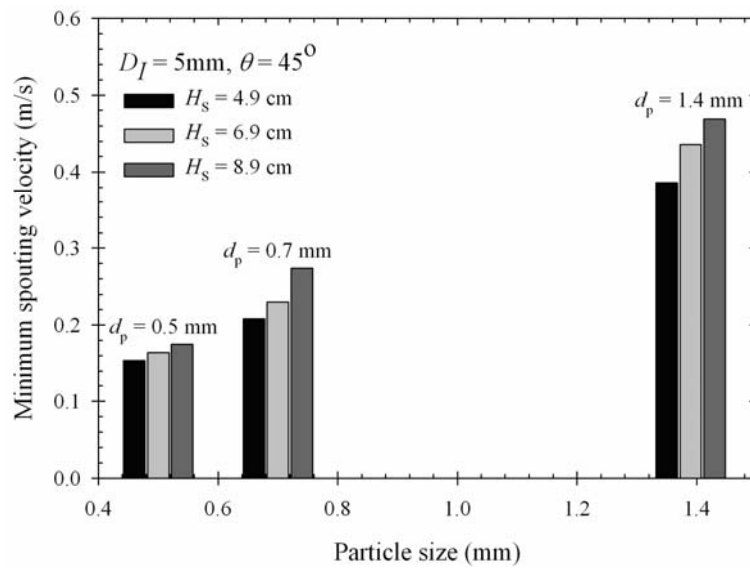


Figure 5.32 Effect of particle size on minimum spouting velocity.

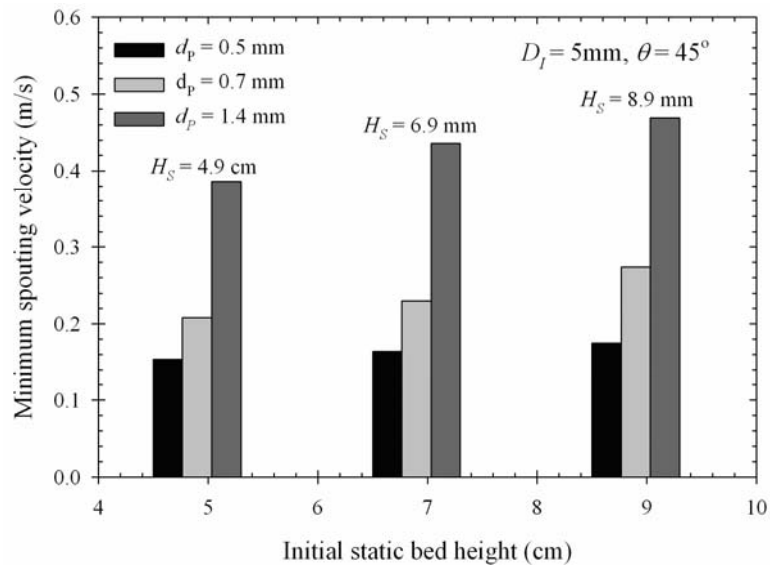


Figure 5.33 Effect of initial bed heights on minimum spouting velocity.

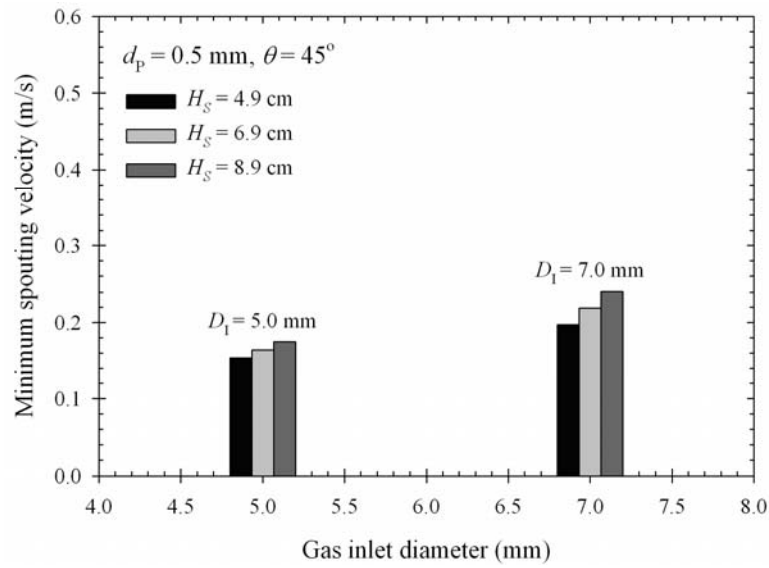


Figure 5.34 Effect of gas inlet diameters on minimum spouting velocity for particle size of 0.5 mm and conical base angle 45° .

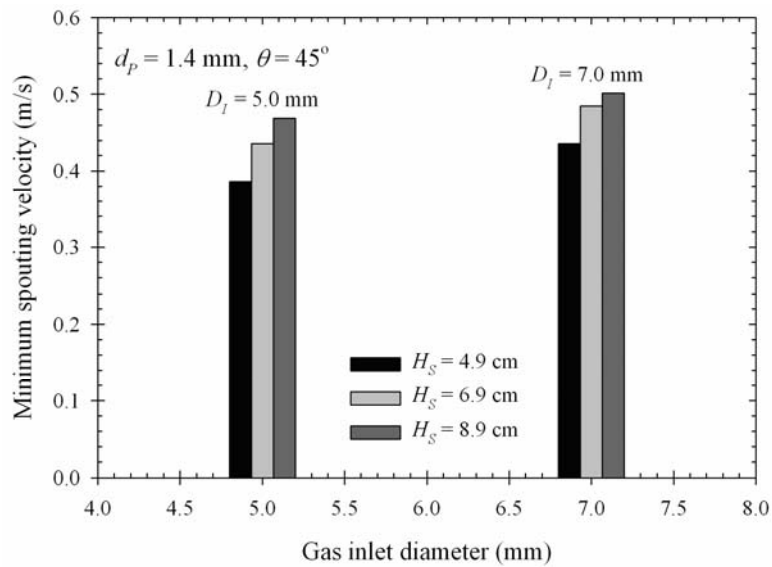


Figure 5.35 Effect of gas inlet diameters on minimum spouting velocity for particle size of 1.4 mm and conical base angle 45° .

Also shown for comparison with experimental data in Table 5.4 are minimum spouting velocities calculated from the expression proposed by Mathur and Gishler (Equation (5.1)). The comparison indicates that the correlation proposed by Mathur and Gishler (1955) provides the prediction with the maximum deviation up to about 30%. The Standard Error of Estimate (SEE) was determined to be 20.5%, using the formula

$$SEE = \sqrt{\sum_{i=1}^N \left(\frac{U_{MS,Exp.} - U_{MS,Cal.}}{U_{MS,Exp.}} \right)^2 / (N - 2)} \quad (5.42)$$

where N is the number of data points which is 25 points in this work. Equation (5.1) was proposed based on a specific system of air-wheat particles, the nature of which is quite different from the air- palm shell char system studied in this work. Therefore, it was decided to propose a more suitable correlation to improve the prediction accuracy for air-palm shell char particle system of the present work.

The general dimensionless equation for predicting minimum spouting velocity can be given as the following (Abdul Salam and Bhattacharya, 2006).

$$U_{MS} = \lambda (2gH_B)^k \left(\frac{d_P}{D_C} \right)^\alpha \left(\frac{D_I}{D_C} \right)^\beta \left(\frac{H_B}{D_C} \right)^\gamma \left[\frac{\rho_P - \rho_f}{\rho_f} \right]^\delta \quad (5.43)$$

where λ , k , α , β , γ and δ are constants estimated by fitting Equation (5.43) with the experimental data.

In this work, the optimization function in MATLAB program was used to fit Equation (5.43) with the experimental data. The objective function is to minimize the sum of square of relative error (SSQR) defined as,

$$SSQR = \sum \left(\frac{U_{MS,exp} - U_{MS,cal}}{U_{MS,exp}} \right)^2 \quad (5.44)$$

where $U_{MS,exp}$ and $U_{MS,cal}$ are the experimental and calculated minimum spouting velocities, respectively.

The fitting results gave the constants as $\lambda = 1.239$, $k = 0.287$, $\alpha = 0.891$, $\beta = 0.263$, $\gamma = 0.0$, and $\delta = 0.373$, with the final proposed correlation reads

$$U_{MS} = 1.239(2gH_S)^{0.287} \left(\frac{d_P}{D_C} \right)^{0.891} \left(\frac{D_I}{D_C} \right)^{0.263} \left[\frac{\rho_P - \rho_f}{\rho_f} \right]^{0.373} \quad (5.45)$$

The minimum spouting velocity computed by employing Equation (5.45) are listed in Table 5.5. Although an improvement on the prediction of minimum spouting velocity using this empirical equation was observed, the prediction results still show relatively large deviation up to 26% for some geometric dimensions of the spouted bed. The standard error of estimate was found to be 11.1% which show the improvement of the prediction compared to Equation (5.1).

Table 5.5 Minimum spouting velocity (U_{MS}) of spouted bed (experimentally determined) for various geometric factors, particle sizes and static bed heights and U_{MS} calculated from Equation.(5.45).

Nozzle diameter (D_I , mm)	Base Angle (θ)	Particle size (d_P , mm)	Bed height (H_S , cm)	Min. Spouting Velocity (U_{MS} , m/s)		% Error
				Exp.	Cal. (Eq(5.45))	
7	60°	0.50	6.3	0.154	0.183	-18.8%
7	60°	0.70	6.3	0.230	0.247	-7.4%
			8.3	0.252	0.268	-6.2%
			10.3	0.274	0.285	-4.0%
7	60°	1.39	6.3	0.436	0.455	-4.4%
			8.3	0.485	0.493	-1.7%
7	45°	0.50	4.9	0.208	0.171	17.8%
			6.9	0.230	0.188	18.3%
			8.9	0.274	0.203	25.9%
7	45°	0.70	4.9	0.230	0.230	0.1%
7	45°	1.39	4.9	0.436	0.424	2.7%
			6.9	0.485	0.468	3.5%
			8.9	0.501	0.504	-0.6%
5	60°	0.50	6.3	0.142	0.169	-19.0%
			8.3	0.164	0.183	-11.6%
5	60°	0.70	6.3	0.230	0.228	0.9%
5	45°	0.50	4.9	0.142	0.157	-10.6%
			6.9	0.152	0.173	-13.8%
			8.9	0.164	0.186	-13.4%
5	45°	0.70	4.9	0.208	0.212	-1.9%
			6.9	0.230	0.234	-1.6%
			8.9	0.274	0.271	1.1%
5	45°	1.39	4.9	0.386	0.390	-1.2%
			6.9	0.436	0.430	1.3%
			8.9	0.469	0.463	1.3%

A different new approach was proposed and tried in this work for the estimation of U_{MS} by applying the theory of a turbulent free-jet (Perry, 2007). In a free-jet flow, a fluid flows into a static fluid through a small nozzle and it will expand and decelerate. The momentum of the jet fluid is transferred to the static fluid to conserve the total momentum. Practically, a jet is considered free when the cross-sectional area of nozzle inlet is less than one-fifth of the total cross-sectional flow area region through which the jet is flowing. The configuration of the turbulent free-jet is shown in Figure 5.36. The nomenclature U_I appearing in the figure is denoted as average jet inlet fluid velocity, D_I is the jet inlet size, Z is the longitudinal distance from fluid inlet, and U is average axial fluid velocity in the flow field. The longitudinal distribution of velocity along the jet center line for the turbulent free-jet characteristics of rounded-inlet circular nozzle can be expressed by the following equation.

$$\frac{U}{U_I} = K_1 \left(\frac{D_I}{Z} \right)^{K_2} \quad (5.46)$$

where K_1 and K_2 are constants.

For the analysis of the minimum spouting velocity, the configuration of a turbulent free-jet in a spouted bed is approximated as shown in Figure 5.37. The spouting fluid or jet fluid is fed into the spouted bed through the jet inlet at the conical base. The solid bed is assumed to be the static fluid just as in the case of free-jet flow. It is noted that the jet fluid is assumed to flow only in the axial direction and no leakage of jet fluid from the spout core into the annulus zone. The jet-fluid is also assumed to be incompressible. The nomenclature P is the upstream pressure due to

the flow of jet fluid or spouting fluid, P^* is the pressure due to the weight of solid particles above the spout core, and P_{atm} is the atmospheric pressure.

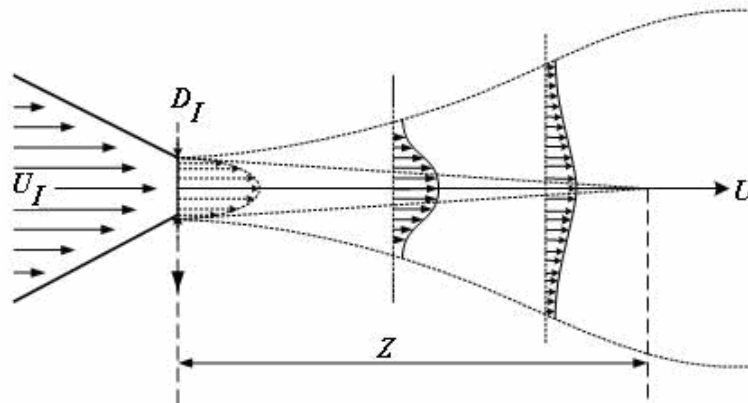


Figure 5.36 Configuration of a turbulent free-jet.

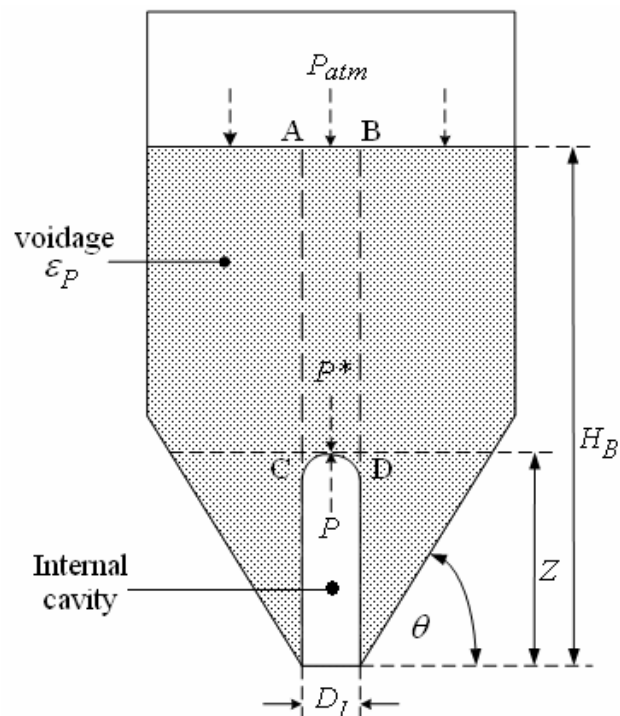


Figure 5.37 Configuration of a turbulent free-jet in spouted bed.

The analysis of the minimum spouting velocity using the turbulent free-jet flow begins by writing the force balance on particles contained in the cylindrical section ABCD by assuming constant height of dense solid bed (H_B) and equal to initial static bed of spouted bed (H_S). Thus,

$$P - P_{atm} = (H_S - Z)(1 - \varepsilon_P)\rho_P g \quad (5.47)$$

where ε_P is bed voidage and its value is assumed to be 0.40 in this work.

By employing the well known Ergun Equation for turbulent flow through a packed bed of spherical particles, the pressure drop across the bed or the difference between P and the atmospheric pressure can be written as,

$$\Delta P = P - P_{atm} = \frac{1.75\rho_F U^2 (1 - \varepsilon_P)(H_S - Z)}{d_P \varepsilon_P^3} \quad (5.48)$$

Equating Equation (5.47) and (5.48) gives

$$\rho_P g = \frac{1.75\rho_F U^2}{d_P \varepsilon_P^3} \quad (5.49)$$

The density of fluid (ρ_F) is assumed to be the density of air at atmospheric pressure and 25°C which is 1.185 kg/m³. Substituting the mean axial jet velocity, U , from Equation (5.46) into Equation (5.49) yields

$$\rho_P g = \frac{1.75\rho_F \left(U_I K_1 (D_I/Z)^{K_2} \right)^2}{d_P \varepsilon_P^3} \quad (5.50)$$

The transformation from fixed bed to the minimum or incipient spouting condition occurs when the length of internal cavity elongates and just touches the bed surface on increasing air flow. Therefore, at U_{MS} the axial velocity in Equation (5.50) is the minimum spouting velocity ($U_I = U_{MS}$) and the longitudinal distance is equal to the static bed height ($Z = H_S$). Using these criteria, Equation (5.50) now becomes

$$U_{MS} = \frac{1}{K_1 (D_I/H_S)^{K_2}} \sqrt{\frac{\rho_P g d_P \varepsilon_P^3}{1.75 \rho_F}} \quad (5.51)$$

The constants K_1 and K_2 can be obtained by fitting this equation (5.51) to the experimental data. The fitted values of K_1 and K_2 were found to be 0.184 and 0.740, respectively. The predicted minimum spouting velocity for each geometric dimensions and particle size are listed in Table 5.6. It is found that Equation (5.51) provides large deviation with maximum deviation of 73% of compared to the experimental data. The standard error of estimate was found to be 31.5%. Figure 5.38 compares the experimental and predicted values of the minimum spouting velocity. The figure shows that about 40% of the predicted values are within $\pm 15\%$ of deviation line. This large deviation should be due to the difference in basic concept of free-jet flow compared to the flow characteristics of spouted bed. The free-jet flow assume that the jet fluid flow through the other stagnant fluid, while the spouting fluid flow through a solid bed. Moreover, in the analysis of free-jet flow for predicting the minimum spouting velocity, it is assumed that the fluid flow only in the axial direction and no leakage of jet fluid from the spout core into the annulus zone which are different from the real system of spouted bed.

Table 5.6 Minimum spouting velocity (U_{MS}) of spouted bed (experimentally determined) for various geometric factors, particle sizes and bed heights, U_{MS} calculated from Equation (5.51).

Nozzle diameter (D_I , mm)	Base angle (θ)	Particle size (d_P , mm)	Bed height (H_S , cm)	Min. spouting velocity (U_{MS} , m/s)		% Error
				Exp.	Cal. (Eq.(5.51))	
7	60°	0.50	6.3	0.154	0.266	-72.8%
7	60°	0.70	6.3	0.230	0.315	-36.9%
			8.3	0.252	0.387	-53.7%
			10.3	0.274	0.455	-66.1%
7	60°	1.39	6.3	0.436	0.444	-1.8%
			8.3	0.485	0.546	-12.5%
7	45°	0.50	4.9	0.208	0.222	-6.7%
			6.9	0.230	0.287	-24.6%
			8.9	0.274	0.346	-26.4%
7	45°	0.70	4.9	0.230	0.263	-14.2%
7	45°	1.39	4.9	0.436	0.370	15.1%
			6.9	0.485	0.478	1.5%
			8.9	0.501	0.577	-15.3%
5	60°	0.50	6.3	0.142	0.178	-25.3%
			8.3	0.164	0.218	-32.7%
5	60°	0.70	6.3	0.230	0.211	8.5%
5	45°	0.50	4.9	0.142	0.147	-3.8%
			6.9	0.152	0.190	-24.7%
			8.9	0.164	0.229	-39.4%
5	45°	0.70	4.9	0.208	0.174	16.1%
			6.9	0.230	0.224	2.5%
			8.9	0.274	0.270	1.3%
5	45°	1.39	4.9	0.386	0.246	36.3%
			6.9	0.436	0.316	27.5%
			8.9	0.469	0.381	18.8%

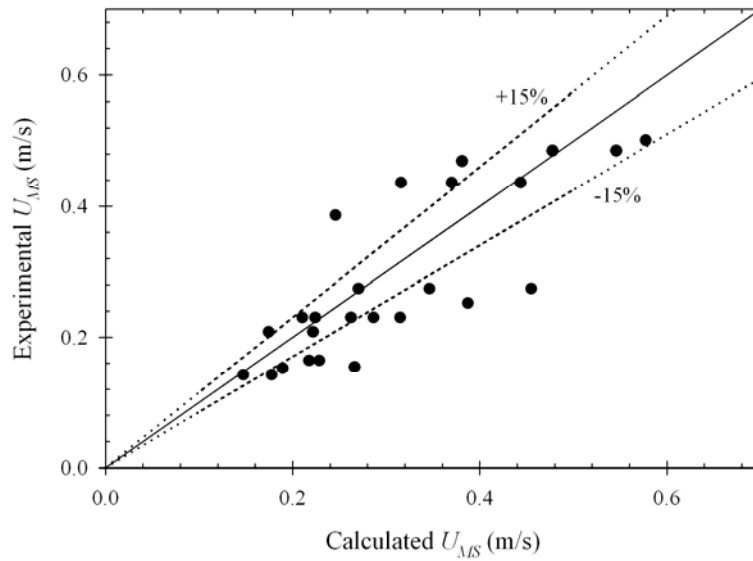


Figure 5.38 Comparison of experimental and calculated minimum spouting velocities by Equation (5.51).

In order to make Equation (5.51) more flexible and to improve its capability in predicting the minimum spouting velocity, this equation will be modified to obtain a semi-empirical correlation by including the effect of spouted bed column diameter (D_C) with free parameters on D_I and H_S , as shown in the following equation.

$$U_{MS} = \alpha_1 \left(\frac{D_I}{D_C} \right)^{\alpha_2} \left(\frac{H_S}{D_C} \right)^{\alpha_3} \sqrt{\frac{\rho_P d_P \varepsilon_P^3}{1.75 \rho_F}} \quad (5.52)$$

By fitting the experimental data with Equation (5.52), the parameters α_1 , α_2 , and α_3 , were determined to be 0.700, 1.501, and -0.309, respectively. The final proposed equation thus becomes

$$U_{MS} = 0.70 \left(\frac{D_I}{D_C} \right)^{1.501} \left(\frac{H_S}{D_C} \right)^{-0.309} \sqrt{\frac{\rho_P d_P \varepsilon_P^3}{1.75 \rho_F}} \quad (5.53)$$

The predicted minimum spouting velocity using Equation (5.53) for each geometric dimensions and particle size are listed in Table 5.7. The predicted results show better improvement of the prediction of minimum spouting velocity, with maximum deviation of 59.0% and the standard error of estimate of 26.1%. Figure 5.39 compares the results between the experimental and predicted values of the minimum spouting velocity using Equation (5.53).

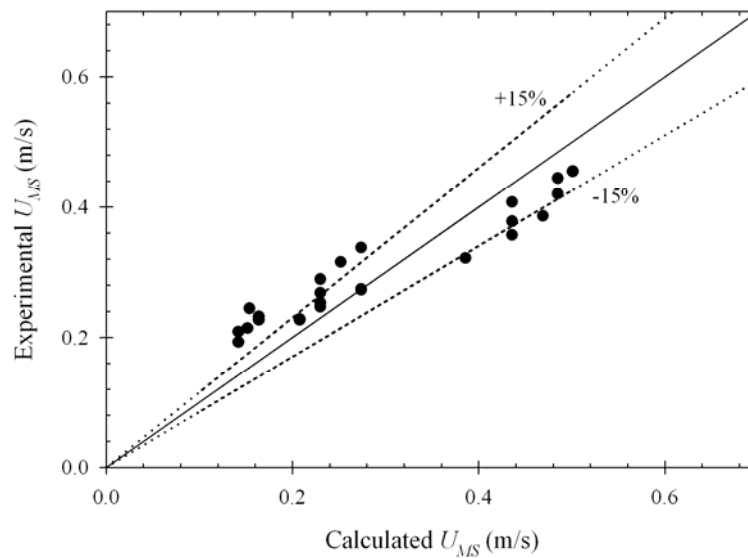


Figure 5.39 Comparison of experimental and calculated minimum spouting velocities by Equation (5.53).

Table 5.7 Minimum spouting velocity (U_{MS}) of spouted bed (experimentally determined) for various geometric factors, particle sizes and bed heights, and U_{MS} calculated from Equation (5.53).

Nozzle diameter (D_I , mm)	Base angle (θ)	Particle size (d_P , mm)	Bed height (H_S , cm)	Min. spouting velocity (U_{MS} , m/s)		% Error
				Exp.	Cal. (Eq. (5.53))	
7	60°	0.50	6.3	0.154	0.244	-58.7%
7	60°	0.70	6.3	0.230	0.289	-25.7%
			8.3	0.252	0.315	-25.1%
			10.3	0.274	0.337	-23.1%
7	60°	1.39	6.3	0.436	0.407	6.6%
			8.3	0.485	0.444	8.4%
7	45°	0.50	4.9	0.208	0.226	-8.9%
			6.9	0.230	0.252	-9.6%
			8.9	0.274	0.273	0.4%
7	45°	0.70	4.9	0.230	0.268	-16.5%
7	45°	1.39	4.9	0.436	0.378	13.4%
			6.9	0.485	0.420	13.4%
			8.9	0.501	0.455	9.2%
5	60°	0.50	6.3	0.142	0.208	-46.8%
			8.3	0.164	0.227	-38.3%
5	60°	0.70	6.3	0.230	0.247	-7.2%
5	45°	0.50	4.9	0.142	0.193	-35.7%
			6.9	0.152	0.214	-40.8%
			8.9	0.164	0.231	-41.1%
5	45°	0.70	4.9	0.208	0.228	-9.6%
			6.9	0.230	0.253	-10.1%
			8.9	0.274	0.274	0.1%
5	45°	1.39	4.9	0.386	0.321	16.8%
			6.9	0.436	0.357	18.2%
			8.9	0.469	0.386	17.7%

The proposed expression for predicting the minimum spouting velocity via Equation (5.53) was also tested for its validity using the experimental data reported by other researchers. Zhong and co-workers (2007) studied the influence of operating pressure on the spout characteristics of a cylindrical spouted bed. The minimum spouting velocity for various operating pressure in the range of 0.1 to 0.4 MPa were reported for millet particle size of 2.3 mm, cylindrical column diameter of 0.1 m, air inlet size of 0.01 m, and 60° of conical base angle. Their results on U_{MS} and those predicted by Equation (5.53) are shown in Table 5.8 for comparison. Maximum deviation of 33.5% is observed and the standard error of estimate was found to be 26.5%, which is the same order as the case of experimental data determined in this study (see Table 5.7).

The total bed height (H_T) at fluid velocity higher than the minimum spouting velocity is another parameter that is required for designing the height of a spouted bed apparatus. In this work, the expression for predicting the total bed height was proposed as the following in dimensionless equation.

$$\frac{H_T}{H_S} = \exp \left[a \left[\frac{U - U_{MS}}{U_{MS}} \right]^b \right] \quad (5.54)$$

This correlation satisfies the condition that, at $U = U_{MS}$, the bed height will be the initial static height ($H_T = H_S$) and all the parameters that affect the total bed height (H_T) are incorporated in the minimum spouting velocity (U_{MS}). By fitting Equation (5.54) to experimental data of total bed height at air flow rate higher than the minimum spouting velocity for all spouting conditions, the fitted parameters, a and b

can be determined, which were found to be 0.318 and 1.101, respectively. The final correlation reads

$$\frac{H_T}{H_S} = \exp \left[0.318 \left[\frac{U - U_{MS}}{U_{MS}} \right]^{1.101} \right] \quad (5.55)$$

Table 5.8 Comparison between Minimum spouting velocity results (U_{MS}) of Zhong et al., 2007 for $\theta = 60^\circ$, $D_I = 0.01$ m, $d_P = 2.3$ mm, and $D_C = 0.10$ m at various pressure and static bed height, and U_{MS} calculated from Equation (5.53).

Pressure (MPa)	Bed height (H_S , m)	Experimental minimum spouting velocity (U_{MS} , m/s)	Predicted minimum spouting velocity using Eq. (5.53) (U_{MS} , m/s)	% Error
0.1	0.15	0.442	0.351	20.5%
	0.20	0.544	0.400	26.6%
	0.25	0.602	0.441	26.7%
	0.30	0.641	0.479	25.3%
0.2	0.15	0.353	0.351	0.5%
	0.20	0.418	0.400	4.4%
	0.25	0.454	0.441	2.8%
	0.30	0.489	0.479	2.0%
0.3	0.15	0.312	0.351	-12.6%
	0.20	0.357	0.400	-11.9%
	0.25	0.381	0.441	-15.9%
	0.30	0.413	0.479	-16.0%
0.4	0.15	0.277	0.351	-26.8%
	0.20	0.308	0.400	-29.7%
	0.25	0.335	0.441	-31.8%
	0.30	0.359	0.479	-33.4%

Equation (5.55) is capable of predicting the total bed heights reasonably well with maximum deviation of 13%. Figure 5.40 shows the deviation between the experimental and predicted values of the total bed height. The figure shows that about 90% of the predicted values are within $\pm 10\%$ of deviation line.

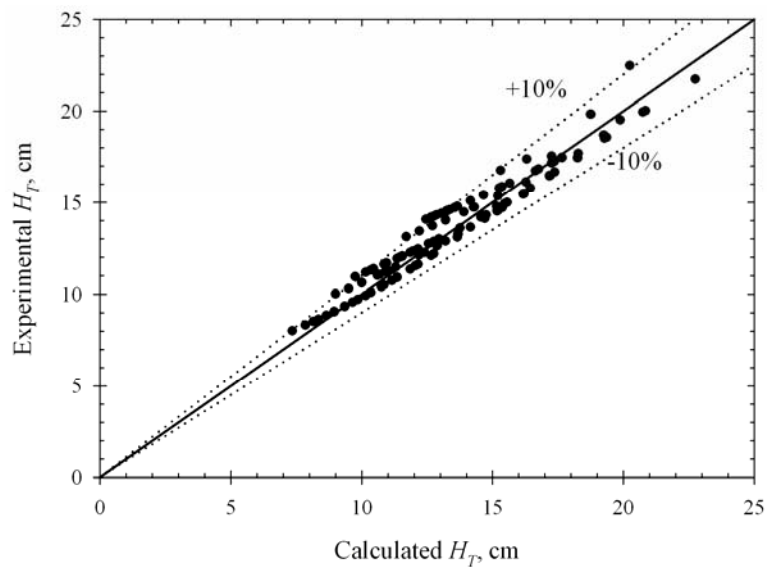


Figure 5.40 Comparison of experimental and calculated total bed height by Equation (5.54).

5.6.2 Preparation of Activated Carbons in the Spouted Bed Activator

Figure 5.41 shows the effect of activation time on the char burn-off during the activation step with CO_2 in the tube furnace and spouted bed activator at 900°C . The spouted bed results show that at the starting of activation step about 10% of char burn-off could be observed, although this value should be zero according to the definition of burn-off. This could be explained by the fact that CO_2 was not admitted into the activator until the final temperature of 900°C was attained. During the heating-up period from room temperature to this final temperature, the activator

was operated in an inert atmosphere of N_2 , where some initial weight loss had occurred due to the process of devolatilization. It is further noted that, up to the maximum burn-off of 35%, the char burn-off appears to increase linearly with activation time, indicating that at this relatively high temperature the gasification reaction is the rate-controlling step in the activation process.

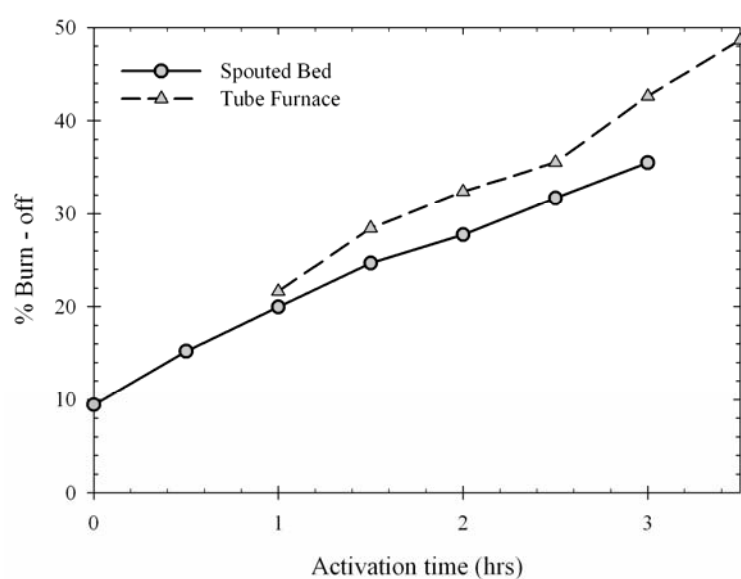


Figure 5.41 Effect of activation time on the extent of char burn-off during activation with CO_2 at $900^\circ C$.

Figure 5.41 also shows that, at the same activation time and temperature, the spouted bed activator gives the activated carbons with lower percentage burn-off as compared to those produced in the tube furnace. This discrepancy should stem from the difference in the mode of contact between CO_2 and particles in the two types of activator. In a spouted bed system, most of fluid flows pass the solid bed through the spouting core containing dilute phase of solid particles, whereas the rest of fluid flows countercurrently with the descending dense solid

particles in the annulus zone. Therefore, the mode of contact between fluid and solid particles is significantly different for spouting core and annulus zone. As a result, the rate of gasification reaction of each particle depends strongly on its local position. The solid particle located in the spouting core will react with CO_2 at higher rate because of higher amount of CO_2 compared to that in the annulus zone. Although the particles can be gasified at high rate in the spouting core, each particle will stay in the spouting core for very short contact time before they reach the fountain zone and dropped down into the annulus zone again. On the other hand, the thin layer of static particles in the tube furnace ensured a uniform contact between activating gas and solid particles, giving longer average reaction time as compared to the spouted bed activator, hence higher values of char burn-off. From this finding, it might be necessary to operate the spouted bed activator near the condition of minimum spouting velocity to allow for efficient air-particle contact throughout the spouted bed. Too high of a gas velocity will force the major portion of air to pass through the central core region with little contact with the particles.

Figure 5.42 shows the BET surface area and micropore area of produced activated carbons in the spouted bed activator as a function of activation times from 1.0 to 3.0 hrs. Both BET and micropore area increase linearly with increasing in activation time and both appear to be parallel to each other over the range of activation time studied. This observation indicates that the pore development of activated carbon gasified for time less than 3.0 hrs should be contributed mainly by the creation of new pores, the majority of which is in the micropore size range. The effect of activation time on the total pore and micropore volume of the derived activated carbons are shown in Figure 5.43 and also shown in this figure is the

percentage microporosity. The plot shows that the total pore and micropore volume increase steadily with increasing of activation time and there is a tendency for the percentage microporosity to decrease slightly by about 6% when activation time is increased from 1.0 to 3.0 hrs. These results confirm that the pore development should result from the combined effect of new pore creation and enlargement of existing pores with the former giving the larger contribution.

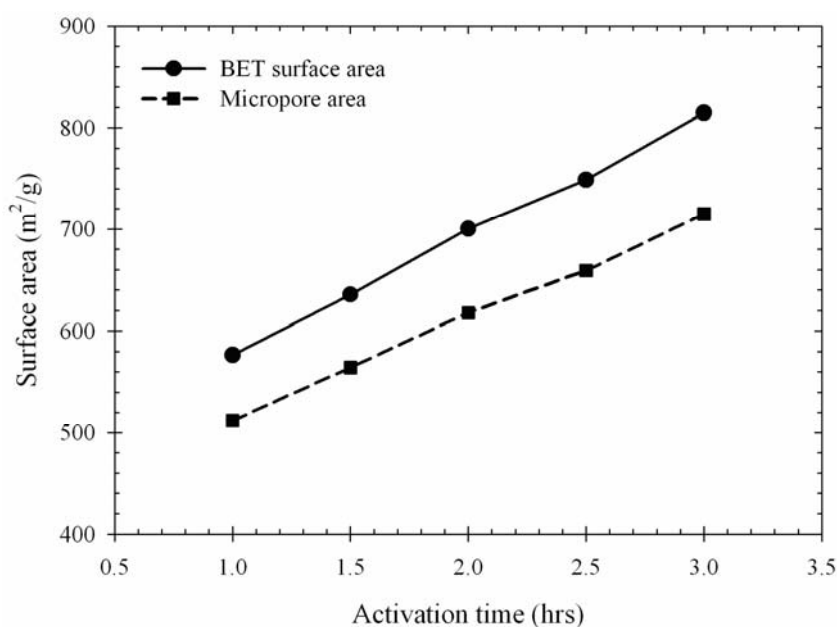


Figure 5.42 Effect of activation time on BET and micropore area of activated carbons prepared at 900°C in the batch spouted bed activator.

In order to show the effect of percentage burn-off on the porous characteristics of activated carbons prepared from the spouted bed activator, the experimental data of BET surface area, total pore volume, and percentage microporosity of produced activated carbons were replotted against the percentage burn-off and they are shown in Figure 5.44 to 5.46, respectively. For the purpose of

comparison, the experimental results of those activated carbons prepared in the tube furnace (see Chapter 3) are also shown in the same figure. Although the spouted bed activator produced the activated carbons with lower degree of burn-off compared to the tube furnace at the same activation time and temperature, the BET surface area and total pore volume of activated carbons prepared from both types of activator were not comparatively different for the same degree of char burn-off. This means that the pore evolution mechanisms of activated carbons for both types of activator are fundamentally the same. Figure 5.47 shows N_2 adsorption isotherm measured at -196°C for activated carbons prepared in the spouted bed activator. It is clear that the activated carbon exhibited the Type I isotherm which further confirms the microporous nature of the derived activated carbon.

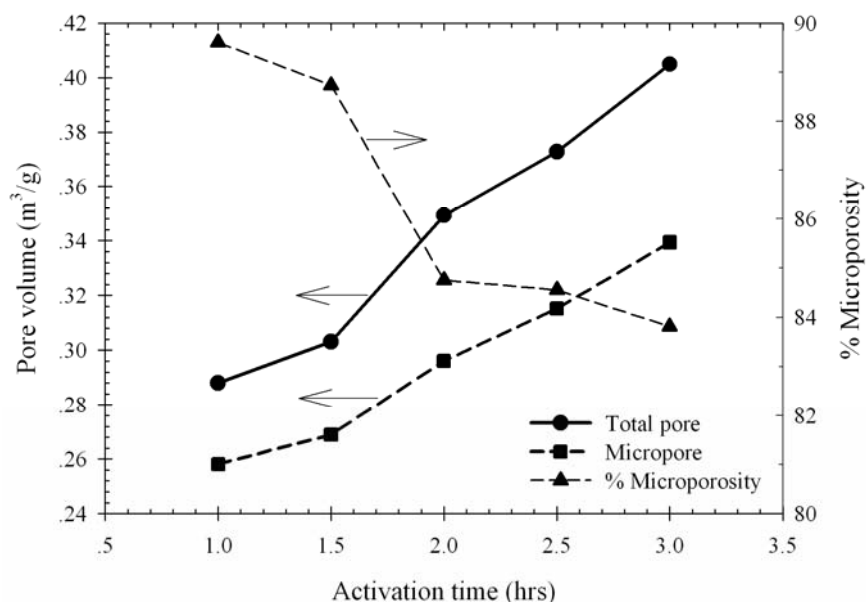


Figure 5.43 Effect of activation time on total and micropore volume, and percentage microporosity of activated carbons prepared at 900°C in the batch spouted bed activator.

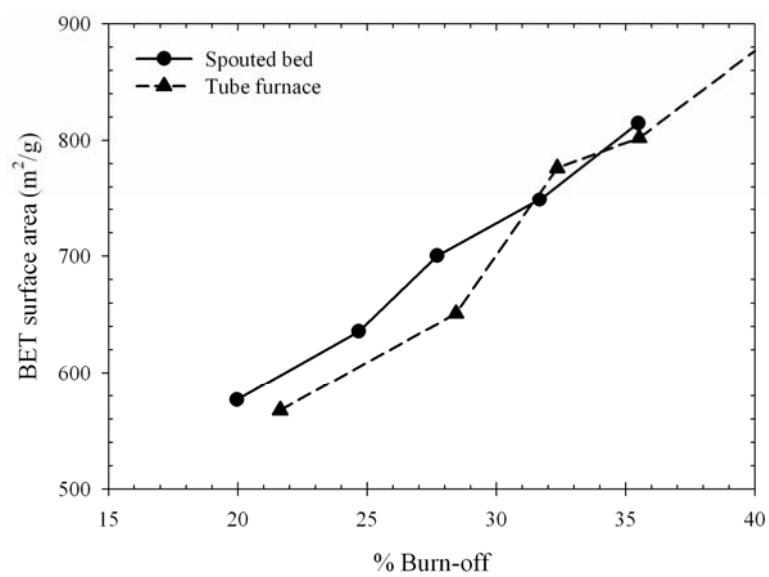


Figure 5.44 Effect Effect of char burn-off on BET surface area.

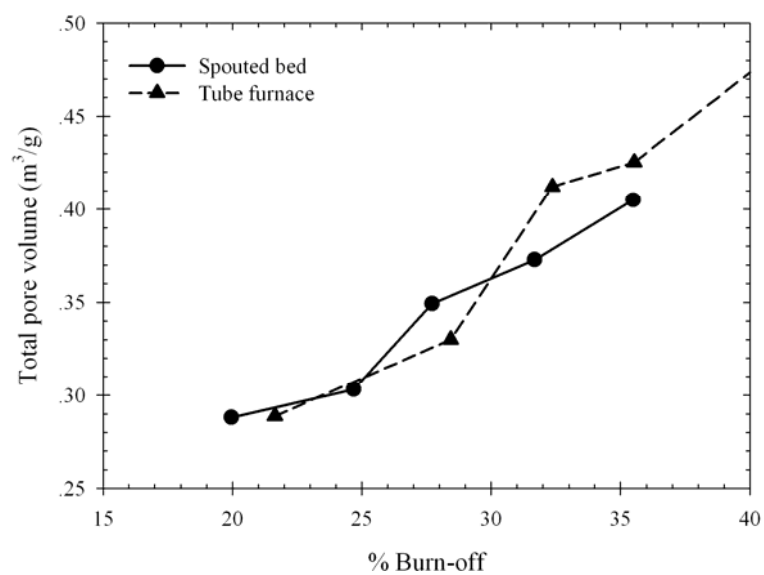


Figure 5.45 Effect of char burn-off on total pore volume.

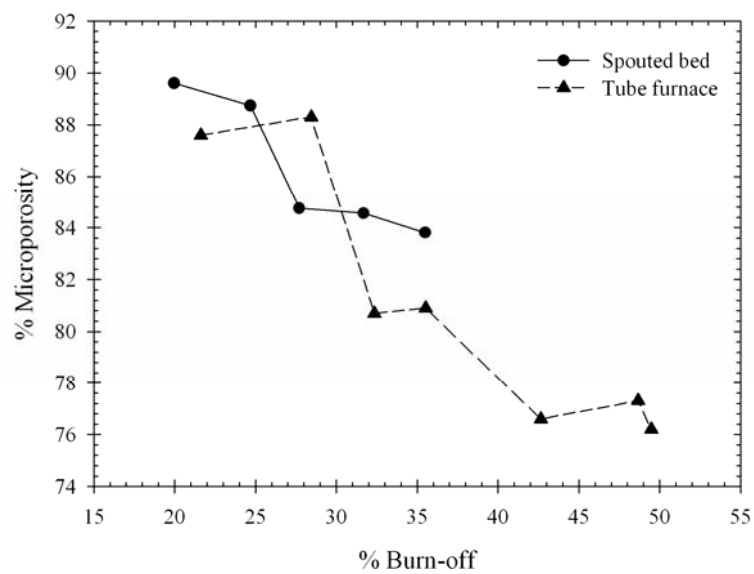


Figure 5.46 Effect of char burn-off on percentage microporosity.

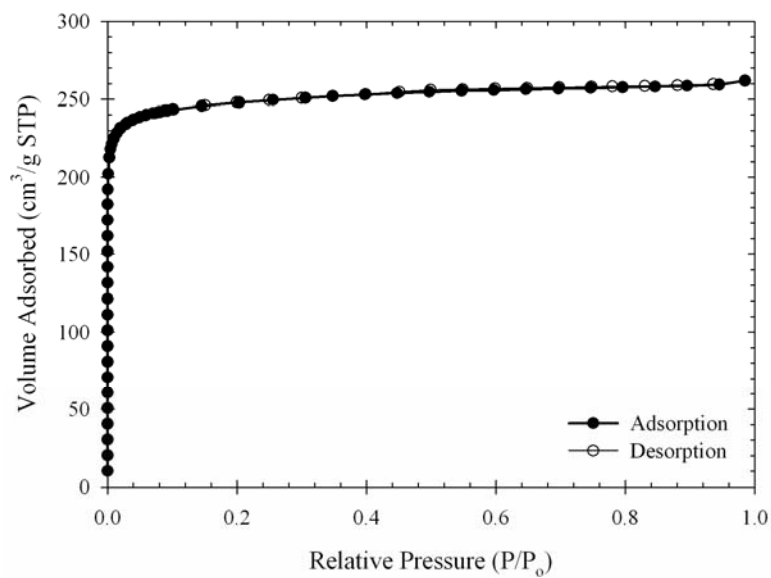


Figure 5.47 N₂ adsorption isotherm at -196°C of activated carbon prepared at 900°C for activation time of 3.0 hrs in the batch spouted bed.

5.6.3 Hydrodynamic Study of Spouted Bed by CFD Simulation

Figure 5.48 shows the simulation results of pressure drop-air flow rate relation for spouted bed with nozzle size of 7 mm, particle size of 0.7 mm, base angle of 60° and 7.2 cm of initial static bed height. For comparison, the corresponding experimental data are also shown plotted on the same figure. It is observed that pressure drop curves of both simulated and experimental results differ somewhat particularly at low air velocities. To help explain the simulated hydrodynamic behavior of spouted bed upon increasing air flow, the physical appearances of solid bed are also displayed in Figure 5.49.

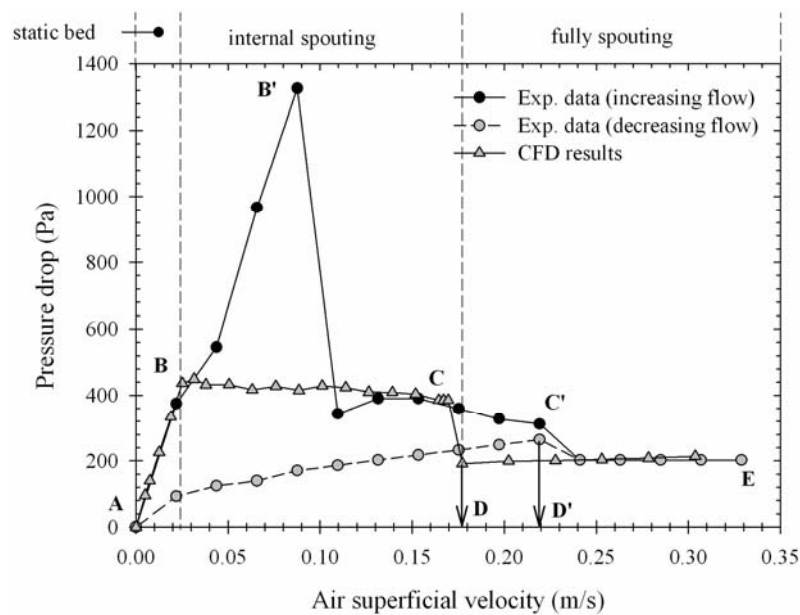


Figure 5.48 The experimental and CFD simulated results of pressure drop-air flow rate diagram.

It is seen from Figure 5.48 that at air velocity lower than 0.03 m/s, the calculated pressure drop increase linearly with air flow rate and agrees well with the

experimental data (line AB). Under this condition, no disturbance of air flow to the stagnant bed is observed. With increasing air flow through the simulated spouted bed beyond this upper limit of 0.03 m/s, e.g. at air velocity of 0.032 m/s, the creation of internal cavity above air inlet region can be observed which becomes larger when the air flow is increased (see Figure 5.49).

The elongation of this internal cavity along the flow axis leads to the decreasing of pressure drop (along BC) due to the enlargement of interface area between particle bed and the internal cavity. The fluid will flow pass the particle bed through that interface with slower velocity when the interface area is enlarged causing the decreasing in pressure drop. This behavior is different from that observed experimentally. The experimental pressure drop still increases with increasing of air flow beyond point B without disturbing the bed. This increase in pressure drop continues until the maximum value is reached (point B'). At slightly higher air flow, the bed starts to expand and immediately transforms into the loosest packed state, giving a reduction in pressure drop. It was observed experimentally that the value of maximum pressure drop depended strongly on the shape and initial packing condition of solid particles. In CFD simulation, the solid particles were assumed to have the spherical shape with uniform size. This would give less contact points among particles and hence the maximum pressure drop would occur at a lower fluid velocity and a gradual change in pressure drop is to be expected along line BC.

With only a slight increase in air flow rate beyond point C, the internal cavity breaks through the bed surface causing the reduction in pressure drop to point D at which the spouting state is fully established. This point (point D) is the minimum spouting velocity predicted by the CFD simulation which is lower than that measured

experimentally (point D'). At air flow rates higher than the minimum spouting velocity, there is no significant effect of air flow rate on the simulated pressure drop. The simulated pressure drop appears to be constant and has the same magnitude with those measured experimentally. It is noted that, for the CFD simulation, the calculated pressure drop for both increasing and decreasing step of air flow were the same and this behavior is different from that observed from the experiment. This deviation should be due to the limitation of the two-fluid model (TFM) employed in the CFD simulation in assuming spherical shape with uniform size for the dispersed solid phase. This assumption cannot represent well the system composed of non-spherical particles like palm shell particles used in this work.

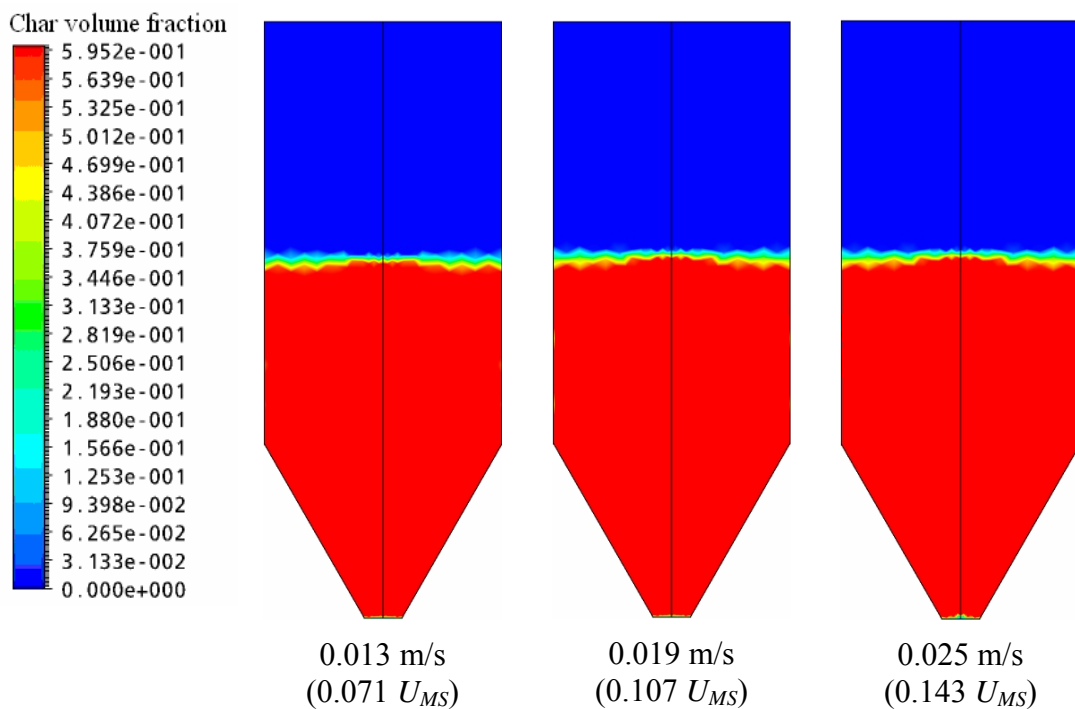


Figure 5.49 Char particle concentration distribution at several air velocities.

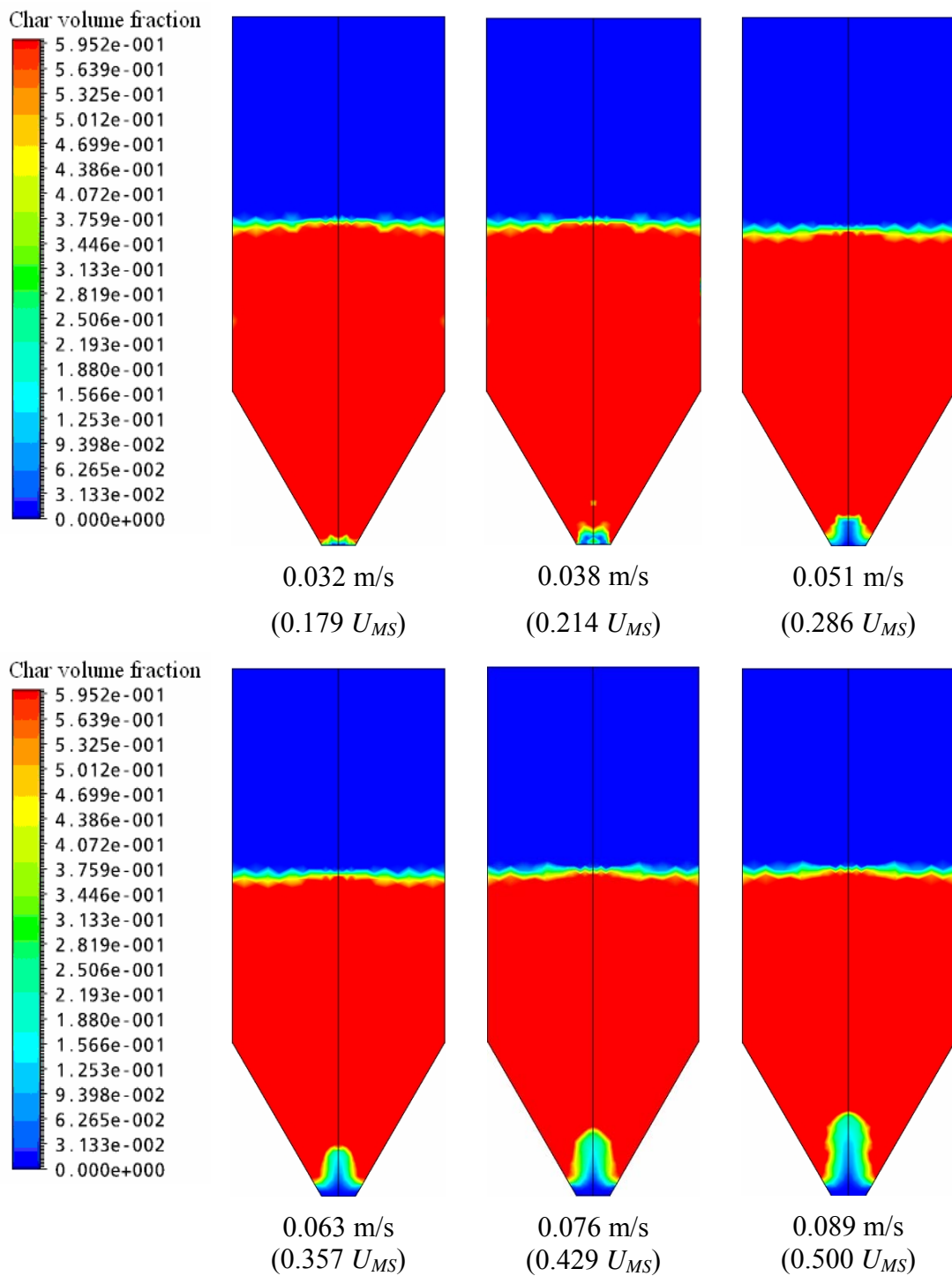


Figure 5.49 Char particle concentration distribution at several air velocities (Cont.).

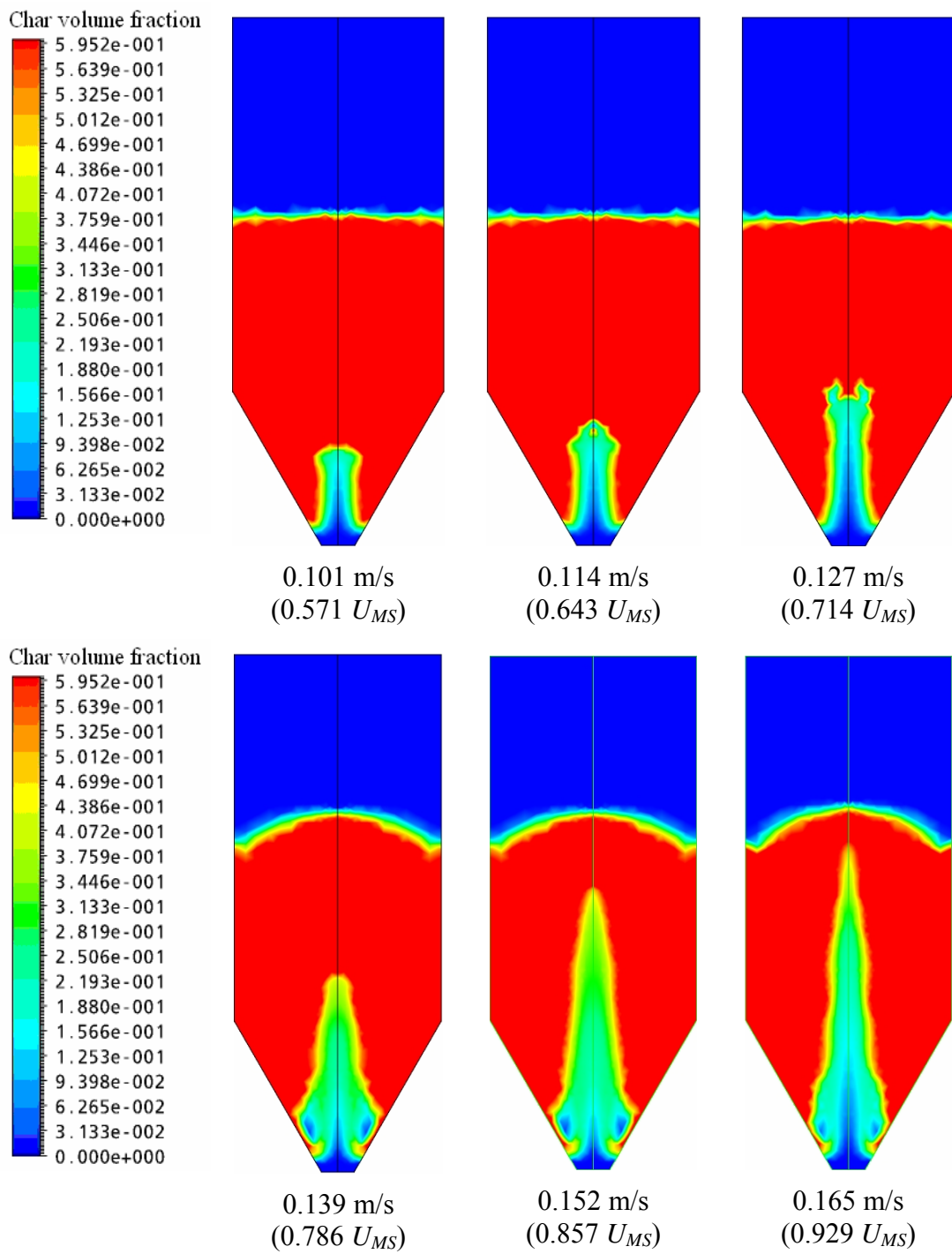


Figure 5.49 Char particle concentration distribution at several air velocities (Cont.).

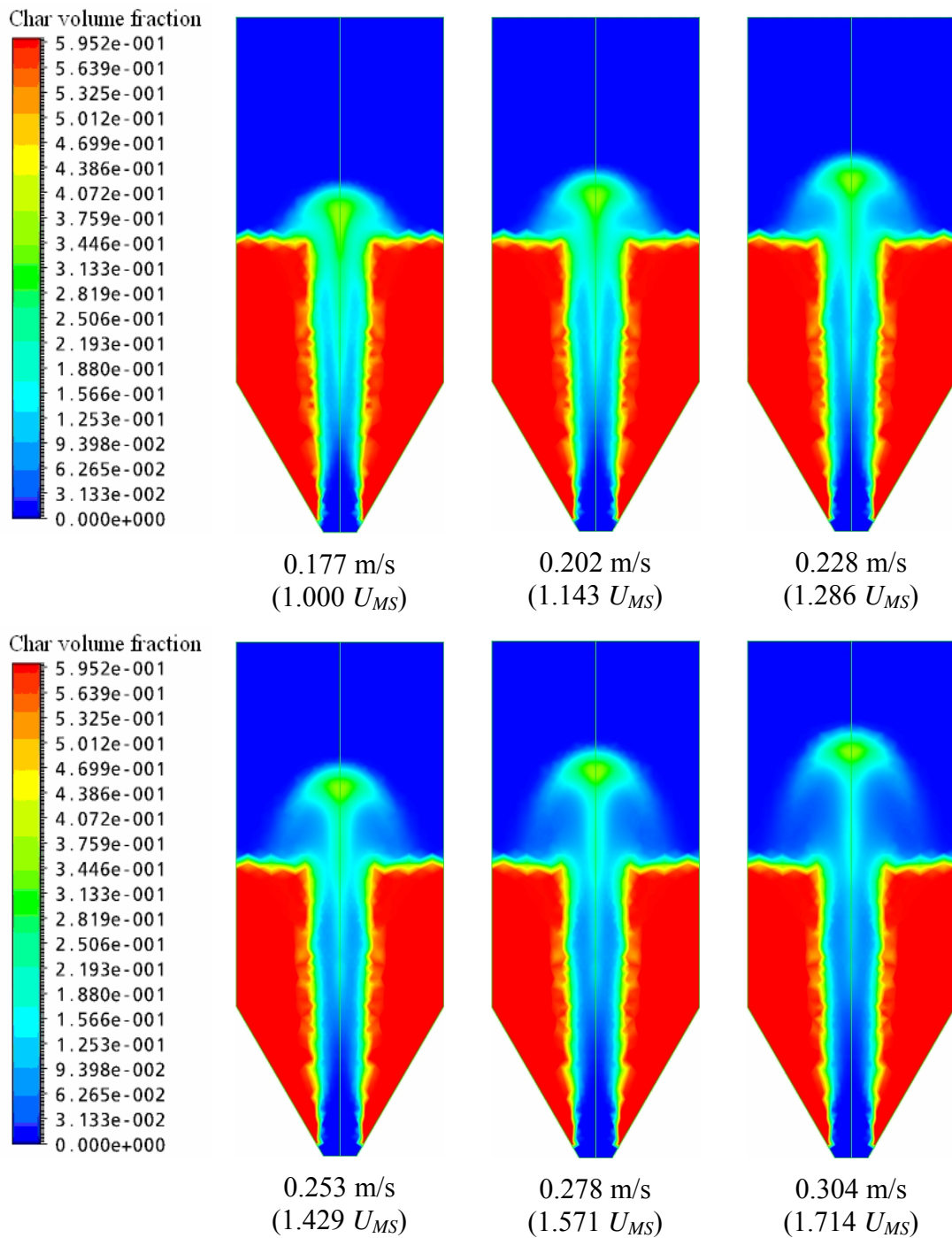


Figure 5.49 Char particle concentration distribution at several air velocities (Cont.).

The minimum spouting velocity (U_{MS}) calculated from CFD modeling is 0.177 m/s which is about 20% lower than that observed from the experiment of

0.228 m/s. This difference should be due to the limitation of CFD model in assuming spherical shape with uniform size for the bed particles. With this assumption, there is no real packing effect of bed particles on the hydrodynamic behavior of spouted bed. On the other hand, the actual char particles are irregular in shape with distribution of sizes from which the packing condition of bed particles should play an important role in the behavior of gas and solid interaction. This packing condition could cause the inter-locking of solid particles which prevents the free movement of solid particles inside the bed. As a result, higher gas flow is required to overcome this increased frictional forces between particles, enabling the formation of internal spouting core region until the full spouting condition is finally achieved. This is the reason why the simulated U_{MS} is lower than that observed experimentally. Although the simulated minimum spouting velocity is lower than the real measured value, the calculated pressure drop over the range of steady spouting exhibits the same general trend of relatively constant on increasing air velocity and agrees reasonably well with the experimental measurement (see Figure 5.48).

Figure 5.50 shows the simulated fountain heights (H_F) of spouted bed as a function of air flow rates higher than the minimum spouting velocity. The figure shows the linear increasing of the simulated fountain height, as the air flow rate is increased whereas the dense bed height remains constant as shown in Figure 5.49. This behavior of spouted bed was also observed in the experiment. Therefore, this should confirm that the CFD simulation gives the correct predictive trend for simulating fluid-solid particle flow systems such as the spouted bed system studied in this work. Also shown in the same figure is the fountain height that was measured experimentally. It is noted that the experimental fountain height is much higher than

those predicted from CFD simulation. This large deviation of the simulated fountain height is probably due to the chosen set of model parameters used in the computation such as the particle restitution coefficient, the maximum particle packing volume fraction, the quality of numerical grids created, and also the time step interval applied. The quality of numerical grids and time step are important for avoiding round-off error occurring in numerical calculation during simulation task.

It should be noted that the accuracy of CFD simulation depends largely on the model parameters used. The use of model parameters should be pre-tested with the experimental data of hydrodynamic information (i.e. minimum spouting velocity, pressure drop, solid bed voidage distribution and velocity profile of fluid and dispersed phase) to improve the accuracy of CFD simulation (Du et al., 2006). In this work, however, the complete data of solid bed voidage and velocity profile of fluid and dispersed phase were not experimentally determined. Therefore, only minimum spouting velocity and pressure drop across the bed were compared with the values predicted from the CFD simulation.

The radial distributions of air and particle velocities at different heights from air inlet are shown in Figure 5.51 and Figure 5.52, respectively, for operating air superficial velocity of $1.143U_{MS}$. It is noted that the regions of spout core and annulus zone located in these figures were estimated based on the air inlet size which approximately equal to the size of simulated spout core (see Figure 5.49). The figure shows that at region near the air inlet of the bed, air velocity is maximum at the center core of spout (see Figure 5.51 for $H = 1-3$ cm). But the maximum value of air velocity systematically shifts closer to the interface between the spout core and annulus zone at higher bed positions (see Figure 5.51 for $H = 4-6$ cm). For particle movement

behavior, there exists a velocity accelerating region near the air inlet of the bed in the spout core (see Figure 5.52 for $H = 1-3$ cm) and a decelerating region in the upper part of the bed (see Figure 5.52 for $H = 4-6$ cm).

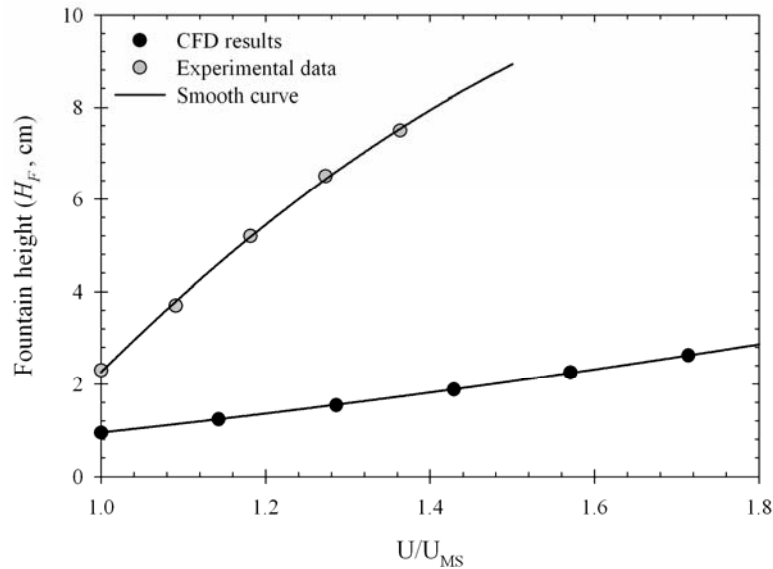


Figure 5.50 Simulated fountain height of spouted bed.

As observed from Figure 5.52, the particle velocities have their maxima at the central core of bed and becomes close to zero at the interface between spout core and annulus. At this interface, particular attention should be paid on the quality of numerical grid used in the simulation because, in actual system, the bed voidage and velocities of fluid and dispersed phase change abruptly. As a result, a rather small grid size was set for the region in the spout core, including spout-annulus interface, becoming larger in the annulus zone to reduce the error occurring from the numerical computation. This behavior of particle movement was the same as the predicted CFD result reported by Du and co-workers (2006). They employed the CFD modeling to

simulate the hydrodynamic behavior (bed voidage profile and particles velocity distribution) of cylindrical spouted bed for air-glass bead system.

Figure 5.53 shows radial distribution of bed voidage at different heights (H) from the air inlet for air velocity of $1.143U_{MS}$. The simulated voidage profiles show that in the spout core, the bed voidage decrease with the increasing height from the air inlet. There exists an empty cavity at the region above air inlet and the voidage become denser at higher height. The maximum bed voidage appears at the spout core axis for the height lower than 2.0 cm and this maximum value move closer to the interface between the spout core and annulus zone when the height is more than 2.0 cm. This observation indicates that there is the formation of particle core at the axis of column and at the position higher than 3.0 cm from the air inlet.

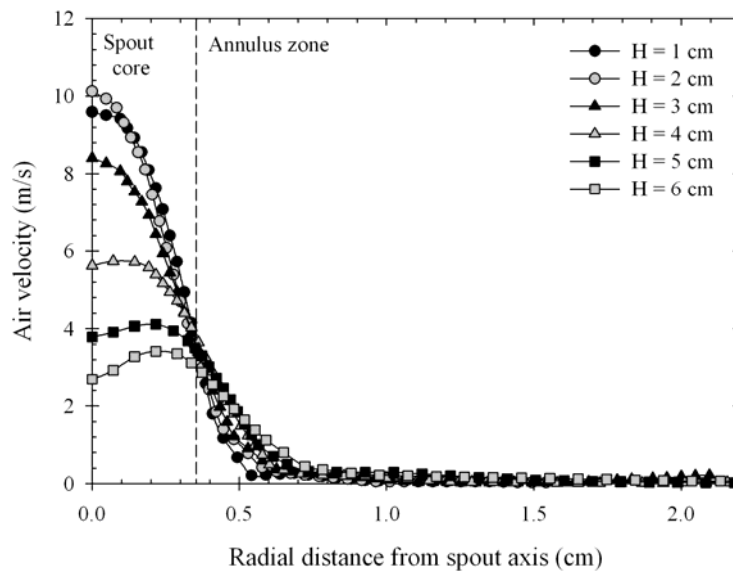


Figure 5.51 Velocity profiles of air at air velocity of $1.143U_{MS}$.

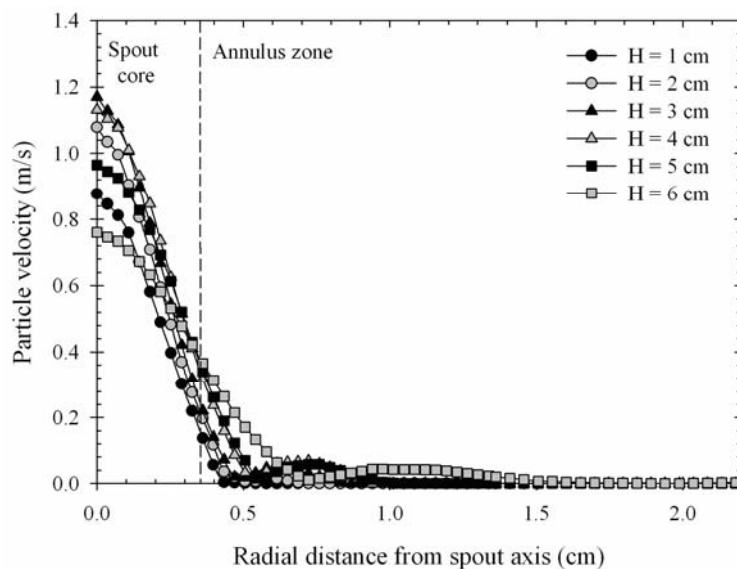


Figure 5.52 Velocity profiles of palm-shell particles at air velocity of $1.143U_{MS}$.

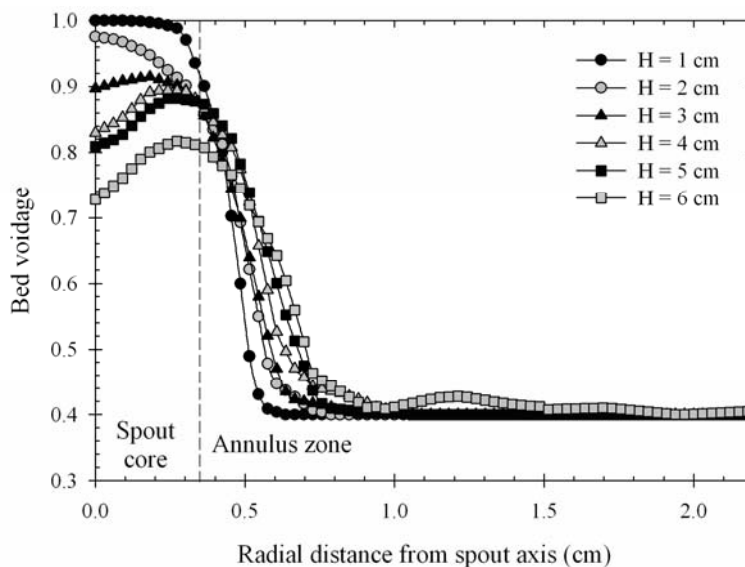


Figure 5.53 Bed voidage profiles of palm-shell char particles at air velocity of $1.143U_{MS}$.

In order to show the influence of operating air velocity on the velocity profile of air and char particles, the radial distribution of velocities at air average

velocity varying from $1.00U_{MS}$ to $1.714U_{MS}$ at several positions above air inlet are shown in Figure 5.54 to 5.59 and Figure 5.60 to 5.65 for air and char particles, respectively. These figures show that, for both air and char particles, the increasing in air flow rate has no effect on the air and particle velocity profiles in the annulus zone. The velocities in the annulus zone of both phase is nearly constant for all position above air inlet when the higher flow of air is fed into the spouted bed. However, as seen the particle velocity in the spout core increases steadily with the increasing of air flow rate.

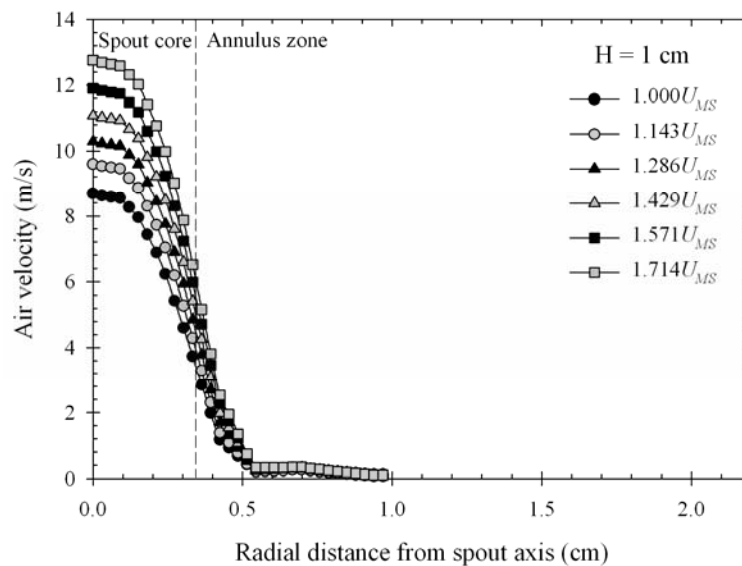


Figure 5.54 Bed voidage profiles of palm-shell char particles at air velocity of $1.143U_{MS}$ for 1.0 cm of height from air inlet.

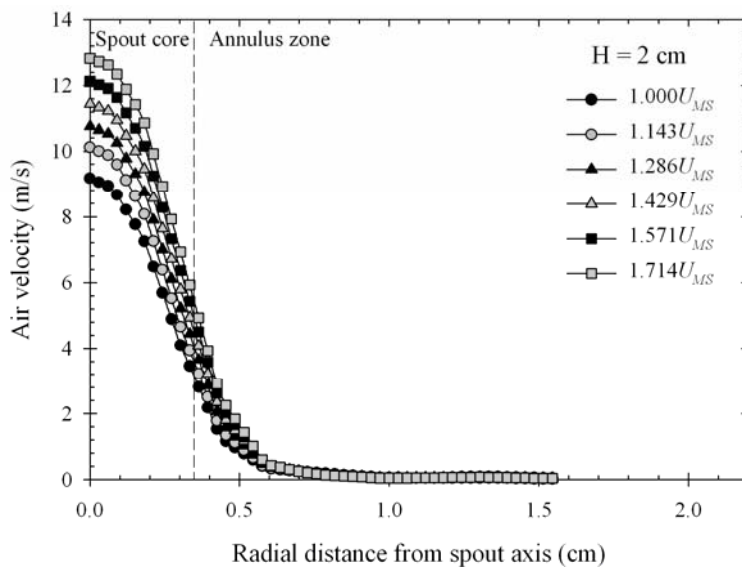


Figure 5.55 Bed voidage profiles of palm-shell char particles at air velocity of $1.143U_{MS}$ for 2.0 cm of height from air inlet.

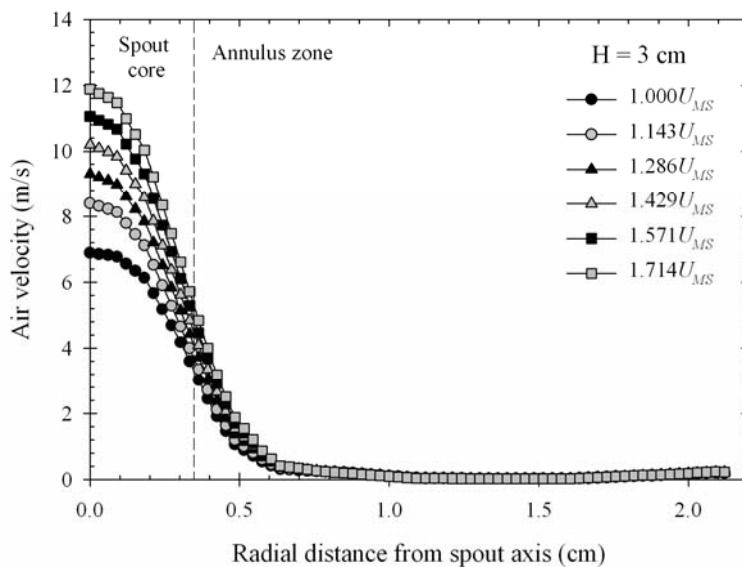


Figure 5.56 Bed voidage profiles of palm-shell char particles at air velocity of $1.143U_{MS}$ for 3.0 cm of height from air inlet.

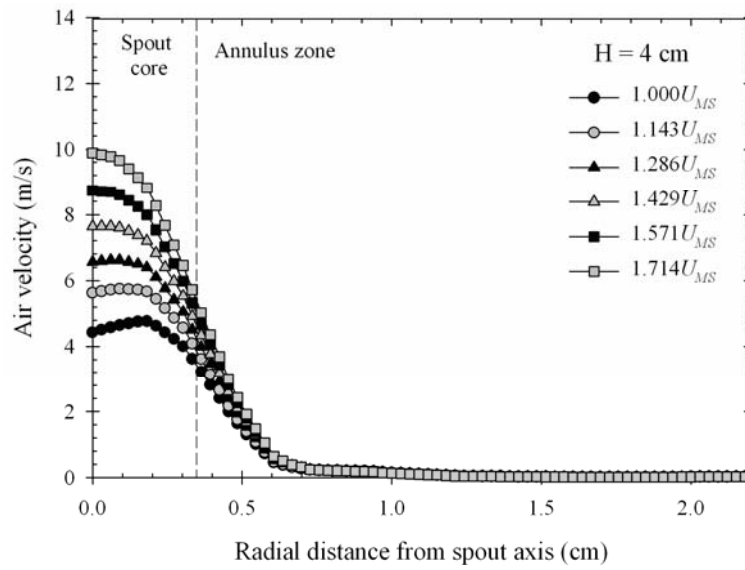


Figure 5.57 Bed voidage profiles of palm-shell char particles at air velocity of $1.143U_{MS}$ for 4.0 cm of height from air inlet.

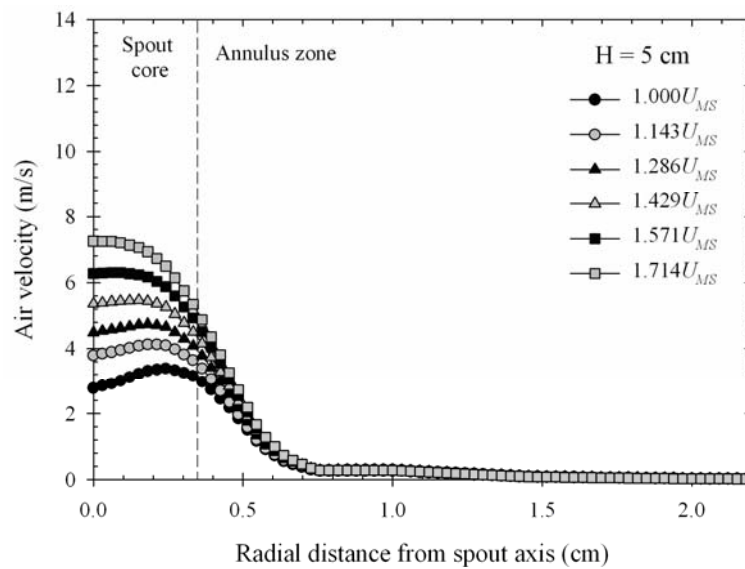


Figure 5.58 Bed voidage profiles of palm-shell char particles at air velocity of $1.143U_{MS}$ for 5.0 cm of height from air inlet.

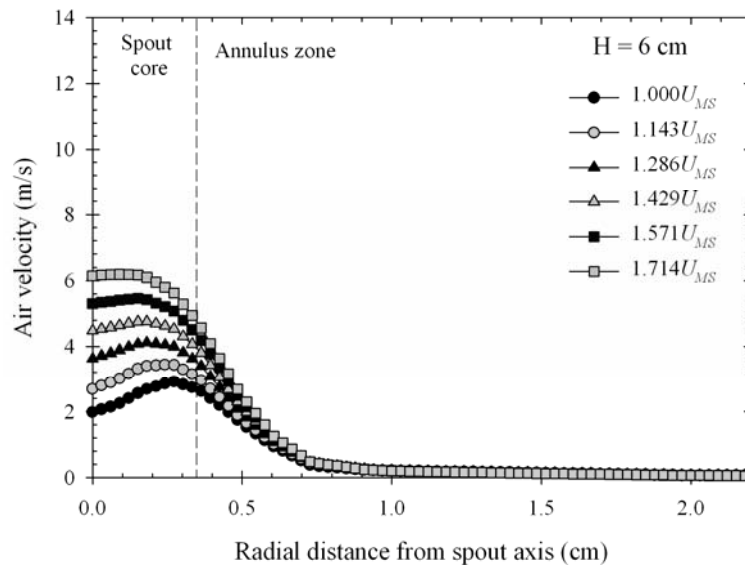


Figure 5.59 Bed voidage profiles of palm-shell char particles at air velocity of $1.143U_{MS}$ for 1.0 cm of height from air inlet.

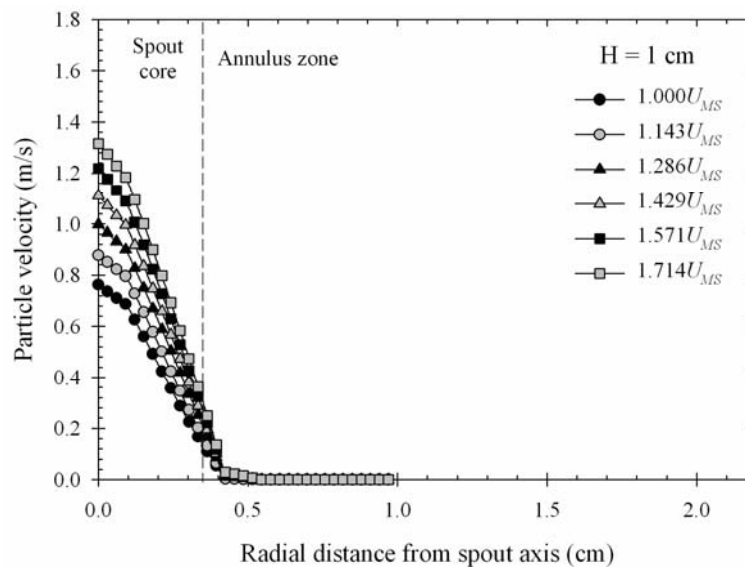


Figure 5.60 Bed voidage profiles of palm-shell char particles at air velocity of $1.000U_{MS}$ to $1.714U_{MS}$ for 1.0 cm of heights from air inlet.

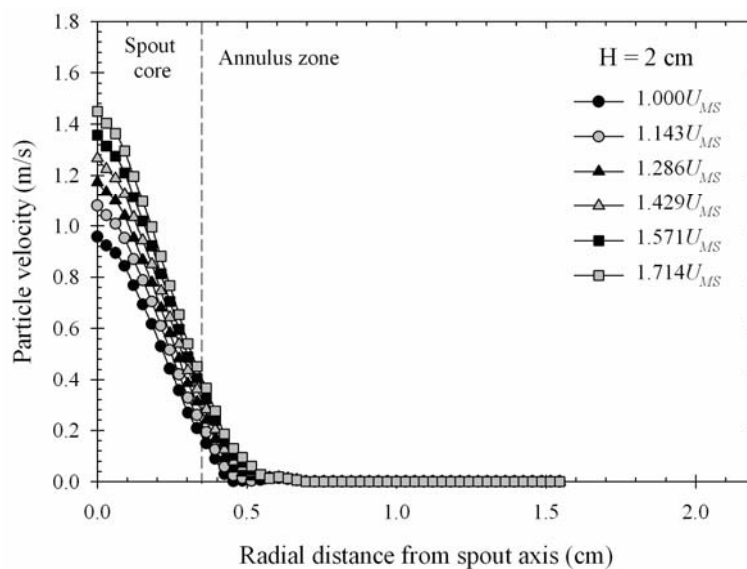


Figure 5.61 Bed voidage profiles of palm-shell char particles at air velocity of $1.000U_{MS}$ to $1.714U_{MS}$ for 2.0 cm of heights from air inlet.

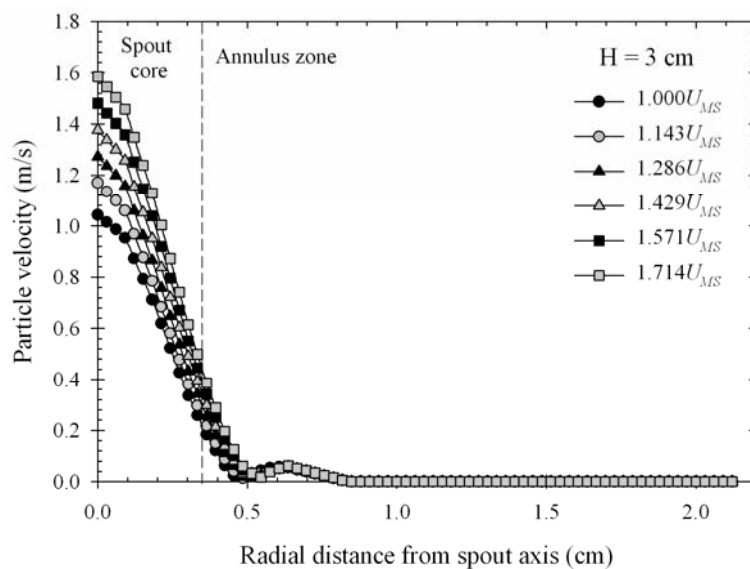


Figure 5.62 Bed voidage profiles of palm-shell char particles at air velocity of $1.000U_{MS}$ to $1.714U_{MS}$ for 3.0 cm of heights from air inlet.

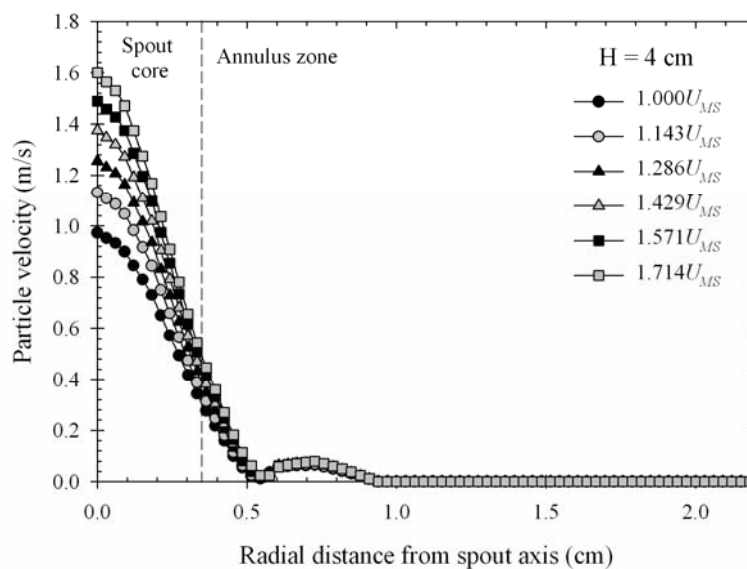


Figure 5.63 Bed voidage profiles of palm-shell char particles at air velocity of $1.000U_{MS}$ to $1.714U_{MS}$ for 4.0 cm of heights from air inlet.

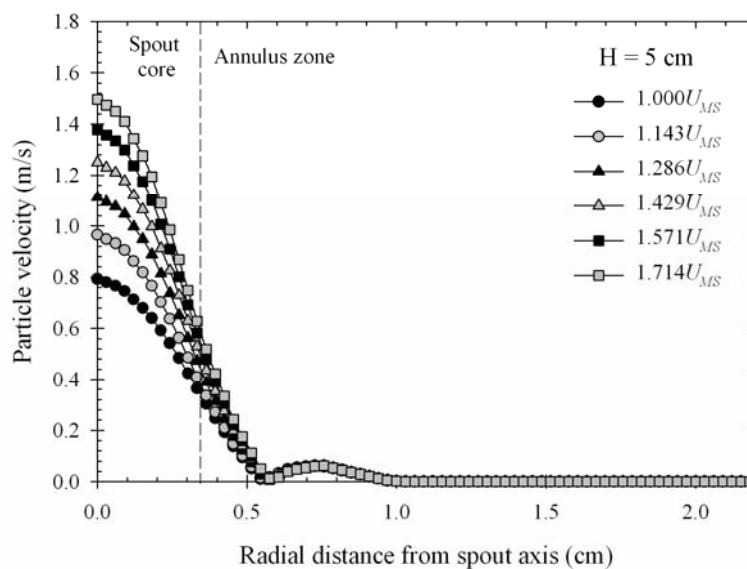


Figure 5.64 Bed voidage profiles of palm-shell char particles at air velocity of $1.000U_{MS}$ to $1.714U_{MS}$ for 5.0 cm of heights from air inlet.

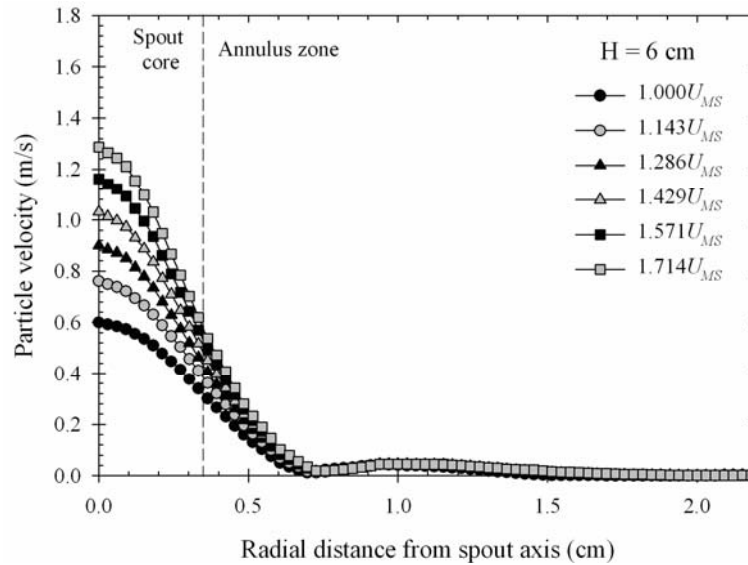


Figure 5.65 Bed voidage profiles of palm-shell char particles at air velocity of $1.000U_{MS}$ to $1.714U_{MS}$ for 6.0 cm of heights from air inlet.

The circulation pattern of char particles in the spouted bed obtained from the CFD simulation is shown in Figure 5.66. The arrow heads represent the moving direction of char particles inside the bed. It is clear that the char particles move upward in the spout core region until they reach the top of fountain and then rain down onto the annulus surface. After that, the particles move downward in the annulus zone. The figure also shows the moving of char particles from annulus zone into the spout core through the interface. Figure 5.67 shows the circulation pattern of air in the spouted bed determined from the CFD modeling. The direction of movement of air is represented by the arrow heads. The figure shows that most air flows upwardly in the spout core region and the rest flows into the annulus zone through the interface. As observed, the flow of air through the fountain zone of spouted bed particles has caused the wake formation of reverse air flow behind the showering particles.

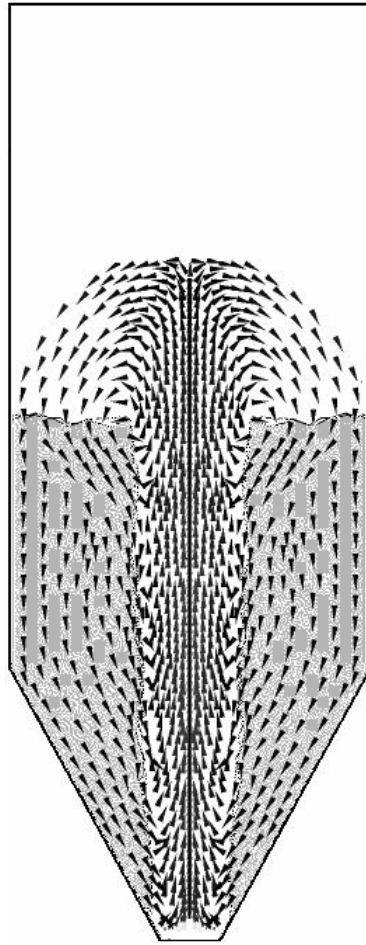


Figure 5.66 Circulation pattern of char particles at air velocity of $1.143U_{MS}$

Although, the CFD simulation results provide some deviations in predicting the hydrodynamic information from the experimental data, such as the minimum spouting velocity, pressure drop-gas flow diagram, and fountain height, the circulation flow pattern of both air and char particle agree considerably well with those reported by Mathur and Epstein (1974). This inconsistency of hydrodynamic data can be circumvented in part by improving the quality of numerical grid used, adjusting the model parameters, and improving the governing equations applied (such as drag force model, turbulent model, etc.). The quality of numerical grid can be

improved by reducing the grid size or adjusting grid size distribution in geometry. Higher quality of numerical grid helps to reduce round-off error occurring in the computational procedure. Generally, the complete experimental data of hydrodynamic information (such as velocity profile, bed voidage, etc) are necessary for pre-testing the accuracy of the model parameters and the governing equations used.

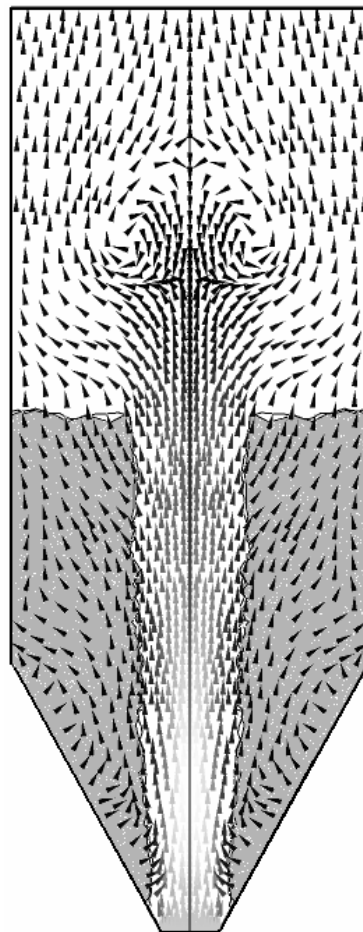


Figure 5.67 Circulation pattern of air at air velocity of $1.143U_{MS}$

5.6.4 CFD Simulation of Spouted Bed Activator

The primary purpose of this part of study was to extend the CFD technique to predict the extent of CO₂ gasification of palm shell char in the spouted bed activator. Generally, the hydrodynamic data of gas and dispersed solid phases, including velocity and concentration profiles, and also pressure gradient data, are required for simulating the kinetics of activation reaction between the activation gas and solid char of the spouted bed activator. The CFD simulation from previous hydrodynamic study was used to provide these hydrodynamic data for the spouted bed activator.

The initial spouting state ($t = 0$) of a simulated system, as displayed in Figure 5.68, was first achieved by running the CFX program in the same fashion as the previous section of hydrodynamic study but without gasification reaction (reaction rate constant is assumed to be zero) and pure carbon dioxide was used instead of air. This simulation was carried out by fixing the system temperature and CO₂ flow rate at 900°C and 0.182 m/s of superficial velocity, respectively, which were the same as those employed in the activation experiment. The time step interval used in this CFD simulation was set to be 10⁻⁴ s. The simulation system was considered to be at steady state when the RMS of residuals were less than 10⁻⁵.

In running CFD program, the CO₂ activation scheme of palm-shell char in the spouted bed activator was simulated by assuming the simplest form of overall first-order reaction with respect only to the molar concentration of CO₂ in the gas phase. The extent of activation reaction was investigated by computing the calculated char burn-off for a series of simulated activation time. This percentage of char burn-off was calculated from the simulated concentration data of char particles inside the

spouted bed activator. The concentration of char particles in each numerical grid was multiplied by the volume of grid to obtain the corresponding mass of char. All calculated char mass of all numerical grids inside the geometry were sum to provide the total mass of char remaining in the activator. Next, the percentage char burn-off is then calculated using Equation (5.41).

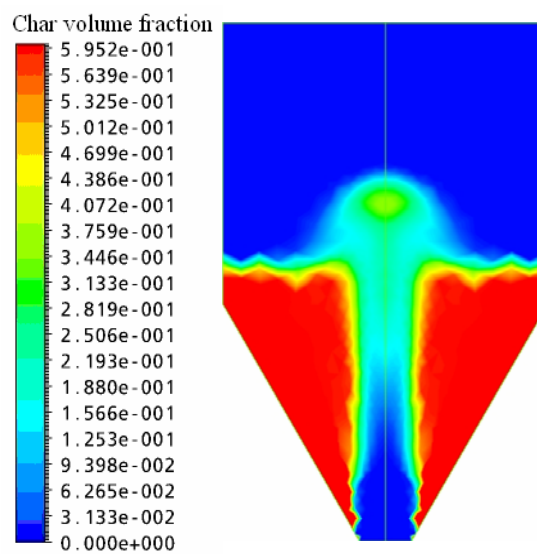


Figure 5.68 Steady-state concentration profile of palm-shell char at $t = 0$ in the spouted bed activator

The effective rate constant (K) of the gasification rate equation (see Equation (5.37)) was found to be $7.57 \times 10^1 \text{ s}^{-1}$. This rate constant was then substituted into the rate equation to give:

$$\begin{aligned} \text{Rate} &= K[\text{CO}_2] \\ &= [7.57 \times 10^1 \text{ s}^{-1}][\text{CO}_2] \end{aligned} \quad (5.56)$$

where $[\text{CO}_2]$ is the molar concentration of CO_2 in the unit of mole/ m^3 .

The CFD calculation was further performed by using the rate equation expressed in Equation (5.56) for the next activation time up to 180 min. The comparison between the experimental and simulated results of char burn-offs at various activation times up to 180 min is shown in Figure 5.69. Excellent agreement between the CFD simulation results and the experimental data for the range of activation time studied can be observed. This indicates that it is logical to describe the gasification reaction scheme of palm-shell char in the spouted bed system by the overall simple first-order reaction with respect to molar concentration of CO_2 . The simulated results of palm-shell char concentration profiles at time 30, 60, 90, 120, 150 and 180 min in the spouted bed activator are given in Figure 5.70.

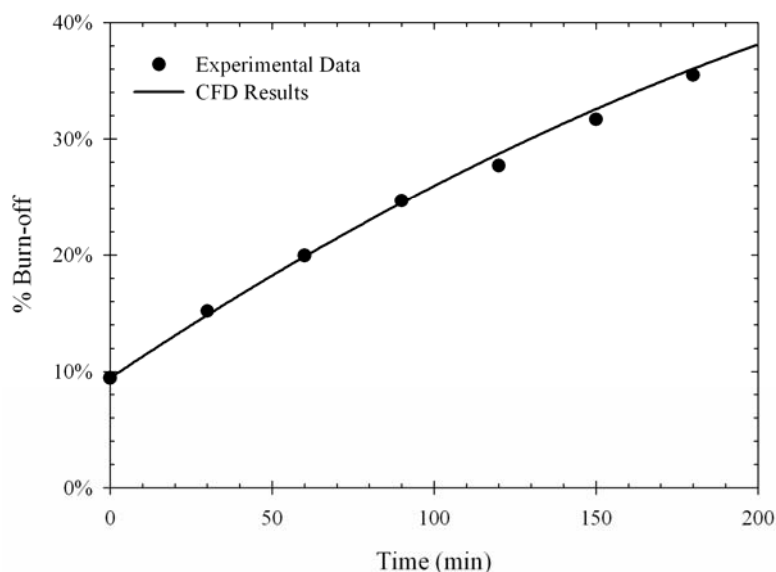


Figure 5.69 Experimental and CFD simulated char burn-off gasified as a function of activation time in the spouted bed activator

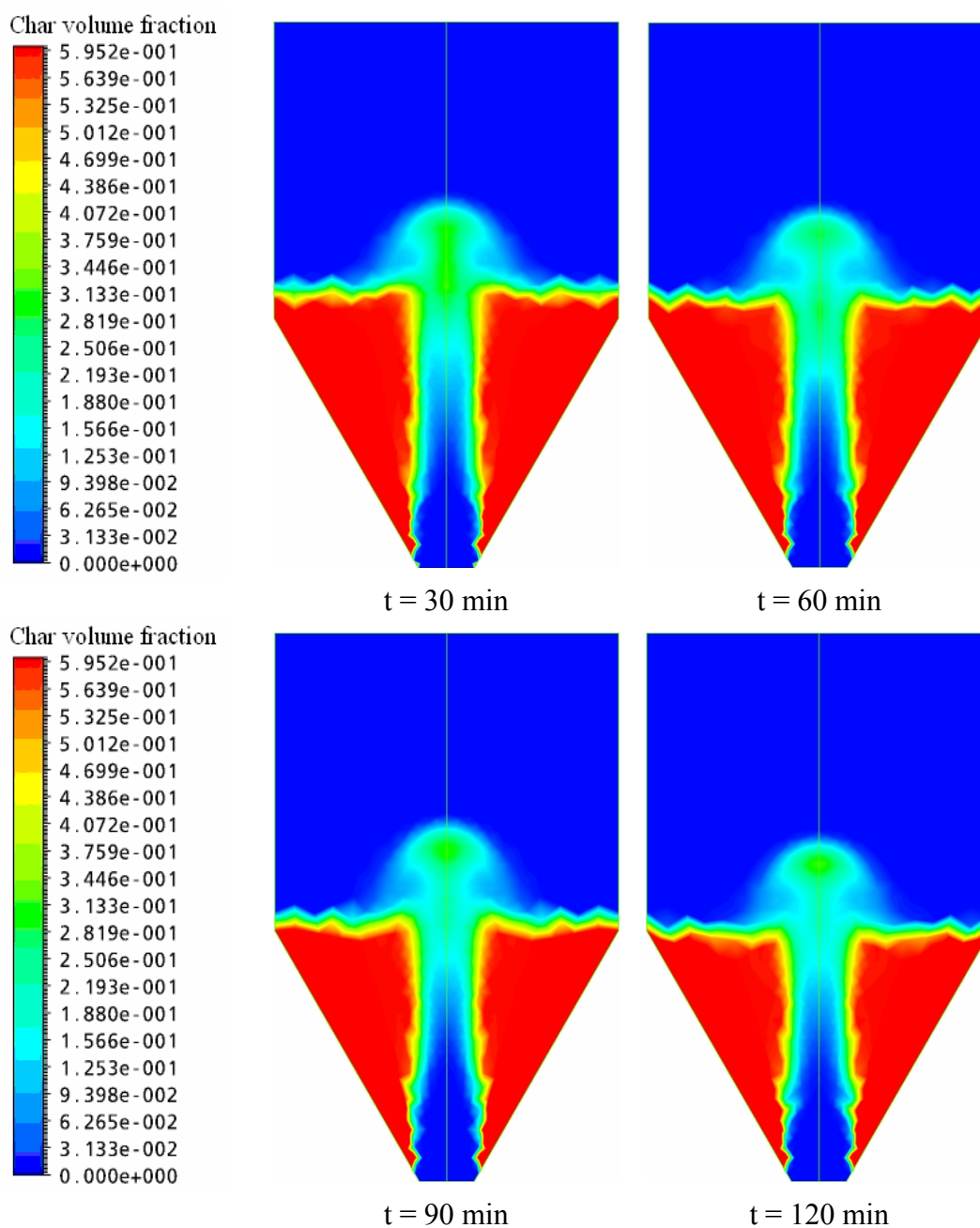


Figure 5.70 Concentration profiles of palm-shell char at different activation times in the spouted bed activator

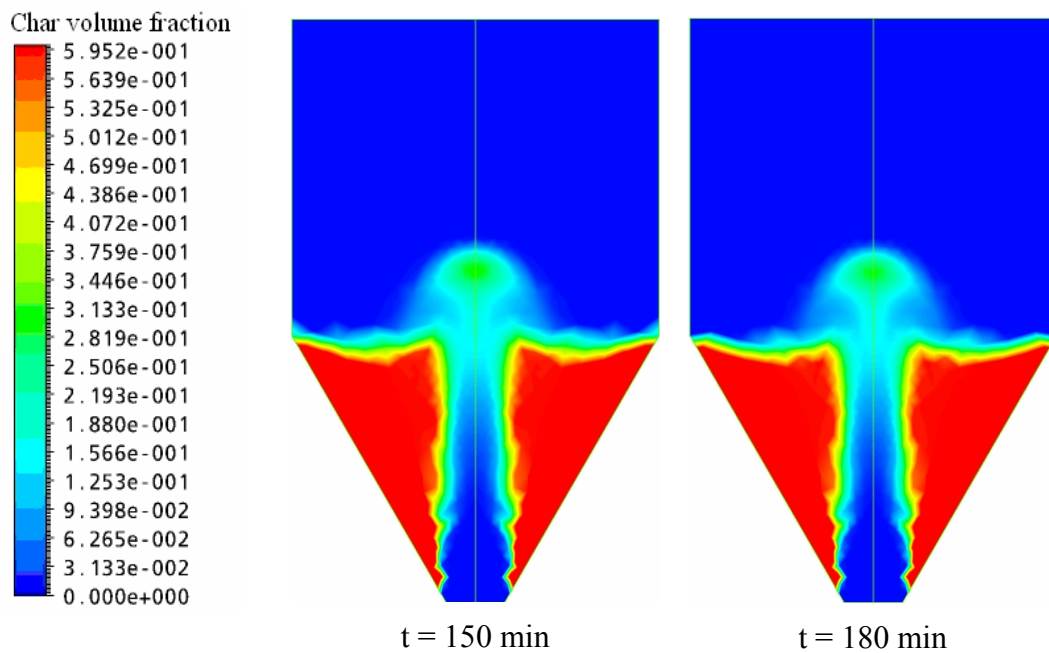


Figure 5.70 Concentration profiles of palm-shell char at different activation times in the spouted bed activator (Cont.)

By combining the modified activation model developed in Chapter 4 with the CFD simulation results of the spouted bed activator, the BET surface area and total pore volume of activated carbons for various char burn-offs can be estimated and compared with experimental results. The model parameters (i.e. total number of crystallites, number of graphene layer per crystallite, interspacing between layers, and number of non-reactive layer) of the modified JDTT model were the same as those used in Chapter 4. As shown in Figure 5.71 and 5.72, the simulated results agree extremely well, within the limit of experimental error, with the experimental data of BET surface area and total pore volume for the whole range of char burn-off studied in this work.

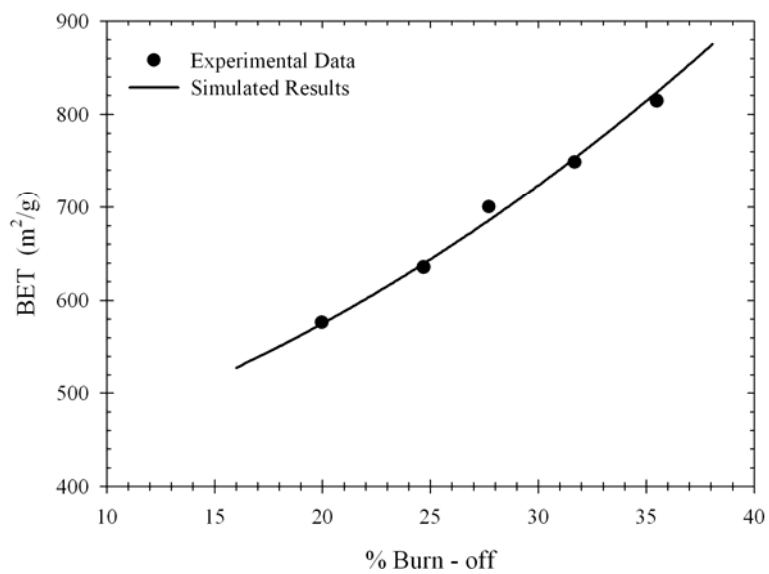


Figure 5.71 Experimental and simulated BET surface area of activated carbons prepared from palm shell in spouted bed activator.

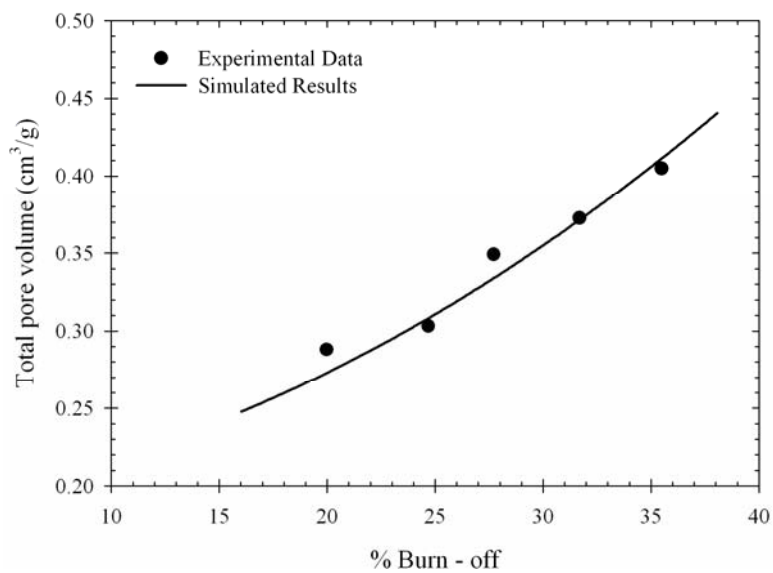


Figure 5.72 Experimental and simulated total pore volume of activated carbons prepared from palm shell in spouted bed activator.

Although the CFD simulation is capable of describing the hydrodynamics and activation scheme of activated carbon in the spouted bed activator, the extremely long computation time is still the major difficulty. By using high-speed PC to perform the CFD simulation of spouted bed activator for actual activation time of 3.0 hrs, it took several months for only one run of simulation condition using a time step interval of 10^{-4} s. In principle, the calculation time could be reduced by increasing the time step interval or numerical grid size. However, the increase in computational time step and numerical grid size could lead to the increasing in round-off error occurring in numerical calculation during the simulation scheme, which in turn could affect significantly on the convergence of simulation results.

5.7 Conclusions

The CFD technique was successfully used for simulating the hydrodynamic behavior and activation scheme of oil-palm shell based activated carbon prepared in a cylindrical spouted bed activator using CO₂ as the activation agent. The two-fluid approach with relevant governing equations (i.e. conservation equation of mass and momentum, KTGF model, drag force model, turbulence model, and kinetics of gasification reaction) was employed in the CFD simulation to predict the velocity profiles of fluid (i.e. air or CO₂) and dispersed-solid (i.e. palm shell char) phases, bed voidage distribution, and kinetic characteristics of the activation process. The validity of the CFD modeling in the prediction of hydrodynamic behavior was examined by comparing the predicted CFD results with the experimental data of spouted bed for air-palm shell char particle system measured at room temperature. Subsequently, the

CFD simulation with the same model parameters (such as restitution coefficient, maximum particle packing volume fraction, etc) as those derived from the hydrodynamic study was used for describing the kinetic scheme of activation process in the spouted bed activator. The predicted CFD results of the degree of char burn-off for several periods of activation time were also compared with the experimental data. The following conclusion can be drawn from this study.

- From the experimental results of hydrodynamic study of spouted bed, the increasing in initial static bed height, particle size and gas inlet diameter of spouted bed led to the increasing in the minimum spouting velocity of fluid.
- The dimensionless correlation for predicting the minimum spouting velocity of spouted bed for air-palm shell char particle system was proposed as the following.

$$U_{MS} = 1.239(2gH_B)^{0.287} \left(\frac{d_P}{D_C}\right)^{0.891} \left(\frac{D_I}{D_C}\right)^{0.263} \left[\frac{\rho_P - \rho_f}{\rho_f}\right]^{0.373}$$

- The correlation equation derived based on the theory of a turbulent free-jet flow for predicting the minimum spouting velocity of spouted bed was also proposed in this work as the following

$$U_{MS} = \frac{1}{0.184(D_I/H_S)^{0.740}} \sqrt{\frac{\rho_P g d_P \varepsilon_P^3}{1.75 \rho_F}}$$

This correlation was further modified to obtain a new semi-empirical correlation to make it more flexible and to improve its capability in predicting the minimum spouting velocity, as shown in the following equation

$$U_{MS} = 0.70 \left(\frac{D_I}{D_C} \right)^{1.501} \left(\frac{H_S}{D_C} \right)^{-0.309} \sqrt{\frac{\rho_P g d_P \varepsilon_P^3}{1.75 \rho_F}}$$

- The simulation on hydrodynamic behavior of spouted bed was effectively performed using the commercial CFD code software, CFX 10.0. By considering the pressure drop-air flow diagram predicted from the CFD simulation as compared to those measured experimentally, the simulation showed the difference in the transition mechanism of solid bed from static to the spouting condition. The CFD modeling predicted the minimum spouting velocity of air to be lower than that measured experimentally. The predicted hydrodynamic information of fluid and dispersed solid phase in the spouted bed, including velocity profile, bed voidage distribution, and pressure drop across the bed, have also been reported.

- The spouted bed activator (with geometric dimensions: 40 mm of cylindrical vessel diameter, 7.0 mm of gas inlet size, and 60° for conical base angle), operated at 1.20 times the minimum spouting velocity of CO₂ (0.182 m/s of superficial velocity) and 4.0 cm of static bed height, gave the activated carbons with lower char burn-off compared to those prepared in the laboratory tube furnace at the same activation temperature and time. However, both types of activator gave comparable porous characteristics of activated carbons (BET surface area and total pore volume) for the same char burn-off.

- First order kinetic scheme with respect to molar concentration of CO₂ was adopted to describe the extent of reaction between the gasification of carbon with CO₂. By fitting the predicted char burn-off at the early stage of activation process (at activation time up to 30 min) with the experimental data, the effective rate constant (K) in the proposed rate expression was determined and found to be $7.57 \times 10^1 \text{ s}^{-1}$. The rate of gasification reaction can thus be written as the following.

$$\begin{aligned} \text{Gasification Rate} &= K[\text{CO}_2] \\ &= [7.57 \times 10^1 \text{ s}^{-1}][\text{CO}_2] \end{aligned}$$

where $[\text{CO}_2]$ is molar concentration of CO₂ in unit of mole/m³. This obtained effective rate constant was then employed to predict the char burn-off for the next longer activation time up to 180 min. The overall prediction of char burn-off agreed very well with the experimental data over the entire range of activation time studied.

- The activation model proposed in Chapter 4 was combined with the predicted char burn-off results to estimate the porous properties (internal surface area and total pore volume) of activated carbons prepared in the spouted bed activator and the agreement with experimental determinations was satisfactory.

5.8 References

Abdul Salam, P. and Bhattacharya, S.C. (2006). A comparative hydrodynamic study of two types of spouted bed reactor designs. **Chemical Engineering Science** 61: 1946-1957.

- Adegoroye, A., Paterson, N., Li, X., Morgan, T., Herod, A.A., Dugwell, D.R. and Kandiyoti, R. (2004). The characterisation of tars produced during the gasification of sewage sludge in a spouted bed reactor. **Fuel** 83: 1949-1960.
- Al-Mayman, S.I. and Al-Zahrani, S.M. (2003). Catalytic cracking of gas oils in electromagnetic fields: reactor design and performance. **Fuel Processing Technology** 80: 169-182.
- Arabiourrutia, M., Lopez, G., Elordi, G., Olazar, M., Aguado, R. and Bilbao, J. (2007). Product distribution obtained in pyrolysis of tyres in a conical spouted bed reactor. **Chemical Engineering Science** 62: 5271-5275.
- Benali, M. and Amazouz, M. (2006). Drying of vegetable starch solutions on inert particles: Quality and energy aspects. **Journal of Food Engineering** 74: 484-489.
- Benyahia, S., Arastoopour, H., Knowlton, T.M. and Massah, H. (2000). Simulation of particles and gas flow behavior in the riser section of a circulating fluidized bed using kinetic theory approach for the particulate phase. **Powder Technology** 112: 24-33.
- Chu, K.W. and Yu, A.B. (2008). Numerical simulation of complex particle–fluid flows. **Powder Technology** 179: 104-114.
- Dalai, K.A., Zaman, J., Hall, E.S. and Tollefson, E.L. (1996). Preparation of activated carbon from Canadian coals using a fixed-bed reactor and a spouted bed-kiln system. **Fuel** 75: 227-237.
- Devahastin, S. and Mujumdar, A.S. (2001). Some hydrodynamic and mixing characteristics of a pulsed spouted bed dryer. **Powder Technology** 117: 189-197.

- Ding, J. and Gidaspow, D. (1990). A bubbling fluidization model using kinetic theory of granular flow. **AIChE Journal** 36: 523-538.
- Do, D.D. (1998). **Adsorption analysis: equilibria and kinetics**. London: Imperial College Press.
- Du, W., Bao, X., Xu, J. and Wei, W. (2006). Computational fluid dynamics (CFD) modeling of spouted bed: Influence of frictional stress, maximum packing limit and coefficient of restitution of particles. **Chemical Engineering Science** 61: 4558-4570.
- Elordi, G., Olazar, M., Aguado, R., Lopez, G. and Bilbao, J. (2007a). Catalytic pyrolysis of high density polyethylene in a conical spouted bed reactor. **Journal of Analytical and Applied Pyrolysis** 79: 450-455.
- Elordi, G., Lopez, G., Olazar, M., Aguado, R. and Bilbao, J. (2007b). Product distribution modelling in the thermal pyrolysis of high density polyethylene. **Journal of Hazardous Materials** 144: 708-714.
- Epstein, N. and Grace J.R. (1997). Spouting of particulate solids. In: M.E. Fayed and L. Otten (eds). **Handbook of powder Science and Technology** (pp532-567). New York: Chapman and Hill.
- Ergun, S. (1952). Fluid flow through packed columns. **Chemical Engineering Progress** 48: 89-94.
- Gidaspow, D. (1994). **Multiphase flow and fluidization : Continuum and kinetic theory descriptions**. Boston: Academic Press.
- He, Y.L., Qin, S.Z., Lim, C.J. and Grace, J.R. (1994). Particle velocity profiles and solid flow pattern in spouted beds. **Canadian Journal of Chemical Engineering** 72: 561-568.

- Hoque, M.M. and Bhattacharya, S.C. (2001). Fuel characteristics of gasified coconut shell in a fluidized and a spouted bed reactor. **Energy** 26: 101-110.
- Jones, W.P. and Launder, B.E. (1972). The prediction of laminarization with a two-equation model of turbulence. **International Journal of Heat and Mass Transfer** 15: 301-314.
- Juarez, F., Monceau, D., Tetard, D., Pieraggi, B. and Vahlas, C. (2003). Chemical vapor deposition of ruthenium on NiCoCrAlYTa powders followed by thermal oxidation of the sintered coupons. **Surface and Coatings Technology** 163-164: 44-49.
- King, D.F. and Harrison, D. (1980). The minimum spouting velocity of a spouted bed at elevated pressure. **Powder Technology** 26: 103-107.
- Konduri, R.K., Altwicker, E.R. and Morgan III, M.H. (1999). Design and scale-up a spouted bed combustor. **Chemical Engineering Science** 54: 185-204.
- Lettieri, P., Felice, R.D., Pacciani, R. and Owoyemi, O. (2006). CFD modeling of liquid fluidized beds in slugging mode. **Powder Technology** 167: 94-103.
- Lun, C.K.K., Savage, S.B., Jeffrey, D.J. and Chepurnity, N. (1984). Kinetic theories for granular flow: inelastic particles in Couette flow and slightly inelastic particles in general flow field. **Journal of Fluid Mechanics** 140: 223-256.
- Lun, C.K.K. and Savage, S.B. (1986). The Effects of an Impact Velocity Dependant Coefficient of Restitution on Stresses Developed by Sheared Granular Materials. **Acta Mechanica** 63: 15-44.
- Marschall, K.J. and Mleczko, L. (1999). CFD modeling of an internally circulating fluidized-bed reactor. **Chemical Engineering Science** 54: 2085-2093.

- Marnasidou, K.G., Voutetakis, S.S., Tjatjopoulos, G.J. and Vasalos, I.A. (1999). Catalytic partial oxidation of methane to synthesis gas in a pilot-plant-scale spouted-bed reactor. **Chemical Engineering Science** 54: 3691-3699.
- Mathur, K.B. and Epstein, N. (1974). **Spouted Beds**. New York: Academic Press.
- Mathur, K.B. and Gishler, P.E. (1955). A technique for contacting gases with coarse solid particles. **AIChE. Journal** 1: 157-164.
- Olazar, M., San Jose, M.J., Izquierdo, M.A., Alvarez, S. and Bilbao, J. (2001a). Local bed voidage in spouted beds. **Industrial & Engineering Chemistry Research** 40: 427-433.
- Olazar, M., San Jose, M.J., Izquierdo, M.A., de Salazar, A.O. and Bilbao, J. (2001b). Effect of operating conditions on solid velocity in the spout, annulus and fountain of spouted beds. **Chemical Engineering Science** 56: 3585-3594.
- Pan, J., Cao, R. and Yuan, Y. (2006). A new approach to the mass production of titanium carbide, nitride and carbonitride whiskers by spouted bed Chemical Vapor Deposition. **Materials letters** 60: 626-629.
- Paulo Filho, M., Rocha, S.C.S. and Lisboa, A.C.L. (2006). Modeling and experimental analysis of polydispersed particles coating in spouted bed. **Chemical Engineering and Processing** 45: 965-972.
- Perry, R.H. (2007). **Perry's Chemical Engineers' Handbook**. (8th ed). New York: McGraw-Hill.
- Rasul, M.G. (2001). Spouted bed combustion of wood charcoal: performance comparison of three different designs. **Fuel** 80: 2189-2191.
- Salam, P.A. and Bhattacharya, S.C. (2006). A comparative study of charcoal gasification in two types of spouted bed reactors. **Energy** 31: 228-243.

- San Jose, M.J., Olazar, M., Alvarez, S. and Bilbao, J. (1998). Local bed voidage in conical spouted bed. **Industrial & Engineering Chemistry Research** 37: 2553-2558.
- Taghipour, F., Ellis, N. and Wong, C. (2005). Experimental and computational of gas-solid fluidized bed hydrodynamics. **Chemical Engineering Science** 60: 6857-6867.
- Versteeg, H.K. and Malalasekera, W. (1995). **An introduction to computational fluid dynamics**. New York: Longman Science & Technical.
- Vieira, M.G.A. and Rocha, S.C.S. (2004). Influence of the liquid saturation degree on the fluid dynamics of a spouted-bed coater. **Chemical Engineering and Processing** 43: 1275-1280.
- Vuthaluru, H.B. and Zhang, D. (2001). Effect of coal defluidisation during spouted-bed combustion of low-rank coals. **Fuel Processing Technology** 70: 41-51.
- Watanabe, H. and Otaka, M. (2006). Numerical simulation of coal gasification in entrained flow coal gasifier. **Fuel** 85: 1935-1943.
- Wen, C.Y. and Yu, T.H. (1966). Mechanics of fluidization. **Chemical Engineering Progress Symposium Series** 62: 100-111.
- Witt, P.J., Perry, J.H. and Schwarz, M.P. (1998). A numerical model for predicting bubble formation in a 3D fluidized bed. **Applied Mathematical Modeling** 22: 1071-1080.
- Yang, W.C. (2003). Other nonconventional fluidized beds. In: W.C. Yang (ed). **Handbook of fluidization and fluid-particle systems** (pp 545-570). New York: Marcel Dekker.

Zhong, W., Li, Q., Zhang, M., Jin, B., Xiao, R., Huang, Y. and Shi, A. (2008). Spout characteristics of a cylindrical spout-fluid bed with elevated pressure. **Chemical Engineering Journal** 139: 42-47.

CHAPTER VI

CONCLUSIONS AND RECOMMENDATIONS

6.1 Conclusions

This work involved the systematic study of preparation of activated carbon from oil-palm solid wastes, including palm shell, fiber, and kernel cake. These precursors are cheap and abundantly available solid wastes from palm-oil milling process in Chonburi Province, Thailand. The project started with the thermal analysis of oil-palm shell, fiber, and kernel to investigate their decomposition characteristics under pyrolysis in N_2 atmosphere using Thermogravimetric Analysis technique (TGA). The influences of heating rate and particle size on the pyrolysis kinetics and final yield of char were investigated. Three kinetic models, including the one step global model, two-step consecutive model, and two-parallel reaction model, were employed to describe the kinetic scheme of pyrolysis reaction of palm shell, fiber, and kernel cake. The kinetic parameters (i.e. pre-exponential factor, activation energy, and reaction order) were determined separately for each model and the model validity in describing the kinetics of pyrolysis scheme was compared. The next task is concerned with the preparation of activated carbons in a laboratory scale tube furnace using a two-step physical activation process with carbon dioxide as an oxidizing gas. The effect of activation temperature and holding time on the porous properties of produced activated carbons, including BET surface, total pore volume, percentage microporosity, and pore size distribution were studied. Subsequently, a modified

structural activation model proposed by Junpirom et al. (2005), called JDTT model, was proposed and used to describe the porosity evolution of palm shell and fiber based activated carbons during the activation process. The final part involved the CFD modeling of hydrodynamics and palm shell char activation process in a cylindrical spouted bed activator using a commercial CFD software package, ANSYS CFX 10.0. The influences of the geometric dimensions of spouted bed, initial static bed height, and particle size on the pressure drop across the bed and minimum spouting velocity were explored. The applicability of CFD simulation in describing the activation process of palm shell char in the spouted bed activator was performed and tested by comparing the predicted degree of char burn-off for several periods of activation time with results from the experiments. The following conclusions can be drawn from this study.

- From TGA study, the pyrolysis of oil-palm solid wastes commenced at the temperature above 250°C for palm shell and above 200°C for palm fiber and kernel and the pyrolysis was almost complete at the temperature around 420°C for oil-palm shell and fiber and 350°C for palm kernel cake. The pyrolysis process of oil-palm shell and fiber consisted of two distinct kinetic schemes, while only one step of kinetic scheme was observed for oil-palm kernel.
- The thermograms obtained using TGA technique showed that the particle size affects significantly on the final yield of char. The yield increased with increasing of particle size. The heating rate had a direct effect on the maximum decomposition rate, with maximum decomposition rate tending to increase and occur at higher temperatures when pyrolyzed at higher heating rates.

- The kinetic study of pyrolysis reaction using Thermogravimetric Analysis technique (TGA) proved that the one-step global model was able to describe the thermal decomposition of oil-palm kernel, while the pyrolysis processes of oil-palm shell and fiber were best described by the two-parallel reactions model proposed in this work.

- The chosen conditions used for producing the chars from oil-palm solid wastes in the tube furnace for further activation step were as follows: 600°C and 2.0 hrs for palm shell, 500°C and 1.0 hr for fiber, and 600°C and 1.0 hr for palm kernel cake, corresponding to 31.9%, 28.2% and 29.6% of char yields, respectively. This carbonization conditions chosen were well above the main devolatilization to ensure carbon-rich chars.

- For the preparation of activated carbons from oil-palm solid wastes in the tube furnace, the optimum activation conditions that gave the maximum in surface area occurred under the following conditions: 950°C and 2.0 hrs for palm shell, 850°C and 2.0 hrs for fiber, and 900°C and 2.5 hrs for palm kernel cake, corresponding to 48.4%, 51.7% and 65.9% of char burn-off, respectively. The maximum BET surface area obtainable under these preparation conditions were 1067, 522 and 789 m²/g for palm shell, fiber and kernel cake, respectively. The oil-palm shell and fiber derived activated carbons consisted mainly of microposity in their structure, while the oil-palm kernel based activated carbon was predominated with mesoporosity.

- The modified JDTT model proposed in this work predicted accurately the measured surface area and total pore volume data as a function of char burn-off. However, the pore size distribution from model prediction gave a broader pore size

distribution compared to the measured PSD, particularly for activated carbon with low degree of char burn-off.

- The experimental results of hydrodynamic study of spouted bed for air-palm shell char particles system indicated that the increasing in initial static bed height, particle size and gas inlet diameter of spouted bed gave rise to the increasing in the minimum spouting velocity of fluid. The particle size appeared to have the greatest influence on the minimum spouting velocity, while the gas inlet size contributed the least effect.

- By employing the commercial CFD software package, ANSYS CFX 10.0, the prediction on hydrodynamic behavior of spouted bed for air-char particle system was effectively performed. The CFD modeling showed the difference in the transition mechanism of solid bed from static condition to spouting beds compared to that observed experimentally. The minimum spouting velocity of air predicted from the CFD simulation was lower than that measured experimentally. The predicted hydrodynamic information of fluid and dispersed solid phase in spouted bed, including velocity profile, bed voidage distribution, and pressure drop across the bed, have been presented.

- The spouted bed activator (with geometric dimensions: 40 mm of cylindrical vessel diameter, 7.0 mm of gas inlet size, and 60° for conical base angle), operated at 1.20 times the minimum spouting velocity of CO_2 (0.182 m/s of superficial velocity) and 4.0 cm of static bed height, provided the activated carbons with lower char burn-off compared to those prepared in the laboratory tube furnace studied at the same activation temperature and time. However, for the same char burn-

off, the porous characteristics of activated carbons (BET surface area and total pore volume) prepared from both types of activators were relatively similar.

- First order kinetic scheme with respect to molar concentration of CO₂ was applied to the CFD simulation to describe the extent of reaction between the carbon and CO₂ in the spouted bed activator. By matching the predicted char burn-off obtaining from the CFD modeling at the early stage of activation process (at activation time 30 min) with the experimental data, the effective rate constant (K) in the proposed rate expression was obtained and found to be $7.57 \times 10^1 \text{ s}^{-1}$. The rate of gasification reaction can be written as the following.

$$\begin{aligned} \text{Gasification Rate} &= K[\text{CO}_2] \\ &= [7.57 \times 10^1 \text{ s}^{-1}][\text{CO}_2] \end{aligned}$$

This rate equation was successfully applied to estimate the char burn-off for the next longer period of activation time up to 180 min.

- The CFD results from the spouted-bed activator were used as input data for the modified activation model to predict satisfactorily the porous properties of activated carbon, thus completing the simulation task for activated carbon production in a spouted bed activator.

6.2 Recommendations for Future Works

- Practically, the preparation of activated carbon using the conventional physical activation technique is separated into two step, carbonization and activation with an oxidizing agent. This work in Chapter 2 was concentrated only on the kinetic

study of thermal decomposition or pyrolysis scheme of oil-palm solid wastes using thermogravimetric analysis technique which is related only to the carbonization step. It is recommended to use the thermogravimetric analysis technique to study the kinetics of gasification scheme between carbon and oxidizing gas during activation step to complete the understanding for both step of carbon preparation process. The study can be performed by heating up the char produced from carbonization step under the surrounding of N_2 flow to the desire activation temperature and then changing N_2 to the oxidizing gas to start the gasification scheme. Variation of sample mass with respect to the activation time (TG data) and its first derivative (DTG data) will be continuously collected. This useful data can then be subsequently used in the analysis of kinetic study of activation step.

- In the preparation of activated carbons from oil-palm solid wastes using the laboratory tube furnace studied in Chapter 3, the char was prepared from only one condition for each sample. The carbonization conditions affect significantly on the porous properties of the produced char which in turn have a direct effect on the porous characteristics of the final prepared activated carbon. Therefore, it is suggested that experiments be performed to study the influence of carbonization conditions on the porous properties of activated carbon.

- For the CFD simulation of hydrodynamic study performed in Chapter 5, the deviation in the prediction of hydrodynamic data can be avoided by improving the quality of numerical grid used, adjusting the model parameters, and improving the governing equations applied (such as drag force model, turbulent model, etc.). The quality of numerical grid can be improved by reducing the grid size or adjusting grid size distribution in geometry. Higher quality of numerical grid helps to reduce round-

off error occurring in computational procedure. The predicted hydrodynamic information is recommended to be pre-tested with the actual experimental data of velocity profiles and bed voidage distribution of both fluid and solid particle phases to examine the validity of model parameters and the governing equations applied.

- Because of the limitation of research time spent in this work, the CFD simulation of the spouted bed activator was performed for only one set of operating condition and geometric dimensions. Further evaluation of current CFD simulation of spouted bed activator is recommended to investigate in more details the effect of various operating conditions and geometric dimensions on the predictive information of hydrodynamic behavior and kinetic characteristics.

APPENDIX

LIST OF PUBLICATIONS

LIST OF PUBLICATIONS

1. Referred Journals

Luangkiattikhun, P., Wongkoblaph, A., and Do, D.D. (2006). Effects of graphene layer Size on the adsorption of fluids on graphitized thermal carbon black: a computer simulation study. **Adsorption Science and Technology** 24: 193-204.

Luangkiattikhun, P., Tangsathitkulchai, C., and Tangsathitkulchai, M. (2008). Non-isothermal thermogravimetric analysis of oil-palm solid wastes. **Bioresource Technology** 99: 986-997.

2. Conference Proceeding

Luangkiattikhun, P., Birkett, G.R., and Do, D.D. (2005). Characterization of microporous activated carbon using high pressure supercritical adsorption. **Chemica 2005**. Queensland, Australia.

Luangkiattikhun, P., Tangsathitkulchai, C., and Tangsathitkulchai, M. (2005). Porous characteristics of activated carbon produced from oil-palm solid wastes by carbon dioxide activation. **Carbon 2005**. Gyeongji, Korea.

Luangkiattikhun, P., Ngernyen, Y., Junpirom, S. (2006). A char gasification model for predicting the porous properties of activated carbons. **Regional Symposium on Chemical Engineering (RSCE 2006)**. Nanyang Technological University, Singapore

BIOGRAPHY

Mr. Pornthep Luangkiattikhun was born on the 15th of August 1979 in Nabon District, Nakhon Si Thammarat. After completing his high school education at his home town, he moved to Nakhon Ratchasima for his undergraduate degree. He earned his Bachelor's degree in Chemical Engineering with second class honor from Suranaree University of Technology (SUT), Nakhon Ratchasima, in 2001. He has received the Royal Golden Jubilee scholarship from the Thailand Research Fund (TRF) to study the Doctor of Philosophy (Ph.D.) Program in Chemical Engineering at SUT since the year 2001.